frontiers | Research Topics

Strong field physics and attosecond science

Edited by
Weifeng Yang, Jing Chen and Sizuo Luo

Published in
Frontiers in Physics

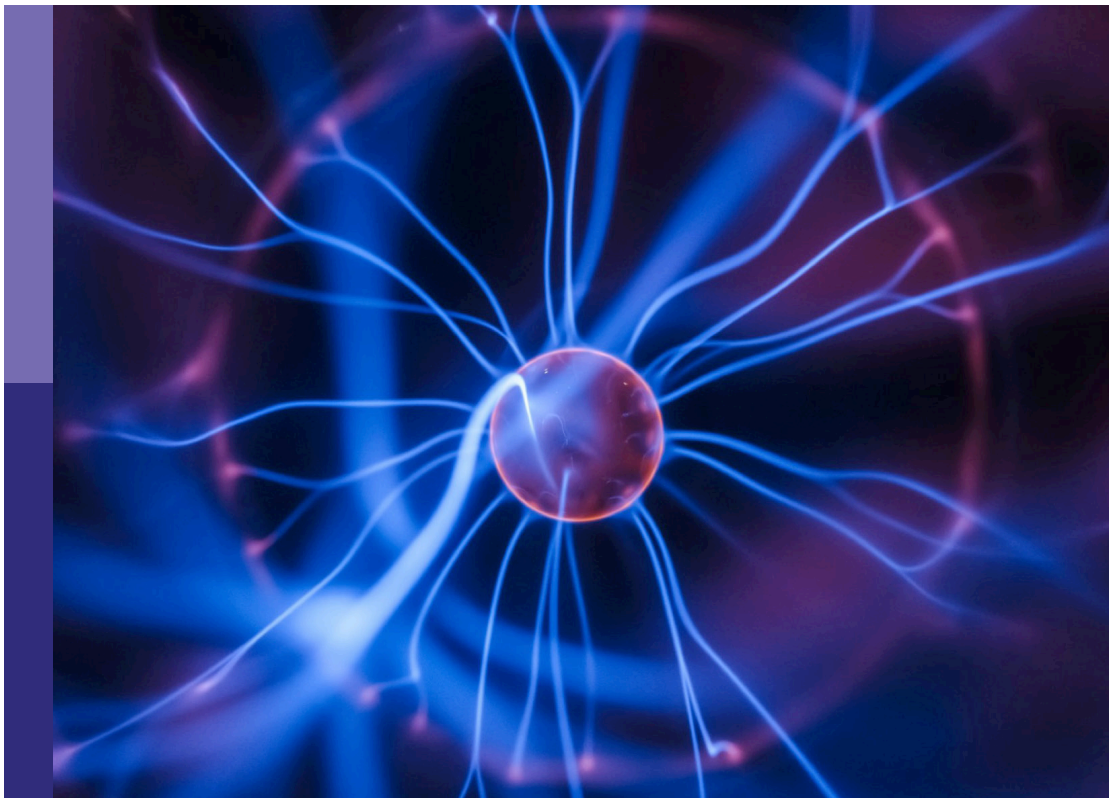

ISSN 1664-8714
ISBN 978-2-8325-2275-2
DOI 10.3389/978-2-8325-2275-2

About Frontiers

Frontiers is more than just an open access publisher of scholarly articles: it is a pioneering approach to the world of academia, radically improving the way scholarly research is managed. The grand vision of Frontiers is a world where all people have an equal opportunity to seek, share and generate knowledge. Frontiers provides immediate and permanent online open access to all its publications, but this alone is not enough to realize our grand goals.

Frontiers journal series

The Frontiers journal series is a multi-tier and interdisciplinary set of open-access, online journals, promising a paradigm shift from the current review, selection and dissemination processes in academic publishing. All Frontiers journals are driven by researchers for researchers; therefore, they constitute a service to the scholarly community. At the same time, the *Frontiers journal series* operates on a revolutionary invention, the tiered publishing system, initially addressing specific communities of scholars, and gradually climbing up to broader public understanding, thus serving the interests of the lay society, too.

Dedication to quality

Each Frontiers article is a landmark of the highest quality, thanks to genuinely collaborative interactions between authors and review editors, who include some of the world's best academicians. Research must be certified by peers before entering a stream of knowledge that may eventually reach the public - and shape society; therefore, Frontiers only applies the most rigorous and unbiased reviews. Frontiers revolutionizes research publishing by freely delivering the most outstanding research, evaluated with no bias from both the academic and social point of view. By applying the most advanced information technologies, Frontiers is catapulting scholarly publishing into a new generation.

What are Frontiers Research Topics?

Frontiers Research Topics are very popular trademarks of the *Frontiers journals series*: they are collections of at least ten articles, all centered on a particular subject. With their unique mix of varied contributions from Original Research to Review Articles, Frontiers Research Topics unify the most influential researchers, the latest key findings and historical advances in a hot research area.

Find out more on how to host your own Frontiers Research Topic or contribute to one as an author by contacting the Frontiers editorial office: frontiersin.org/about/contact

Strong field physics and attosecond science

Topic editors

Weifeng Yang — Hainan University, China

Jing Chen — Institute of Applied Physics and Computational Mathematics (IAPCM), China

Sizuo Luo — Lund University, Sweden

Citation

Yang, W., Chen, J., Luo, S., eds. (2023). *Strong field physics and attosecond science*. Lausanne: Frontiers Media SA. doi: 10.3389/978-2-8325-2275-2

Table of contents

frontiers | Frontiers in Physics

TYPE Editorial
PUBLISHED 24 January 2023
DOI 10.3389/fphy.2023.1135021

OPEN ACCESS

EDITED AND REVIEWED BY
Lorenzo Pavesi,
University of Trento, Italy

*CORRESPONDENCE
Weifeng Yang,
wfyang@hainanu.edu.cn
Sizuo Luo,
luosz@jlu.edu.cn
Jing Chen,
chen_jing@iapcm.ac.cn

SPECIALTY SECTION
This article was submitted to Optics and Photonics, a section of the journal Frontiers in Physics

RECEIVED 31 December 2022
ACCEPTED 10 January 2023
PUBLISHED 24 January 2023

CITATION
Yang W, Luo S and Chen J (2023), Editorial: Strong field physics and attosecond science.
Front. Phys. 11:1135021.
doi: 10.3389/fphy.2023.1135021

Editorial: Strong field physics and attosecond science

Weifeng Yang[1]*, Sizuo Luo[2,3]* and Jing Chen[4]*

[1]Department of Physics, School of Science, Hainan University, Haikou, China, [2]Department of Physics, Lund University, Lund, Sweden, [3]Institute of atomic and molecular physics, Jilin University, Changchun, China, [4]Institute of Applied Physics and Computational Mathematics, Beijing, China

KEYWORDS

strong field, ultrafast optical, attosecond science, multiphoton ionization, above-threshold ionization, tunneling ionization, double ionization, high harmonic generation

Editorial on the Research Topic
Strong field physics and attosecond science

Light-matter interaction is an essential process in nature. The development of light pulses in the few-femtosecond to attosecond duration allows scientists to tackle ultrafast processes in atoms, molecules, and more complex systems. Many new strong field phenomena have attracted wide attention, such as multiphoton ionization, above-threshold ionization, non-sequential double ionization, high-order harmonic generation, attosecond pulse generation, coherent EUV emission, etc. These phenomena have been of interest from the perspectives of both fundamental physics and potential applications. In this Research Topic, authors address several recent developments and applications of ultrafast technology in strong field physics and contribute eight quality articles as explained below.

The studies of high-order harmonic generation promoted the development of non-linear optics from IR to XUV. Recently, Yang et al. experimentally investigated enhanced coherent EUV emission from Rydberg atoms. Substantial neutral atoms can be excited after tunneling in a strong laser field, in the process known as frustrated tunneling ionization. The generation of coherent emission from the excited-state atoms produced by the frustrated tunneling ionization is demonstrated to be dependent on the chirp of the laser pulse. This chirp dependence also provides a new way to investigate the dynamics of Rydberg states. Kong et al. explored the influence of mechanical strains on the high-order harmonic generation in the monolayer hexagonal boron nitride crystal by using time-dependent density functional theory. They found that the band structure is sensitive to the structural deformation modulated by strains. This result may be useful in probing lattice deformations in crystals and heuristic to enhance the optoelectronic efficiency of solid-state nano-devices.

Novel non-linear effects triggered by the femtosecond laser filamentation have attracted widespread attention, such as laser power density clamping in the filamentation, super-continuous white light, and self-steepening effects. In this Research Topic, Li et al. investigated the fluorescence emission of the multiple combustion intermediates from the femtosecond filamentation with an ultrashort laser pulse at the wavelength of 1,030 nm, from which they proposed an optimizing rule to improve the signal-to-noise ratio of the fluorescence emission intensity in the ethanol/air flame using femtosecond laser filament excitation. This research promotes a further application of the femtosecond laser pulses to simultaneously monitor the multiple combustion intermediates.

Plenty of ultrafast processes are directly triggered by photoionization, which is the foundation of many ultrafast phenomena and is very useful in revealing microscopic physical mechanisms. For example, valence electron excitation plays a critical role in

strong-field processes, and a recent experiment shows that, in addition to the direct ionization of low-lying molecular orbital, the bond-softening mechanism with laser coupling between the ground state and an electronically excited state in a polyatomic molecule can significantly contribute to electron excitation Hu et al. Amplitude and phase describe the quantum attributes of electron wavepackets, Neoričić et al. studied resonant two-photon ionization of helium atoms via the 1s3p, 1s4p, and 1s5p states, and the phase of the photoelectron wavepackets was measured by an attosecond interferometric technique. With the ability to combine good angular resolution, high energy resolution, and attosecond-time-resolution in the experiments, the fast phase variations across emission angles and energies were measured. Decoding the amplitude and phase information angularly and spectrally for an electron wavepacket from a photoemission provides the ability to record 3D movies of photoelectrons at the attosecond time scales. In addition, over-barrier ionization is an interesting Research Topic in strong-field physics. Wang et al. investigated this process of hydrogen atoms in intense circularly and elliptically polarized laser fields, which demonstrates that the photoelectron momentum distributions show a spiral distribution. They further explored the relationship between the instantaneous ionization rate and initial transverse momentum in over-barrier ionization and pointed out that the non-adiabatic effect and long range Coulomb interaction play important roles. Wang et al. examined the photoelectron momentum distribution of hydrogen atoms in the super-intense ultra-short high-frequency pulses by numerically solving the time-dependent Schrödinger equation. They observed dynamic interference effects even in a tightly bounded system when there are circularly polarized pulses present in addition to the linearly polarized laser field. The Coulomb re-scattering effect is responsible for the observed substantial variations in photoelectron momentum distributions by linearly and circularly polarized extreme ultraviolet pulses. On the other hand, non-sequential double ionization has drawn much attention because it contains extensive information about collision dynamics and electron-electron correlation. Ben et al. investigated this from Ar atoms in the combined fields of linearly polarized laser and circularly polarized laser through 3D semiclassical simulations. By tuning the delay time between the two laser pulses, the double ionization yields and recollision trajectories with different return times can be controlled. This research shows that the electron dynamics in one or few optical cycles can be controlled in multicycle laser fields, which do not have to be limited to few-cycle laser pulses.

In conclusion, this Research Topic presents the latest advances and trends concerning strong-field physics and attosecond science. Our special thanks to the Frontiers in Physics team for the technical assistance with publishing. Many more efforts are still ongoing in this fascinating area. We expect that this field will attract increasing attention and benefit potential applications in the near future.

Author contributions

All authors listed have made a substantial, direct, and intellectual contribution to the work and approved it for publication.

Acknowledgments

We would like to acknowledge all the authors, reviewers, editors, and publishers, who have supported this Research Topic.

Conflict of interest

The authors declare that the research was conducted in the absence of any commercial or financial relationships that could be construed as a potential conflict of interest.

Publisher's note

frontiers | Frontiers in Physics

TYPE Original Research
PUBLISHED 08 September 2022
DOI 10.3389/fphy.2022.976734

OPEN ACCESS

EDITED BY
Weifeng Yang,
Hainan University, China

REVIEWED BY
Hongcheng Ni,
East China Normal University, China
Yueming Zhou,
Huazhong University of Science and Technology, China

*CORRESPONDENCE
Yunquan Liu,
yunquan.liu@pku.edu.cn

SPECIALTY SECTION
This article was submitted to Optics and Photonics,
a section of the journal
Frontiers in Physics

RECEIVED 23 June 2022
ACCEPTED 21 July 2022
PUBLISHED 08 September 2022

CITATION
Wang J, Guo Z, Fang Y, Yu X and Liu Y (2022), Over-barrier ionization of hydrogen atom in intense circular and elliptical laser fields.
Front. Phys. 10:976734.
doi: 10.3389/fphy.2022.976734

Over-barrier ionization of hydrogen atom in intense circular and elliptical laser fields

Jiguo Wang[1], Zhenning Guo[1], Yiqi Fang[1], Xiaoyang Yu[1] and Yunquan Liu[1,2,3,4]*

[1]Department of Physics and State Key Laboratory for Mesoscopic Physics, Peking University, Beijing, China, [2]Collaborative Innovation Center of Quantum Matter, Beijing, China, [3]Collaborative Innovation Center of Extreme Optics, Shanxi University, Taiyuan, China, [4]Center for Applied Physics and Technology, HEDPS, Peking University, Beijing, China

We investigate the over-barrier ionization of hydrogen atoms in intense circularly and elliptically polarized laser fields. By solving the time-dependent Schrödinger equation, we simulate the photoelectron momentum distributions with the peak laser field intensity ranging from tunneling ionization to over-barrier ionization regime. It is shown that the photoelectron momentum distributions reveal a spiral distribution in the over-barrier ionization regime, which is in contrast with the typical donut distribution sculpted by above-threshold ionization peaks in the tunneling ionization regime. To analyze the intriguing photoelectron behavior, we further develop a semi-classical model by considering the non-adiabatic effect and the depletion effect of the ground state. The photoelectron momentum distributions calculated by the semi-classical model agree well with the results of the time-dependent Schrödinger equation. Based on these results, we further explore the relationship between the instantaneous ionization rate and initial transverse momentum in over-barrier ionization. It is worth noting that such a relationship is not easy to be clearly revealed in tunneling ionization regime as the final electron momentum is significantly modified by the inter-cycle interference. Moreover, we also show that the non-adiabatic effect and long-range Coulomb interaction play important roles in the over-barrier ionization.

KEYWORDS

over-barrier ionization, photoelectron momentum spectrum, time-dependent schrödinger equation (TDSE), semi-classical model, strong field physics

Introduction

In the strong-field community, when atoms and molecules are exposed in intense laser fields, a series of interesting physical phenomena can be revealed, including the above-threshold ionization (ATI) [1–3], molecular dissociation, Coulomb explosion [4–6], and non-sequential double (multiple) ionization [7–9]. As well known, strong-field ionization can be characterized using the Keldysh parameter $\gamma = \omega(2I_p)^{1/2}/E$ [10], where ω, E, I_p are the angular frequency of driving light, electric field strength, and ionization potential of atoms, respectively. When the amplitude of the driving laser field is

small ($\gamma \gg 1$), the ionization is dominated by multi-photon ionization (MPI) [11–13]. In this case, the photoionization tends to be depicted in the frequency picture, and its ionization rate is proportional to I^n, where I is the laser intensity and n is the number of photons absorbed. When the amplitude of the driving laser field is large ($\gamma \ll 1$), the Coulomb potential of atoms is pronouncedly bent to be a barrier. Then the electrons can tunnel through the suppressed barrier into the classical region, which is called tunneling ionization (TI) [14–18]. So far, multi-photon ionization and tunneling ionization have been intensively studied.

If the laser intensity further increases, the suppressed Coulomb barrier could be lower than the energy of the ground state atom. The bounded electron would be liberated from the parent ion directly, which is called over barrier ionization (OBI) [19]. The threshold strength of the driving laser field for OBI can be estimated by $I_p^2/4Z$ (Here Z is the charge of the residual ion) [20]. This formula is derived on the assumption that the electrons only move in one-dimensional (1D) Cartesian space. Tong and Lin have developed an empirical formula to describe the ionization rate over a wide range of laser intensity, including the OBI regime [21]. Meanwhile, several experimental and theoretical studies of the OBI have been reported. In Ref. [22], the authors have made a systematic scan of the ionization rate of noble gases from the TI to OBI regime. Using the magneto-optically trapped target reaction microscope (MOTREMI), the photoelectron energy and momentum spectra of single ionization of lithium in the OBI regime have been measured [23], and these results were then analyzed by solving the time-dependent Schrödinger equation (TDSE) [24]. By measuring the electron transverse momentum distributions of the neon atom in $^3P_2$ metastable state near the OBI regime, Ivanov, et al., showed that the cusp-like structure of transverse momentum is independent of laser ellipticity in OBI regime [25, 26]. Recently, by using MOTREMI, the momentum distributions of Rb^{n+} recoil ions up to $n = 4$ have been measured, which exhibit multiband structures as the light field polarization varies from linear polarization to circular polarization [27].

In this paper, we theoretically study the photoionization of hydrogen atoms driven by intense elliptically and circularly polarized laser fields. By solving TDSE, we show that the photoelectron momentum distributions reveal a unique helical structure in the OBI regime, which has been rarely discovered in the MPI and TI regimes. To interpret the underlying mechanism, we further develop a semi-classical model (SCM), in which the depletion effect of ground state wavefunction and non-adiabatic effect have been considered. The simulated results of the SCM and TDSE show a great agreement. We reveal that the photoelectrons emitted in the leading edge of the laser pulse are streaked into momentum-resolved final states, allowing one to establish the time-to-angle mapping. Utilizing the correspondence between the final momentum and ionization moments, we explore the initial condition of ejected photoelectrons. The simulated results indicate that the non-adiabatic effect and long-range Coulomb potential still play important roles in OBI.

Theoretical methods

Quantum simulation

We obtain the photoelectron momentum distributions by numerically solving the TDSE based on the split-operator spectral (SOS) method [28–30]. In principle, the SOS method is suitable for all linear eigenvalue issues involving any number of dimensions, and it does not require special basis functions or potentials in the form of analytic expression. However, to ensure the accuracy of SOS method, an adequate sampling rate in space and time is necessary [31–33].

When an intense laser field interacts with a hydrogen atom, the TDSE within single-electron approximation and dipole approximation is given by (unless otherwise stated, atomic units ($m_e = e = \hbar = 4\pi\varepsilon_0 = 1$) are used throughout this paper)

$$i\frac{\partial}{\partial t}\varphi(\mathbf{r},t) = \left[-\frac{\nabla^2}{2} + V(\mathbf{r},t)\right]\varphi(\mathbf{r},t) \tag{1}$$

where $\mathbf{r}$ is the electronic coordinate measured from the center of the nucleus and $V(\mathbf{r},t)$ is the synthesized potential imposed on the electron, including the action of hydrogen ion and laser field. The synthesized potential can be written as

$$V(\mathbf{r},t) = -\frac{1}{|\mathbf{r}|} - \mathbf{E}(t)\cdot\mathbf{r} \tag{2}$$

where $\mathbf{E}(t)$ is the electric field of driving laser pulses. We notice that the synthesized potential reaches its maximum $V_{max} = -2\sqrt{|\mathbf{E}(t)|}$ at the distance of $|\mathbf{r}| = \sqrt{1/|\mathbf{E}(t)|}$. Therefore, if the laser electric field is strong enough, the synthesized potential can be lower than the ionization potential of atoms, namely $V_{\max} < -I_p$. In this case, the strong-field ionization enters into the OBI regime. Specifically, for a hydrogen atom ($I_p = 0.5$ a.u.), we can estimate that the OBI occurs when the laser field strength is larger than $E_{OBI} = 0.0625$ a.u., corresponding to the laser intensity $\sim 2.74 \times 10^{14}$ W/cm^2.

To find a clear physical picture of the OBI, we use elliptically and circularly polarized laser fields in the simulation. The selection of these two laser fields can avoid the rescattering of ejected electrons so that we can highlight the effect taken by the laser strength. Here, the electric field $\mathbf{E}(t)$ is given by

$$\mathbf{E}(t) = E\cdot f(t)\left\{\sin(\omega t+\phi)\cdot\mathbf{e}_x + \varepsilon\cos(\omega t+\phi)\cdot\mathbf{e}_y\right\} \tag{3}$$

where ε, ω and ϕ are the laser ellipticity, angular frequency, and carrier envelope phase (CEP), respectively.$f(t)$=sin^2($\omega t/2n$) is the sine-square temporal envelope, where n is the cycle number of the laser pulse and here it is chosen to be $n = 10$. For a sufficiently

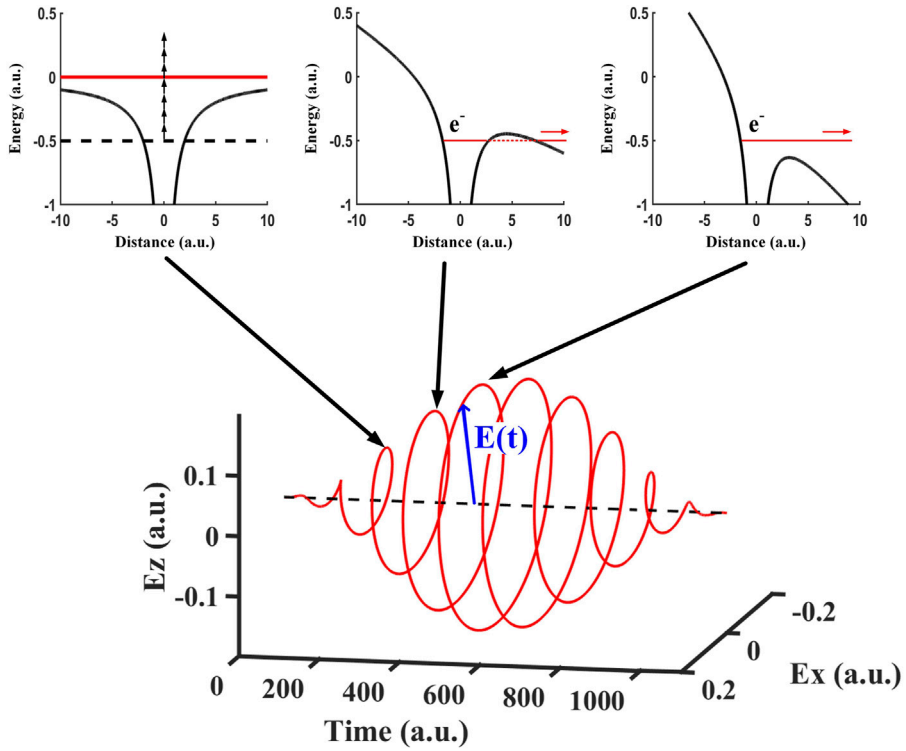

FIGURE 1
The electric field of a circularly polarized pulse laser with the peak electric field strength of 0.2 a.u. Three insets represent three different kinds of ionization and mark the corresponding electric field strength. The blue arrow represents the instantaneous electric field strength.

strong circularly polarized pulse laser, as the electric field increases the ionization model changes from MPI to TI, and finally to OBI within a single laser pulse, as shown in Figure 1. We have performed a series of simulations with the center wavelength of 800 nm, and the peak intensity varying from 1.1×10^{14} W/cm^2 to 6.3×10^{15} W/cm^2, corresponding electric field strength changing from 0.04 a.u. to 0.3 a.u.

We utilize a symmetrically split operator algorithm for advancing the solution of TDSE by an incremental time Δt. This can be expressed as

$$\psi(\mathbf{r}, t+\Delta t) = \exp\left(\frac{i\Delta t\nabla^2}{4}\right)\exp(-i\Delta t V)\exp\left(\frac{i\Delta t\nabla^2}{4}\right)\psi(\mathbf{r}, t) + O(\Delta t^3) \tag{4}$$

Here, $\psi(\mathbf{r}, t=0)$ is the initial wavefunction of the electron, which can be prepared by imaginary-time propagation [34]. Eq. 4 is equivalent to a free particle propagation over a half time increment, a phase change from the action of the potential over a total time increment, and a free propagation over the remaining half increment. The operator $\exp(i\Delta t\nabla^2/4)$ applied to $\psi(\mathbf{r}, t)$ is difficult to calculate in coordinate space. However, it can be realized by using the band-limited Fourier series representation.

$$\psi(\mathbf{r}, t) = \sum_{m=-\frac{N}{2}+1}^{\frac{N}{2}} \sum_{n=-\frac{N}{2}+1}^{\frac{N}{2}} \psi_{mn}(t)\exp\left[i\frac{2\pi}{L}mx + ny\right] \tag{5}$$

After the electron wavefunction being operated by $\exp(i\Delta t\nabla^2/4)$, we will have

$$\psi_{mn}\left(t+\frac{\Delta t}{2}\right) = \psi_{mn}(t)\exp\left[-\left(\frac{i\Delta t}{4}\right)\left(\frac{2\pi}{L}\right)^2(m^2+n^2)\right] \tag{6}$$

where N is the number of grid points, and L is the length of the computational grid. At the end of the pulse, the wave function is propagated for another three cycles to make sure that the low-energy electrons could travel far enough from the parent ion to be collected in calculation. At each time step t_j, we extract the ionized part $\psi_{\text{ionized}}(\mathbf{r}, t_j)$ from the total wave function,

$$\begin{aligned}\psi(\mathbf{r}, t_j) &= \psi(\mathbf{r}, t_j)[1 - F_A(\mathbf{r}, R_c)] + \psi(\mathbf{r}, t_j)F_A(\mathbf{r}, R_c)\\ &= \psi_{\text{unionized}}(\mathbf{r}, t_j) + \psi_{\text{ionized}}(\mathbf{r}, t_j),\end{aligned} \tag{7}$$

where $F_A(\mathbf{r}, R_c) = [1 + \exp(-\frac{|\mathbf{r}|-R_c}{\Delta})]^{-1}$ is a smooth absorbing function, and R_c is the boundary to distinguish if the electron

is ionized or not. Then the ionized wavefunction would be converted into momentum space.

$$\phi\left(\mathbf{p}, t_j, t_j\right) = \frac{1}{2\pi}\int \psi_{\text{ionized}}\left(\mathbf{r}, t_j\right)\exp\left\{-\mathrm{i}\left[\mathbf{p} + \mathbf{A}\left(t_j\right)\right]\cdot\mathbf{r}\right\}\mathrm{d}\mathbf{r} \quad (8)$$

where $\mathbf{A}$ is the vector potential of the laser field, and analytically propagates under the Volkov Hamiltonian to the end of the simulation,

$$\phi\left(\mathbf{p}, t_{\text{end}}, t_j\right) = \exp\left\{-i\int_{t_j}^{t_{\text{end}}}\frac{1}{2}\left[\mathbf{p} + \mathbf{A}\left(t\right)\right]^2\mathrm{d}t\right\}\phi\left(\mathbf{p}, t_j, t_j\right) \quad (9)$$

At last, we obtain the total photoelectron momentum distribution $\phi\left(\mathbf{p}, t_{\text{end}}\right) = \sum_j \phi\left(\mathbf{p}, t_{\text{end}}, \mathrm{t}_j\right)$ by summing the wave packets in momentum space ionized at different t_j.

Semiclassical model

The physical process of SCM is based on the traditional strong-field ionization model [35–37] with the improvement of the initial momentum distribution and the depletion effect. The initial tunneling coordinates of tunneling electrons are obtained by the saddle-point approximation [38, 39], in which the non-adiabatic effect and phase in the ionization process are included in the SCM [40, 41]. In the saddle-point method, the electron transition amplitude between the ground state and Volkov state is approximated by summing over the quantum orbits [1, 42],

$$M\left(\mathbf{p}\right) = \sum_s \frac{2^{-\frac{1}{2}}\left(2I_p\right)^{\frac{5}{4}}}{\mathbf{E}\left(t_s\right)\cdot\left[\mathbf{p} + \mathbf{A}\left(t_s\right)\right]}\exp\left(iS_{\mathrm{S},\mathbf{p}}\right) \quad (10)$$

where $S_{\mathrm{S},\mathbf{p}} = -\int \mathrm{d}t\{\frac{1}{2}[\mathbf{p} + \mathbf{A}\left(t_s\right)]^2 + I_p\}$ is the classical action and t_s is the saddle point of time, given by

$$\frac{\partial S_{\mathrm{S},\mathbf{p}}}{\partial t} = \frac{1}{2}\left[\mathbf{p} + \mathbf{A}\left(t_s\right)\right]^2 + I_p = 0 \quad (11)$$

The initial momentum and position are given by $\mathbf{v} = \mathbf{p} + \mathbf{A}\left(\mathrm{Re}\{t_s\}\right)$, $\mathbf{r} = \mathrm{Re}\{\int_{t_s}^{t_r}\mathrm{d}t\left[\mathbf{p} + \mathbf{A}\left(t\right)\right]\}$, where $t_r = \mathrm{Re}\{\mathrm{t_s}\}$ is the ionization moment. The motion of released electron is obtained by solving Newton's motion equations $\ddot{\mathbf{r}} = -Z\mathbf{r}/r^3 - \mathbf{E}\left(t\right)$. This kind of practice uses for reference from Coulomb-corrected strong-field approximation, which can deal well with the influence of Coulomb potential [43].

Besides, the depletion of ground state wavefunction cannot be ignored because of the high ionization rate in the intense laser field. We can suppose the instantaneous ionization rate can be expressed by the product of static field ionization rate and residual electron probability.

$$\frac{\mathrm{d}P_{\text{ionized}}\left(t\right)}{\mathrm{d}t} = P_{\text{bound}}\left(\mathrm{t}\right)\cdot W\left(\mathbf{E}\left(t\right)\right) \quad (12)$$

where $P_{\text{ionized}}\left(t\right) = 1 - P_{\text{bound}}\left(t\right) = \exp\{-\int_{-\infty}^{t} W\left(\mathbf{E}\left(\mathrm{t}\right)\right)\mathrm{d}t\}$ is the cumulative ionization probability in a laser pulse and $W\left(\mathbf{E}\left(\mathrm{t}\right)\right)$ is an empirically-corrected formula for static field ionization rate [21]. Here, since the OBI is driven by the circularly and elliptically polarized laser fields, the rescattering effect of electrons is suppressed.

Results and discussion

In Figure 2, we show the two-dimensional photoelectron momentum distributions simulated by TDSE, for a wide range of electronic field strength from $E = 0.04$ a.u. to 0.3 a.u., corresponding to the transition from TI to OBI regime. In the TI regime (Figure 2A), the photoelectron momentum spectrum has a donut-shaped distribution sculpted by an obvious ATI structure resulting from inter-cycle interference [11]. With the conversion of the electric field strength from the TI regime to the OBI regime, the photoelectron momentum spectra show characteristic spiral distributions, along with the disappearance of ATI peaks, as shown in Figures 2B–D. The spiral structures are gradually stretched with the increasing electric field strength. These phenomena have been never revealed in previous works. Additionally, one can find these spiral-shaped structures are nearly overlapped with the negative vector potentials of the driving lasers (the red lines in Figure 2).

Within the strong-field approximation, the final momentum of the measured electron is determined by the negative vector potential $-\mathbf{A}\left(t_i\right)$, where t_i is the ionization instant [44, 45]. In the OBI regime, the field-strength dependent ionization rate is high enough for saturation so that most electrons are ionized in the rising edge of a laser pulse. Because the shape of the negative vector potential is a spiral curve in the rising edge, the photoelectron distributions show a similar spiral structure in momentum space, as shown in Figures 2B–D. Besides, one can note that the electrons ionized at different moments of the same laser cycle would be mapped into different directions, and the electrons ionized in different laser cycles would be mapped into different radii in momentum space. Therefore, the inter-cycle interference patterns have been suppressed in the OBI regime, resulting in the disappearance of ATI peaks. Moreover, the momentum-resolved final states of electrons mean that one can establish the one-to-one correspondence between final momenta and ionization moments via the relation $\mathbf{p} = -\mathbf{A}\left(t_i\right)$, which will be helpful to investigate the initial condition of ejected photoelectrons.

To reveal the physical mechanism of OBI, we have further calculated the photoelectron momentum distributions by the SCM including the non-adiabatic effect and the depletion of bound electrons. The simulated results are shown in Figure 3, which agree well with the TDSE simulation. In addition to reproducing the momentum distributions of TDSE, the SCM also offers an intuitive description of the initial condition of the ejected photoelectrons in the OBI regime. In SCM, we can give the instantaneous ionization rate with the depletion effect of

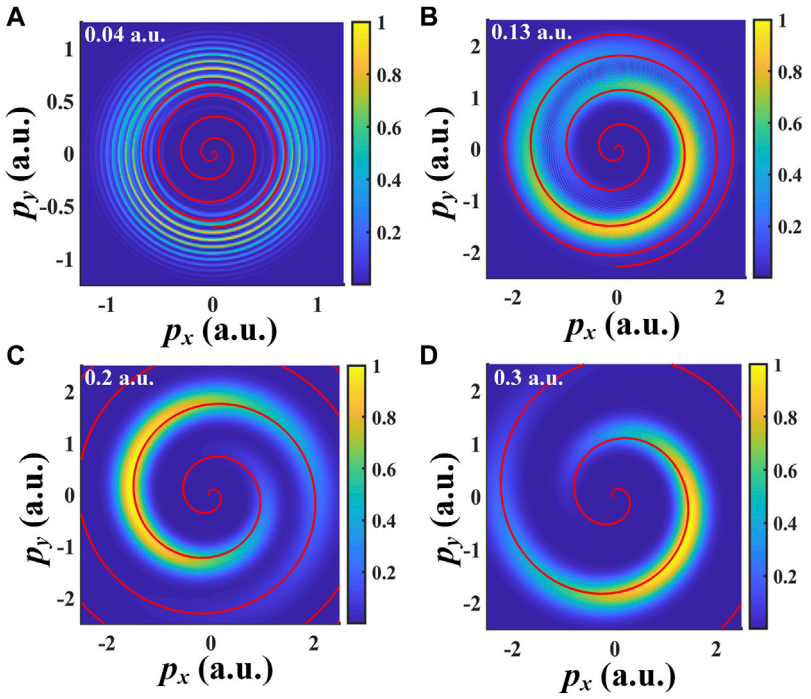

FIGURE 2
The photoelectron momentum spectra calculated by TDSE, corresponding electric field strength are **(A)** 0.04 a.u. **(B)** 0.13 a.u. **(C)** 0.2 a.u. **(D)** 0.3 a.u. The field-driven momentum $-\mathbf{A}(t_i)$ is shown by the red line.

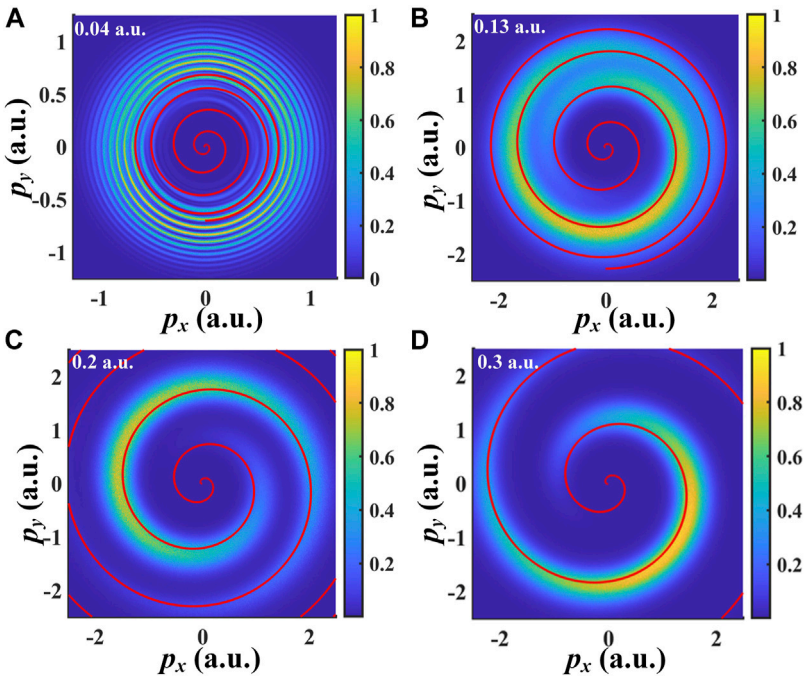

FIGURE 3
The photoelectron momentum spectra calculated by SCM, corresponding electric field strength are **(A)** 0.04 a.u. **(B)** 0.13 a.u. **(C)** 0.2 a.u. **(D)** 0.3 a.u. The field-driven momentum $-\mathbf{A}(t_i)$ is shown by the red line.

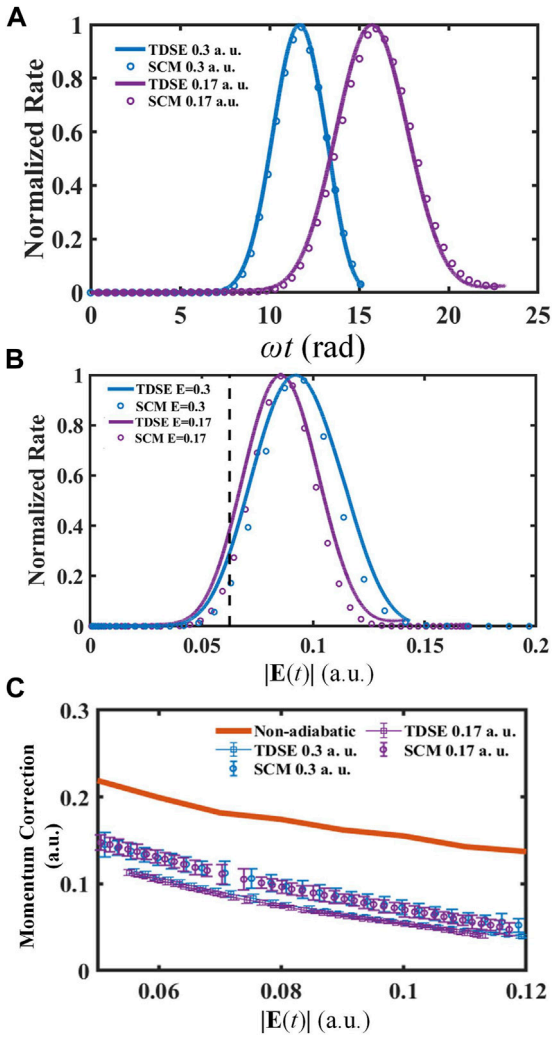

FIGURE 4
The comparisons between TDSE and SCM. **(A)** The ionization rates normalized by the maximum. The blue and purple lines represent the ionization rates given by TDSE with different peak electric field strengths, 0.3 and 0.17 a.u. The blue and purple circles represent the counterparts in SCM. **(B)** The same as **(A)** but the horizontal ordinate is the instantaneous electric field strength in rising edge instead of time. The black dotted line represents the threshold of the OBI regime, E_{OBI} = 0.0625 a.u. **(C)** The red line represents the correction of initial transverse momentum deviation from non-adiabatic effect. The bule and purple lines represent the total momentum correction $\mathbf{p}_i + \mathbf{p}_{cc}$ in TDSE, and the blue and purple circles represent the counterparts in SCM.

bound electrons, as indicated in Figure 4A. In order to compare the ionization rate under the same electric field strength conveniently, we also calculate the ionization rate as a function of the instantaneous electric field, as shown in Figure 4B. The black dotted line represents the threshold to come into the OBI regime for a hydrogen atom (E_{OBI}0.0625 a.u.). When the electric field is weaker than the threshold field strength, the instantaneous electric field dominates the process, and the rate increases exponentially as the field strength increases. However, if the electric field is larger than the threshold, the increase of ionization rate gradually slows down and even begins to decline due to the depletion effect of bounded electron wavefunction. In the past, the instantaneous ionization rate is only a function of instantaneous electric field strength. But after considering the depletion effect, the pulse envelope, determined by the peak electric strength E, also plays an important role. One can note the curve with E0.3 a.u. (blue circles in Figure 4B) is shifted to the right than the curve with E0.17 a.u. (purple circles), which means that with higher peak strength, there are more electrons remaining unionized until the laser field reaches a higher intensity. Utilizing the one-to-one correspondence between final momenta and ionization moments, we can extract the ionization rates from the momentum distributions calculated by TDSE, represented by blue and purple lines in Figure 4A,B, which support the conclusions of SCM.

As seen in SCM, the non-adiabatic ionization coordinates are important ingredients for the simulation. In the next step, we explore the initial transverse momentum deviation, which is included in the difference between the negative vector potential and the most probable final momentum. Taking the non-adiabatic effect into account, one can obtain the correction of initial transverse momentum [46], represented by the red line in Figure 4C. Then it was also influenced by the Coulomb potential in the propagation process after ionized. Therefore, the final momentum can be expressed by $\mathbf{p} = -\mathbf{A}(t_i) + \mathbf{p}_i + \mathbf{p}_{cc}$, where $\mathbf{p}_i$ is the initial transverse momentum deviation and $\mathbf{p}_{cc}$ is the correction due to the Coulomb potential. Utilizing the correspondence between the final electron momentum and the ionization moment, one can draw the total corrections $\mathbf{p}_i + \mathbf{p}_{cc}$ of both SCM and TDSE by calculating $\mathbf{p} - [-\mathbf{A}(t_i)]$, which are shown in Figure 4C. Although there is no reliable method to directly obtain the initial transverse momentum deviation $\mathbf{p}_i$ from TDSE, the agreement of total correction $\mathbf{p}_i + \mathbf{p}_{cc}$ between SCM and TDSE suggests the correction of initial momentum in SCM is enlightening. Besides, by comparing the results with different peak electric field strengths (0.3 a.u. represented by blue line and circles, and 0.17 a.u. represented by purple line and circles), it is intuitive to find the momentum correction is only dependent on the instantaneous electric field. And as the electric field strength increases, the momentum corrections become smaller. One can see that there is a tiny difference between the results of TDSE and SCM. This discrepancy is caused due to insufficient consideration of the change of barrier width caused by the increase of laser intensity in the SCM.

We further calculate the photoelectron momentum distributions in the OBI regime by using a laser pulse with different ellipticities and CEPs. The results are shown in Figure 5, where the left column is calculated by TDSE and the right column is calculated by SCM. As shown in Figure 5A,B, for an elliptically polarized laser field with E0.2 a.u., ε0.6, the shape of electron momentum spectra is squashed along the minor axis

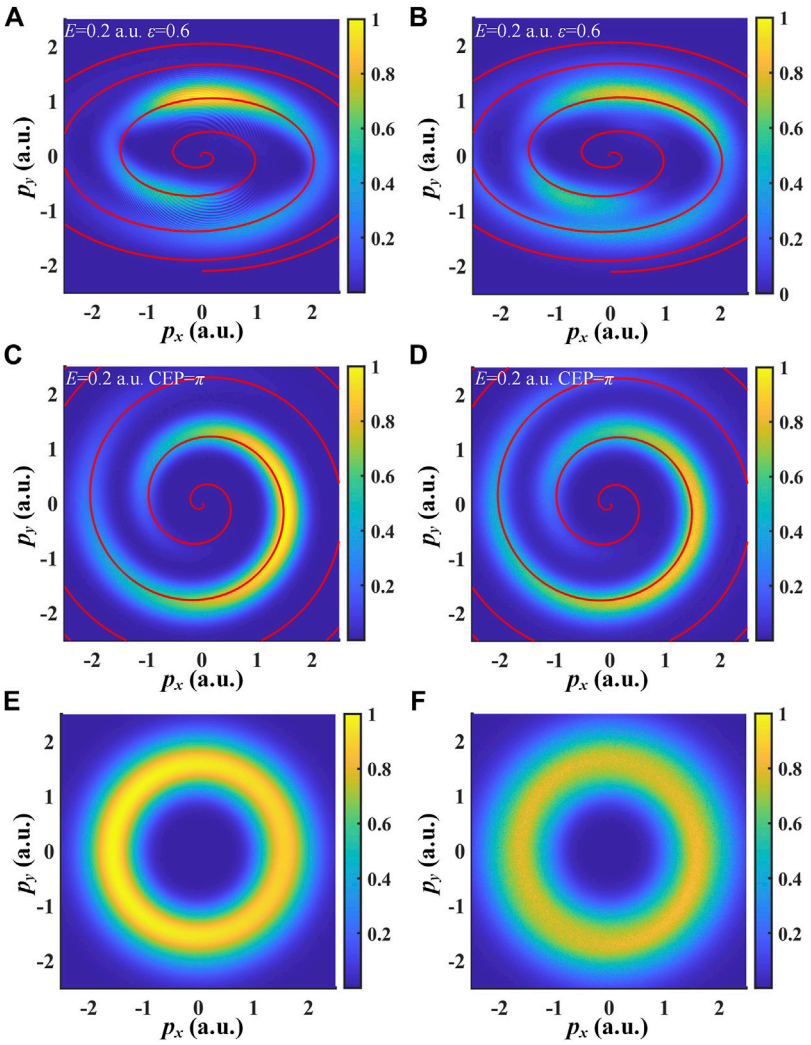

FIGURE 5
The calculated photoelectron momentum distributions for different ellipticities and CEPs. The left column is calculated by TDSE and the right column is calculated by SCM. **(A,B)** E = 0.2 a.u., ε = 0.6, CEP = 0; **(C,D)** E = 0.2 a.u., ε = 1, CEP = π; **(E,F)** the superposition of photoelectron spectra with different CEPs.

due to the change of negative vector potential. There are several extrema of ionization rate because the electric field strength is not monotonous any longer at the rising edge. For a long laser pulse, the CEP is always thought to have no influence. But in the OBI regime, when CEP is varied, the shape of negative vector potential will be rotated and result in a rotated photoelectron momentum spectrum. The results are shown in Figure 5C,D, using a circularly polarized laser with peak electric field strength of 0.2 a.u. and CEP of π. This suggests that in order to perform a strong-field ionization experiment with a laser intensity in the OBI regime, the CEP of the pulse laser should be stabilized. Otherwise, the final electron momentum distribution will be averaged by the results of different laser CEPs, and thus it reveals an annulus as shown in Figure 5E,F.

Conclusion

In conclusion, we have theoretically studied the OBI of hydrogen atoms under the intense circularly and elliptically polarized laser pulses. The simulated photoelectron momentum distributions reveal an interesting spiral structure, and such structure can be reproduced by the modified SCM. It suggests that the non-adiabatic effect and depletion of ground state wavefunction are very important in the OBI regime. Utilizing the corresponding relation between the ionization moment and final momentum, we have analyzed the initial condition of ejected photoelectrons. Moreover, the developed SCM has been used in the calculation for the laser pulse with different

ellipticities and CEPs. This work presents an intuitive physical picture of the photoionization process in the OBI regime. Due to the momentum-resolved final states of electrons ionized at different moments in one cycle, one can fully resolve the sub-cycle dynamics of photoelectrons in the OBI.

Data availability statement

The original contributions presented in the study are included in the article/Supplementary Material, further inquiries can be directed to the corresponding author.

Author contributions

All authors listed have made a substantial, direct, and intellectual contribution to the work and approved it for publication.

Funding

We thank the support of the National Natural Science Foundation of China (Grant No. 92050201 and 11774013).

Conflict of interest

The authors declare that the research was conducted in the absence of any commercial or financial relationships that could be construed as a potential conflict of interest.

Publisher's note

All claims expressed in this article are solely those of the authors and do not necessarily represent those of their affiliated organizations, or those of the publisher, the editors and the reviewers. Any product that may be evaluated in this article, or claim that may be made by its manufacturer, is not guaranteed or endorsed by the publisher.

References

1. Becker W, Grasbon F, Kopold R, Milošević D, Paulus G, Walther H. Above-threshold ionization: From classical features to quantum effects. *Adv Mol Opt Phys* (2002) 48:35–98. doi:10.1016/S1049-250X(02)80006-4

2. Eberly JH, Javanainen J, Rzążewski K. Above-threshold ionization. *Phys Rep* (1991) 204(5):331–83. doi:10.1016/0370-1573(91)90131-5

3. Schafer K, Yang B, DiMauro L, Kulander K. Above threshold ionization beyond the high harmonic cutoff. *Phys Rev Lett* (1993) 70(11):1599–602. doi:10.1103/PhysRevLett.70.1599

4. Bocharova I, Karimi R, Penka EF, Brichta J-P, Lassonde P, Fu X, et al. Charge resonance enhanced ionization ofCO2Probed by laser Coulomb explosion imaging. *Phys Rev Lett* (2011) 107(6):063201. doi:10.1103/PhysRevLett.107.063201

5. Posthumus J, Giles A, Thompson M, Codling K. Field-ionization, Coulomb explosion of diatomic molecules in intense laser fields. *J Phys B: Mol Opt Phys* (1996) 29(23):5811. doi:10.1088/0953-4075/29/23/022

6. Stapelfeldt H, Constant E, Corkum P. Wave packet structure and dynamics measured by Coulomb explosion. *Phys Rev Lett* (1995) 74(19):3780–3. doi:10.1103/PhysRevLett.74.3780

7. Becker W, Liu X, Ho PJ, Eberly JH. Theories of photoelectron correlation in laser-driven multiple atomic ionization. *Rev Mod Phys* (2012) 84(3):1011–43. doi:10.1103/RevModPhys.84.1011

8. Fittinghoff DN, Bolton PR, Chang B, Kulander KC. Observation of nonsequential double ionization of helium with optical tunneling. *Phys Rev Lett* (1992) 69(18):2642–5. doi:10.1103/PhysRevLett.69.2642

9. Walker B, Sheehy B, DiMauro LF, Agostini P, Schafer KJ, Kulander KC. Precision measurement of strong field double ionization of helium. *Phys Rev Lett* (1994) 73(9):1227–30. doi:10.1103/PhysRevLett.73.1227

10. Keldysh L. Ionization in the field of a strong electromagnetic wave. *Sov Phys JETP* (1965) 20(5):1307–14.

11. Agostini P, Fabre F, Mainfray G, Petite G, Rahman NK. Free-free transitions following six-photon ionization of xenon atoms. *Phys Rev Lett* (1979) 42(17):1127–30. doi:10.1103/PhysRevLett.42.1127

12. Voronov G, Delone G, Delone N, Kudrevatova O. Multiphoton ionization of the hydrogen molecule in the strong electric field of ruby laser emission. *J Exp Theor Phys* (1965) 2:237.

13. Fabre F, Petite G, Agostini P, Clement M. Multiphoton above-threshold ionisation of xenon at 0.53 and 1.06 μm. *J Phys B: Mol Phys* (1982) 15(9):1353–69. doi:10.1088/0022-3700/15/9/012

14. Ge P, Han M, Deng Y, Gong Q, Liu Y. Universal description of the attoclock with two-color corotating circular fields. *Phys Rev Lett* (2019) 122(1):013201–6. doi:10.1103/PhysRevLett.122.013201

15. Delone N, Krainov VP. Energy and angular electron spectra for the tunnel ionization of atoms by strong low-frequency radiation. *J Opt Soc Am B* (1991) 8(6):1207–11. doi:10.1364/JOSAB.8.001207

16. Corkum P, Burnett N, Brunel F. Above-threshold ionization in the long-wavelength limit. *Phys Rev Lett* (1989) 62(11):1259. doi:10.1103/PhysRevLett.62.1259

17. Teeny N, Yakaboylu E, Bauke H, Keitel CH. Ionization time and exit momentum in strong-field tunnel ionization. *Phys Rev Lett* (2016) 116(6):063003. doi:10.1103/PhysRevLett.116.063003

18. Han M, Ge P, Fang Y, Yu X, Guo Z, Ma X, et al. Unifying tunneling pictures of strong-field ionization with an improved attoclock. *Phys Rev Lett* (2019) 123(7):073201–5. doi:10.1103/PhysRevLett.123.073201

19. Calvert J, Goodall S, Wang X, Xu H, Kheifets AS, Ivanov I, et al. Transverse electron momentum distribution in tunneling and over the barrier ionization by strong-field laser pulses. *J Phys Conf Ser* (2015) 635:19002. doi:10.1088/1742-6596/635/9/092073

20. Augst S, Strickland D, Meyerhofer DD, Chin S-L, Eberly JH. Tunneling ionization of noble gases in a high-intensity laser field. *Phys Rev Lett* (1989) 63(20):2212–5. doi:10.1103/PhysRevLett.63.2212

21. Tong X, Lin C. Empirical formula for static field ionization rates of atoms and molecules by lasers in the barrier-suppression regime. *J Phys B: Mol Opt Phys* (2005) 38(15):2593–600. doi:10.1088/0953-4075/38/15/001

22. Augst S, Meyerhofer DD, Strickland D, Chin S-L. Laser ionization of noble gases by coulomb-barrier suppression. *J Opt Soc Am B* (1991) 8(4):858–67. doi:10.1364/JOSAB.8.000858

23. Schuricke M, Zhu G, Steinmann J, Simeonidis K, Ivanov I, Kheifets A, et al. Strong-field ionization of lithium. *Phys Rev A* (2011) 83(2):023413. doi:10.1103/PhysRevA.83.023413

24. Morishita T, Lin CD. Photoelectron spectra and high rydberg states of lithium generated by intense lasers in the over-the-Barrier ionization regime. *Phys Rev A* (2013) 87(6):063405. doi:10.1103/PhysRevA.87.063405

25. Ivanov I. Evolution of the transverse photoelectron-momentum distribution for atomic ionization driven by a laser pulse with varying ellipticity. *Phys Rev A* (2014) 90(1):013418. doi:10.1103/PhysRevA.90.013418

26. Ivanov I, Kheifets A, Calvert J, Goodall S, Wang X, Xu H, et al. Transverse electron momentum distribution in tunneling and over the barrier ionization by laser pulses with varying ellipticity. *Sci Rep* (2016) 6(1):19002–8. doi:10.1038/srep19002

27. Yuan J, Liu S, Wang X, Shen Z, Ma Y, Ma H, et al. Ellipticity-dependent sequential over-barrier ionization of cold rubidium. *Phys Rev A* (2020) 102(4): 043112. doi:10.1103/PhysRevA.102.043112

28. Feit M, Fleck J, Jr, Steiger A. Solution of the schrödinger equation by a spectral method. *J Comput Phys* (1982) 47(3):412–33. doi:10.1016/0021-9991(82)90091-2

29. Feit M, Fleck J, Jr. Solution of the schrödinger equation by a spectral method II: Vibrational energy levels of triatomic molecules. *J Chem Phys* (1983) 78(1): 301–8. doi:10.1063/1.444501

30. Hermann MR, Fleck J, Jr. Split-operator spectral method for solving the time-dependent schrödinger equation in spherical coordinates. *Phys Rev A* (1988) 38(12): 6000. doi:10.1103/PhysRevA.38.6000

31. Fleck JA, Morris J, Feit M. Time-dependent propagation of high energy laser beams through the atmosphere. *Appl Phys* (1976) 10(2):129–60. doi:10.1007/BF00896333

32. Feit M, Fleck J. Computation of mode eigenfunctions in graded-index optical fibers by the propagating beam method. *Appl Opt* (1980) 19(13):2240–6. doi:10.1364/AO.19.002240

33. Feit M, Fleck J. Spectral approach to optical resonator theory. *Appl Opt* (1981) 20(16):2843–51. doi:10.1364/AO.20.002843

34. Protopapas M, Keitel CH, Knight PL. Atomic physics with super-high intensity lasers. *Rep Prog Phys* (1997) 60(4):389–486. doi:10.1088/0034-4885/60/4/001

35. Corkum PB. Plasma perspective on strong field multiphoton ionization. *Phys Rev Lett* (1993) 71(13):1994–7. doi:10.1103/PhysRevLett.71.1994

36. Paulus GG, Becker W, Nicklich W, Walther H. Rescattering effects in above-threshold ionization: A classical model. *J Phys B: Mol Opt Phys* (1994) 27(21): L703–8. doi:10.1088/0953-4075/27/21/003

37. Min L, Geng JW, Hong L, Deng Y, Wu C, Peng LY, et al. Classical-quantum correspondence for above-threshold ionization. *Phys Rev Lett* (2014) 112(11): 113002. doi:10.1103/PhysRevLett.112.113002

38. Bleistein N, Handelsman RA. *Asymptotic expansions of integrals*. San Francisco: Ardent Media (1975).

39. Gribakin G, Kuchiev MY. Multiphoton detachment of electrons from negative ions. *Phys Rev A* (1997) 55(5):3760–71. doi:10.1103/PhysRevA.55.3760

40. Han M, Ge P, Shao Y, Liu MM, Deng Y, Wu C, et al. Revealing the sub-barrier phase using a spatiotemporal interferometer with orthogonal two-color laser fields of comparable intensity. *Phys Rev Lett* (2017) 119(7):073201–6. doi:10.1103/PhysRevLett.119.073201

41. Li M, Geng J-W, Han M, Liu M-M, Peng L-Y, Gong Q, et al. Subcycle nonadiabatic strong-field tunneling ionization. *Phys Rev A* (2016) 93(1):013402. doi:10.1103/PhysRevA.93.013402

42. Salières P, Carré B, Le Déroff L, Grasbon F, Paulus G, Walther H, et al. Feynman's path-integral approach for intense-laser-atom interactions. *Science* (2001) 292(5518):902–5. doi:10.1126/science.108836

43. Popruzhenko V. Keldysh theory of strong field ionization: History, applications, difficulties and perspectives. *J Phys B: Mol Opt Phys* (2014) 47(20): 204001. doi:10.1088/0953-4075/47/20/204001

44. Reiss HR. Effect of an intense electromagnetic field on a weakly bound system. *Phys Rev A* (1980) 22(5):1786–813. doi:10.1103/PhysRevA.22.1786

45. Faisal FH. Multiple absorption of laser photons by atoms. *J Phys B: Mol Phys* (1973) 6(4):L89–92. doi:10.1088/0022-3700/6/4/011

46. Li M, Liu M-M, Geng J-W, Han M, Sun X, Shao Y, et al. Experimental verification of the nonadiabatic effect in strong-field ionization with elliptical polarization. *Phys Rev A* (2017) 95(5):053425. doi:10.1103/PhysRevA.95.053425

frontiers | Frontiers in Physics

TYPE Original Research
PUBLISHED 30 September 2022
DOI 10.3389/fphy.2022.1029954

OPEN ACCESS

EDITED BY
Weifeng Yang,
Hainan University, China

REVIEWED BY
Huailiang Xu,
Jilin University, China
Yi Liu,
University of Shanghai for Science and Technology, China

*CORRESPONDENCE
Jinming Chen,
jmchen@phy.ecnu.edu.cn
Zhaoxiang Liu,
zxliu@phy.ecnu.edu.cn
Ya Cheng,
ya.cheng@siom.ac.cn

SPECIALTY SECTION
This article was submitted to Optics and Photonics,
a section of the journal
Frontiers in Physics

RECEIVED 28 August 2022
ACCEPTED 13 September 2022
PUBLISHED 30 September 2022

CITATION
Li Z, Chen J, Liu Z, Li Y, Chu Y, Chen Y and Cheng Y (2022), Free-radical fluorescence emissions induced by 1,030 nm femtosecond laser filamentation in ethanol flame.
Front. Phys. 10:1029954.
doi: 10.3389/fphy.2022.1029954

Free-radical fluorescence emissions induced by 1,030 nm femtosecond laser filamentation in ethanol flame

Ziting Li[1], Jinming Chen[2]*, Zhaoxiang Liu[2]*, Yi Li[1], Yuxi Chu[1], Ye Chen[1] and Ya Cheng[2]*

[1]Tianjin Fire Research Institute of Ministry of Emergency Management, Tianjin, China, [2]The Extreme Optoelectromechanics Laboratory, School of Physics and Materials Science, East China Normal University, Shanghai, China

We experimentally investigated clean optical emissions from multiple combustion intermediates including free radicals C_2, CH, and CN at multiple wavelengths induced by ultrashort 1,030-nm laser pulses. We systematically study the evolution of the fluorescence emissions induced by the femtosecond laser filament in the combustion field with the parameters such as the laser pulse energy, pulse duration, and focal length. Compared with the previous work, we promote that the fluorescence emissions of the combustion product can be manipulated effectively by controlling the femtosecond laser characteristics including pulse energy, duration, and the focusing conditions. This process helps to optimize its signal-to-noise ratio, which provides a further application of the femtosecond laser pulses to sense the combustion intermediates.

KEYWORDS

femtosecond filament, combustion field, combustion intermediates, fluorescence emissions, combustion diagnostics

Introduction

In recent years, the rapid development of the ultrafast laser technology has made it easier to obtain high power femtosecond laser pulses, and novel nonlinear effects triggered by the femtosecond laser filamentation process have attracted widespread attention, such as laser power density clamping in the filament, super-continuous white light, THz generation, and self-steepening effects [1–3]. Based on these unique nonlinear effects, ultrafast strong-field laser filament formation has shown great promise for applications in atmospheric environmental sensing, air lasers, artificial weather control, and other applied research fields [4–9]. In the field of combustion, the ultrafast intense-field laser filament-induced nonlinear spectroscopy can be used for combustion diagnosis. On the one hand, ultrafast strong-field lasers can be used to measure combustion intermediate radical products with ultrashort lifetime in the combustion field and reveal various ultrafast complex physicochemical processes existing in the combustion field [7]. On the other hand, the high clamping intensity of the femtosecond filament can

be used for multi-photon excitation of combustion intermediates to achieve simultaneous multi-component measurements and to solve the limitation of tuning the laser wavelength for detecting different combustion components [4, 9].

The combustion process of fuels creates a very complex environment with a large number of intermediate products and many chemical reactions taking place. Although filamentation parameters of ultrafast intense-field laser transmission have been measured in flames and it has been demonstrated that ultrafast intense-field laser filamentation-induced nonlinear spectroscopy can be used for simple flame combustion diagnostics [10–20], this research is still in its infancy. Some of the main current advances in the diagnostic analysis of combustion fields using ultrafast intense-field laser filamentation include the verification of the universality of ultrafast intense-field laser filamentation nonlinear spectroscopy for combustion diagnosis of different fuels, the proposed use of ultrafast intense-field laser filamentation-induced excitation phenomena to solve the fluorescence quenching problem in combustion fields, the viable pump–probe approach to measure ultrafast processes of the soot particles in flames with femtosecond time resolution [21], the demonstration of the minimum ignition energy can decrease to the sub-mJ level using an ultrashort femtosecond laser [22], and ultrafast combustion diagnosis using femtosecond filamentation-induced flame nonlinear spectroscopy. This study is intended to systematically investigate the optimization of the fluorescence emissions of ultrafast strong-field laser filament-induced spectroscopy in ethanol flames using the ultrafast laser at the center wavelength of 1,030 nm with changeable pulse energy, duration, and the focusing conditions, with the aim of better application to remote combustion diagnostics.

Experiment setup

As shown in Figure 1, the experiment was conducted with a Yb: the KGW femtosecond laser system (PHAROS, Light Conversion), which delivers 190 fs (FWHM) pluses with a central wavelength at 1,030 nm and a maximum pulse energy of 2 mJ at 10 kHz repetition frequency. The pulse energy and pulse duration of the laser were adjusted, respectively, by an electrically operated attenuator and pulse chirp modulator installed inside the PHAROS laser. The output beam from the laser system was reflected by a dichroic mirror with high reflectivity of 800–1,200 nm and high transmission for UV and visible light at a 45° incidence angle. The femtosecond laser pulse was focused into the flame on an alcohol burner array by the lens (L1) with different focal lengths to generate a bright filamentation as shown in the inset of Figure 1. The alcohol burner array was set on a stage with an adjustable position to ensure that the filament can pass through the core of the flame when changing different focal lengths. The total length of the alcohol burner array with five burner wicks is approximately 40 mm. The fluorescence generated from the filament was collected and collimated in a backward direction by the same lens. After passing through the two dichroic mirrors, the fluorescence in the UV and visible range was focused into an imaging spectrometer with a grating of 1,200 grooves/mm (Kymera 328i, Andor) by an f = 6 cm lens (L2). A damper was used to collect the pump beam and forward emissions such as third harmonic and white light, which was aligned to prevent the forward radiation scattering back to the spectrometer.

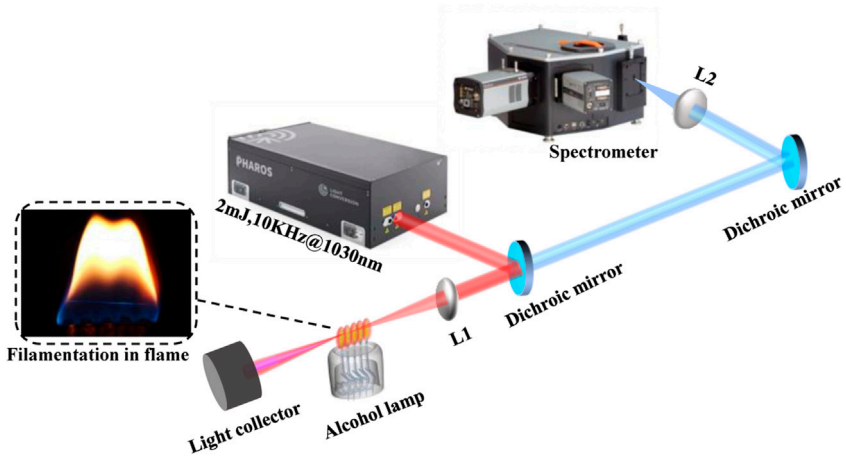

FIGURE 1
Schematic diagram of the experimental setup.

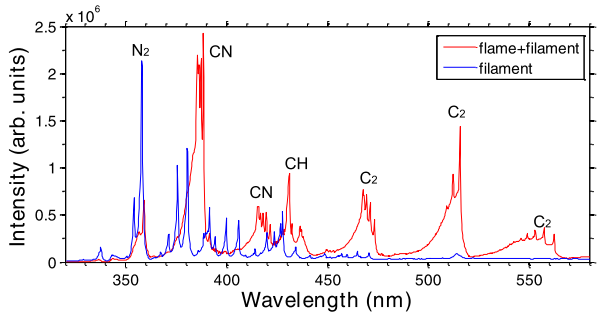

FIGURE 2
Backward fluorescence spectra obtained when the femtosecond filament transmits through air (blue line) and flame (red line).

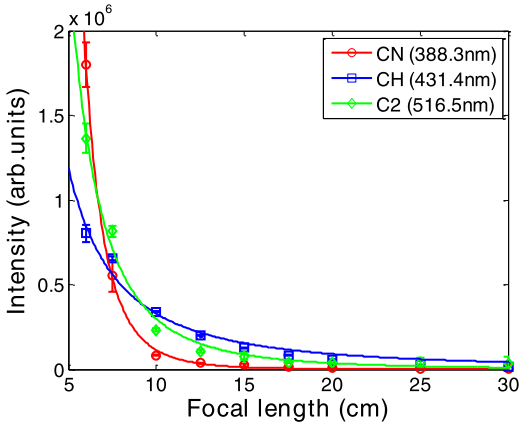

FIGURE 3
Dependence of intensity of the fluorescence from CN (red circle), C_2 (green diamond), and CH (blue square) radicals on the focal length. The experimental data are fitted with the power exponential function.

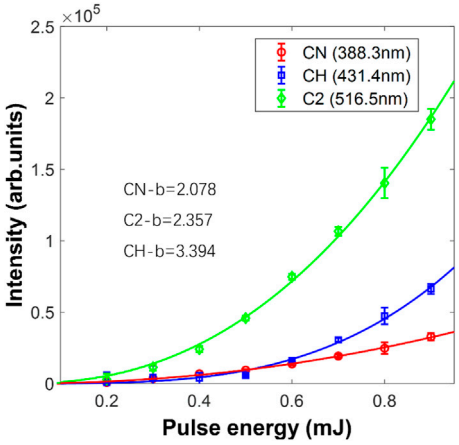

FIGURE 4
Measured (circle) and fitted (solid line) dependence of the emission intensity of CN at 388.3 nm (red), that of CH at 431.4 nm (blue), and C_2 at 516.5 nm (green) on the input laser energy.

Result and discussion

Figure 2 shows the backward fluorescence spectra of with/without the ethanol/air flame generated by the femtosecond laser pulse filament with laser energy of 2 mJ. The spectra are acquisitioned using the spectrometer and the background noise has been subtracted. In addition, the spectra signal of the flame without the interaction of the femtosecond laser mainly originated from the thermal noise and flame light which is two orders of magnitude weaker compared with the fluorescence signal. As the femtosecond filament transmits through the air without ethanol/air flame, the fluorescence spectra mainly show the spectral lines of N_2 and N_2^+, as indicated by the blue line in Figure 2, while as the femtosecond filament transmits through the ethanol/air flame, the N_2 and N_2^+ fluorescence emissions were quenched, and there exist spectral bands around 388.34, 431.42, and 516.52 nm which correspond to $B^2\Sigma(v=0)-X^2\Sigma(v'=0)$ transition of the CN radical, $A^2\Delta(v=0)-X^2\Pi(v'=0)$ transition of the CH radical, and $A^3\Pi_g(v=0)-X'^3\Pi_u(v'=0)$ transition of C_2, respectively (red line). Compared with the previous work results in Ref. [17], the emission of CH and C_2 radicals became significant in the fluorescence spectrum. In particular, the emission of the C_2 radical at the wavelength around 515 nm became dominant, which probably originates from the two-photon resonant enhancement of the insert pump laser pulse with the wavelength of 1,030 nm. By selecting a suitable wavelength of the pump pulse, the clean enhanced fluorescence emission can be achieved, and the signal-to-noise ratio can be improved.

In addition, to further optimize the free-radical CN, C_2, and CH fluorescence emission in the flame, we measured the intensity of the fluorescence emission at different focal lengths. The laser pulse energy and repetition frequency were fixed at 2 mJ and 10 kHz, respectively. As shown in Figure 3, the intensity of the three free-radical fluorescence emissions decreases with the increasing focal length. The conditions of the focal length mainly affect the interaction length and intensity, that is, the longer focal length, longer interaction length, and lower intensity. The results indicated that the optical intensity plays an important role in fluorescence generation compared to the interaction length. In addition, the 388 nm which corresponds to the CN radical fluorescence emission decay the fastest with an increasing focal length, which shows that the CN molecule fluorescence is more sensitive to the focusing condition. Therefore, as a result, a tighter focus can be used to improve the fluorescence intensity and improve the fluorescence emissions.

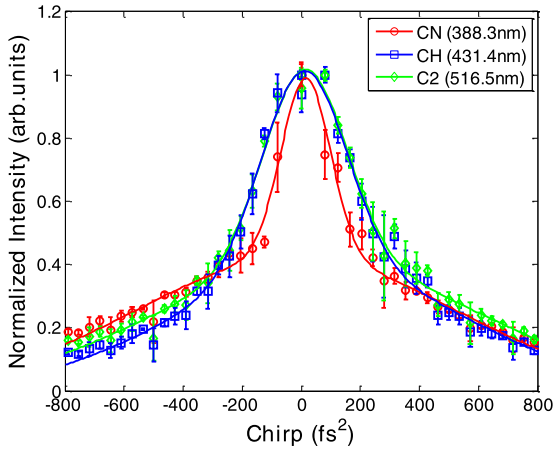

FIGURE 5
Measured (circle) and fitted (solid line) dependence of the emission intensity of CN at 388.3 nm (red), that of CH at 431.4 nm (blue), and C_2 at 516.5 nm (green) on the chirp of the pump laser pulse.

Furthermore, we changed the pulse energy from 0 to 1 mJ by adjusting an electrically operated attenuator installed inside the laser, then the pump laser beam is focused by a spherical lens (f = 75 mm) into the flame. As shown in Figure 4, we measured the intensity of CN radical emission at 388.3 nm (red), that of CH at 431.4 nm (blue), and C_2 at 516.5 nm (green) as a function of incident laser energy. It can be seen that the three signals display a superliner dependence on incident laser energy. The experimental data can be well fitted by a power dependence which gives a value of b = 2.078, 2.357, and 3.394, respectively. Obviously, the fluorescence emission of the three free radicals overcomes the quenching effect in combustion diagnosis. In addition, the two-photon effect of the 1,030 nm femtosecond laser pulses can improve the excitation efficiency of C_2 radiation emission at 516.5 nm.

Last, we changed the chirp of the pump laser pulse by adjusting a pulse chirp modulator installed inside the laser, here; the chirp of the pump laser pulse is defined by the quadratic phase term ϕ'' *via* the relation $\beta = \tau_0^2/8\ln 2$ and $\gamma = 1 + \phi''^2/4\beta^2$, where τ_0 is the duration (FWHM) of the transform-limited pulse. Then the duration of the chirped pulse τ can be expressed as $\sqrt{\gamma}\tau_0$, which was measured by the single shot autocorrelator (SSA) before the focusing lens. The fluorescence emission intensity of the CN, CH, and C_2 free radicals were plotted as a function of the chirp of the pump pulse, as presented in Figure 5. Here, the signal intensities of the three emissions are normalized. It can be clearly observed that the three fluorescence emissions at 388.3, 431.4, and 516.5 nm reach the maximum when the chirp $\phi'' = 0$, and the transition signal of CN seems to be more sensitive to the chirp of the insert pump pulse, indicating that the transform-limited pulse can efficiently generate the fluorescence emissions for combustion diagnosis. Thus, the changes of pulse energy, duration, and the focusing conditions actually can affect the filament characteristics of the femtosecond laser which plays an important role in the fluorescence emission. In short, the intensity of fluorescence emission is strongly dependent on the excited intensity of the pump laser and the interaction length. Longer laser duration and lower pulse energy mean the weaker clamping intensity with the results of weaker fluorescence emission. In addition, with the increase in the focal length, the interaction length becomes longer, however, with a weaker excited intensity, resulting in a weaker fluorescence signal. It means that the excited pump intensity has a greater effect on fluorescence emission than the interaction length.

In conclusion, we systematically investigate generation of the fluorescence emission of the multiple combustion intermediates from the femtosecond filament with the ultrashort laser pulse at the wavelength of 1,030 nm. By studying the evolution of the fluorescence emission with the focusing conditions, pulse energy, and pulse duration, we proposed an optimizing rule to improve the signal-to-noise ratio of the fluorescence emission intensity in the ethanol/air flame using femtosecond laser filament excitation, which will be promoting a further application of the femtosecond laser pulses to simultaneously monitoring the multiple combustion intermediates.

Data availability statement

The original contributions presented in the study are included in the article/Supplementary Material; further inquiries can be directed to the corresponding authors.

Author contributions

ZTL, JC, and YaC conceived the study and wrote the manuscript. Writing assistance was provided by ZXL and YXC. Optical design support was provided by YeC and YiL.

Funding

This work was supported by the National Natural Science Foundation of China (Grants Nos 11904315, 12004221, and 12074063).

Acknowledgments

We acknowledge the support from the Tianjin Fire Research Institute of the Ministry of Emergency Management. We acknowledge Extreme Optoelectromechanics Laboratory,

School of Physics and Materials Science, East China Normal University for optical laboratory and device support.

Conflict of interest

The authors declare that the research was conducted in the absence of any commercial or financial relationships that could be construed as a potential conflict of interest.

Publisher's note

All claims expressed in this article are solely those of the authors and do not necessarily represent those of their affiliated organizations, or those of the publisher, the editors, and the reviewers. Any product that may be evaluated in this article, or claim that may be made by its manufacturer, is not guaranteed or endorsed by the publisher.

References

1. Liu W. Intensity clamping during femtosecond laser filamentation. *Chin J Phys* (2014) 52(1-II):465–89. doi:10.6122/CJP.52.465

2. Couairon A, Mysyrowicz A. Femtosecond filamentation in transparent media. *Phys Rep* (2007) 441:47–189. doi:10.1016/j.physrep.2006.12.005

3. Chin SL, Hosseini SA, Liu W, Luo Q, Théberge F, AköZbek N, et al. The propagation of powerful femtosecond laser pulses in opticalmedia: Physics, applications, and new challenges. *Can J Phys* (2005) 83:863–905. doi:10.1139/p05-048

4. Xu H, Cheng Y, Chin SL, Sun HB. Femtosecond laser ionization and fragmentation of molecules for environmental sensing. *Laser Photon Rev.* (2015) 9:275–93. doi:10.1002/lpor.201400208

5. Yao J, Zeng B, Xu H, Li G, Chu W, Ni J, et al. High-brightness switchable multiwavelength remote laser in air. *Phys Rev A (Coll Park)* (2011) 84:051802. doi:10.1103/PhysRevA.84.051802

6. Rohwetter P, Kasparian J, Stelmaszczyk K, Hao Z, Henin S, Lascoux N, et al. Laser-induced water condensation in air. *Nat Photon* (2010) 4:451–6. doi:10.1038/nphoton.2010.115

7. Kasparian J, Rodríguez M, Méjean G, Yu J, Salmon E, Wille H, et al. White-light filaments for atmospheric analysis. *Science* (2003) 301:61–4. doi:10.1126/science.1085020

8. Guandalini A, Eckle P, Anscombe M, Schlup P, Biegert J, Keller U. 5.1 fs pulses generated by filamentation and carrier envelope phase stability analysis. *J Phys B: Mol Opt Phys* (2006) 39:S257–64. doi:10.1088/0953-4075/39/13/S01

9. Chin SL, Xu HL, Luo Q, Théberge F, Liu W, Daigle JF, et al. Filamentation "remote" sensing of chemical and biological agents/pollutants using only one femtosecond laser source. *Appl Phys B* (2009) 95:1–12. doi:10.1007/s00340-009-3381-7

10. Li HL, Xu HL, Yang BS, Chen QD, Zhang T, Sun HB. Sensing combustion intermediates by femtosecond filament excitation. *Opt Lett* (2013) 38:1250–2. doi:10.1364/OL.38.001250

11. Li H, Wei C, Zang H, Xu H, Chin SL. Critical power and clamping intensity inside a filament in a flame. *Opt Express* (2016) 24:3424. doi:10.1364/OE.24.003424

12. Li H, Chu W, Xu H, Cheng Y, Chin SL, Yamanouchi K, et al. Simultaneous identification of multi-combustion-intermediates of alkanol-air flames by femtosecond filament excitation for combustion sensing. *Sci Rep* (2016) 6:27340–7. doi:10.1038/srep27340

13. Li S, Li Y, Shi Z, Sui L, Li H, Li Q, et al. Fluorescence emission induced by the femtosecond filament transmitting through the butane/air flame. *Spectrochimica Acta A: Mol Biomol Spectrosc* (2018) 189:32–6. doi:10.1016/j.saa.2017.08.006

14. Zang HW, Li HL, Su Y, Fu Y, Hou MY, Baltuška A, et al. Third-harmonic generation and scattering in combustion flames using a femtosecond laser filament. *Opt Lett* (2018) 43:615–8. doi:10.1364/OL.43.000615

15. Li Z, Chen J, Liu Z, Yao J, Yu J, Li Y, et al. Nonintrusive temperature measurement of a combustion field by femtosecond laser-induced third harmonic generation. *J Phys B: Mol Opt Phys* (2022) 55:075401. doi:10.1088/1361-6455/ac60ad

16. Chu W, Li H, Ni J, Zeng B, Yao J, Zhang H, et al. Lasing action induced by femtosecond laser filamentation in ethanol flame for combustion diagnosis. *Appl Phys Lett* (2014) 104:091106. doi:10.1063/1.4867503

17. Zhou YS, Wang MM, Lu Y, Silvain JF, Lu YF. Spectroscopic Sensing of O2–C2H2–C2H4 flames for diamond growth using femtosecond filamentation. *Cryst Growth Des* (2017) 17:3443–9. doi:10.1021/acs.cgd.7b00385

18. Kotzagianni M, Couris S. Femtosecond laser induced breakdown for combustion diagnostics. *Appl Phys Lett* (2012) 100:264104. doi:10.1063/1.4731781

19. Baudelet M, Guyon L, Yu J, Wolf JP, Amodeo T, Fréjafon E, et al. Spectral signature of native CN bonds for bacterium detection and identification using femtosecond laser-induced breakdown spectroscopy. *Appl Phys Lett* (2006) 88:063901. doi:10.1063/1.2170437

20. Yuan S, Wang T, Lu P, Leang Chin S, Zeng H. Humidity measurement in air using filament-induced nitrogen monohydride fluorescence spectroscopy. *Appl Phys Lett* (2014) 104:091113. doi:10.1063/1.4867267

21. Zang H, Fu Y, Hou M, Li H, Yamanouchi K, Xu H. Ultrafast swelling and shrinking of soot in alkanol–air flames induced by femtosecond laser filamentation. *Combustion and Flame* (2020) 212:345–51. doi:10.1016/j.combustflame.2019.11.009

22. Zang H, Li H, Zhang W, Fu Y, Chen S, Xu H, et al. Robust and ultralow-energy-threshold ignition of a lean mixture by an ultrashort-pulsed laser in the filamentation regime. *Light Sci Appl* (2021) 10:49–7. doi:10.1038/s41377-021-00496-8

frontiers | Frontiers in Physics

TYPE Original Research
PUBLISHED 30 September 2022
DOI 10.3389/fphy.2022.1004021

OPEN ACCESS

EDITED BY
Yangjian Cai,
Shandong Normal University, China

REVIEWED BY
Yahong Chen,
Soochow University, China
Pengfei Lan,
Huazhong University of Science and Technology, China
Libin Fu,
Graduate School of China Academy of Engineering Physics, China

*CORRESPONDENCE
Weifeng Yang,
wfyang@hainanu.edu.cn
Xiaolei Hao,
xlhao@sxu.edu.cn
Jing Chen,
chen_jing@iapcm.ac.cn

SPECIALTY SECTION
This article was submitted to Optics and Photonics, a section of the journal Frontiers in Physics

RECEIVED 26 July 2022
ACCEPTED 13 September 2022
PUBLISHED 30 September 2022

CITATION
Ben S, Han Y, Yang W, Yu W, Hao X, Song X, Li W and Chen J (2022), Controlling electron recollision with combined linear and circular polarization. *Front. Phys.* 10:1004021. doi: 10.3389/fphy.2022.1004021

Controlling electron recollision with combined linear and circular polarization

Shuai Ben[1], Yifan Han[2], Weifeng Yang[1]*, Weiwei Yu[2], Xiaolei Hao[3]*, Xiaohong Song[1], Weidong Li[4] and Jing Chen[5,6]*

[1]Department of Physics, School of Science, Hainan University, Haikou, China, [2]School of Physics and Electronic Technology, Liaoning Normal University, Dalian, China, [3]Department of Physics, Institute of Theoretical Physics, State Key Laboratory of Quantum Optics and Quantum Optics Devices, Collaborative Innovation Center of Extreme Optics, Shanxi University, Taiyuan, China, [4]Shenzhen Key Laboratory of Ultraintense Laser and Advanced Material Technology, Center ForAdvanced Material Diagnostic Technology, College of Engineering Physics, Shenzhen Technology University, Shenzhen, China, [5]Institute of Applied Physics and Computational Mathematics, Beijing, China, [6]HEDPS, Center for Applied Physics and Technology, Peking University, Beijing, China

We theoretically investigate the non-sequential double ionization of Ar atoms in the combined fields of linearly polarized laser and circularly polarized laser through 3D semiclassical simulations. By partially overlapping the two time-delayed multicycle laser pulses, we construct an optical waveform whose polarization ellipticity increase slowly for consecutive optical cycles. This composite laser pulses with the time-dependent ellipticity can tunnel-ionize atoms and steer the first tunneling electron to recollision with the second bound electron through different trajectories, in which the recollision occurs with different return times of the first ionized electron. Through tuning delay time between the two laser pulses, the double ionization yields and recollision trajectories with different return times can be controlled. The time-dependent ellipticity with different delay time can enhance or suppress the probability of different return times. This work provides a scheme exploring electron dynamics in few optical cycle or even subcycle time scale in a multicycle laser field without having to be limited to near-single-cycle laser pulses.

KEYWORDS

non-sequential double ionization, strong filed physics, ultra-fast laser pulse, semiclassical model, recollision

1 Introduction

The research on the interaction of atoms and molecules with intense laser pulses plays a key role in a comprehensive understanding of the nonlinear physics. Plenty of ultrafast processes are directly related to photoionization, which is the foundation of many strong field phenomena such as high harmonic generation (HHG), attosecond pulse synthetization [1–5], above threshold ionization (ATI) [6], and non-sequential double ionization (NSDI) [7]. NSDI has drawn much attention because of containing extensive information about collision dynamics and electron-electron correlation [8]. Researchers widely hold the idea that NSDI is described by a three-step model [9]. In this model, one

electron tunnel ionizes when the laser field is strong enough and then is driven back to the parent ion as the oscillating electric field reverses its direction. It recollides with the parent ion and transfers a part of energy to it, which enables the second NSDI event. This model is a semiclassical perspective.

In order to achieve deep insight into the collision dynamics in strong field physics, various ionization channels in recollision process have been explored in details, such as electron multiple rescattering processes. The rescattering or recollision with multiple return times is considered to play an important role in the laser-atom interactions, especially driven by the midinfrared laser fields. For example, the finite tunnel distance inherent in strong-field ionization can be extracted from an experimental observable through studying laser-driven electron multiple scattering [10]. The low energy structure of strong field ionization by mid-IR laser pulses is considered to be related to the multiple rescattering [11,12]. Multiple rescattering processes also play an important role in HHG in an intense laser field [13–15]. In addition, multiple-return-collision (MRC) trajectories have been explored in NSDI with linearly [16,17] or elliptically [18–20], polarized laser field in recent years, in which sub-cycle dynamics was investigated and Coulomb-potential effects was considered to play an indispensable role.

In another aspect, it is expected that various recollision channels could be artificially controlled. With the development of the laser technology, more complex combined laser pulses have been employed to investigate the strong field physics, which makes many ultrafast dynamics controllable. For example, controlling the dynamics of double electron emission in non-sequential double ionization by tuning the subcycle shape of the orthogonal laser field [21]. Photoelectron intracycle interference can be controlled by polarization-gated laser pulses [22]. The ionization by two-color counter-rotating and co-rotating circularly polarized fields has been studied experimentally and theoretically [23,24]. Controlling of NSDI dynamics was also explored through this kind of bicircular fields [25–28]. Recently, a new phenomenon of electron vortices has attracted much attention. The vortex structures in the momentum distributions of photoelectron wave packets comes from the photoionization of atoms with sequences of two time-delayed counter-rotating circularly polarized laser pulses [29–35]. The local enhancement of the laser pulse is achieved by superimposing the terahertz field, thereby realizing the control of the electron dynamics [36].

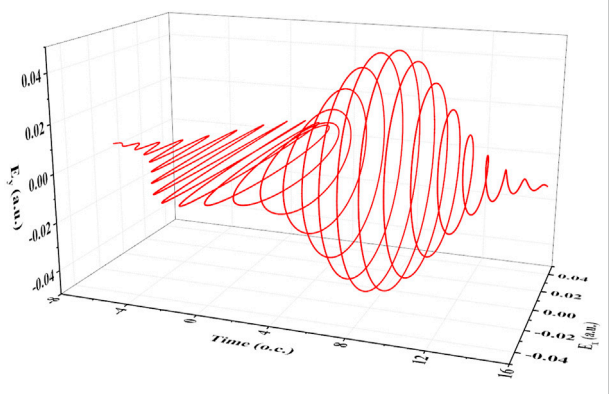

FIGURE 1
The electric field form of the laser field pulse combined with linearly polarized and circularly polarized laser of the time delay ΔT = 8 o.c.

Based on the above analysis, it is believed that the MRC channel should be controlled by shaping the laser pulses. In this paper, we propose and numerically demonstrate a scheme to control return times before recollision in NSDI by the complex field with combining linearly and circularly polarized pulses. This kind of combined laser field has the characteristics of time-dependent ellipticity, in which the polarization gradually transitions from linear polarization to circular polarization. By changing the time delay between the two laser beams, the transition property of the time-dependent ellipticity in the superposition region can be adjusted, and different degrees of lateral effect can be exerted on the first ionized electron for different return times. Therefore, the control mechanism of recollision trajectories with different return times can be realized. Atomic units are used throughout the paper unless stated otherwise.

2 Theoretical method

In this work, the semiclassical model [37,38] is used to describe the NSDI process of Ar. One electron (recolliding) tunnel ionizes through the Coulomb barrier. The initial state of the tunnelling electron is defined according to Ammosov-Delone-Krainov theory [39]. The initial exit point is along the laser-field direction and near the barrier. The initial electron momentum is taken to be equal to zero along the laser field while the transverse one is given by a Gaussian distribution. The initially bound electron is described by a microcanonical distribution [40]. The weight of each classical trajectory that we propagate in time is given by

$$\omega(t_0, v_0) \propto \exp\left[-\frac{2(2I_p)^{3/2}}{3E(t_0)}\right]\exp\left[-\frac{(2I_p)^{1/2}v_0^2}{E(t_0)}\right], \quad (1)$$

Where t_0 is tunnel-ionization time, v_0 is initial transverse momentum and I_p is the first ionization potential. Then, the subsequent evolution of the two electrons is governed by classical equations of motion. Hamilton canonical equation is

$$\dot{q}_i = \frac{\partial H}{\partial p_i}, \dot{p}_i = -\frac{\partial H}{\partial q_i}, (i = 1, 2), \quad (2)$$

with the Hamiltonian function

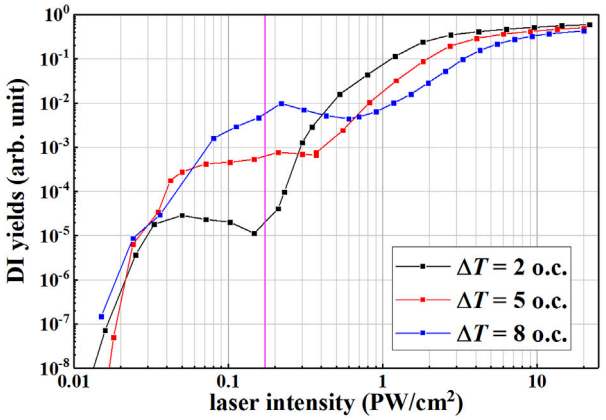

FIGURE 2
Variation curve of double ionization yield with linearly polarized laser intensity for three different delay times under compound laser field. The vertical pink lines indicate the non-sequential double ionization of Ar atoms in a compound laser field with a field strength of 0.16 PW/cm^2.

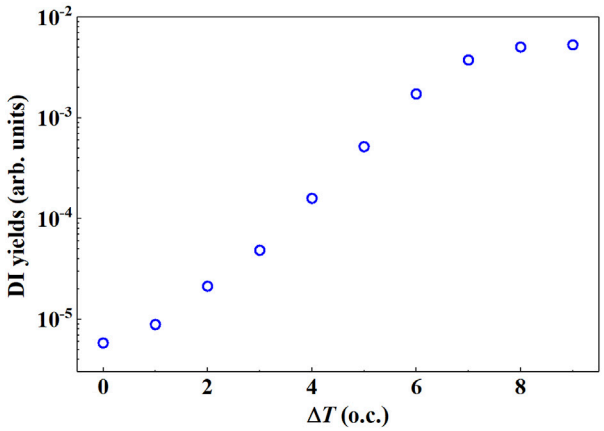

FIGURE 3
Relationship between double ionization yield and time-delay of compound laser field. The electric field strength is 0.16 PW/cm^2.

$$H = \frac{\mathbf{p}_1^2}{2} + \frac{\mathbf{p}_2^2}{2} - \frac{2}{|\mathbf{r}_1|} - \frac{2}{|\mathbf{r}_2|} + \frac{1}{|\mathbf{r}_1 - \mathbf{r}_2|} + (\mathbf{r}_1 + \mathbf{r}_2) \cdot \mathbf{E}(t), \quad (3)$$

where q_i and p_i are the canonical coordinates and canonical momentum of the electron.The form of the composite laser field can be written as

$$\mathbf{E}(t) = \mathbf{E}_1(t) + \mathbf{E}_2(t), \quad (4)$$

$$\mathbf{E}_1(t) = E_0 f(t) \cos(\omega_1 t)\hat{\mathbf{x}}, \quad (5)$$

$$\mathbf{E}_2(t) = \frac{E_0 f(t - \Delta T)}{\sqrt{2}} \{\cos[\omega_2 (t - \Delta T)]\hat{\mathbf{x}} + \sin[\omega_2 (t - \Delta T)]\hat{\mathbf{y}}\}, \quad (6)$$

where $\omega_1 = \omega_2 = 0.0583$ ($\lambda_1 = \lambda_2 = 780$ nm) is the frequency (wavelength) of the two laser pulses, and E_0 is the electric field strength of linearly polarized laser field. The pulse envelope is $f(t) = \exp[-4\ln 2(t^2/\tau^2)]$, and $\tau = 18$ fs indicates full width at half-maximum (FWHM). The delay time of the circularly polarized laser relative to the linearly polarized laser is expressed as ΔT.

In our model calculation 10^8 initial points are generated, and the tunnel-ionization time t_0 is selected randomly in the time interval $[-\tau, \tau + \Delta T]$. The Hamilton canonical equation is solved by using the Runge-Kutta algorithm.

Figure 1 shows the schematic diagram of the composite laser electric field with the time delay $\Delta T = 8$ o.c. The superimposed part makes the polarization of the laser electric field transition from linear polarization to circular polarization. With different delay time, the time-dependent ellipticity has different variation tendency, which provides a controlling mechanism of electron dynamics.

3 Results and discussion

After determining the laser form, we appropriately select three different delay times $\Delta T = 2$ o.c., $\Delta T = 5$ o.c., and $\Delta T = 8$ o.c. (corresponds to 0.3τ, 0.7τ and 1.1τ) to calculate the curve of the double ionization yield with the linearly polarized laser intensity, as shown in Figure 2. It can be seen from the figure that for all the delay times, the area where the field strength is lower than 0.7 PW/cm^2 presents a "knee" structure, indicating that the main mechanism of double ionization is NSDI. In the "knee" structure area, the longer the time delay of the two laser pulses, the higher the double ionization yield. This is because the longer time delay makes the two laser pulses farther away from each other, and the respective characteristics of linearly polarized and circularly polarized lasers are prominent. It is can also been seen by blue line in Figure 6. For $\Delta T = 8$ o.c., very small time-dependent ellipticity covers large range of LP, while large time-dependent ellipticity covers most range of CP. The probability of collision of ionized electrons increases under the action of linearly polarized laser pulses. No collision process under circularly polarized laser pulses.

When the time delay is small, the superposition degree of the linearly polarized laser pulse and the circularly polarized laser pulse is large, the ellipticity of the recombination field is large as well. As shown by the red line in Figure 6, the time-dependent ellipticity with $\Delta T = 2$ o.c. offers a larger lateral effect for almost all of the peak region of laser pulse. Therefore the collision process of ionized electrons is reduced. The NSDI process is suppressed.

In addition, the position of "knee" structures tends to be shifted to the left as decrease of the delay time. Please note that the horizontal axis in Figure 2 is the intensity of linearly polarized

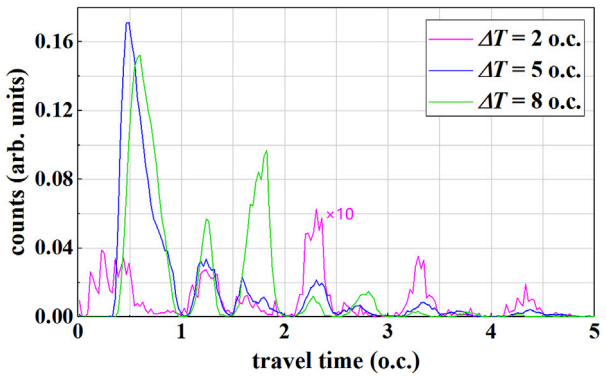

FIGURE 4
The drift time distribution of ionized electrons with the time delay 2 o.c. (pink line, multiply by 10), 5 o.c. (blue line), and 8 o.c. (green line). The results are calculated with 2×10^8 initial points.

laser pulse, which is smaller than the compound laser intensity. As a result, the position of "knee" structures should be shifted to the left relative to the original situation (composed laser intensities) in a way, and the greater the degree of overlap (smaller delay time), the greater the shift to the left.

However, in the high field strength region, that is, the sequential double ionization (SDI) mechanism region, a longer time delay corresponds to a lower double ionization yield. Considering the pulse envelope shape, a longer delay time means a lesser degree of superposition, which in turn leads to a smaller peak field strength of the composite field. The law of smaller time delays is the opposite. In the SDI mechanism, double ionization does not have to undergo a collision process, and the ionization efficiency of two electrons only depends on the magnitude of the field strength.

For different delay times ΔT, the curves of double ionization yield with laser intensity all show the feature of "knee" structure. We calculated the effect of time delay on double ionization yield at the electric field strength of 0.16 PW/cm^2. As shown by the pink vertical line in Figure 2.

Overall, the double ionization yield increases with the increase of the time delay ΔT (as shown in Figure 3), which is consistent with the result of the curve of double ionization yield versus laser intensity. In addition, the double ionization yield will stabilize as ΔT tends to increase, because the two laser pulses have been separated, and only the linearly polarized laser pulse influences the NSDI. On the other hand, the double ionization yield is minimal with the time delay $\Delta T = 0$, because the two laser pulses are completely coincident and the combined laser transform into elliptical polarization. NSDI is suppressed to the greatest extent.

To account for the existence of fixed-form ionization channels in the recombined fields, we calculate the time distributions of ionized electron drift with time delays of 2 o.c. (pink line), 5 o.c. (blue line), and 8 o.c. (green line). As shown in Figure 4, the overall drift time distribution presents a multi-peak structure. The intensity of each peak is different under different delay times, but the peak position does not change much. This shows that there are various fixed forms of collision under the action of the laser field, and at the same time, they change with the change of the superposition degree of the two lasers.

According to the Simpleman theory, driven by the linearly polarized laser field, the electron ionization returns to the origin for the first time at $0.75T$ (where T is an optical period). However, due to the periodic characteristics of laser oscillation, the time of returning to the origin for the following different times is $0.75T + nT(n = 0, 1, 2, \ldots)$. According to the symmetry characteristics during the half optical cycle, the return time also satisfies $0.25T + nT(n = 0, 1, 2, \ldots)$. Different peaks justly correspond to recollision trajectories with different return times.

In order to more intuitively show that different peaks in the drift time distribution correspond to different return times, we plot the collision trajectories of the ionized electrons for the first, second, third, and multiple returns. The first peak in the time distribution (Figure 4) corresponds to the situation where the electrons return to collide for the first time after ionization, and we draw its recollision trajectory, as shown in Figure 5A. The black line in Figure 5A represents the recollision trajectory of the first ionized electron. After the electron is ionized, it returns to the nuclear region for the first time and recollides with the bound state electron. The red line shows the trajectory of bound electrons. This kind of trajectory is the general ionization channel under the first peak if the delay time is large enough (green and blue lines in Figure 4), while it is relatively suppressed at a short time delay (pink line in Figure 4).

As shown in Figure 5B, the recolliding electron is ionized first, and reaches the vicinity of 40 a.u. in the polarization direction, and then reverses for the first time under the action of the oscillating laser field, and pass by the nuclear region for the first time during the reverse motion. The second reversal occurs near −24 a.u., and finally collides with the second bound state electron with it returns to the nuclear region for the second time, resulting in non-sequential double ionization. The electron trajectory in this process is a typical second-return collision trajectory.

Figure 5C shows the trajectory of the third return collision. The ionized electrons are driven by the laser to pass by the nuclear region two times, and finally recollides with the bound electron at the third return, resulting in double ionization. The influence of these two MRC trajectories (Figures 5B,C) cannot be neglected when the delay time is large (the green line in Figure 4).

The complex trajectories of the ionized electrons with more return times are shown in Figure 5D. This NSDI channel is prominent when delay time is small due to the larger lateral influence of combined laser with near-elliptical

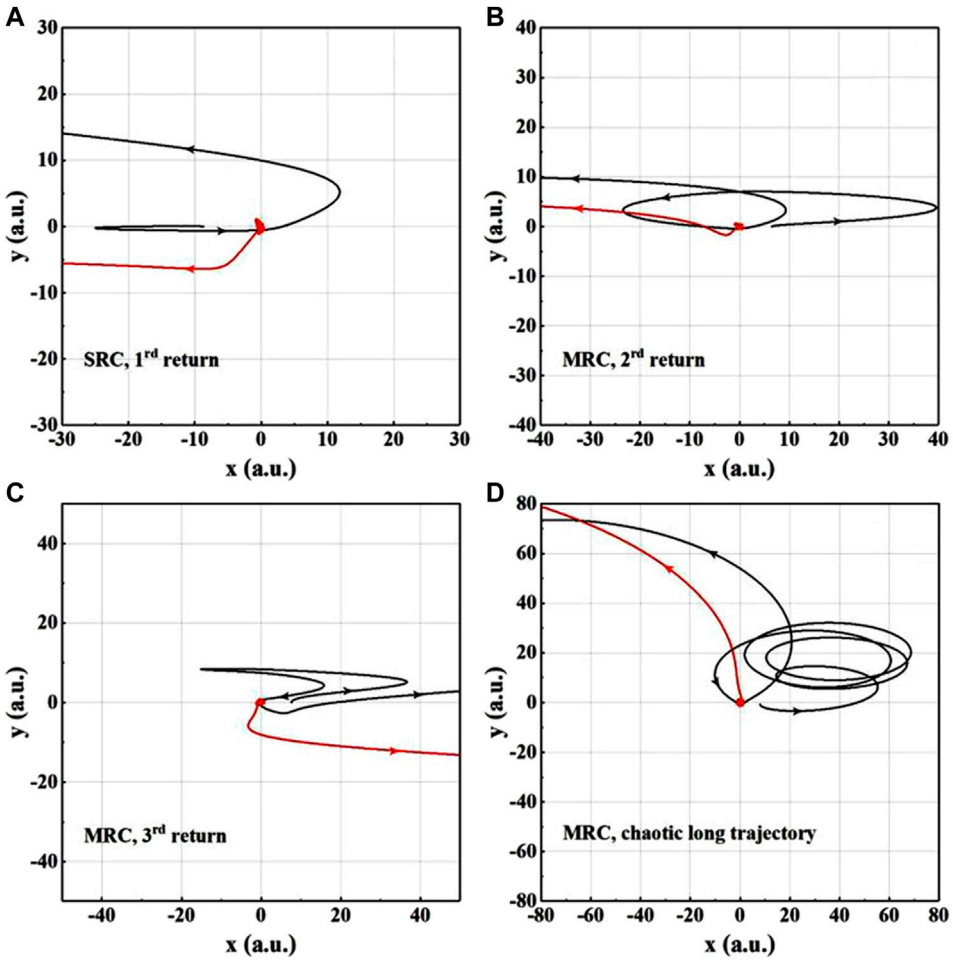

FIGURE 5
Ionized electrons return to collision trajectory for the first time **(A)**, second times **(B)**, third times **(C)** and many times **(D)**, respectively.

polarization [41]. The collision trajectories of this multi-period motion are highly chaotic, and the electron wave packet dispersion effect is obvious. Therefore, diverse MRC trajectories all work but the ionization yields are lower (the pink line in Figure 4).

In the MRC trajectories, the ionized electrons pass through the nuclear region, at a distance from the ion nucleus in the y-direction. This lateral distance shrinks again with the electrons return to the nuclear region a certain number of times. This electron lateral drift process is closely related to the initial lateral velocity of electrons under the action of linearly polarized laser and is influenced by the Coulomb attraction of ion nuclei. This Coulomb attraction causes the electron wave packet to shrink laterally to a certain extent with passing near the nuclear region, which is the Coulomb focusing effect [42–46].

The ellipticity of the composite laser field changes with time. The effect of the laser electric field in the lateral direction and the Coulomb focusing effect will occur to different degrees from the lateral drift caused by the initial lateral velocity of the electrons. The electrons return to the parent nucleus ions after different drift times and undergo a collision process, and their flight trajectories show collision trajectories with multiple returns. In our simulations, the superposition of the two laser beams to different degrees makes the ellipticity change with time to different degrees, which in turn controls the electrons to recollide with trajectories with different return times in a higher degree of freedom to generate the NSDI process.

From Eqs. 5, 6, the time-dependent ellipticity can be expressed as

$$\epsilon(t) \approx \frac{\frac{1}{\sqrt{2}} f(t-\Delta T)}{f(t)-\frac{1}{\sqrt{2}} f(t-\Delta T)}, \tag{7}$$

Taking the peak position of the linearly polarized laser as time zero, the variation of $\epsilon(t)$ represents the correction of the

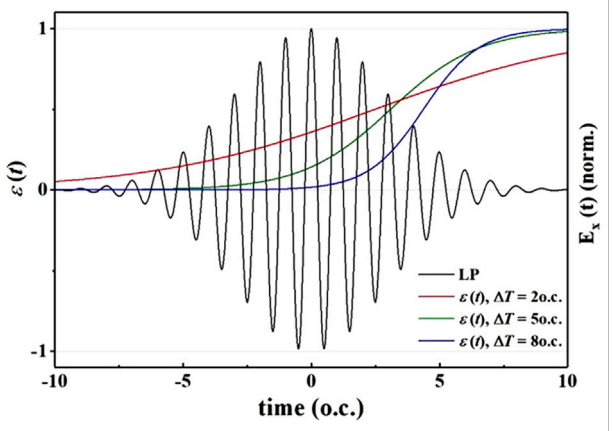

FIGURE 6
Variation of ellipsometry in laser field with different time delays. The solid black line shows the time-dependent electric field of the linearly polarized laser in the x-direction. The red, green, and blue lines show the ellipticity versus time curves for delay times ΔT = 2 o.c., 5 o.c., and 8 o.c., respectively.

electric field properties of the linearly polarized laser. Therefore, we compare the time curve of the electric field of the linearly polarized laser along the x-direction with the curve $\epsilon(t)$. The lines are drawn in the same figure as the solid black line in Figure 6. The delay time is selected as ΔT = 2 o.c., 5 o.c., and 8 o.c. are shown by the red, green, and blue lines in Figure 6. The three curves reflect the change of the composite laser field from linear polarization to circular polarization with time. The longer the delay time, the faster $\epsilon(t)$ increases, and the more lag the area swept over.

The rising transition region of the red line covers the region of several larger peaks of the linearly polarized laser in a relatively larger range with ΔT = 2 o.c. Most of the electrons ionized near the laser peak are driven by the recombination field with higher ellipticity, which causes the lateral drift of the ionized electrons due to the lateral laser drive to be stronger than that caused by the initial lateral velocity. The first ionized electron prefers to stay away from the nuclear region. Therefore, most of the electrons will return to the parent nucleus in multi-period chaotic trajectories with longer drift times to collide with ions to induce NSDI [as shown in Figure 5D]. This is the reason why the ionized electron drift time is distributed over a larger range (the pink line in Figure 4).

The rising region of the blue line representing the time-dependent ellipticity overlaps the electric field of the linearly polarized laser to a small extent with ΔT = 8 o.c., which means that the changing ellipticity has less influence on the linearly polarized laser. The collision is mainly determined by several electric field peaks in the linearly polarized laser platform region. The number of electron returns is greatly affected by the initial lateral velocity and Coulomb focusing effect. The subsequent circularly polarized laser is ineffective. Therefore, as shown by the green line in Figure 4, the peak intensity of the drift time corresponding to the collision trajectories of the first three returns is stronger, and the peaks corresponding to the trajectories of other drift times are relatively suppressed.

The time-dependent ellipticity curve is shown by the green dotted line with ΔT = 5 o.c. in Figure 6. The control effect of electrons is between the above two cases. Compared with the case of ΔT = 8 o.c., the rising region of $\epsilon(t)$ only affects part of the region of the linearly polarized laser platform. The effect of the laser electric field in the lateral direction excludes the MRC trajectories. Therefore, compared with green line in Figure 4, more peaks corresponding to long drift times are suppressed, making the first peak relatively prominent (blue line in Figure 4). On the other hand, the enhancement of the first isolated peak indicates that the first return to the collision trajectory reaches the maximum. This is because compared to the case of ΔT = 2 o.c., the lateral effect of the laser electric field compensates the initial lateral velocity of the ionized electrons with the electrons return for the first time so that this channel reaches the maximum enhancement.

4 Conclusion

In summary, the NSDI of Ar in a superimposed linearly and circularly polarized compound field is investigated. The waveform change of the composite laser field is controlled by adjusting the time delay. The double ionization yield increases with the electric field strength in the electric field with different time delays. The electric field strength is chosen as 0.16 PW/cm^2 according to the relationship between time delay and double ionization yield. We plot the drift time distribution of ionized electrons for different delay times. By analyzing the drift time distribution of ionized electrons and electron ionization trajectories, the movement of ionized electrons in the electric field has different collision trajectories. The shape of the electric field determines the dominant trajectories of electron double ionization. the regulation of the NSDI ionization recollision trajectory form can be achieved by adjusting the delay time of the composite laser field. The MRC controlling mechanism is expected to shed more light on laser-induced electron diffraction (LIED) [47–49] or laser-induced inelastic diffraction (LIID) [50], in which electrons with different return times are considered to play different and key role in laser-induced ultrafast imaging. Our study shows that the electron dynamics in one or few optical cycle can be controlled in a multicycle laser fields, which do not have to be limited to few-cycle laser pulses.

Data availability statement

The raw data supporting the conclusions of this article will be made available by the authors, without undue reservation.

Author contributions

All authors listed have made a substantial, direct, and intellectual contribution to the work and approved it for publication.

Funding

This work was supported by the National Key Research and Development Program of China (Grant No. 2019YFA0307700), National Natural Science Foundation of China (Grant Nos. 91950101, 12074240, 11874246, 11604131, 12204136, 12204135, and 12264013), Hainan Provincial Natural Science Foundation of China (Grant Nos. 122CXTD504 and 122QN217), Natural Science Foundation of Liaoning Province of China (Grant No. LQ2020022), Sino-German Mobility Programme (Grant No. M-0031).

Conflict of interest

The authors declare that the research was conducted in the absence of any commercial or financial relationships that could be construed as a potential conflict of interest.

Publisher's note

All claims expressed in this article are solely those of the authors and do not necessarily represent those of their affiliated organizations, or those of the publisher, the editors and the reviewers. Any product that may be evaluated in this article, or claim that may be made by its manufacturer, is not guaranteed or endorsed by the publisher.

References

1. Krausz F, Ivanov M. Attosecond physics. *Attosecond Physics Rev Mod Phys* (2009) 81:163–234. doi:10.1103/RevModPhys.81.163

2. Chang Z, Corkum P. Attosecond photon sources: The first decade and beyond [invited]. *J Opt Soc Am B* (2010) 27:B9. doi:10.1364/JOSAB.27.0000B9

3. Xue B, Tamaru Y, Fu Y, Yuan H, Lan P, Mücke OD, et al. A custom-tailored multi-tw optical electric field for gigawatt soft-x-ray isolated attosecond pulses. *Ultrafast Sci* (2021) 2021:1. doi:10.34133/2021/9828026

4. Hoflund M, Peschel J, Plach M, Dacasa H, Veyrinas K, Constant E, et al.Focusing properties of high-order harmonics. *Ultrafast Sci* (2021) 2021:1. doi:10.34133/2021/9797453

5. Zuo R, Trautmann A, Wang G, Hannes W, Yang S, Song X, et al.Neighboring atom collisions in solid-state high harmonic generation. *Ultrafast Sci* (2021) 2021:1. doi:10.34133/2021/9861923

6. Becker W, Grasbon F, Kopold R, Milošević D, Paulus G, Walther HAbove-threshold ionization: From classical features to quantum effects. *Adv Mol Opt Phys* (2002) 48:35–98. doi:10.1016/S1049-250X(02)80006-4

7. Becker W, Liu XJ, Ho PJ, Eberly JHTheories of photoelectron correlation in laser-driven multiple atomic ionization. *Rev Mod Phys* (2012) 84:1011–43. doi:10.1103/RevModPhys.84.1011

8. Corkum PB. Recollision physics. *Phys Today* (2011) 64:36–41. doi:10.1063/1.3563818

9. Corkum PB. Plasma perspective on strong-field multiphoton ionization. *Phys Rev Lett* (1993) 71:1994–7. doi:10.1103/PhysRevLett.71.1994

10. Hickstein DD, Ranitovic P, Witte S, Tong XM, Huismans Y, Arpin P, et al.Direct visualization of laser-driven electron multiple scattering and tunneling distance in strong-field ionization. *Phys Rev Lett* (2012) 109:073004. doi:10.1103/PhysRevLett.109.073004

11. Tong XM, Ranitovic P, Hickstein DD, Murnane MM, Kapteyn HC, Toshima N. Enhanced multiple-scattering and intra-half-cycle interferences in the photoelectron angular distributions of atoms ionized in midinfrared laser fields. *Phys Rev A (Coll Park)* (2013) 88:013410. doi:10.1103/PhysRevA.88.013410

12. Wolter B, Lemell C, Baudisch M, Pullen MG, Tong XM, Hemmer M, et al.Formation of very-low-energy states crossing the ionization threshold of argon atoms in strong mid-infrared fields. *Phys Rev A (Coll Park)* (2014) 90:063424. doi:10.1103/PhysRevA.90.063424

13. Hernández-García C, Pérez-Hernández JA, Popmintchev T, Murnane MM, Kapteyn HC, Jaron-Becker A, et al.Zeptosecond high harmonic kev x-ray waveforms driven by midinfrared laser pulses. *Phys Rev Lett* (2013) 111:033002. doi:10.1103/PhysRevLett.111.033002

14. Li PC, Sheu YL, Laughlin C, Chu SI. Dynamical origin of near- and below-threshold harmonic generation of cs in an intense mid-infrared laser field. *Nat Commun* (2015) 6:7178. doi:10.1038/ncomms8178

15. Li PC, Sheu YL, Jooya HZ, Zhou XX, Chu SI. Exploration of laser-driven electron-multirescattering dynamics in high-order harmonic generation. *Sci Rep* (2016) 6:32763. doi:10.1038/srep32763

16. Jia X, Hao X, Fan D, Li W, Chen J. S-matrix and semiclassical study of electron-electron correlation in strong-field nonsequential double ionization of Ne. *Phys Rev A (Coll Park)* (2013) 88:033402. doi:10.1103/PhysRevA.88.033402

17. Hao X, Bai Y, Li C, Zhang J, Li W, Yang W, et al.Recollision of excited electron in below-threshold nonsequential double ionization. *Commun Phys* (2022) 5:31. doi:10.1038/s42005-022-00809-2

18. Wu M, Wang Y, Liu X, Li W, Hao X, Chen J. Coulomb-potential effects in nonsequential double ionization under elliptical polarization. *Phys Rev A (Coll Park)* (2013) 87:013431. doi:10.1103/PhysRevA.87.013431

19. Kang H, Henrichs K, Kunitski M, Wang Y, Hao X, Fehre K, et al.Timing recollision in nonsequential double ionization by intense elliptically polarized laser pulses. *Phys Rev Lett* (2018) 120:223204. doi:10.1103/PhysRevLett.120.223204

20. Kang H, Henrichs K, Wang Y, Hao X, Eckart S, Kunitski M, et al.Double ionization of neon in elliptically polarized femtosecond laser fields. *Phys Rev A (Coll Park)* (2018) 97:063403. doi:10.1103/PhysRevA.97.063403

21. Zhang L, Xie X, Roither S, Zhou Y, Lu P, Kartashov D, et al.Subcycle control of electron-electron correlation in double ionization. *Phys Rev Lett* (2014) 112:193002. doi:10.1103/PhysRevLett.112.193002

22. Wang Y, Yu S, Lai X, Kang H, Xu S, Sun R, et al.Separating intracycle interferences in photoelectron momentum distributions by a polarization-gated pulse. *Phys Rev A (Coll Park)* (2018) 98:043422. doi:10.1103/PhysRevA.98.043422

23. Mancuso CA, Hickstein DD, Grychtol P, Knut R, Kfir O, Tong X, et al.Strong-field ionization with two-color circularly polarized laser fields. *Phys Rev A (Coll Park)* (2015) 91:031402. doi:10.1103/PhysRevA.91.031402

24. Mancuso CA, Dorney KM, Hickstein DD, Chaloupka JL, Tong X, Ellis JL, et al.Observation of ionization enhancement in two-color circularly polarized laser fields. *Phys Rev A (Coll Park)* (2017) 96:023402. doi:10.1103/PhysRevA.96.023402

25. Chaloupka JL, Hickstein DD. Dynamics of strong-field double ionization in two-color counterrotating fields. *Phys Rev Lett* (2016) 116:143005. doi:10.1103/PhysRevLett.116.143005

26. Mancuso CA, Dorney KM, Hickstein DD, Chaloupka JL, Ellis JL, Dollar FJ, et al.Controlling nonsequential double ionization in two-color circularly polarized femtosecond laser fields. *Phys Rev Lett* (2016) 117:133201. doi:10.1103/PhysRevLett.117.133201

27. Eckart S, Richter M, Kunitski M, Hartung A, Rist J, Henrichs K, et al.Nonsequential double ionization by counterrotating circularly polarized two-color laser fields. *Phys Rev Lett* (2016) 117:133202. doi:10.1103/PhysRevLett.117.133202

28. Chen Z, Su J, Zeng X, Huang X, Li Y, Huang C. Electron angular correlation in nonsequential double ionization of molecules by counter-rotating two-color circularly polarized fields. *Opt Express* (2021) 29:29576. doi:10.1364/OE.439864

29. Djiokap JMN, Hu SX, Madsen LB, Manakov NL, Meremianin AV, Starace AF. Electron vortices in photoionization by circularly polarized attosecond pulses. *Phys Rev Lett* (2015) 115:113004. doi:10.1103/PhysRevLett.115.113004

30. Yuan KJ, Chelkowski S, Bandrauk AD. Photoelectron momentum distributions of molecules in bichromatic circularly polarized attosecond uv laser fields. *Phys Rev A (Coll Park)* (2016) 93:053425. doi:10.1103/PhysRevA.93.053425

31. Pengel D, Kerbstadt S, Johannmeyer D, Englert L, Bayer T, Wollenhaupt M. Electron vortices in femtosecond multiphoton ionization. *Phys Rev Lett* (2017) 118:053003. doi:10.1103/PhysRevLett.118.053003

32. Xiao XR, Wang MX, Liang H, Gong Q, Peng LY. Proposal for measuring electron displacement induced by a short laser pulse. *Phys Rev Lett* (2019) 122:053201. doi:10.1103/PhysRevLett.122.053201

33. Li M, Zhang G, Ding X, Yao J. Carrier envelope phase description for an isolated attosecond pulse by momentum vortices. *Chin Phys Lett* (2019) 36:063201. doi:10.1088/0256-307X/36/6/063201

34. Ben S, Chen S, Bi CR, Chen J, Liu XS. Investigation of electron vortices in time-delayed circularly polarized laser pulses with a semiclassical perspective. *Opt Express* (2020) 28:29442. doi:10.1364/OE.400846

35. Bayer T, Wollenhaupt M. Molecular free electron vortices in photoionization by polarization-tailored ultrashort laser pulses. *Front Chem* (2022) 10:899461. doi:10.3389/fchem.2022.899461

36. Balogh E, Kovacs K, Dombi P, Fulop JA, Farkas G, Hebling J, et al.Single attosecond pulse from terahertz-assisted high-order harmonic generation. *Phys Rev A (Coll Park)* (2011) 84:023806. doi:10.1103/PhysRevA.84.023806

37. Chen J, Liu J, Fu LB, Zheng WM. Interpretation of momentum distribution of recoil ions from laser-induced nonsequential double ionization by semiclassical rescattering model. *Phys Rev A (Coll Park)* (2000) 63:011404. doi:10.1103/PhysRevA.63.011404

38. Ye DF, Liu X, Liu J. Classical trajectory diagnosis of a fingerlike pattern in the correlated electron momentum distribution in strong field double ionization of helium. *Phys Rev Lett* (2008) 101:233003. doi:10.1103/PhysRevLett.101.233003

39. Ammosov MV, Delone NB, Krainov VP. Tunnel ionization of complex atoms and atomic ions in electromagnetic field. *High Intensity Laser Process* (1986) 91:2008. doi:10.1117/12.938695

40. Delone NB, Krainov VP. Energy and angular electron spectra for the tunnel ionization of atoms by strong low-frequency radiation. *J Opt Soc Am B* (1991) 8:1207. doi:10.1364/JOSAB.8.001207

41. Wang X, Eberly JH. Elliptical trajectories in nonsequential double ionization. *New J Phys* (2010) 12:093047. doi:10.1088/1367-2630/12/9/093047

42. Rudenko A, Zrost K, Ergler T, Voitkiv AB, Najjari B, Jesus V, et al.Coulomb singularity in the transverse momentum distribution for strong-field single ionization. *J Phys B: Mol Opt Phys* (2005) 38:L191–8. doi:10.1088/0953-4075/38/11/L01

43. Shafir D, Soifer H, Vozzi C, Johnson AS, Hartung A, Dube Z, et al.Trajectory-resolved coulomb focusing in tunnel ionization of atoms with intense, elliptically polarized laser pulses. *Phys Rev Lett* (2013) 111:023005. doi:10.1103/PhysRevLett.111.023005

44. Kelvich SA, Becker W, Goreslavski SP. Coulomb focusing and defocusing in above-threshold-ionization spectra produced by strong mid-ir laser pulses. *Phys Rev A (Coll Park)* (2016) 93:033411. doi:10.1103/PhysRevA.93.033411

45. Richter M, Kunitski M, Schöffler M, Jahnke T, Schmidt L, Dörner R. Ionization in orthogonal two-color laser fields: Origin and phase dependences of trajectory-resolved coulomb effects. *Phys Rev A (Coll Park)* (2016) 94:033416. doi:10.1103/PhysRevA.94.033416

46. Song X, Xu J, Lin C, Sheng Z, Liu P, Yu X, et al.Attosecond interference induced by coulomb-field-driven transverse backward-scattering electron wave packets. *Phys Rev A (Coll Park)* (2017) 95:033426. doi:10.1103/PhysRevA.95.033426

47. Blaga CI, Xu J, DiChiara AD, Sistrunk E, Zhang K, Agostini P, et al.Imaging ultrafast molecular dynamics with laser-induced electron diffraction. *Nature* (2012) 483:194–7. doi:10.1038/nature10820

48. Wolter B, Pullen MG, Le AT, Baudisch M, Doblhoff-Dier K, Senftleben A, et al.Ultrafast electron diffraction imaging of bond breaking in di-ionized acetylene. *Science* (2016) 354:308–12. doi:10.1126/science.aah3429

49. Hao X, Bai Y, Zhao X, Li C, Zhang J, Wang J, et al.Effect of coulomb field on laser-induced ultrafast imaging methods. *Phys Rev A (Coll Park)* (2020) 101:051401. doi:10.1103/PhysRevA.101.051401

50. Quan W, Hao X, Hu X, Sun R, Wang Y, Chen Y, et al.Laser-induced inelastic diffraction from strong-field double ionization. *Phys Rev Lett* (2017) 119:243203. doi:10.1103/PhysRevLett.119.243203

frontiers | Frontiers in Physics

TYPE Correction
PUBLISHED 24 November 2022
DOI 10.3389/fphy.2022.1093134

OPEN ACCESS

APPROVED BY
Frontiers Editorial Office,
Frontiers Media SA, Switzerland

*CORRESPONDENCE
Weifeng Yang,
wfyang@hainanu.edu.cn
Xiaolei Hao,
xlhao@sxu.edu.cn
Jing Chen,
chen_jing@iapcm.ac.cn

SPECIALTY SECTION
This article was submitted to Optics and Photonics, a section of the journal Frontiers in Physics

RECEIVED 08 November 2022
ACCEPTED 10 November 2022
PUBLISHED 24 November 2022

CITATION
Ben S, Han Y, Yang W, Yu W, Hao X, Song X, Li W and Chen J (2022), Corrigendum: Controlling electron recollision with combined linear and circular polarization.
Front. Phys. 10:1093134.
doi: 10.3389/fphy.2022.1093134

Corrigendum: Controlling electron recollision with combined linear and circular polarization

Shuai Ben[1], Yifan Han[2], Weifeng Yang[1]*, Weiwei Yu[2], Xiaolei Hao[3]*, Xiaohong Song[1], Weidong Li[4] and Jing Chen[5,6]*

[1]Department of Physics, School of Science, Hainan University, Haikou, China, [2]School of Physics and Electronic Technology, Liaoning Normal University, Dalian, China, [3]Department of Physics, Institute of Theoretical Physics, State Key Laboratory of Quantum Optics and Quantum Optics Devices, Collaborative Innovation Center of Extreme Optics, Shanxi University, Taiyuan, China, [4]Shenzhen Key Laboratory of Ultraintense Laser and Advanced Material Technology, Center ForAdvanced Material Diagnostic Technology, College of Engineering Physics, Shenzhen Technology University, Shenzhen, China, [5]Institute of Applied Physics and Computational Mathematics, Beijing, China, [6]HEDPS, Center for Applied Physics and Technology, Peking University, Beijing, China

KEYWORDS

non-sequential double ionization, strong filed physics, ultra-fast laser pulse, semiclassical model, recollision

A Corrigendum on
Controlling electron recollision with combined linear and circular polarization

by Ben S, Han Y, Yang W, Yu W, Hao X, Song X, Li W and Chen J (2022). Front. Phys. 10:1004021. doi: 10.3389/fphy.2022.1004021

In the published article, there was an error in the Funding statement. Foundation codes 12204136, 12204135, and 12264013 were misplaced under the Hainan Provincial Natural Science Foundation of China. These codes should be under the National Natural Science Foundation of China. The correct Funding statement appears below.

Funding

This work was supported by the National Key Research and Development Program of China (Grant No. 2019YFA0307700), National Natural Science Foundation of China (Grant Nos. 91950101, 12074240, 11874246, 11604131, 12204136, 12204135, and 12264013), Hainan Provincial Natural Science Foundation of China (Grant Nos. 122CXTD504 and 122QN217), Natural Science Foundation of Liaoning Province of China (Grant No. LQ2020022), Sino-German Mobility Programme (Grant No. M-0031).

The authors apologize for this error and state that this does not change the scientific conclusions of the article in any way. The original article has been updated.

Publisher's note

frontiers | Frontiers in Physics

TYPE Original Research
PUBLISHED 05 October 2022
DOI 10.3389/fphy.2022.964586

OPEN ACCESS

EDITED BY
Venugopal Rao Soma,
University of Hyderabad, India

REVIEWED BY
Kamal Singh,
Indian Institute of Science Education and Research Mohali, India
Sivarama Krishnan,
Indian Institute of Technology Madras, India

*CORRESPONDENCE
L. Neoričić,
lana.neoricic@fysik.lth.se
D. Busto,
david.busto@fysik.lth.se

†These authors have contributed equally to this work

SPECIALTY SECTION
This article was submitted to Optics and Photonics, a section of the journal Frontiers in Physics

RECEIVED 08 June 2022
ACCEPTED 01 September 2022
PUBLISHED 05 October 2022

CITATION
Neoričić L, Busto D, Laurell H, Weissenbilder R, Ammitzböll M, Luo S, Peschel J, Wikmark H, Lahl J, Maclot S, Squibb RJ, Zhong S, Eng-Johnsson P, Arnold CL, Feifel R, Gisselbrecht M, Lindroth E and L'Huillier A (2022), Resonant two-photon ionization of helium atoms studied by attosecond interferometry. *Front. Phys.* 10:964586. doi: 10.3389/fphy.2022.964586

Resonant two-photon ionization of helium atoms studied by attosecond interferometry

L. Neoričić[1*†], D. Busto[1,2*†], H. Laurell[1], R. Weissenbilder[1], M. Ammitzböll[1], S. Luo[1], J. Peschel[1], H. Wikmark[1], J. Lahl[1], S. Maclot[1], R. J. Squibb[3], S. Zhong[1], P. Eng-Johnsson[1], C. L. Arnold[1], R. Feifel[3], M. Gisselbrecht[1], E. Lindroth[4] and A. L'Huillier[1]

[1]Department of Physics, Lund University, Lund, Sweden, [2]Institute of Physics, Albert Ludwig University, Freiburg, Germany, [3]Department of Physics, University of Gothenburg, Gothenburg, Sweden, [4]Department of Physics, Stockholm University, AlbaNova University Center, Stockholm, Sweden

We study resonant two-photon ionization of helium atoms via the 1*s*3*p*, 1*s*4*p* and 1*s*5*p*^{1}P$_1$ states using the 15th harmonic of a titanium-sapphire laser for the excitation and a weak fraction of the laser field for the ionization. The phase of the photoelectron wavepackets is measured by an attosecond interferometric technique, using the 17th harmonic. We perform experiments with angular resolution using a velocity map imaging spectrometer and with high energy resolution using a magnetic bottle electron spectrometer. Our results are compared to calculations using the two-photon random phase approximation with exchange to account for electron correlation effects. We give an interpretation for the multiple π-rad phase jumps observed, both at and away from resonance, as well as their dependence on the emission angle.

KEYWORDS

attosecond, photoionization, photoelectron interferometry, photoionization dynamics, attosecond dynamics

1 Introduction

Attosecond techniques using single pulses [1, 2] or pulse trains [3, 4] combined with a synchronized laser field have become essential tools for the study of photoionization processes in atoms and molecules. The phase information provided by techniques such as streaking [5] or RABBIT (Reconstruction of Attosecond Beating By Interference of Two-photon transitions) [3] complements cross-section measurements, giving insight into the photoionization temporal dynamics [2, 4]. Experiments have been performed in different atomic [6–8] and molecular [9–11] systems, and in broad photon energy regions, typically between 20 and 100 eV [6, 12]. When atoms or molecules are ionized into "flat", structureless continua, the phase does not vary much with energy, apart from the threshold region, which may be affected by the variation of the so-called Coulomb phase and a laser-induced "continuum-continuum" phase [13, 14]. In contrast,

pronounced phase variations are observed in the vicinity of Cooper minima [4, 8] and broad shape resonances in atomic or molecular systems [7, 11].

These studies require broadband radiation, single attosecond pulses or attosecond pulse trains, typically spanning a few tens of eV in energy, in order to resolve ultrafast dynamics with time scales in the attosecond regime. Attosecond techniques may also be applied to the study of two-photon resonant processes, where the first, extreme ultraviolet (XUV) photon comes into resonance with a bound [15–18] or quasi-bound autoionizing state [9, 19]. The study of resonant two-photon ionization usually demands a higher spectral resolution than that of non-resonant processes, and the time scales are in the femtosecond range. In the early measurements [15, 20], the XUV frequency was tuned the across the resonance. Recently, powerful energy-resolved methods like "rainbow" RABBIT have been developed [21]. In particular, the nontrivial phase variation around the $2s2p$ doubly excited state in helium [21, 22], and the $3s^{-1}4p$ window resonance in argon [23] have been extensively studied. In simple cases like helium, the temporal dynamics of the wavepacket created by resonant photoionization can be recovered [21, 22].

Angle detection brings a new dimension, momentum, to this type of measurement, allowing the reconstruction of coherent electron wavepackets in time and space. This has been beautifully shown for two-photon resonant ionization of Ne via the $3p^5 3d\,^1P_1$ state [16], and recently of He via the $1s3p$ and $1s4p\,^1P_1$ states [18]. Photoionization studies with angular resolution [18, 24–26] have pointed out that additional phase jumps as a function of emission angle appear due to the interference of angular channels, beside the phase jumps as a function of energy.

Here, we study two-photon resonant ionization of helium through intermediate states in the $1snp\ ^1P_1$ Rydberg series with n = 3–5. We generate odd high-order harmonics of an infrared (IR) laser field, and tune the IR laser frequency in order to reach the $1s3p$, $1s4p$ or a coherent superposition of $1s4p$ and $1s5p$ states with the 15th harmonic. We further ionize by absorption of an additional IR photon. We analyze the phase of the created wavepacket by interferometry using another, non-resonant two-photon process leading to the same final state, namely, absorption of the 17th harmonic and emission of an IR photon. We perform two series of experiments, one with angular resolution and moderate energy resolution using a velocity map imaging spectrometer (VMIS) and one with high energy resolution and no angular resolution using a magnetic bottle electron spectrometer (MBES). In the latter case, we also rotate the polarization of the probe field in order to eliminate one of the angular channels. We discuss the theory of "below-threshold" interferometry in the angle-integrated and angle-resolved cases and we compare our experimental results with simulations using the two-photon random phase approximation with exchange (RPAE) [27] to account for electron correlation effects. This allows us to interpret the multiple phase jumps observed both as a function of energy and emission angle.

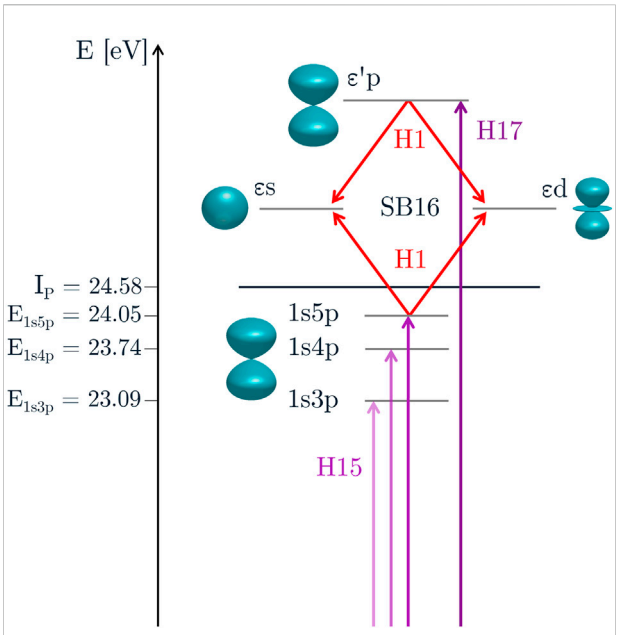

FIGURE 1
Energy levels and excitation processes involved in the present study. The violet (red) arrows denote excitation by the 15th and 17th harmonics (fundamental). The spherical harmonics corresponding to the different angular momentum channels are indicated in cyan.

2 Principle of the experiment

Our experiment is based on the RABBIT technique, with a focus on a narrow spectral region just below the ionization threshold (I_p) of helium, as illustrated in Figure 1. The 15th harmonic (H15) of the fundamental laser field is tuned into resonance with one or several Rydberg states. Harmonics of order 17 and above have enough energy to ionize the system and generate a comb of photoelectron peaks spaced by $2\hbar\omega$. In the presence of a dressing field with photon energy $\hbar\omega$, two quantum paths lead to the same final state in the continuum, resulting in the formation of sidebands (SBs). Varying the relative time-delay between the XUV and IR pulses causes periodic modulations in the SB16 signal, which can generally be written as

$$I_{SB} = |A^+|^2 + |A^-|^2 + 2|A^+||A^-|\cos(2\omega\tau - \Delta\varphi), \qquad (1)$$

where $A^{\pm}$ denotes the amplitude of the absorption (+) and emission (−) paths. The oscillation phase can be decomposed as $\Delta\varphi = \Delta\varphi_{XUV} + \Delta\varphi_A$, where $\Delta\varphi_{XUV}$ is the group delay of the attosecond pulses and $\Delta\varphi_A$ originates from the two-photon ionization process. SB16 differs from the other sidebands as the absorption path is below the ionization threshold. In a first set of experiments, we record the SB16 signal as a function of energy and angle. In a second one, we perform an angle-integrated measurement with high spectral resolution. In both cases, we extract both the amplitude of the signal oscillating at frequency

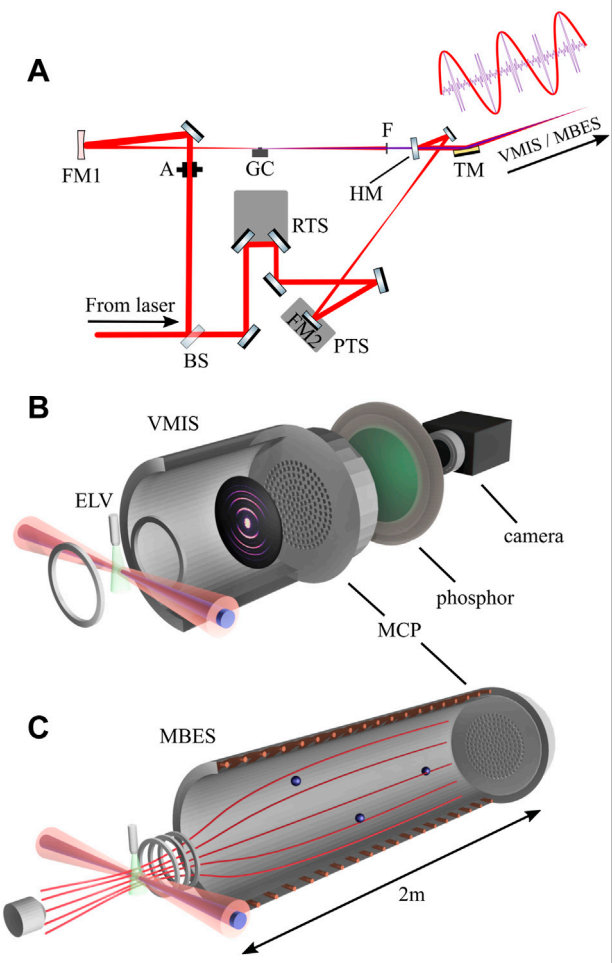

FIGURE 2
Experimental setup: **(A)** Optical interferometer allowing us to create an attosecond pulse train and a delayed dressing field; **(B)** Velocity map imaging spectrometer; **(C)** Magnetic bottle electron spectrometer. We use the following abbreviations: BS, beam splitter; A, aperture; FM, focusing mirror; GC, gas cell; RTS, rough translation stage; PTS, piezo-driven translation stage; HM, holey mirror; F, filter; TM, toroidal mirror; ELV, Even-Lavie valve; MCP, microchannel plates.

2ω and the phase of the oscillation by applying a spectrally resolved RABBIT analysis [3, 21, 28]. In this implementation of the RABBIT technique, sometimes called "below-threshold RABBIT" [15, 17, 18, 29], the interesting information is the phase change due to resonant two-photon ionization, which is "read" by interferometry with the emission path (absorption of the 17th harmonic and emission of an IR photon).

3 Experimental method

A Ti:Sa-based laser operating at 1 kHz provided 3 mJ pulses with a central wavelength tunable from 780 to 820 nm and a FWHM bandwidth of approximately 40 nm. The pulses were split using a 70–30 beamsplitter, so that the intense fraction could be used as the pump beam and the weaker one as the probe, as illustrated in Figure 2A. The pump was focused into an 8 mm long pulsed gas cell containing a rare gas, thereby generating odd harmonics of the fundamental IR field. The resulting spectrum was filtered with a 200 nm thick aluminium filter so as to suppress the transmission of the pump beam into the detection region. The probe pulses were directed onto a piezomotor-driven delay stage and recombined with the XUV pulses in a helium jet. The intensity of the probe in the interaction region was reduced in order to avoid two-IR-photon absorption.

Two complementary experimental measurements were performed, as indicated in Figures 2B,C. In the angle-resolved experiment (b), a velocity map imaging spectrometer [30, 31] was installed for the electron detection and the helium atoms were provided by an Even-Lavie valve pulsed at 500 Hz [32]. To optimize the 15th and 17th harmonic signal, the gas target was chosen to be xenon or krypton in the VMIS measurements. The photoelectrons were detected with a microchannel plate leading to a phosphor screen, recorded by a camera. The resulting images captured the projection of the momentum of electrons in the plane perpendicular to their travel. The momentum maps were recorded as a function of the delay between the pump and probe pulses, in steps of 250 as. The photoelectron momentum distribution was obtained at each delay by performing an inverse Abel transform on the VMIS images [33]. In order to minimize the appearance of mathematical artefacts in the centre of the inverted images, a well-known problem of inversion methods based on Legendre polynomial decomposition, an iterative inversion algorithm based on [34] was applied. The oscillation phase for each energy and angle bin was extracted by fitting a cosine function to the recorded time-delay signal.

The high spectral resolution measurements were carried out using an MBES for the electron detection, with a 2 m long flight tube and a 4π sr collection angle [see Figure 2C]. The energy resolution was better than 80 meV at low kinetic energies. He atoms were provided by an effusive gas jet. The delay between the two beams was stabilized with an RMS error of less than 20 as. In the MBES measurements, high-order harmonics were generated in argon. The laser central wavelength was chosen to be 782 nm and the bandwidth 30 nm, so that the spectral region covered by the 15th harmonic included the $1s4p\,^1P_1$ resonance. The relative contributions of s and d angular channels to the two-photon transition amplitude were varied by rotating the polarization of the probe in a direction either parallel or perpendicular to the polarization of the pump pulse.

4 Theoretical method

4.1 Two-photon matrix element

The two-photon transition matrix element connecting the initial state $|a\rangle$ with the continuum state $|q\rangle$ via all dipole-

allowed intermediate states can be written in the lowest order of perturbation theory as

$$M_{qa}^{\pm}(\Omega,\omega) = -i\lim_{\xi\to 0^+}\sum_p \frac{\langle q \mid ez \mid p\rangle\langle p \mid ez \mid a\rangle}{\epsilon_a + \hbar\Omega - \epsilon_p + i\xi} E_q E_1^{\pm}. \quad (2)$$

Here ϵ_a and ϵ_p represent the energies of the initial and intermediate states, E_q, $E_1^+ = E_1$ the q^{th} harmonic and laser fields, with frequencies Ω and ω, respectively. In this expression, electron correlation is neglected and lowest-order perturbation theory for the interaction with the radiation fields is assumed. In addition, both fields are described as monochromatic and linearly polarized along the same direction (z). Energy conservation implies that $\epsilon_q = \epsilon_a + \hbar\Omega \pm \hbar\omega$, where the sign ± refers to absorption or emission of the IR photon. Note that in the latter case, E_1^- is the complex conjugate of E_1^+. Since the IR laser field is delayed by τ relative to the XUV field, $E_1^{\pm} \propto e^{\mp i\omega\tau}$. When the second photon absorption or emission is above the threshold ($\hbar\Omega > I_p$), the two-photon matrix element is intrinsically complex. When $\hbar\Omega < I_p$, which is the case when the 15$^{\text{th}}$ harmonic is absorbed, the lowest-order contribution can be chosen to be real, but if electron correlation is accounted for, as discussed in Section 4.3, the matrix element is again intrinsically complex.

4.2 Angular momentum channels

The next step consists in using spherical coordinates and introducing the different angular momentum channels (see Figure 1). Two-photon ionization of He leads to s- or d-final states, and the angle-resolved two-photon amplitude can be written as

$$A_{\parallel}^{\pm}(\theta) \propto \sum_{L=0,2} Y_{L,0}(\theta,0)\begin{pmatrix} L & 1 & 1 \\ 0 & 0 & 0 \end{pmatrix} e^{i\left(\eta_L - \frac{L\pi}{2}\right)}\mathbb{M}_L^{\pm} \quad (3)$$

Here $L = 0, 2$ is the angular momentum of the final state, η_L the energy-dependent scattering phase, sum of the Coulomb phase and a contribution from the short-range potential. The phase $L\pi/2$ describes the effect of the centrifugal potential. $Y_{L,0}$ denotes a spherical harmonic, and $\mathbb{M}_L^{\pm}$ is the reduced two-photon matrix element [35], which depends on the photon energies. The amplitude varies with the polar angle θ, but due to the cylindrical symmetry, not with the azimuth. Since the ionization is from an s-orbital, the photoelectron can only occupy an $m = 0$ state with respect to the XUV-field polarization.

If the polarization of the laser field is turned 90° with respect to the XUV field, the interaction with the IR field will change the magnetic quantum number, as defined with respect to the XUV field, by $\Delta m = \pm 1$. Since the ionization is from an s-orbital, only one angular momentum channel, the d-channel, survives.

$$A_{\perp}^{\pm}(\theta,\phi) \propto -Y_{2,1}(\theta,\phi)\begin{pmatrix} 2 & 1 & 1 \\ -1 & 1 & 0 \end{pmatrix} e^{i\eta_2}\mathbb{M}_2^{\pm} \quad (4)$$

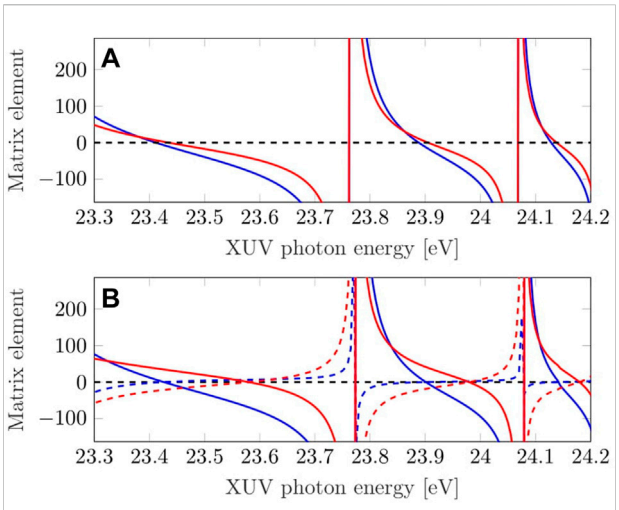

FIGURE 3
Absorption matrix elements to the s (red) and d (blue) continuum. The real and imaginary parts are shown respectively in the solid and dashed lines. The matrix elements in **(A)** do not include electron correlation while the matrix elements in **(B)** are obtained using RPAE.

In this case, the angular dependence will be that of a d-wave.

4.3 Electron correlation

The two-color two-photon RPAE approach [27] is used to calculate correlated two-photon matrix elements that include channel coupling, after both one- and two-photon interaction, as well as ground state correlation. The method, which is described in detail in Ref. [27], is gauge-independent and was originally developed for above-threshold ionization, but is here used in a scenario where, in the absorption path, no individual photon is able to ionize the atom by itself. To facilitate the comparison with experimental results, experimental energies are used for the bound excited states that are encountered in the sum over intermediate states p: $1s3p\,^1\mathrm{P}_1$, $1s4p\,^1\mathrm{P}_1$, and $1s5p\,^1\mathrm{P}_1$. Both time orders of the photon interaction are considered, but the result is completely dominated by the time order where the XUV photon is absorbed in the first step, as described by Eq. 2. The emission path of the RABBIT scan is over a smooth spectral region in the continuum and the phase change over the small energy interval discussed here is small. In the absorption path, the situation is very different. The bound state resonances are narrow, with only light-induced broadening possible (see below). If monochromatic XUV light is tuned over such an excited state resonance, the denominator in Eq. 2 abruptly changes sign and a sharp π-rad jump of the phase is expected at the resonance energy. Phase jumps are also to be expected when (and if) the matrix elements in the numerator change sign.

Figure 3 presents the real and imaginary parts of the two-photon transition amplitudes in the absorption path for the *s* and the *d* channels without (a) and with (b) electron correlation. The transition matrix elements from the ground state to the bound excited states and from these states to the continuum can be chosen to be real. Therefore, the amplitudes are real-valued in (a). At resonance, where the amplitude diverges, the phase variation is simply due to a sign change, while the one in between resonances, referred to as anti-resonant, it happens because the amplitude goes to zero. The phase jump in between the resonances happens at approximately the same energy for both the *s* and the *d* channel.

Through the introduction of electron correlation into the ionization process, the matrix elements acquire an imaginary part leading to a phase shift of the outgoing photoelectron. The phase variation at resonance is slightly smoother, while the energy where the anti-resonant phase jump takes place is now different for the *s* and the *d* channels. When incoherently adding the contributions from the two channels, this leads to a smoother phase variation at anti-resonances. On the other hand, when these contributions are added coherently, the resulting phase jump depends on the angle of emission, as discussed more in detail below.

4.4 Ionization-induced broadening and finite pulse effects

It is possible to go beyond lowest-order perturbation theory for the dressing field close to resonance in a simple way, by adding an intensity-dependent AC-Stark shift (δ_p) and ionization-induced width (γ_p) to the resonance energy ($\epsilon_p \rightarrow \epsilon_p + \delta_p + i\gamma_p$). The added complex term in the denominator will induce a change in the phase dependence across the resonance. Changing ϵ_p into $\epsilon_p + \delta_p + i\gamma_p$ in the denominator of Eq. 2 leads to an additional phase term,

$$\chi_p = \mathrm{arctg}\left[\frac{\gamma_p}{\epsilon_a + \hbar\Omega - \epsilon_p - \delta_p}\right]. \tag{5}$$

Close to the resonance, the phase varies as arctg ($\gamma_p/\delta\epsilon$), where $\delta\epsilon$ goes through zero. The derivative of this function close to zero (and hence the slope of the phase variation with energy) is equal to $-1/\gamma_p$. Since γ_p is proportional to the probe intensity, the absolute value of the slope of the phase variation across the resonance is expected to decrease as the intensity increases. In some of the simulations presented below, we include an ionization-induced width equal to 10 meV, corresponding to a probe intensity of 6×10^{11} W/cm^2. We do not include any Stark shift, however, since the origin of the energy axis in the experiment is not precisely known. Our experimental data are adjusted to the unshifted position of the resonant states.

To compare with experimental results, we also include bandwidth effects through convolution with appropriate line profiles. Using Gaussian profiles defined by the central frequencies Ω_0, ω_0 and bandwidths σ_q, σ_1 for the XUV and IR fields respectively, the matrix elements leading to the same final energy ϵ_q are summed up as

$$M^{\pm}_{qa} = \frac{1}{2\pi\sigma_1\sigma_q}\int M^{\pm}_{qa}\left(\omega_{qa} \mp \omega, \omega\right) e^{-\frac{(\omega-\omega_0)^2}{2\sigma_1^2} - \frac{\left(\omega_{qa} \mp \omega - \Omega_0\right)^2}{2\sigma_q^2}} d\omega, \tag{6}$$

where $\hbar\omega_{qa} = \epsilon_q - \epsilon_a$.

Theory of below-threshold RABBIT in helium

We now generalize the theory of RABBIT to the particular case where absorption of the lowest harmonic takes place in the discrete spectrum [29]. We consider two-photon ionization of He, with only a single angular channel for the first XUV photon absorption. In the angle-resolved case, the sideband signal is

$$I_{\mathrm{SB}}(\theta, \tau) = |A^{+}_{\parallel}(\theta, \tau) + A^{-}_{\parallel}(\theta, \tau)|^2, \tag{7}$$

where τ denotes the delay between the XUV and the IR fields, and θ is the emission angle. The amplitudes for the absorption and emission paths are defined as

$$A^{\pm}_{\parallel}(\theta, \tau) \propto -Y_{00}\sqrt{\frac{1}{3}}e^{i\eta_0}\mathbb{M}^{\pm}_0 + Y_{20}(\theta, 0)\sqrt{\frac{2}{15}}e^{i(\eta_2 - \pi)}\mathbb{M}^{\pm}_2. \tag{8}$$

The coherent addition of the four terms included in Eqs 7 and 8 depends on the phases $\arg[e^{i(\eta_L - L\pi/2)}\mathbb{M}^{\pm}_L]$. For the emission path, as in the ordinary RABBIT description with the intermediate state of the two-photon transition in the continuum, in the asymptotic limit, we have [14],

$$\arg\left(e^{i\left[\eta_L - \frac{L\pi}{2}\right]}\mathbb{M}^{-}_L\right) = \eta^{-}_1 + \pi + \phi^{L-}_{cc} + \phi^{-}_{\mathrm{XUV}} - \omega\tau. \tag{9}$$

Here η^{-}_1 denotes the scattering phase in the *p*-continuum, at the energy corresponding to the absorption of the 17$^{\mathrm{th}}$ harmonic, ϕ^{L-}_{cc} is the additional phase due to the continuum-continuum emission process, which slightly depends on the angular momentum [36, 37], ϕ^{-}_{XUV} is the phase of the 17$^{\mathrm{th}}$ harmonic and τ is the delay between the XUV and IR fields. For the absorption path,

$$\arg\left(e^{i\left[\eta_L - \frac{L\pi}{2}\right]}\mathbb{M}^{+}_L\right) = \eta_L - \frac{L\pi}{2} + \phi_L + \phi^{+}_{\mathrm{XUV}} + \omega\tau. \tag{10}$$

η_L is here the scattering phase of the final state (*s* or *d*), ϕ_L reflects the sign changes of the two-photon matrix element at resonance or anti-resonance, as well as the effect of electron correlation (see Figure 3) and ϕ^{+}_{XUV} is the phase of the 15$^{\mathrm{th}}$ harmonic. In contrast to the case where both paths are above the threshold, the asymmetry between the two paths does not allow us to eliminate the scattering phase of the final state and extract the

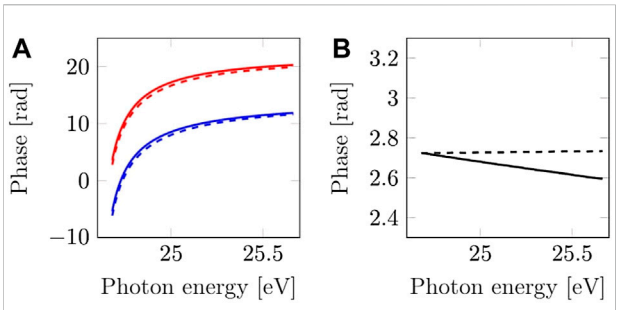

FIGURE 4
(A) Phase $\eta_L - L\pi/2$ (blue) and ϕ_{cc}^{L-} (red) as a function of energy for $L = 0$ (solid) and $L = 2$ (dashed); **(B)** Reference phase $\varphi_{ref}^{L} = \eta_L - \eta_1^- - \phi_{cc}^{L-} - L\pi/2 - \pi$ for $L = 0$ (solid) and $L = 2$ (dashed).

Wigner time delay [14]. A RABBIT measurement allows, however, the study of the phase variation (ϕ_L) of the two-photon matrix element across the resonance.

5.1 Angle-integrated below-threshold RABBIT

In an angle-integrated measurement, the θ-integration of $I_{SB}(\theta, \tau)$ eliminates the cross-products between different angular momentum channels (due to the orthogonality of the spherical harmonics) which now add incoherently,

$$I_{SB}(\tau) \propto \frac{1}{3}\left[|\mathbb{M}_0^+|^2 + |\mathbb{M}_0^-|^2 + 2|\mathbb{M}_0^+||\mathbb{M}_0^-|\cos(\Delta\varphi_0)\right] + \frac{2}{15}\left[|\mathbb{M}_2^+|^2 + |\mathbb{M}_2^-|^2 + 2|\mathbb{M}_2^+||\mathbb{M}_2^-|\cos(\Delta\varphi_2)\right], \tag{11}$$

where

$$\Delta\varphi_L = \arg\left(e^{i\left[\eta_L - \frac{L\pi}{2}\right]}\mathbb{M}_L^+\right) - \arg\left(e^{i\left[\eta_L - \frac{L\pi}{2}\right]}\mathbb{M}_L^-\right). \tag{12}$$

In ordinary (above-threshold) RABBIT,

$$\Delta\varphi_L = 2\omega\tau - \Delta\phi_{XUV} - \Delta\eta_1 - \Delta\phi_{cc}^{L}, \tag{13}$$

where $\Delta\eta_1 = \eta_1^- - \eta_1^+$, $\Delta\phi_{XUV} = \phi_{XUV}^- - \phi_{XUV}^+$ and $\Delta\phi_{cc}^{L} = \phi_{cc}^{L-} - \phi_{cc}^{L+}$. Neglecting the small L-dependence of $\Delta\phi_{cc}$ [37], the two oscillatory terms in Eq. 11 are in phase, meaning that RABBIT measurement allows to unambiguously determine the phase $\Delta\eta_1$ [4, 14] and the Wigner delay approximated by $\Delta\eta_1/2\omega$. When one path is below threshold, however,

$$\Delta\varphi_L = 2\omega\tau - \Delta\phi_{XUV} + \varphi_{ref}^{L} + \phi_L, \tag{14}$$

with $\varphi_{ref}^{L} = \eta_L - \eta_1^- - \phi_{cc}^{L-} - L\pi/2 - \pi$. Eq. 11 describes the incoherent addition of two terms oscillating with the same frequency 2ω, but with a different phase variation as a function of energy (ϕ_L) and different reference phase (φ_{ref}^{L}), complicating the interpretation of the extracted phase. Although both η_L and ϕ_{cc}^{L-} vary significantly close to the threshold due to the influence of the Coulomb potential, as shown in Figure 4A, the reference phase φ_{ref}^{L} does not depend much on the energy or on L in the range investigated in the present work (Figure 4B). This implies that when $\phi_0 \simeq \phi_2$, for example at resonance, both terms in Eq. 11 vary with a similar phase offset. However, when ϕ_L changes sign because the L-dependent matrix element goes to zero, which happens at different energies for the s and d channels, the interpretation of the phase extracted from the experimental measurement is not clear. This is where angle-resolved measurements or the use of different polarizations for the excitation fields become useful.

5.2 Angle-resolved below-threshold RABBIT

We first rewrite Eq. 8 as

$$A_\parallel^\pm(\theta) \propto e^{i\eta_0}\mathbb{M}_0^\pm + \sqrt{2}P_2(\cos\theta)e^{i\eta_2}\mathbb{M}_2^\pm, \tag{15}$$

where we have introduced P_2, the Legendre polynomial of order 2, equal to $(3x^2 - 1)/2$. Using Eqs 9 and 10, we have

$$A_\parallel^-(\theta) + A_\parallel^+(\theta) \propto e^{i\left(-\omega\tau + \phi_{XUV}^- + \eta_1^-\right)}\left[e^{i\phi_{cc}^{0-}}|\mathbb{M}_0^-| - \sqrt{2}P_2(\cos\theta)e^{i\phi_{cc}^{2-}}|\mathbb{M}_2^-|\right] - e^{i\left(\omega\tau + \phi_{XUV}^+\right)}\left[e^{i\left(\eta_0 + \phi_0\right)}|\mathbb{M}_0^+| + \sqrt{2}P_2(\cos\theta)e^{i\left(\eta_2 + \phi_2\right)}|\mathbb{M}_2^+|\right]. \tag{16}$$

We define $\chi^\pm(\theta)$ as the argument of the quantities inside the brackets. The angle-resolved RABBIT signal can be written as

$$I_{SB}(\theta) = |A_\parallel^+(\theta) + A_\parallel^-(\theta)|^2 \propto |A_\parallel^+(\theta)|^2 + |A_\parallel^-(\theta)|^2 + 2|A_\parallel^+(\theta)||A_\parallel^-(\theta)|\cos\left[2\omega\tau - \Delta\phi_{XUV} - \eta_1^- - \Delta\chi(\theta)\right], \tag{17}$$

where $\Delta\chi(\theta) = \chi^-(\theta) - \chi^+(\theta)$. In contrast to the angle-integrated result, we now have a single oscillatory signal. The price to pay is that the phase depends not only on the energy but also on the emission angle θ. Eq. 17 can be expanded into a Legendre polynomial decomposition as in [36, 37]. We will not do that in the present work, but concentrate on the understanding of the phase variation with emission angle.

5.3 Angular phase jumps

In contrast to what we have discussed so far, which is the phase difference between the absorption and the emission paths [Eqs. 14 and 17], we now consider the phase difference between the angular channels for the absorption and the emission paths individually,

$$\Delta\varphi^+ = \eta_0 - \eta_2 + \phi_0 - \phi_2 \tag{18}$$

$$\Delta\varphi^- = \phi_{cc}^{0-} - \phi_{cc}^{2-} - \pi. \tag{19}$$

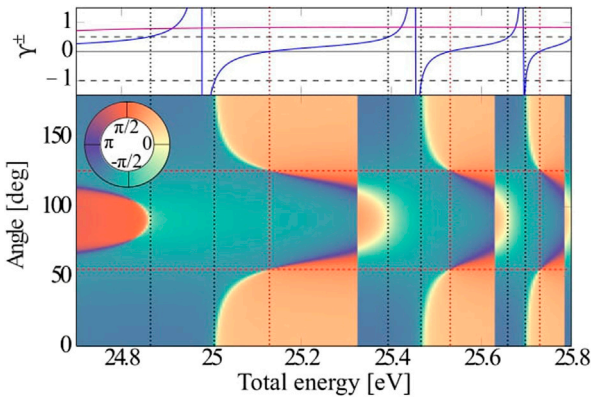

FIGURE 5
Phase variation of the absorption path as a function of angle and energy. The top figure shows the variation of $\Upsilon^{\pm}$ with energy together with the limits of the inequality in Eq. 22 (dashed horizontal black lines). The absorption path is shown in blue and the emission path, which does not lead to any phase jump, in magenta. The black vertical dotted lines indicate the energies at which Υ^{+} intersects the black dashed lines. This indicates the limits of the spectral region displaying phase jumps in angle. The vertical red dotted lines indicate the energies at which Υ^{+} changes sign, leading to a change in the direction of the phase jump in angle. At these energies, the phase jump occurs at the magic angle. The cyclic color bar is shown in the top left corner of the bottom figure.

Factorizing the phase terms, the quantities inside the bracket in Eq. 16 are proportional to $\exp(i\Delta\varphi^{\pm})|\mathbb{M}_0^{\pm}| + \sqrt{2}P_2|\mathbb{M}_2^{\pm}|$. There will be a phase jump in the path considered (emission or absorption) as a function of the emission angle whenever the real part of this expression changes sign. Introducing

$$\Upsilon^{\pm} = \frac{|\mathbb{M}_0^{\pm}|}{\sqrt{2}|\mathbb{M}_2^{\pm}|}\cos\Delta\varphi^{\pm}, \tag{20}$$

a phase jump will happen at an angle θ such that

$$P_2(\cos\theta) = -\Upsilon^{\pm}. \tag{21}$$

This equation has a solution only if

$$-1 \le \Upsilon^{\pm} \le \frac{1}{2}. \tag{22}$$

These two inequalities set conditions for a sign change as a function of angle, and hence a phase jump, in the absorption or emission paths. We also note that when $|\mathbb{M}_0^{\pm}| \ll \sqrt{2}|\mathbb{M}_2^{\pm}|$, or when $\Delta\varphi^{\pm} \approx \pm\,\pi/2$, a phase jump will happen at an angle such that $P_2(\cos\theta)$ is close to zero, i.e. at a node of Y_{20}, 54.7° or 125.3° (often referred to as "magic" angles). In contrast, if $|\mathbb{M}_0^{\pm}| \gg \sqrt{2}|\mathbb{M}_2^{\pm}|$ and $\Delta\varphi^{\pm} \neq \pm\,\pi/2$, the inequality (22) is not fulfilled, leading to an absence of a phase jump as a function of angle. $\Delta\varphi^{-}$ is positive and, in general, small, increasing close to the threshold [36]. We find that $\Upsilon^{-} \ge 1/2$ so that no phase jump can be found in the emission path. The absorption path will in contrast exhibit different energy regions with or without a phase jump, depending on whether Eq. 22 is fulfilled or not. Because of the non-zero imaginary part of $\exp(i\Delta\varphi^{\pm})|\mathbb{M}_0^{\pm}| + \sqrt{2}P_2|\mathbb{M}_2^{\pm}|$, the phase jump as a function of angle is smaller than π rad. The direction of the phase jump depends on the sign of $\Delta\varphi^{+}$. This is illustrated in Figure 5, showing both $\Upsilon^{\pm}$ as a function of energy, and the phase variation of the absorption path as a function of angle (vertical axis) and energy (horizontal axis). The black dashed lines indicate the different energy regions, where a phase jump as a function of angle is to be or not be expected.

5.4 Delay-integrated asymmetry parameters

The sideband signal can be expressed using the angle-integrated signal, $I_{SB}(\tau)$, and two delay-dependent asymmetry parameters ($\beta_i(\tau)$, i = 2, 4) as [26, 38, 39]

$$I_{SB}(\theta,\tau) = \frac{I_{SB}(\tau)}{4\pi}\left[1 + \sum_{i=2,4}\beta_i(\tau)P_i(\cos\theta)\right]. \tag{23}$$

Another way to parameterize the sideband angular dependence [35] is to extract the angle-integrated signal and asymmetry parameters, $I_{SB}^{\pm}$ and $\beta_i^{\pm}$ for the absorption and emission processes separately, and then similar quantities for the oscillating cross term $A_{\parallel}^{+*}A_{\parallel}^{-}$ (or its complex conjugate). The delay-integrated angular β_i-parameters [39] can be simply obtained as [35]

$$\beta_i = \frac{\beta_i^{+}I_{SB}^{+} + \beta_i^{-}I_{SB}^{-}}{I_{SB}^{+} + I_{SB}^{-}}. \tag{24}$$

They are the sum of the ordinary β-parameters for the absorption and emission paths, weighted with the relative strength of each path.

6 Experimental results

6.1 Angle-integrated measurements

Figure 6 presents results obtained with the velocity map imaging spectrometer. We show the angle-integrated intensity (A) and phase (B) for sideband 16, as a function of the total energy absorbed in the two-photon ionization process. Several measurements have been performed, such that the 15th harmonic spans a large energy region across the $1snp\,^1P_1$ (n = 3–5) series. Figure 6A presents three broad maxima, approximately centered at the position of the resonances. The relative intensities of the maxima are arbitrary, since the three measurements have been performed with different central laser frequencies. Therefore, we normalize the maxima in Figure 6A. The broadening is partly due to the XUV and IR bandwidths leading to a convolution of the

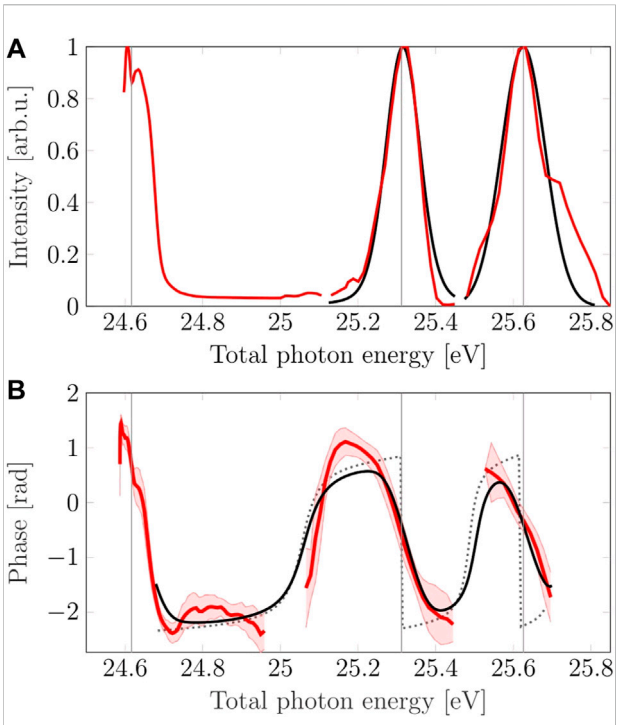

FIGURE 6
Two-photon ionization via $1snp$ states with n = 3, 4, 5. **(A)** Angle-integrated intensity. Red line: measurement, black line: RPAE-based simulations. Relative heights of individual peaks are not to scale. **(B)** Angle-integrated phase. Red solid line: measured data, shaded areas: error of the weighted average. RPAE-based simulations excluding (grey dashed line) and including (black solid line) the effect of the pulse bandwidth and power-induced broadening (γ_p = 10 meV). Vertical grey lines indicate the energies corresponding to the $1snp\,^1P_1$ resonances with n = 3, 4, 5.

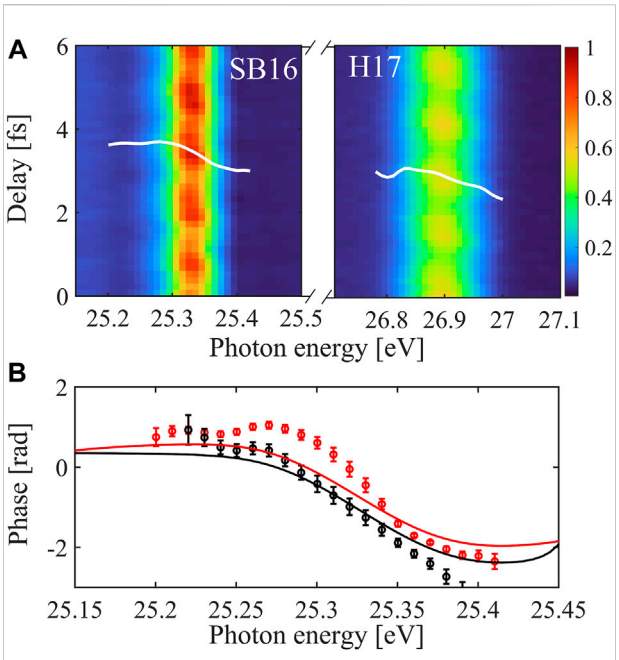

FIGURE 7
Angle-integrated measurements with the MBES. **(A)** Zoom-in on the oscillations of SB16 and H17. The extracted phase variation is indicated by the white lineouts. **(B)** Phase of SB16. Data points: phase measured with parallel (red) and perpendicular (black) XUV and IR polarizations; solid curves: calculated total phase for parallel XUV and IR polarizations (red) and d-wave only phase (black).

amplitudes (see Eq. (6)), to the ionization-induced additional width, as well as to the spectrometer resolution. The first peak corresponding to the $1s3p\,^1P_1$ resonance exhibits a double structure, that could be due to a continuum structure induced by the interference between direct non-resonant two-photon ionization and ionization from the $1s3p\,^1P_1$ bound state [40]. Such a feature has been previously observed in photoelectron spectroscopy [18], transient absorption measurements [41], as well in numerical simulations [15].

Figure 6B shows the phase variation of the angle-integrated sideband 16 intensity. The presented curves are obtained by performing a weighted averaging over a few measurements, as detailed in the SM. Phase jumps of approximately $-\pi$ rad can be observed when the 15th harmonic energy becomes equal to that of the $np\,^1P_1$ states. Likewise, anti-resonant phase jumps of opposite sign and similar magnitude can be seen in between each two successive resonant jumps [17, 18]. The splitting of the $1s3p\,^1P_1$ state is also accompanied by a phase variation.

Figure 6 further shows the results of a two-photon RPAE calculation, not including (dotted black curve, only shown in (b)) and including (black curve) bandwidth effects, with σ_1 = 25 meV, σ_q = 150 meV, as well as an additional width due to ionization from the Rydberg state (γ_p = 10 meV). These simulations reproduce the behavior of the intensity and phase variation across the resonances.

6.2 Parallel and perpendicular polarizations

High-spectral-resolution angle-integrated RABBIT measurements were performed in the energy region around the $1s4p\,^1P_1$ resonance. Figure 7A shows a zoom-in on SB16 and H17. As expected [17], their oscillations are out of phase and both exhibit a π-rad variation across the photoelectron peak width.

In this measurement, our aim is to compare measurements with the dressing field polarization parallel (0°) and perpendicular (90°) to that of the XUV, while keeping the probe intensity at the same value. Both s and d channels coexist in the parallel configuration, while only the d channel

is allowed when the probe polarization is perpendicular to that of the pump, since only $\Delta m = \pm 1$ transitions are possible. In these measurements, we normalize the phase variation to that of the non-resonant sideband 18, which exhibits a flat phase. A comparison between parallel and perpendicular IR polarizations is shown in Figure 7B. The black and red symbols and solid curves correspond to the parallel and perpendicular case, respectively. We observe a smooth phase variation across the resonance rather than a sudden π-rad jump, in agreement with the results shown in Figure 6. In order to reproduce this behavior in theoretical calculations, it is necessary to include both ionization broadening and folding due to finite pulse effects. In the region investigated, close to the $1s4p$ resonance, the phase variations of the s and d channels are very similar, so that the parallel or perpendicular configurations do not yield very different phase measurements.

6.3 Delay-integrated photolectron angular distributions

Figure 8 presents the variation of the β_2 and β_4 parameters for the delay-integrated signal. These coefficients vary significantly across the observed energy range, with maxima close to the $1s3p^1P_1$, $1s4p^1P_1$ and $1s5p^1P_1$ resonances. The experimental behavior is reproduced by the calculations, here shown without including any folding, i.e. assuming a monochromatic dressing field, at a wavelength of 782 nm. The strong variation of the β_2 and β_4 parameters between two resonances indicates a varying angular distribution, due to a change in the relative amplitude and phase of the s and d angular channels.

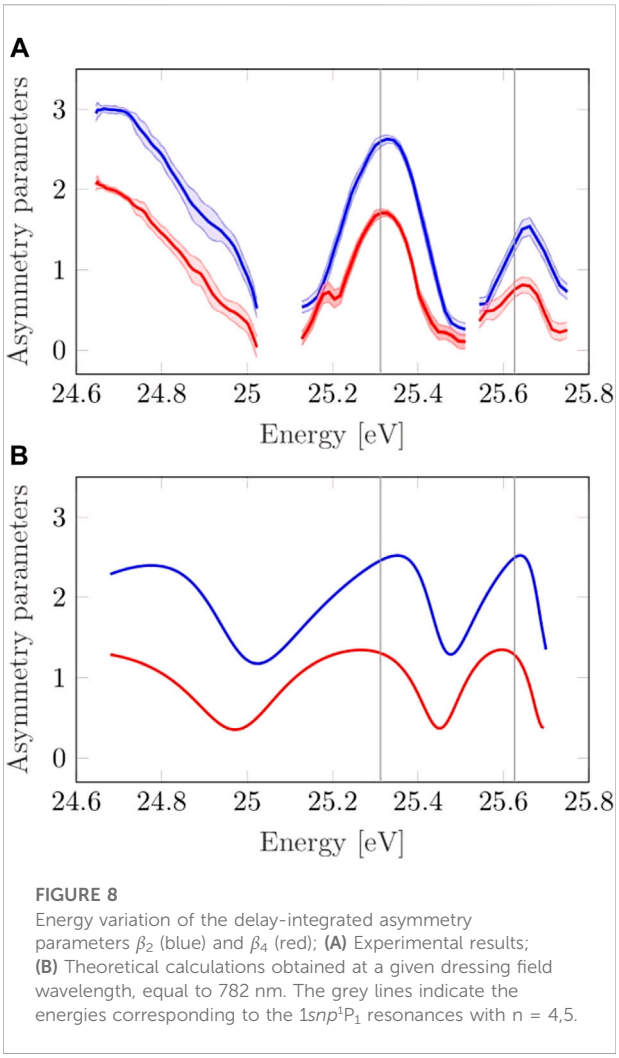

FIGURE 8
Energy variation of the delay-integrated asymmetry parameters β_2 (blue) and β_4 (red); **(A)** Experimental results; **(B)** Theoretical calculations obtained at a given dressing field wavelength, equal to 782 nm. The grey lines indicate the energies corresponding to the $1snp^1P_1$ resonances with n = 4,5.

6.4 Angle-resolved phase measurements

We here concentrate on the spectral region around the $1s4p^1P_1$ resonance. Figure 9 displays the phase variation as a function of angle and energy. The phase is indicated in color, following a cyclic representation, thus avoiding unwrapping issues. The phase decreases (increases) when moving clockwise (anti-clockwise) in the cyclic color bar. Figure 9A, right shows the measured values in the angle and energy region, delimited by a dashed contour, where the signal is sufficiently high for a reliable phase and amplitude retrieval. Figure 9A, left shows the results of the two-photon-RPAE calculation. The two results agree quite well. The angular modulations of the experimental signal in the region 0–57°, 21.15–25.3 eV are comparable to the experimental error bar (<0.8 rad). In the following, we focus on the interpretation of the theoretical results, which give a more complete picture of the phase variation as a function of both energy and angle. In order to gain a deeper insight into the interplay of the different angular channels, we show the sideband variation where we selectively suppress the resonant path to the s continuum (Figure 9B, left) or to the d continuum (Figure 9B, right).

Overall, the phase variation observed in Figure 9A, left is more similar to that of a pure d wave (Figure 9B, left) than that of a pure s wave (Figure 9B, right). Nonetheless, as shown in the following, a detailed analysis of the sideband angle- and energy-resolved phase variation shows that it is the result of a complex interplay of the two partial waves. In the following, we focus on interpreting the phase variation in the vicinity of three spectral regions, indicated with coloured half-circles in Figure 9A.

First, at the position of the $4p$ resonance, indicated by a red half-circle close to 25.31 eV, a sharp π-rad phase jump along the energy axis is observed at all emission angles. In this region both the s and d channels experience a π-rad jump due to the resonance such that the angle-resolved measurements do not provide additional information compared to the angle-integrated ones.

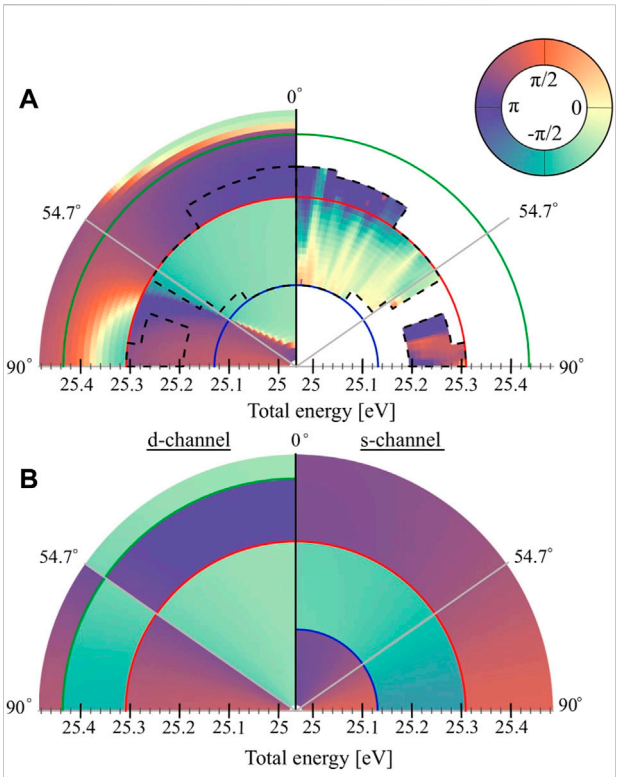

FIGURE 9
Angle-and-energy-resolved relative phase of SB16 around the 4p resonance. **(A)** Comparison between experiment (right) and theory (left). Only the experimental results with significant signal-over-noise ratio are presented. This region is indicated by the black dashed line. The radial coordinate is the total energy, while the polar angle is the electron emission angle relative to the polarization axis. The cyclic color bar is shown in the top right of the figure. In **(B)**, we present the contribution of the *s* (right) and *d* (left) waves in the absorption path to the total phase variation.

An anti-resonant phase jump along the energy axis can observed in the vicinity of the green half-circle. In this region, the matrix element $\mathbb{M}_2^+$ crosses 0 and changes sign such that the relative weight of the *s* and *d* resonant paths varies very fast as a function of energy. As a result, a strong angular dependence of the position of the phase jump can be observed in Figure 9A, left: at angle above 54.7° the phase jump appears above the green line, while at angles below the magic angle, the phase jump appears at energies below the green line. This is consistent with the fact that $\mathbb{M}_2^+$ and Y_{20} should have opposite signs in order for the real part of $A_\parallel^+(0)$ to cancel.

At 54.7°, where Y_{20} has a node, the phase variation as a function of energy is fully dominated by the *s* channel as can be observed by comparing Figure 9A, left with Figure 9B, right. In addition, in the close vicinity of the spectral region where $\mathbb{M}_2^+$ cancels no phase variation as a function of emission angle is observed in (Figure 9A, left), since the *s* channel dominates. This corresponds to the spectral region shown in Figure 5 where the inequalities in Eq. (22) are not fulfilled.

In contrast to the region close to the 4*p* resonance, here angle-resolved measurements provide a lot of information on the competition between the *s* and *d* resonant channels that cannot be obtained from angle-integrated measurements.

Finally, over a large energy range, from 25 to 25.3 eV, a sharp phase jump can be observed as a function of angle close to 54.7°. In this spectral region the *d* resonant channel strongly dominates and the phase jump as a function of angle reflects the change of sign of Y_{20}. The exact angle at which the phase jumps and the magnitude of the phase jump depends on the relative weight between *s* and *d*. When $\mathbb{M}_0^+ = 0$ (blue circle), the phase exhibits a sharp π-rad jump exactly at the magic angle, while the phase jumps occurs at lower (higher) angles below (above) the blue line. Interestingly, although the *d* channel dominates, the change of sign of $\mathbb{M}_0^+$ across the blue line manifests as a change of direction of the angular phase jump.

This analysis shows that by examining the positions of the phase jumps as a function of angle and energy, it is possible to infer not only the position of the resonance, but also the positions of the sign changes of $\mathbb{M}_L^+$, even in the case where two-photon ionization is very much dominated by one contribution, the *d* channel. This also shows that phase measurements as a function of angle and energy give a lot of information about the relative contributions of the two angular channels.

7 Conclusion

In conclusion, we have studied the phase and intensity of two-photon ionization through the $1s3p\,^1P_1$, $1s4p\,^1P_1$ and $1s5p\,^1P_1$ resonance series, using an interferometric method. While the intensity variation presents a series of peaks at the positions of the resonance, the phase undergoes π-rad phase changes both at and in between the resonances. Going through the resonance, the phase decreases linearly with energy with a total phase variation of π rad at all emission angles. The smaller the ionization induced by the dressing field, the more rapid this linear decrease in phase is. The phase variation remains similar when varying the relative polarization of the XUV and dressing fields. A second sharp phase variation of π rad is observed between two resonances. This anti-resonant phase variation is strongly dependent on the emission angle and reflects the angle- and polarization-dependent interplay between the two angular channels contributing to the two-photon ionization process.

We have shown both experimentally and theoretically that, even for a simple atomic system like helium, angle-resolved measurements, as well as measurements with different polarizations, provide invaluable insight to the physics of resonant two-photon ionization. They should become an essential tool to the investigation of more complex atoms or molecules.

Data availability statement

The raw data supporting the conclusion of this article will be made available by the authors, without undue reservation.

Author contributions

LN, DB, HL, RW, MA, SL, JP, HW, JL, SM, SZ, and CA performed the experiments. RJS and RF, provided the MBES and helped in its operation. JP, HW, JL, SM, and PE-J provided the VMIS and helped in its operation. LN analyzed the data with the help of DB, SL, and HL. EL performed the many-body perturbation theory calculations. DB, EL and AL'H formalized the theory of resonant two-photon ionization. MG and AL'H supervized the project. LN, DB, EL, and AL'H wrote the article with input from all the authors.

Funding

The authors AL'H and MA are partly supported by the Wallenberg Center for Quantum Technology (WACQT) funded by the Knut and Alice Wallenberg foundation. The authors acknowledge support from the Swedish Research Council (2013-8185, 2016-04907, 2017-04106, 2018-03731, 2020-0520, 2020-03315, 2020–06384), the Swedish Foundation for Strategic Research (FFL12-0101), the European Research Council (advanced grant QPAP, 884900) and the Knut and Alice Wallenberg Foundation. JL acknowledges financial support by the European Union's Horizon 2020 research and innovation program under the Marie Skłodowska-Curie Grant Agreement 641789 (MEDEA).

Conflict of interest

The authors declare that the research was conducted in the absence of any commercial or financial relationships that could be construed as a potential conflict of interest.

Publisher's note

All claims expressed in this article are solely those of the authors and do not necessarily represent those of their affiliated organizations, or those of the publisher, the editors and the reviewers. Any product that may be evaluated in this article, or claim that may be made by its manufacturer, is not guaranteed or endorsed by the publisher.

Supplementary material

The Supplementary Material for this article can be found online at: https://www.frontiersin.org/articles/10.3389/fphy.2022.964586/full#supplementary-material

References

1. Goulielmakis E, Uiberacker M, Kienberger R, Baltuska A, Yakovlev V, Scrinzi A, et al. Direct measurement of light waves. *Science* (2004) 305:1267–9. doi:10.1126/science.1100866

2. Schultze M, Fieß M, Karpowicz N, Gagnon J, Korbman M, Hofstetter M, et al. Delay in photoemission. *Science* (2010) 328:1658–62. doi:10.1126/science.1189401

3. Paul PM, Toma ES, Breger P, Mullot G, Augé F, Balcou P, et al. Observation of a train of attosecond pulses from high harmonic generation. *Science* (2001) 292:1689–92. doi:10.1126/science.1059413

4. Klünder K, Dahlström JM, Gisselbrecht M, Fordell T, Swoboda M, Guénot D, et al. Probing single-photon ionization on the attosecond time scale. *Phys Rev Lett* (2011) 106:143002. doi:10.1103/physrevlett.106.143002

5. Kienberger R, Goulielmakis E, Uiberacker M, Baltuska A, Yakovlev V, Bammer F, et al. Atomic transient recorder. *Nature* (2004) 427:817–21. doi:10.1038/nature02277

6. Ossiander M, Siegrist F, Shirvanyan V, Pazourek R, Sommer A, Latka T, et al. Attosecond correlation dynamics. *Nat Phys* (2017) 13:280–5. doi:10.1038/nphys3941

7. Zhong S, Vinbladh J, Busto D, Squibb RJ, Isinger M, Neoričić L, et al. Attosecond electron–spin dynamics in Xe 4d photoionization. *Nat Commun* (2020) 11:5042. doi:10.1038/s41467-020-18847-1

8. Alexandridi C, Platzer D, Barreau L, Busto D, Zhong S, Turconi M, et al. Attosecond photoionization dynamics in the vicinity of the Cooper minima in argon. *Phys Rev Res* (2021) 3:L012012. doi:10.1103/physrevresearch.3.l012012

9. Haessler S, Fabre B, Higuet J, Caillat J, Ruchon T, Breger P, et al. Phase-resolved attosecond near-threshold photoionization of molecular nitrogen. *Phys Rev A (Coll Park)* (2009) 80:011404. doi:10.1103/physreva.80.011404

10. Huppert M, Jordan I, Baykusheva D, von Conta A, Wörner HJ. Attosecond delays in molecular photoionization. *Phys Rev Lett* (2016) 117:093001. doi:10.1103/physrevlett.117.093001

11. Nandi S, Plésiat E, Zhong S, Palacios A, Busto D, Isinger M, et al. Attosecond timing of electron emission from a molecular shape resonance. *Sci Adv* (2020) 6:eaba7762. doi:10.1126/sciadv.aba7762

12. Isinger M, Squibb RJ, Busto D, Zhong S, Harth A, Kroon D, et al. Photoionization in the time and frequency domain. *Science* (2017) 358:893–6. doi:10.1126/science.aao7043

13. Pazourek R, Nagele S, Burgdörfer J. Attosecond chronoscopy of photoemission. *Rev Mod Phys* (2015) 87:765–802. doi:10.1103/revmodphys.87.765

14. Dahlström JM, Guénot D, Klünder K, Gisselbrecht M, Mauritsson J, L'Huillier A, et al. Theory of attosecond delays in laser-assisted photoionization. *Chem Phys* (2013) 414:53–64. doi:10.1016/j.chemphys.2012.01.017

15. Swoboda M, Fordell T, Klünder K, Dahlström JM, Miranda M, Buth C, et al. Phase measurement of resonant two-photon ionization in helium. *Phys Rev Lett* (2010) 104:103003. doi:10.1103/physrevlett.104.103003

16. Villeneuve DM, Paul H, Vrakking MJJ, Niikura H. Coherent imaging of an attosecond electron wave packet. *Science* (2017) 356:1150–3. doi:10.1126/science.aam8393

17. Drescher L, Witting T, Kornilov O, Vrakking MJJ. Phase dependence of resonant and antiresonant two-photon excitations. *Phys Rev A (Coll Park)* (2022) 105:L011101. doi:10.1103/physreva.105.l011101

18. Autuori A, Platzer D, Lejman M, Gallician G, Maëder L, Covolo A, et al. Anisotropic dynamics of two-photon ionization: An attosecond movie of photoemission. *Sci Adv* (2022) 8:eabl7594. doi:10.1126/sciadv.abl7594

19. Barreau L, Leon Petersson C, Klinker M, Camper A, Marante C, Gorman T, et al. Disentangling spectral phases of interfering autoionizing states from attosecond interferometric measurements. *Phys Rev Lett* (2019) 122:253203. doi:10.1103/physrevlett.122.253203

20. Kotur M, Guénot D, Jiménez-Galán Á, Kroon D, Larsen EW, Louisy M, et al. Spectral phase measurement of a Fano resonance using tunable attosecond pulses. *Nat Commun* (2016) 7:10566. doi:10.1038/ncomms10566

21. Gruson V, Barreau L, Jiménez-Galan À, Risoud F, Caillat J, Maquet A, et al. Attosecond dynamics through a Fano resonance: Monitoring the birth of a photoelectron. *Science* (2016) 354:734–8. doi:10.1126/science.aah5188

22. Busto D, Barreau L, Isinger M, Turconi M, Alexandridi C, Harth A, et al. Time–frequency representation of autoionization dynamics in helium. *J Phys B: Mol Opt Phys* (2018) 51:044002. doi:10.1088/1361-6455/aaa057

23. Turconi M, Barreau L, Busto D, Isinger M, Alexandridi C, Harth A, et al. Spin–orbit-resolved spectral phase measurements around a Fano resonance. *J Phys B: Mol Opt Phys* (2020) 53:184003. doi:10.1088/1361-6455/ab9f0b

24. Heuser S, Galán Á, Cirelli C, Marante C, Sabbar M, Boge R, et al. Angular dependence of photoemission time delay in helium. *Phys Rev A (Coll Park)* (2016) 94:063409. doi:10.1103/physreva.94.063409

25. Cirelli C, Marante C, Heuser CLM, Petersson S, Jiménez-Galán Á, Argenti L, et al. Anisotropic photoemission time delays close to a fano resonance. *Nat Commun* (2018) 9:955. doi:10.1038/s41467-018-03009-1

26. Busto D, Vinbladh J, Zhong S, Isinger M, Nandi S, Maclot S, et al. Fano's propensity rule in angle-resolved attosecond pump-probe photoionization. *Phys Rev Lett* (2019) 123:133201. doi:10.1103/physrevlett.123.133201

27. Vinbladh J, Dahlström JM, Lindroth E. Many-body calculations of two-photon, two-color matrix elements for attosecond delays. *Phys Rev A (Coll Park)* (2019) 100:043424. doi:10.1103/physreva.100.043424

28. Müller A, Laubscher M. Spectral phase and amplitude interferometry for direct electric-field reconstruction. *Opt Lett* (2001) 26:1915. doi:10.1364/ol.26.001915

29. Kheifets AS, Bray AW. RABBITT phase transition across the ionization threshold. *Phys Rev A (Coll Park)* (2021) 103:L011101. doi:10.1103/physreva.103.l011101

30. Eppink ATJB, Parker DH. Velocity map imaging of ions and electrons using electrostatic lenses: Application in photoelectron and photofragment ion imaging of molecular oxygen. *Rev Sci Instrum* (1997) 68:3477–84. doi:10.1063/1.1148310

31. Rading L, Lahl J, Maclot S, Campi F, Coudert-Alteirac H, Oostenrijk B, et al. A versatile velocity map ion-electron covariance imaging spectrometer for high-intensity xuv experiments. *Appl Sci (Basel)* (2018) 8:998. doi:10.3390/app8060998

32. Even U. Pulsed supersonic beams from high pressure source: Simulation results and experimental measurements. *Adv Chem* (2014) 2014:1–11. doi:10.1155/2014/636042

33. Smith LM, Keefer DR, Sudharsanan S. Abel inversion using transform techniques. *J Quant Spectrosc Radiat Transf* (1988) 39:367–73. doi:10.1016/0022-4073(88)90101-x

34. Vrakking MJJ. An iterative procedure for the inversion of two-dimensional ion/photoelectron imaging experiments. *Rev Sci Instrum* (2001) 72:4084–9. doi:10.1063/1.1406923

35. Saha S, Vinbladh J, Sörngå rd J, Ljungdahl A, Lindroth E. Angular anisotropy parameters for photoionization delays. *Phys Rev A (Coll Park)* (2021) 104:033108. doi:10.1103/physreva.104.033108

36. Fuchs J, Douguet N, Donsa S, Martín F, Burgdörfer J, Argenti L, et al. Time delays from one-photon transitions in the continuum. *Optica* (2020) 7:154–61. doi:10.1364/optica.378639

37. Peschel J, Busto D, Plach M, Bertolino M, Hoflund M, Maclot S, et al. Attosecond dynamics of multi-channel single photon ionization. *Nat Commun* (2022) 13:5205. doi:10.1038/s41467-022-32780-5

38. Cooper J, Zare RN. Angular distribution of photoelectrons. *J Chem Phys* (1968) 48:942–3. doi:10.1063/1.1668742

39. Joseph J, Holzmeier F, Bresteau D, Spezzani C, Ruchon T, Hergott JF, et al. Angle-resolved studies of XUV–IR two-photon ionization in the RABBITT scheme. *J Phys B: Mol Opt Phys* (2020) 53:184007. doi:10.1088/1361-6455/ab9f0d

40. Knight PL, Lauder MA, Dalton BJ. Laser-induced continuum structure. *Phys Rep* (1990) 190:1–61. doi:10.1016/0370-1573(90)90089-k

41. Chini M, Wang X, Cheng Y, Wu Y, Zhao D, Telnov DA, et al. Sub-cycle oscillations in virtual states brought to light. *Sci Rep* (2013) 3:1105. doi:10.1038/srep01105

frontiers | Frontiers in Physics

TYPE Original Research
PUBLISHED 12 October 2022
DOI 10.3389/fphy.2022.1032671

OPEN ACCESS

EDITED BY
Weifeng Yang,
Hainan University, China

REVIEWED BY
Ruifeng Lu,
Nanjing University of Science and Technology, China
Xiaowei Sheng,
Anhui Normal University, China

*CORRESPONDENCE
Wan-Dong Yu,
wandongyu@pku.edu.cn

SPECIALTY SECTION
This article was submitted to Optics and Photonics,
a section of the journal
Frontiers in Physics

RECEIVED 31 August 2022
ACCEPTED 29 September 2022
PUBLISHED 12 October 2022

CITATION
Kong X-S, Wu X-Y, Geng L and Yu W-D (2022), Strain effects on high-harmonic generation in monolayer hexagonal boron nitride.
Front. Phys. 10:1032671.
doi: 10.3389/fphy.2022.1032671

Strain effects on high-harmonic generation in monolayer hexagonal boron nitride

Xiao-Shuang Kong, Xiao-Yuan Wu, Lei Geng and Wan-Dong Yu*

State Key Laboratory for Mesoscopic Physics and Frontiers Science Center for Nano-optoelectronics, School of Physics, Peking University, Beijing, China

Based on the time-dependent density functional theory, we theoretically investigate the influence of mechanical strains on the high-order harmonic generation (HHG) in the monolayer hexagonal boron nitride (hBN) crystal. We show that mechanical strains can largely modify the band structure and facilitate the harmonic emission. Compared to uniaxial strains, we find that biaxial strains may enhance the HHG yield significantly, and the HHG spectroscopy generated by a linearly polarized laser is closely related to the symmetry of the deformed hBN. Moreover, when driven by a circularly polarized laser, we find that the appearance of the 3*n*-order harmonics manifests the restoration of the three-fold rotational symmetry. Our results will be useful in controlling the HHG spectroscopy and probing lattice deformations in crystals.

KEYWORDS

mechanical strains, high-order harmonic generation, monolayer hexagonal boron nitride crystal, time-dependent density functional theory, laser-matter interaction

1 Introduction

Since the high-order harmonic generation (HHG) from the bulk ZnO was first observed in 2010 [1], much attention has been paid to the HHG from crystalline solids, which may provide a direct access to high-efficiency and high-stability light sources [2]. State-of-the-art experiments have recorded HHG in various condensed-matter systems [3–7], providing a great opportunity to all-optically image the electronic structure and ultrafast processes [5], such as valance charge imaging [4], energy band reconstruction [3, 8], Berry curvature measurement [6, 9], lattice symmetry probe [9–11] and transition moment visualization [12]. Due to the complicated interaction between solids and the intense laser field, the HHG mechanism from solids can not be sufficiently explained by the atomic three-step model [13]. At a basic level, interband and intraband transitions were demonstrated to be critical for solid HHG [14]. Up-to-now, the coupling mechanism between interband and intraband processes has not been fully understood, and more importantly, a general rule to manipulate the solid-state harmonics has not yet been proposed.

Among various solid-state materials, the ability to continuously tune the electronic structure is one of the most attractive properties of two-dimensional (2D) materials. The atomic thickness of 2D materials makes their electronic and optical properties very sensitive to external perturbations [15]. The HHG from 2D materials brings some distinctive features. For example, it has been demonstrated both experimentally [6] and theoretically [16] that the HHG from the isolated monolayer MoS_2 is more efficient than that from its bulk forms. Also, it is found that the even-order HHG in the monolayer MoS_2 is predominantly polarized perpendicular to the pump field, which is caused by the intraband anomalous transverse current arising from the Berry curvature of the material [6]. The HHG in the monolayer graphene shows an anomalous dependence on the laser ellipticity [7]. The monolayer hBN can generate bulk-like harmonics when it is driven by an in-plane polarized laser field, and atomic-like harmonics when driven by an out-of-plane polarized pulse [15–17]. In addition, Yu *et al.* [17] investigated the double-plateau structure of the HHG spectrum in the bilayer hBN crystal with the driven laser pulse at grazing incidence. They found that the photon energy of the second plateau far beyond atomic-like harmonics can be well explained by the inclusion of backscattering of ionized electrons.

In addition to modulate laser parameters, tailoring the electronic structure of solid-state materials has also been proven to be a powerful way to control the HHG. For example, this can be achieved by doping [18, 19] or growing nanostructures on the surface [20, 21], lowering the dimensionality of the material [6, 16], and changing the layer stack [16, 22, 23]. It is worth mentioning that the mechanical engineering is one of the most commonly used methods to tune the lattice deformation, band gap and the carrier effective mass, providing an effective way to change the transition temperature of the ferromagnetic-paramagnetic [24, 25], metal-insulator [26] and superconductor [27, 28]. Interestingly, the semiconductor-metal transition in the thin film $MoTe_2$ can be realized at room temperature by applying tensile strains [29, 30].

Strain engineering, as a traditional low-cost route to manipulate the electronic structure, has been widely used in material sciences. By imposing strains, e.g., stretching or compressing the lattice structure, the device performance as well as optical properties can be effectively regulated [31, 32]. Therefore, it does stand to reason that tailoring the HHG from solid-state materials can also be achieved by applying strains. So far, to the best of our knowledge, controlling the HHG from 2D materials *via* strains remains seldom explored. Recently, Guan *et al.* demonstrated the high sensitivity of HHG by applying uniaxial strains in the monolayer MoS_2 and showed strong correlations between intraband and interband contributions [33]. Generally speaking, by exerting biaxial stretching strains, the harmonic efficiency can be facilitated due to the downshifting energy level of the conduction band [34]. Besides, Qin *et al.* [35] showed that, under biaxial and uniaxial strains, the harmonic intensity in the zero-gap monolayer silicene can be significantly enhanced up to an order of magnitude.

As a prototype of 2D materials, the hBN attracts great interest due to its outstanding optical and structural performances, e.g., a wide band gap, excellent structrual stability [36], hardly damaged under radiations [15], and strong exciton coincidences [37]. The hBN relevant materials have been demonstrated to be a promising candidate for the HHG, such as Graphene/hBN heterostructures [22], hBN stacking forms [16] and hole-defect hBN structures [19]. More importantly, *ab initio* calculations showed that the exertion of strains can effectively tune the bandgap structure of the monolayer hBN, and with a certain large lateral deformation, the single-layer hBN may be turned from insulator to semiconductor [38].

In this paper, we focus on the stretching effect on the HHG. As an example, we theoretically investigate the HHG from the monolayer hBN crystal within the time-dependent density functional theory (TDDFT). Compared to the previous research, we systematically study the influence of uniaxial and biaxial strains along the zigzag direction and the armchair direction on HHG from the monolayer hBN crystal. To launch a more convincing dynamics, we compute the initial ground-state density for each stretching geometry. For the nonlinear HHG response, we consider two kinds of laser fields, i.e., the linearly polarized and the counter-rotating bicircular pulses.

This paper is organized as follows: In Section 2, we introduce the framework of the TDDFT method and numerical details. In Section 3, we discuss the strained band structure and the HHG in the monolayer hBN. Finally, in Section 4, we summarize and discuss the prospects of our results.

2 Method

The electron dynamics of the monolayer hBN is investigated by solving the following time-dependent Kohn–Sham (KS) equations (atomic units is adopted and the spin notation is omitted hereafter) [39, 40],

$$i\hbar\frac{\partial}{\partial t}\psi_i(\mathbf{r},t)=\left(-\frac{\nabla^2}{2}+V_H[\rho(\mathbf{r},t)]+V_{ext}(\mathbf{r},t)+V_{xc}[\rho(\mathbf{r},t)]\right)\psi_i(\mathbf{r},t), \quad (1)$$

where ψ_i are KS orbitals and the subscript i corresponds to both a band and a k-point index. The KS effective potential consists of three parts: the classical Hartree potential V_H, the electronic exchange-correlation (xc) potential V_{xc}, and the external potential V_{ext} that contains the incident laser field and the electron-ion Coulomb potential. The total density $\rho(\mathbf{r}, t)$ is defined by summing up all the orbital densities,

$$\rho(\mathbf{r},t)=\sum_i|\psi_i(\mathbf{r},t)|^2. \quad (2)$$

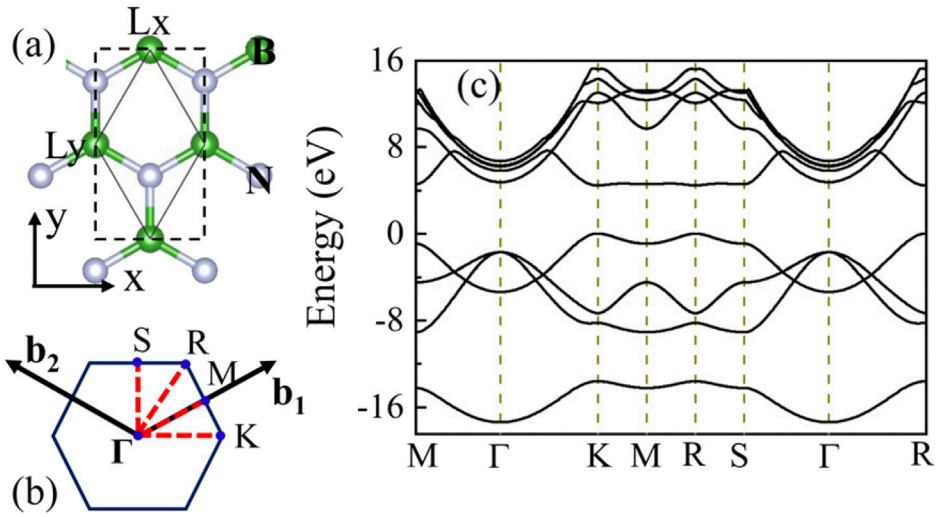

FIGURE 1
(A) Schematic diagram of the strain-free monolayer hBN. The primitive (hexagonal) cell and cubic unit cell are framed by solid and dashed lines. **(B)** The first Brillouin zone of the strain-free monolayer hBN and the corresponding high symmetric points Γ, K, M, R, and S in the reciprocal space. **(C)** The band structure of the strain-free monolayer hBN.

The microscopic electric current density $\mathbf{j}(\mathbf{r}, t)$ is computed from time-evolved KS orbitals:

$$\mathbf{j}(\mathbf{r},t) = -e\sum_i \mathrm{Re}\left[\psi_i^*(\mathbf{r},t)\left(-i\hbar\nabla + \frac{e}{c}\mathbf{A}(t)\right)\psi_i(\mathbf{r},t)\right]. \quad (3)$$

Then, the HHG spectrum is obtained from the total time-dependent electronic current $\mathbf{j}(\mathbf{r}, t)$ by the following Fourier transform,

$$\mathrm{Y}(\omega) = \left|\mathrm{FT}\left[\frac{\partial}{\partial t}\int_\Omega \mathbf{j}(\mathbf{r},\mathrm{t})\mathrm{d}^3\mathbf{r}\right]\right|^2, \quad (4)$$

where Ω is the volume of the computational box.

In the present work, we consider both uniaxial and biaxial stretching strains applied to the monolayer hBN crystal. For strained geometries, we optimize lattice parameters of the monolayer hBN by using the Vienna *ab intio* Software Package (VASP) [41, 42]. The projected augmented wave [43, 44] pseudopotentials are employed with a cutoff energy of 500 eV for the plane-wave basis, and the *xc* functional is treated with the generalized gradient approximation of the Perdew–Burke–Ernzerhof (PBE) functional. The ground-state structural optimizations are carried out using a cubic cell which contains four atoms, i.e., two boron atoms and two nitrogen atoms, as shown in Figure 1A. The corresponding Brillouin zone (BZ) integrations are approximated by adopting the special *k*-point sampling of the Monhkorst-Pack scheme with a size of 28 × 16 points. The uniaxial deformations are imposed by stretching the crystal lattice on either the *x* [$\varepsilon_{uni.(x)}$] or the *y* [$\varepsilon_{uni.(y)}$] direction, and the biaxial deformations are applied in both the *x* and the *y* directions ($\varepsilon_{bi.}$). Due to the Poisson effect [45, 46], the lattice tends to be compressed along the direction perpendicular to the uniaxial stretching direction. Therefore, during the optimization, when the uniaxial strain [$\varepsilon_{uni.(x)}$ or $\varepsilon_{uni.(y)}$] is applied, the *x* (or *y*)-direction lattice parameter L_x (or L_y) in the cubic cell is fixed, and the L_y (or L_x) is obtained by the minimum process that the system relaxes to its lowest energy state. For the symmetric strain distribution ($\varepsilon_{bi.}$), we scale both the L_x and L_y by the same ratio. Here, stretching percents in the range from 0 to 6% are considered, where $\varepsilon = 0$ manifests a strain-free operation, and $\varepsilon > 0$ corresponds to a stretching operation.

After the lattice parameter optimization, the corresponding simplified two-atom primitive cell framed by the thin black solid lines in Figure 1A is used for ground-state calculations and time-dependent propagations, which is performed within OCTOPUS package [47, 48]. In all the calculations, nuclei are fixed, so that the energy transfer from electrons to ions is not considered. The lattice parameter of the primitive cell for the unstrained monolayer hBN is 4.73 a_0. The length of the simulation box in the out-of-plane direction is 66 a_0. A complex absorbing boundary condition [49] is employed to prevent the possible electronic wave-packet reflection, and the width of the absorbing boundary is 3 a_0 laying on the edges of the computational box. All the physical quantities are discretized in a three-dimensional box with a uniform grid size of 0.33 a_0. We employ a local-density approximation (LDA) [50] for the electronic exchange-correlation, and Hartwigsen-Goedecker-Hutter (HGH) pseudopotentials [51] for core-electron potentials. The 2D BZ is sampled by a 44 × 44 Monkhorst–Pack *k*-point mesh for self-

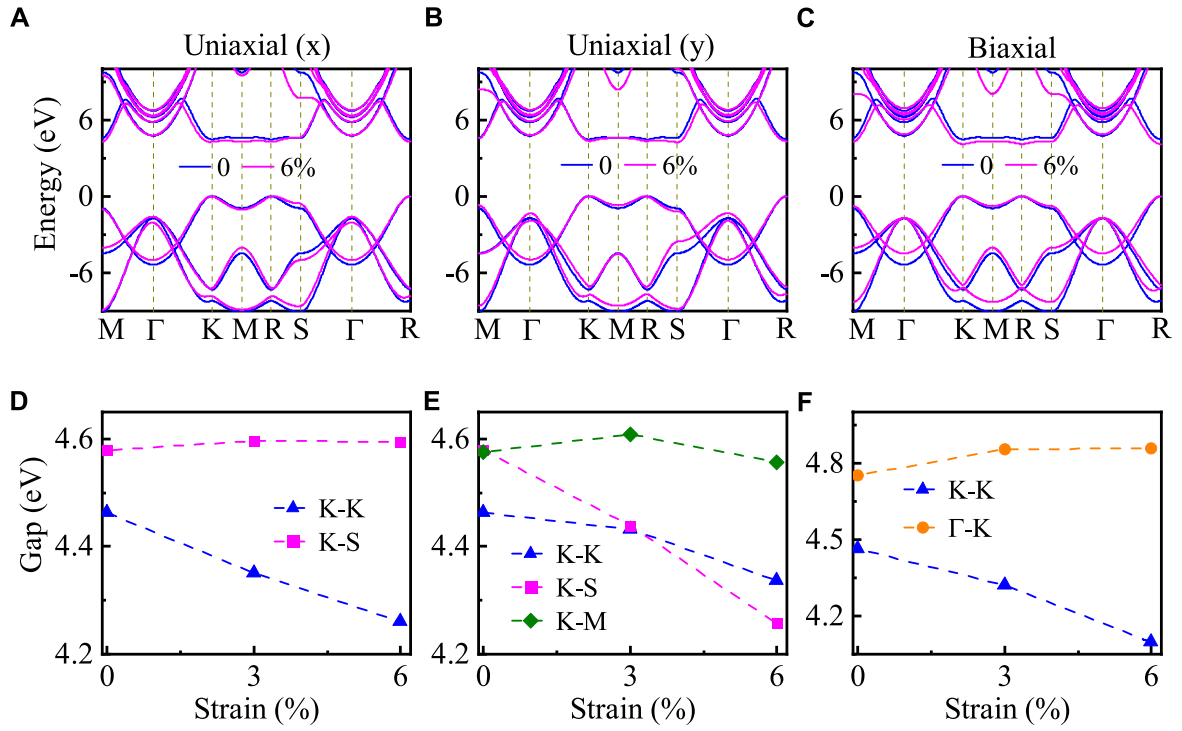

FIGURE 2
The band structures of the monolayer hBN with the uniaxial strain along **(A)** the *x* direction, **(B)** the *y* direction, and **(C)** the biaxial strain along both the *x* and *y* directions. The blue and magenta curves are for $\varepsilon = 0$ and $\varepsilon = 6\%$, respectively. $\varepsilon = 0$ is the strain-free case. The corresponding strain-dependent direct and indirect band gap in the monolayer hBN are shown in **(D)** – **(F)**.

consistent converged calculations. The monolayer hBN is exposed to a linearly or a counter-rotating bichromatic circularly polarized mid-infrared laser field, polarized along the in-plane direction. The laser-matter interaction is described in the velocity gauge with the vector potential $\mathbf{A}(t)$ given by,

$$\begin{aligned}\mathbf{A}(t) &= \mathbf{A}_1(t) + \mathbf{A}_2(t) \\ &= \sum_{i=1}^{2} A_{i0} f(t) \left[\frac{1}{\sqrt{1+\epsilon_i^2}} \cos(\omega_i t)\hat{\mathbf{e}}_x \right. \\ &\quad \left. \pm \frac{\epsilon_i}{\sqrt{1+\epsilon_i^2}} \sin(\omega_i t)\hat{\mathbf{e}}_y \right],\end{aligned} \tag{5}$$

where A_{i0} is the peak vector potential. ϵ_i and ω_i are the ellipticity and the frequency of the *i*th pulse, respectively. The laser pulse envelope $f(t)$ is a sin-square profile. For the linearly polarized laser, A_{20} and ϵ_i are set to be zero. For the bichromatic circularly polarized field, $A_{10} = A_{20}$, $\epsilon_i = 1$ and $\omega_2 = 2\omega_1$. The "±" in Eq. 5 is used to distinguish a circularly polarized field with the left-handed (+) or the right-handed (−) rotation. Both kinds of laser pulses share the same pulse length, and contain 8 cycles of the fundamental pulse. The electric field $\mathbf{E}(t)$ relates to the $\mathbf{A}(t)$ by $\mathbf{E}(t) = -\frac{1}{c}\frac{\partial}{\partial t}\mathbf{A}(t)$. The total energy of the incident laser field in the current work always remains the same as the fundamental linearly polarized pulse with a peak laser intensity of 10^{12} W/cm^2.

3 Results and discussion

The strain-free monolayer hBN is a direct-gap insulator with a hexagonal lattice. The top view of the crystal structure is shown in Figure 1A. Figures 1B,C show the first BZ and the band structure, respectively. The minimum direct band gap is located at K point with a magnitude of ~ 4.5 eV, in good agreement with other calculations [38, 52]. For the strain-free hBN, the energy at the high symmetry points of S and M in the band structure is degenerate, as well as the R and K points.

By taking the lattice structure of the strain-free monolayer hBN as a reference, the symmetry of the reciprocal space will be changed under different strain strengths. In Figures 2A–C, we show electronic band structures of the monolayer hBN that under different stretching percents. We find that the band structure strongly depends on the strength and direction of the applied strains, and the band energies shift when strains are applied. For the cases of $\varepsilon_{uni.(x)}$ and ε_{bi}, the top of the valence

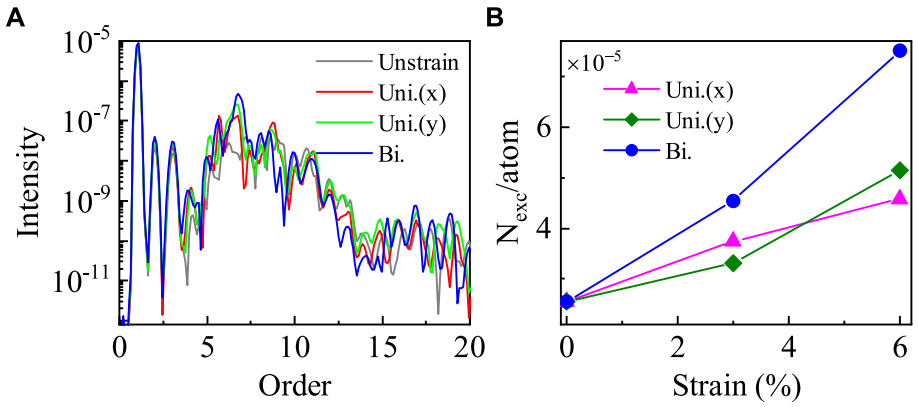

FIGURE 3
(A) The total HHG spectra in the monolayer hBN with the stretching percent of $\varepsilon = 6\%$ under the linear pulse polarized along the *x* direction. The laser wavelength is 1,600 nm with a peak intensity of 10^{12} W/cm^2. The gray solid line is for the HHG spectra in the strain-free case. **(B)** The strain-dependent excited electron number after the laser ends for different strains strengths.

band (VB) and the bottom of the conduction band (CB) locate at K point, and the increase of the stretching percent always results in the decrease of the direct bandgap. For the $\varepsilon_{uni.(y)}$ case, the monolayer hBN has a direct bandgap under small strains. However, its bandgap turns into indirect for larger stretching magnitude. Biaxial strains usually modify the bandgap more seriously than uniaxial strains. For instance, when $\varepsilon_{uni.(x)} = 6\%$ (or $\varepsilon_{uni.(y)} = 6\%$), the direct bandgap at K point decreases to ~ 4.3 eV, while when $\varepsilon_{bi.} = 6\%$, the direct band gap decreases to 4.1 eV. The shifting trend of the bandgap under strains in this work agrees with that in Ref. [38].

To explain the strain effect on the HHG, we first study the HHG spectra of the monolayer hBN crystal under different strains, driven by a linearly polarized laser pulse. Our results show that the distortion of the band structure alters significantly the in-plane harmonic emission. Since the phonon effect is not considered in the present work, the electronic indirect transition may not contribute to the harmonic generation. Figure 3A shows the total HHG intensity in the monolayer hBN under stretching strain values of $\varepsilon = 0$ and $\varepsilon = 6\%$. Compared with the strain-free case, both uniaxial and biaxial strains lead to the enhancement of the HHG intensity. The strain-dependent excited electron number (N_{exc}) of the monolayer hBN after the laser field ends is shown in Figure 3B. The N_{exc} is larger under the biaxial stretching, and the corresponding HHG intensity is slightly stronger than that in the uniaxial strain cases. This may be attributed to the fact that reducing the bandgap makes electrons easier transfer from the VB to the CB. This finding is in consistent with the strain-controlled HHG mechanism in silicene, in which both the intraband and the interband HHG can be enhanced due to the increase of electronic population in the CB [35].

To explain the strained HHG mechanism, we plotted the time-frequency HHG with stretching strains in Figure 4. We find that the strained HHG mechanism is closely related to the symmetry of the monolayer hBN. For the strain-free hBN, it has the reflection symmetry with respect to the B-N bond, and the three-fold rotation symmetry with respective to the center of the hexagonal lattice [53]. However, when applied stretching strains, some symmetries are destroyed, resulting in a concert change in the HHG spectra. Specifically, under uniaxial stretching along the *x* or the *y* direction, the three-fold rotation symmetry is broken, while the reflection symmetry in the *x* direction is preserved. This gives rise to different HHG mechanisms that only odd harmonics are found in the *x* direction and only even harmonics are found in the *y* direction. Besides, we demonstrate that high harmonics are emitted as discrete bursts in phase concerted with the change of vector potentials, and magenta lines in Figure 4 stand for the absolute value of the vector potentials. This suggests that the electronic interband transition is the dominant mechanism for the stretching-strained harmonic emission [54].

To further investigate the energy transfer from the laser field to the strained monolayer hBN, Figure 5A shows the energy absorption per atom at different laser rotation angles that defined as the angle between the laser polarization and the x direction. The laser field is initially polarized in the *x* direction, and then rotates counterclockwise, as shown in the insert in Figure 5A.

The energy absorption is an effective representation to clarify the laser-matter energy connection. The energy transfer function *W* in the unit cell volume of Ω can be defined as

$$W = \Omega \int_{-\infty}^{t_{end}} dt' \mathbf{E}(t') \cdot \mathbf{j}(t'), \tag{6}$$

where t_{end} is the moment that the laser pulse ends. In Figure 5A, for the strain-free case, *W* vibrates with a period of ~ 60 degrees, indicating a high anisotropy of the monolayer hBN. Maximum

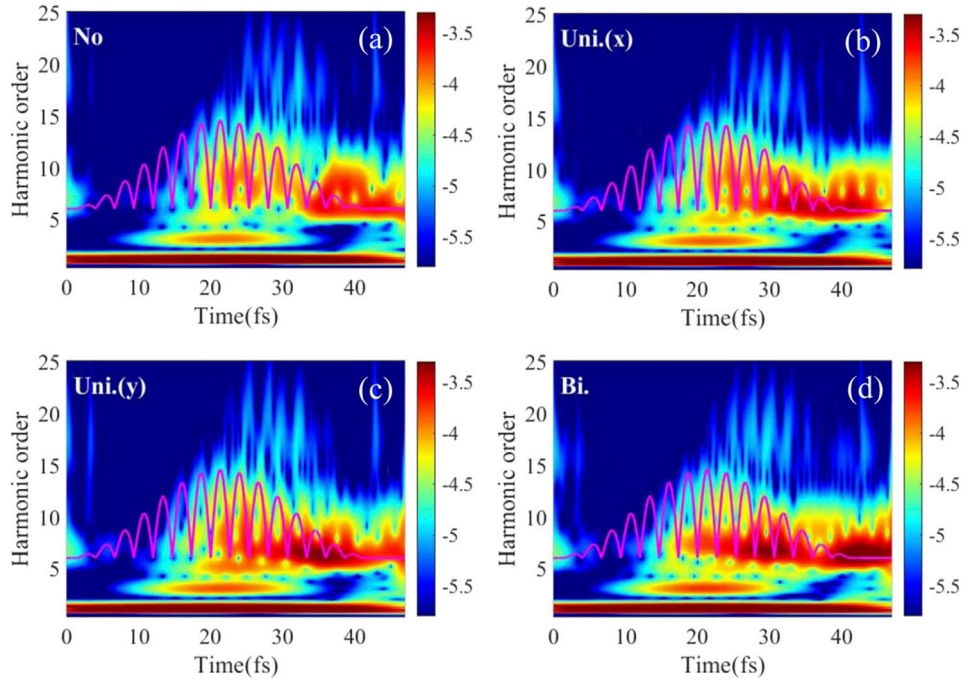

FIGURE 4
The time-frequency logarithmic intensity of *x*-polarized harmonics under different stretching percents, radiated by a linear polarized laser pulse along the *x* direction: **(A)** strain-free; only uniaxial stretching imposed along **(B)** the *x* direction with $\varepsilon_{uni.(x)}$ = 6% and **(C)** the *y* direction with $\varepsilon_{uni.(y)}$ = 6%; **(D)** biaxial stretching with $\varepsilon_{bi.}$ = 6%.

values of *W* are found when the laser polarization is parallel to the B-N bond (30°, 90°, 150°), and minimal values are identified when the laser polarization is paralled to either the B-B or the N-N bond (0°, 60°, 120°, 180°). When the lattice structure is stretched along the *y* direction, the original hexagonal geometry is lost. Therefore, the B-B (or N-N) distance in the *x* direction is slightly compressed and the B-N bond in the *y* direction is stretched. Interestingly, we find that *W* is larger under $\varepsilon_{uni.(y)}$ = 6% than the strain-free case when the laser is polarized around the 0° angle, and becomes smaller when the laser is polarized around the 90° angle. This demonstrates that the anisotropy is greatly enhanced in the stretching case. Neufeld *et al.* also found that the harmonic yield in the plateau region oscillates periodically in accordance with the instantaneous structural changes in the lattice, and the dominant HHG contribution arises when the laser polarization is parallel to the compressed B-N bond [55].

The high-energy harmonics around the cutoff region are sensitive to the interatomic distance and electronegativity [4], in other words, it can be used to reconstruct the geometric symmetry of the material. To this end, we study the (15th-22nd)-integrated HHG yield. As shown in Figures 5B,C, triangle symbols represent the composed HHG yield parallel to the polarization direction and circle symbols represent the yield component perpendicular to the polarization direction. It can be seen that the total harmonic yield is in consistent with the change of the energy absorption in Figure 5A. For both the ε = 0 and $\varepsilon_{uni.(y)}$ = 6%, the parallel contribution to the total HHG yield is dominant. The weak perpendicular component of HHG is generally attributed to the Berry curvature. In addition, contributions of orientation-dependent HHG yield from the parallel and the perpendicular configuration are opposite to each other. A more detailed analysis of the selection rule for the strain-free monolayer hBN can be found in our previous paper [53].

Figure 6 shows the non-perturbative anisotropy map of the HHG from the monolayer hBN obtained *via* rotating the polarization of the linearly polarized driving field. We analyze the two polarization components of the harmonics, i.e., perpendicular and parallel to the linearly polarized laser field. For the ε = 0 and the $\varepsilon_{uni.(y)}$ = 6% cases, the crystal symmetry is quite different. The parallel and the perpendicular HHG components reflect the symmetry of the hexagonal layered structure. Compared with the parallel component, the weak HHG perpendicular component is dominated by the even harmonics, as shown in Figure 6B. When the laser polarization is in the B-B (or N-N) direction, pure odd harmonics are embodied in the parallel component and pure even harmonics in the perpendicular component. The perpendicular harmonic component is forbidden when

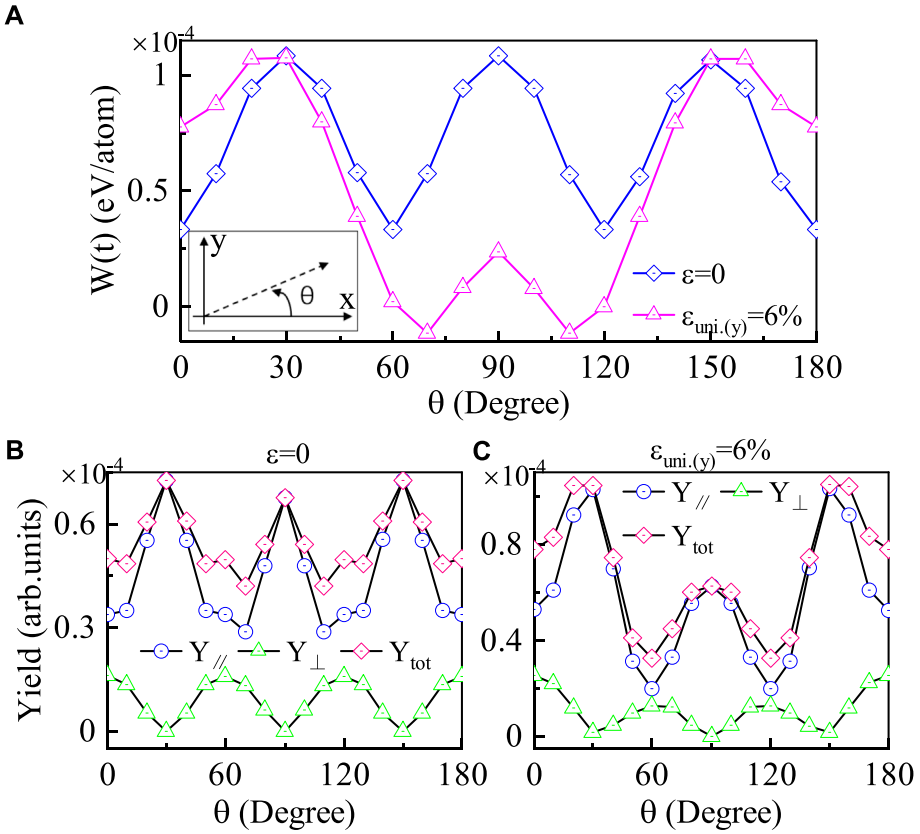

FIGURE 5
(A) The calculated energy absorption per atom of the monolayer hBN as a function of the laser rotation angle under stretching percents of $\varepsilon = 0$ and $\varepsilon_{uni.(y)} = 6\%$. The inset shows the angle of the laser in-plane polarization. The laser field is first polarized in the x direction and then rotated counterclockwise. The harmonic yield as a function of the laser rotation for cases of $\varepsilon = 0$ **(B)** and $\varepsilon_{uni.(y)} = 6\%$ **(C)**. The HHG yield component that parallel or perpendicular to the linearly polarized field is denoted by circle and triangle symbols, respectively. Cubic symbols are the total harmonic yield.

the laser is polarized along the B-N bond. For the $\varepsilon_{uni.(y)} = 6\%$ case, the breaking of the three-fold rotation symmetry is reflected by the perpendicular HHG spectrogram, e.g., the mirror symmetry with respect to the B-N bond is broken at 30° and 150°. Therefore, the HHG perpendicular component is strictly forbidden when the laser is polarized in the y direction, and the odd harmonic yield in Figure 6D is higher than that in Figure 6B. One has demonstrated that the polarization properties of the solid-state HHG are largely governed by the crystal symmetry by comparing the experimental measurements with the theoretical results [56]. The similar odd/even order contrast has been reported for many other crystals, such as the monolayer MoS_2 [6], the bulk ZnO [56], α-quartz crystals [9, 57], etc. These results show that the polarization-dependent harmonics provide a powerful way to probe the crystal spatial symmetry.

For the HHG selection rule, it has been proven that the HHG emission must obey the same symmetry owned by the target system and the driving field [58, 59]. Therefore, if the incident laser field has the three-fold rotation symmetry as same as the monolayer hBN lattice, the $3n$-order harmonics should be missing. According to this, we investigate the harmonic generation in the monolayer hBN under $\varepsilon_{uni.(y)}$ stretching driven by a bichromatic counter-rotating circularly polarized laser pulse. Such a laser pulse is a combination of a circularly polarized fundamental field of frequency ω_1 (1,600 nm) and its counter-rotating second harmonic ω_2 (800 nm), which exhibits a three-fold rosette pattern as shown in the insert of Figure 7. The intensity of both two single circularly polarized pluses is set to be $I_1 = I_2 = 5 \times 10^{11}$ W/cm^2. For the strain-free case, governed by the selection rule, it is obvious that the $3n$th harmonics are forbidden. However, as the uniaxial stretching percent increases, the forbidden $3n$th harmonics gradually restore. In this case, the uniaxial stretching breaks the three-fold rotation symmetry, and the selection rule is replaced by selection deviations [60]. Comparing with the results of $\varepsilon_{uni.(y)} = 3\%$ and $\varepsilon_{uni.(y)} = 6\%$, one can find that a larger

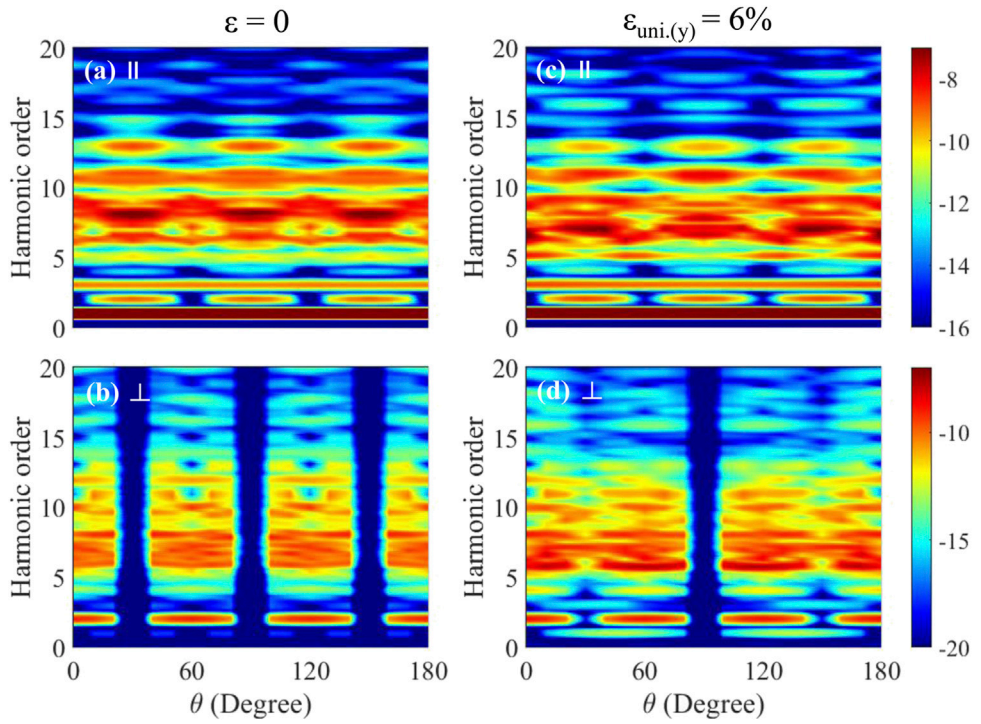

FIGURE 6
Logarithmic colormap for the polarization-dependent harmonic intensity in the monolayer hBN. Left panels: the HHG in the strain-free monolayer hBN for the **(A)** parallel and **(B)** the perpendicular components. Right panels: The HHG in the stretching monolayer hBN with $\varepsilon_{uni.(y)}$ = 6% for the **(C)** parallel and **(D)** the perpendicular components.

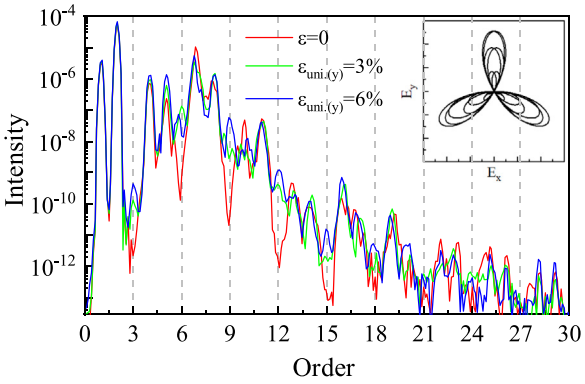

FIGURE 7
The HHG in the stretching and strain-free monolayer hBN driven by a two-color counter-rotated circularly polarized laser pulse. The insert is the Lissajous curve of the applied laser field.

stretching percent gives rise to a stronger 3*n*th harmonic signal. This suggests that exerting a stronger external perturbation may result in a larger deviation, and such a signal is useful to reconstruct the lattice deformation.

4 Conclusion

In conclusion, we have studied the strain-dependent HHG in the monolayer hBN crystal within the TDDFT. The monolayer hBN is exposed to an intense linearly polarized or a counter-rotating bichromatic circularly polarized mid-infrared laser field. To ensure the structural stability of the hBN crystal, stretching percents are limited in the range of 0–6%. Using the strain-free monolayer hBN as a reference, we studied band structures and the resulting HHG under two typical kinds of strains, i.e., the uniaxial and the biaxial stretching strains. We find the band structure is sensitive to the structural deformation modulated by strains. For both the uniaxial and biaxial cases, the interband dynamics is the dominant mechanism in the strained monolayer hBN. By rotating the laser polarization direction, the HHG spectra from the strained monolayer hBN exhibit some special features compared with that from the strain-free case. The results show that the anisotropy of HHG spectra is closely related to the structural symmetry of the strained hBN. Furthermore, when exposed to a bichromatic counter-rotating circularly polarized laser pulse, the restoration of 3*n*th harmonics is a potential probe to reconstruct the lattice deformation. Therefore, our work provides a useful way to control the HHG by applying

mechanical strains, and the results may be heuristic to enhance the optoelectronic efficiency of solid-state nano-devices.

Data availability statement

The datasets for this study can be obtained from the authors upon reasonable requests.

Author contributions

KX did all the calculations and wrote the manuscript. YW contributed to supervision and manuscript revision. GL, WX, and YW commented on the manuscript. All authors contributed to manuscript revision and approved the submitted version.

Funding

This work is supported by the National Natural Science Foundation of China (NSFC) under Grant Nos. 12104019 and 11725416 and 11961131008 and by the National Key R&D Program of China under Grant No. 2018YFA0306302.

Conflict of interest

The authors declare that the research was conducted in the absence of any commercial or financial relationships that could be construed as a potential conflict of interest.

Publisher's note

All claims expressed in this article are solely those of the authors and do not necessarily represent those of their affiliated organizations, or those of the publisher, the editors and the reviewers. Any product that may be evaluated in this article, or claim that may be made by its manufacturer, is not guaranteed or endorsed by the publisher.

References

1. Ghimire S, DiChiara AD, Sistrunk E, Agostini P, DiMauro LF, Reis DA. Observation of high-order harmonic generation in a bulk crystal. *Nat Phys* (2011) 7: 138–41. doi:10.1038/nphys1847

2. Ghimire S, DiChiara AD, Sistrunk E, Ndabashimiye G, Szafruga UB, Mohammad A, et al. Generation and propagation of high-order harmonics in crystals. *Phys Rev A (Coll Park)* (2012) 85:043836. doi:10.1103/physreva.85.043836

3. Luu TT, Garg M, Kruchinin SY, Moulet A, Hassan MT, Goulielmakis E. Extreme ultraviolet high-harmonic spectroscopy of solids. *Nature* (2015) 521: 498–502. doi:10.1038/nature14456

4. You YS, Reis D, Ghimire S. Anisotropic high-harmonic generation in bulk crystals. *Nat Phys* (2017) 13:345–9. doi:10.1038/nphys3955

5. Ndabashimiye G, Ghimire S, Wu M, Browne DA, Schafer KJ, Gaarde MB, et al. Solid-state harmonics beyond the atomic limit. *Nature* (2016) 534:520–3. doi:10.1038/nature17660

6. Liu H, Li Y, You YS, Ghimire S, Heinz TF, Reis DA. High-harmonic generation from an atomically thin semiconductor. *Nat Phys* (2017) 13:262–5. doi:10.1038/nphys3946

7. Yoshikawa N, Tamaya T, Tanaka K. High-harmonic generation in graphene enhanced by elliptically polarized light excitation. *Science* (2017) 356:736–8. doi:10.1126/science.aam8861

8. Vampa G, Hammond TJ, Thiré N, Schmidt BE, Légaré F, McDonald CR, et al. All-optical reconstruction of crystal band structure. *Phys Rev Lett* (2015) 115: 193603. doi:10.1103/physrevlett.115.193603

9. Luu TT, Wörner HJ. Measurement of the berry curvature of solids using high-harmonic spectroscopy. *Nat Commun* (2018) 9:916. doi:10.1038/s41467-018-03397-4

10. Han S, Ortmann L, Kim H, Kim YW, Oka T, Chacon A, et al. Extraction of higher-order nonlinear electronic response in solids using high harmonic generation. *Nat Commun* (2019) 10:3272. doi:10.1038/s41467-019-11096-x

11. Tancogne-Dejean N, Mücke OD, Kärtner FX, Rubio A. Impact of the electronic band structure in high-harmonic generation spectra of solids. *Phys Rev Lett* (2017) 118:087403. doi:10.1103/physrevlett.118.087403

12. Uchida K, Pareek V, Nagai K, Dani K, Tanaka K. Visualization of two-dimensional transition dipole moment texture in momentum space using high-harmonic generation spectroscopy. *Phys Rev B* (2021) 103:L161406. doi:10.1103/physrevb.103.l161406

13. Corkum PB. Plasma perspective on strong field multiphoton ionization. *Phys Rev Lett* (1993) 71:1994–7. doi:10.1103/physrevlett.71.1994

14. Vampa G, McDonald C, Orlando G, Klug D, Corkum P, Brabec T. Theoretical analysis of high-harmonic generation in solids. *Phys Rev Lett* (2014) 113:073901. doi:10.1103/physrevlett.113.073901

15. Tancogne-Dejean N, Rubio A. Atomic-like high-harmonic generation from two-dimensional materials. *Sci Adv* (2018) 4:eaao5207. doi:10.1126/sciadv.aao5207

16. Le Breton G, Rubio A, Tancogne-Dejean N. High-harmonic generation from few-layer hexagonal boron nitride: Evolution from monolayer to bulk response. *Phys Rev B* (2018) 98:165308. doi:10.1103/physrevb.98.165308

17. Yu C, Jiang S, Wu T, Yuan G, Peng Y, Jin C, et al. Higher harmonic generation from bilayer nanostructures assisted by electron backscattering. *Phys Rev B* (2020) 102:241407. doi:10.1103/physrevb.102.241407

18. Huang T, Zhu X, Li L, Liu X, Lan P, Lu P. High-order-harmonic generation of a doped semiconductor. *Phys Rev A (Coll Park)* (2017) 96:043425. doi:10.1103/physreva.96.043425

19. Mrudul M, Tancogne-Dejean N, Rubio A, Dixit G. High-harmonic generation from spin-polarised defects in solids. *Npj Comput Mater* (2020) 6:10. doi:10.1038/s41524-020-0275-z

20. Han S, Kim H, Kim YW, Kim YJ, Kim S, Park IY, et al. High-harmonic generation by field enhanced femtosecond pulses in metal-sapphire nanostructure. *Nat Commun* (2016) 7:13105. doi:10.1038/ncomms13105

21. Du TY, Guan Z, Zhou XX, Bian XB. Enhanced high-order harmonic generation from periodic potentials in inhomogeneous laser fields. *Phys Rev A (Coll Park)* (2016) 94:023419. doi:10.1103/physreva.94.023419

22. Chen ZY, Qin R. High harmonic generation in graphene–boron nitride heterostructures. *J Mater Chem C Mater* (2020) 8:12085–91. doi:10.1039/d0tc02036b

23. Mrudul M, Dixit G. High-harmonic generation from monolayer and bilayer graphene. *Phys Rev B* (2021) 103:094308. doi:10.1103/physrevb.103.094308

24. Pertsev N, Zembilgotov A, Tagantsev A. Effect of mechanical boundary conditions on phase diagrams of epitaxial ferroelectric thin films. *Phys Rev Lett* (1998) 80:1988–91. doi:10.1103/physrevlett.80.1988

25. Haeni J, Irvin P, Chang W, Uecker R, Reiche P, Li Y, et al. Room-temperature ferroelectricity in strained $SrTiO_3$. *Nature* (2004) 430:758–61. doi:10.1038/nature02773

26. Cao J, Ertekin E, Srinivasan V, Fan W, Huang S, Zheng H, et al. Strain engineering and one-dimensional organization of metal–insulator domains in single-crystal vanadium dioxide beams. *Nat Nanotechnol* (2009) 4:732–7. doi:10.1038/nnano.2009.266

27. Takahashi H, Igawa K, Arii K, Kamihara Y, Hirano M, Hosono H. Superconductivity at 43 k in an iron-based layered compound $Lao_{1-x}F_{xFeAs}$. *Nature* (2008) 453:376–8. doi:10.1038/nature06972

28. Gao L, Xue Y, Chen F, Xiong Q, Meng R, Ramirez D, et al. Superconductivity up to 164 k in $HgBa_2Ca_{m-1}Cu_mO_{2m+2+\delta}$ (m = 1, 2, and 3) under quasihydrostatic pressures. *Phys Rev B* (1994) 50:4260–3. doi:10.1103/physrevb.50.4260

29. Song S, Keum DH, Cho S, Perello D, Kim Y, Lee YH. Room temperature semiconductor–metal transition of $MoTe_2$ thin films engineered by strain. *Nano Lett* (2016) 16:188–93. doi:10.1021/acs.nanolett.5b03481

30. Guan MX, Liu XB, Chen DQ, Li XY, Qi YP, Yang Q, et al. Optical control of multistage phase transition via phonon coupling in $MoTe_2$. *Phys Rev Lett* (2022) 128:015702. doi:10.1103/physrevlett.128.015702

31. Mennel L, Furchi MM, Wachter S, Paur M, Polyushkin DK, Mueller T. Optical imaging of strain in two-dimensional crystals. *Nat Commun* (2018) 9:516. doi:10.1038/s41467-018-02830-y

32. Conley HJ, Wang B, Ziegler JI, Haglund RF, Jr, Pantelides ST, Bolotin KI. Bandgap engineering of strained monolayer and bilayer MoS_2. *Nano Lett* (2013) 13:3626–30. doi:10.1021/nl4014748

33. Guan MX, Lian C, Hu SQ, Liu H, Zhang SJ, Zhang J, et al. Cooperative evolution of intraband and interband excitations for high-harmonic generation in strained MoS_2. *Phys Rev B* (2019) 99:184306. doi:10.1103/physrevb.99.184306

34. Wang Z, Jiang S, Yuan G, Wu T, Li C, Qian C, et al. Strain effect on the orientation-dependent harmonic spectrum of monolayer aluminum nitride. *Sci China Phys Mech Astron* (2020) 63:257311. doi:10.1007/s11433-019-1467-2

35. Qin R, Chen ZY. Strain-controlled high harmonic generation with Dirac fermions in silicene. *Nanoscale* (2018) 10:22593–600. doi:10.1039/c8nr07572g

36. Pouch JJ, Alterovitz SA. *Synthesis and properties of boron nitride*. Aedermannsdorf: Trans Tech, Aedermannsdorf (1990).

37. Bourrellier R, Amato M, Galvão Tizei LH, Giorgetti C, Gloter A, Heggie MI, et al. Nanometric resolved luminescence in h-BN flakes: Excitons and stacking order. *ACS Photon* (2014) 1:857–62. doi:10.1021/ph500141j

38. Li J, Gui G, Zhong J. Tunable bandgap structures of two-dimensional boron nitride. *J Appl Phys* (2008) 104:094311. doi:10.1063/1.3006138

39. Runge E, Gross EK. Density-functional theory for time-dependent systems. *Phys Rev Lett* (1984) 52:997–1000. doi:10.1103/physrevlett.52.997

40. Leeuwen R. V. Mapping from densities to potentials in time-dependent density-functional theory. *Phys Rev Lett* (1999) 82:3863–6. doi:10.1103/physrevlett.82.3863

41. Kresse G, Furthmüller J. Efficient iterative schemes for *ab initio* total-energy calculations using a plane-wave basis set. *Phys Rev B* (1996) 54:11169–86. doi:10.1103/physrevb.54.11169

42. Kresse G, Furthmüller J. Efficiency of *ab-initio* total energy calculations for metals and semiconductors using a plane-wave basis set. *Comput Mater Sci* (1996) 6:15–50. doi:10.1016/0927-0256(96)00008-0

43. Blöchl PE. Projector augmented-wave method. *Phys Rev B* (1994) 50:17953–79. doi:10.1103/physrevb.50.17953

44. Kresse G, Joubert D. From ultrasoft pseudopotentials to the projector augmented-wave method. *Phys Rev B* (1999) 59:1758–75. doi:10.1103/physrevb.59.1758

45. Poisson SD. *Traité de Mécanique (Chez Courcier, Paris)* 2(1811):476.

46. Greaves GN, Greer AL, Lakes RS, Rouxel T. Poisson's ratio and modern materials. *Nat Mater* (2011) 10:823–37. doi:10.1038/nmat3134

47. Andrade X, Strubbe D, De Giovannini U, Larsen AH, Oliveira MJ, Alberdi-Rodriguez J, et al. Real-space grids and the octopus code as tools for the development of new simulation approaches for electronic systems. *Phys Chem Chem Phys* (2015) 17:31371–96. doi:10.1039/c5cp00351b

48. Tancogne-Dejean N, Oliveira MJ, Andrade X, Appel H, Borca CH, Le Breton G, et al. Octopus, a computational framework for exploring light-driven phenomena and quantum dynamics in extended and finite systems. *J Chem Phys* (2020) 152:124119. doi:10.1063/1.5142502

49. De Giovannini U, Larsen AH, Rubio A. Modeling electron dynamics coupled to continuum states in finite volumes with absorbing boundaries. *Eur Phys J B* (2015) 88:56. doi:10.1140/epjb/e2015-50808-0

50. Onida G, Reining L, Rubio A. Electronic excitations: Density-functional versus many-body green's-function approaches. *Rev Mod Phys* (2002) 74:601–59. doi:10.1103/revmodphys.74.601

51. Hartwigsen C, Goedecker S, Hutter J. Relativistic separable dual-space Gaussian pseudopotentials from H to Rn. *Phys Rev B* (1998) 58:3641–62. doi:10.1103/physrevb.58.3641

52. Ooi N, Rairkar A, Lindsley L, Adams J. Electronic structure and bonding in hexagonal boron nitride. *J Phys : Condens Matter* (2005) 18:97–115. doi:10.1088/0953-8984/18/1/007

53. Kong XS, Liang H, Wu XY, Peng LY. Symmetry analyses of high-order harmonic generation in monolayer hexagonal boron nitride. *J Phys B: Mol Opt Phys* (2021) 54:124004. doi:10.1088/1361-6455/ac066f

54. Wu M, Ghimire S, Reis DA, Schafer KJ, Gaarde MB. High-harmonic generation from bloch electrons in solids. *Phys Rev A (Coll Park)* (2015) 91:043839. doi:10.1103/physreva.91.043839

55. Neufeld O, Zhang J, Giovannini UD, Hübener H, Rubio A. Probing phonon dynamics with multidimensional high harmonic carrier-envelope-phase spectroscopy. *Proc Natl Acad Sci U S A* (2022) 119:e2204219119. doi:10.1073/pnas.2204219119

56. Jiang S, Gholam-Mirzaei S, Crites E, Beetar JE, Singh M, Lu R, et al. Crystal symmetry and polarization of high-order harmonics in ZnO. *J Phys B: Mol Opt Phys* (2019) 52:225601. doi:10.1088/1361-6455/ab470d

57. Wu XY, Liang H, Kong XS, Gong Q, Peng LY. Multiscale numerical tool for studying nonlinear dynamics in solids induced by strong laser pulses. *Phys Rev E* (2022) 105:055306. doi:10.1103/physreve.105.055306

58. Alon OE, Averbukh V, Moiseyev N. Selection rules for the high harmonic generation spectra. *Phys Rev Lett* (1998) 80:3743–6. doi:10.1103/physrevlett.80.3743

59. Neufeld O, Podolsky D, Cohen O. Floquet group theory and its application to selection rules in harmonic generation. *Nat Commun* (2019) 10:405. doi:10.1038/s41467-018-07935-y

60. Tzur ME, Neufeld O, Bordo E, Fleischer A, Cohen O. Selection rules in symmetry-broken systems by symmetries in synthetic dimensions. *Nat Commun* (2022) 13:1312. doi:10.1038/s41467-022-29080-3

frontiers | Frontiers in Physics

TYPE Brief Research Report
PUBLISHED 28 October 2022
DOI 10.3389/fphy.2022.990002

OPEN ACCESS

EDITED BY
Weifeng Yang,
Hainan University, China

REVIEWED BY
Pedro Duarte Amaro,
New University of Lisbon, Portugal
Kun Zhao,
Institute of Physics (CAS), China

*CORRESPONDENCE
Yinghui Zheng,
zhengyh@zjlab.ac.cn
Zhinan Zeng,
zengzn@zjlab.ac.cn

SPECIALTY SECTION
This article was submitted to Optics and Photonics,
a section of the journal
Frontiers in Physics

RECEIVED 09 July 2022
ACCEPTED 14 October 2022
PUBLISHED 28 October 2022

CITATION
Yang C, Lou Z, Yang F, Ge X, Zheng Y, Zeng Z and Li R (2022), Control of coherent extreme-ultraviolet emission around atomic potential through laser chirp.
Front. Phys. 10:990002.
doi: 10.3389/fphy.2022.990002

Control of coherent extreme-ultraviolet emission around atomic potential through laser chirp

Chun Yang[1,2], Zhiyuan Lou[1], Fan Yang[1], Xiaochun Ge[1], Yinghui Zheng[1]*, Zhinan Zeng[1]* and Ruxin Li[1]

[1]State Key Laboratory of High Field Laser Physics, Shanghai Institute of Optics and Fine Mechanics, Chinese Academy of Sciences, Shanghai, China, [2]Center of Materials Science and Optoelectronics Engineering, University of Chinese Academy of Sciences, Beijing, China

Substantial neutral atoms can tunnel to excited states in an intense laser field and subsequently generate coherent emission through free induction decay. We experimentally observe an enhanced coherent emission in the harmonic slightly below the threshold, which is consistent with the free induction decay of Rydberg states produced by the frustrated tunnelling ionization (FTI) process. We further find that the intensity of the coherent emission significantly depends on the chirp of laser pulses. The simulations based on the strong field approximation model show that laser chirp affects the probability that the returned electrons recombine to the Rydberg states. Our result shows that coherent emission can be controlled by laser chirp, which facilitates understanding the dynamics of the Rydberg atom and coupling mechanism between the below-threshold harmonics and atomic energy level. In addition, the coherent below-threshold FTI emission we observed has small divergence which is good for EUV light source applications.

KEYWORDS

frustrated tunnelling ionization, chirp, high-order harmonic generation, Rydberg states, ionization potential, time dependent Schrödinger equation, coherent extreme-ultraviolet emission

1 Introduction

The investigations of high-order harmonic generation (HHG) [1, 2] in atomic and molecular systems promote the development of non-linear optics. A bound-state electron can be released from parent ion through the tunnelling ionization process when the instantaneous intense laser external field becomes comparable to the binding Coulomb field. Then, the released electron obtains kinetic energy in the laser field and recollides with the parent ion; subsequently, the kinetic energy of the collision is converted into radiation energy. This widely accepted physical picture called the three-step model [3, 4] has attracted extensive research interest such as atomic and molecular dynamics [5, 6], attosecond science [7–9], and coherent extreme-ultraviolet source [10].

In the previous reports, the above-threshold HHG has been extensively studied, and recent works show that the below (or near)-threshold harmonics (BTH) present complex and interesting phenomena. When the BTH spectrally overlap with the atomic energy levels, resonance-enhanced vacuum ultraviolet (VUV) emission [10] can be generated with phase-matching and high-efficiency. Although BTH generation [11–15] is largely incompatible with the three-step model of HHG, the surprising result is that these harmonics still arise from a non-perturbative process [16]. The cross-correlation frequency resolved optical gating (XFROG) [17] characterization shows that the BTH has a clear non-perturbative negative group delay dispersion (GDD), and the mechanism for BTH generation is similar to the semi-classical re-scattering process responsible for plateau harmonics. It is also found that the effects induced by the Coulomb potential also have a critical impact on these harmonics [11].

Near the threshold of the atomic or molecular ionization, some new coherent extreme-ultraviolet emissions [18, 19] through frustrated tunnelling ionization (FTI) process [20–24] called "FTI emission" have been reported. In the case of FTI, an electron is released from the parent ion by tunnelling ionization and oscillates in the superposition of the Coulomb field and the laser field, which is similar to the first two steps of the three-step model. Nevertheless, when the laser pulse is turned off, the released electrons return to the vicinity of the parent ion with zero kinetic energy, where the wave packets overlap spatially with the Rydberg states [25–27], rather than direct recombination to the ground state as described in the three-step model. Also, even at extreme high-laser intensities, atoms or molecules are not fully ionized and a fraction of them will appear as high-Rydberg states at the end of the laser pulse [28]. In this way, atoms or molecules can be coherently excited and obtain energy by surviving the laser pulse [29] in the Rydberg states and subsequently generate coherent EUV emission through free-induction decay (FID) [30–33]. The FTI emission is generated in the transition between the Rydberg states and the ground state, where the energy difference determines the frequency of emission. The FTI emission can be spatially controlled by adjusting the spatial chirp of driving pulses [18, 19], but the effect of temporal chirp of laser pulses on FTI emission has not been reported.

In this work, we investigate the FTI emission overlapping with HHG around the ionization potential of Kr atoms, I_p, excited by the chirp-controlled laser. The results show that behavior of the spectra can be strongly affected by the temporal chirp of the laser field and totally different for the parts above and below the ionization potential. The part above the I_p always presents the absorption, while the part below the I_p presents the emission which can be tuned by the laser chirp. By solving a one-dimensional time-dependent Schrödinger equation (1D TDSE), it is found that after the ground-state electron is excited, the probability of electron recombination to the Rydberg states is different under the positive and negative chirps. The positive chirp is conducive to electron recombination to the Rydberg states, in which case the probability of the electron returning to the vicinity of the parent ion with zero kinetic energy is higher. The excited state population at chirp coefficient b = 0.03 is about 5 times that of the unchirped laser field and 10 times that of the b = 0.03 laser field. We can control the emission intensity through chirp; furthermore, the FTI emission below the I_p we observed exhibits a small divergence. Our findings provide a new way to observe the complex electron behavior around the ionization potential I_p and to manipulate the FTI emission, contribute to the mechanism of the BTH, and open up the possibility of EUV light source applications such as lithography [34, 35] and EUV spectroscopy.

2 Experimental results

The BTH are driven by a commercial titanium–sapphire laser system (Coherent LEGEND-HE-Cyro, 800 nm, 1 kHz, 40 fs, 10 mJ pulse energy), which can be tuned to generate pulses with different chirps measured 40–300 fs duration (full width at half maxima, FWHM). The laser pulses were focused by a lens with 500 mm focal length to a 2 mm-length cell filled with Kr atoms under constant pressure to generate harmonics. The energy before the focal lens is 0.5 mJ, and the peak laser intensity of the chirp-free 42 fs pulse is about $1.34 \times 10^{14}\mathrm{Wcm}^{-2}$. The transmitted beams from the gas cell are filtered by a 300 nm-thick indium (In) foil, and the filtered HHG is collected in a reflection geometry by a spherical mirror which focuses the emissions onto the slit of the VUV spectrometer (McPherson, 234/302) which is located 950 mm away from the gas cell. The spectrometer has been calibrated with a xenon lamp and a mercury vapor lamp. In this experiment, the wavelength of 9th-order harmonic is 88.89 nm, and the corresponding photon energy is 13.9483 eV which is almost equal to the ionization energy of krypton (I_p = 13.9996 eV), which means 9th harmonic can cover many Rydberg states around the ionization potential I_p of Kr atom. Unless otherwise specified, the following experimental conditions are the same.

The existence of the Rydberg states implies differences between the 9th and other harmonics, and we compare different harmonics with the same experimental parameters. Figure 1 shows experimentally measured spectra of the 9th-order harmonic (A) and higher order harmonics (B) from Kr. The upper figures of Figures 1A,B show the harmonic spectra measured by the CCD. The horizontal axis represents the photon energy and the vertical axis is the divergence of the harmonic, which is calculated according to the distance from the gas cell to the CCD. The red line marks the coherence line emissions ($4p^6 \rightarrow 4p^5ns$) near the Kr ionization energy, and the energy levels for coherence line emissions refer to the NIST Atomic Spectra Database, ASD [36]. The figures below represent the vertical

10.3389/fphy.2022.990002

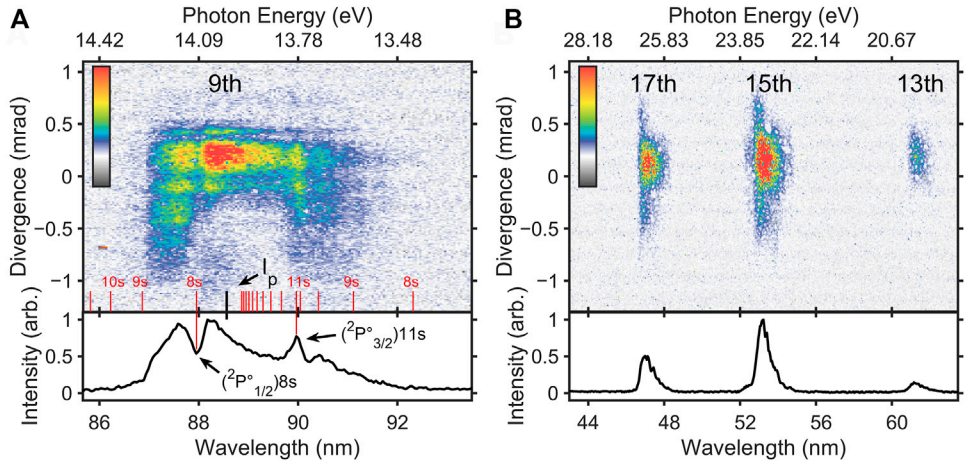

FIGURE 1
Comparison of the 9th-harmonic **(A)** and higher order harmonic (13th, 15th, and 17th) **(B)** spectra from krypton. The upper figures show the harmonic spectra measured by the CCD. The horizontal axis represents the photon energy, and the vertical axis is the divergence of the harmonic, which is calculated according to the distance from the gas cell to the CCD. The red line marks the coherence line emissions ($4p^6 \rightarrow 4p^5ns$) near the Kr ionization energy. The figures below represent the vertical integration of the upper figures, and the horizontal axis is converted to the corresponding wavelength. The indium foil filter was replaced with aluminum foil with the same thickness when acquiring 13th, 15th, and 17th spectra because of low-transmittance.

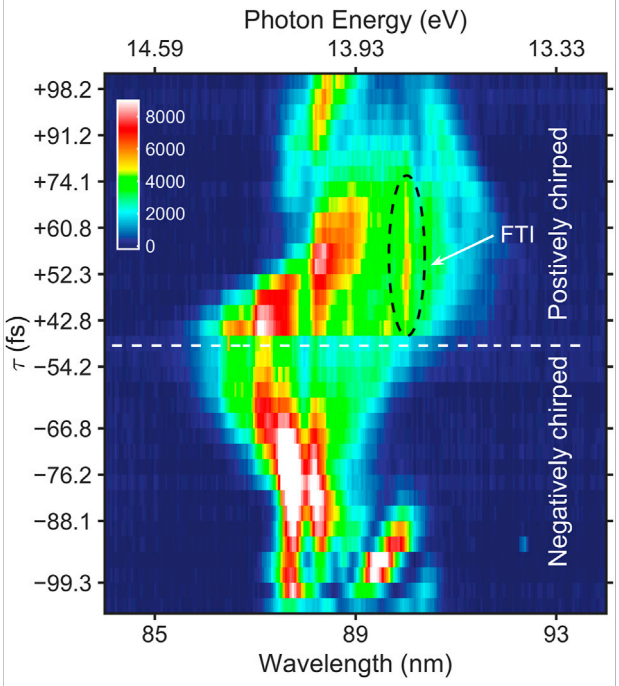

FIGURE 2
Variation of spectrum with laser chirp. The corresponding FWHM pulse duration τ shown as the y-axis varies from −100 fs to +100 fs, where "+" and "−" signs indicate the positive and negative chirp, respectively. The FTI emission is marked by black dotted circles.

integration of the upper figures, and the horizontal axis is converted to the corresponding wavelength. When acquiring 13th–17th spectra, the indium foil filter is replaced with aluminum foil with the same thickness because of low-transmittance. Compared with the higher order harmonics, the 9th harmonic spectrum exhibits both absorption [labelled as $(^2P^o_{1/2})8s$, 87.95 nm] and enhanced emission [labelled as $(^2P^o_{3/2})11s$, 89.96 nm] due to the Kr levels. The photon energy of enhanced emission is lower than the ionization energy I_p (corresponding to the Kr II $[4p^5\,(^2P^o_{3/2})]$ limit). It can also be seen from these figures that the divergence of the enhanced emission is ~1 mrad, close to that of the 9th harmonic, indicating that this is a radiation with good coherence. Comparatively, there is no such structure in the higher order harmonic (13th, 15th, and 17th) spectra. So, the enhancement part of below-threshold 9th harmonic that differs from higher order harmonics is what we care about.

Typically, the HHG process can be coherently controlled by using a chirped laser [37]. Figure 2 shows the variation of spectrum with the laser chirp, corresponding to the FWHM pulse duration τ from −42 fs to +100 fs, the corresponding laser intensity ranging from $1.34 \times 10^{14}\mathrm{Wcm}^{-2}$ to $5.51 \times 10^{13}\mathrm{Wcm}^{-2}$, where "+" and "−" signs indicate the positive and negative chirp, respectively. Apparently, Figure 2 shows that the shape and position of the FTI emission are controlled by the chirp. When the laser pulse is positively chirped, the wavelength position of FTI is fixed, as marked by black dotted

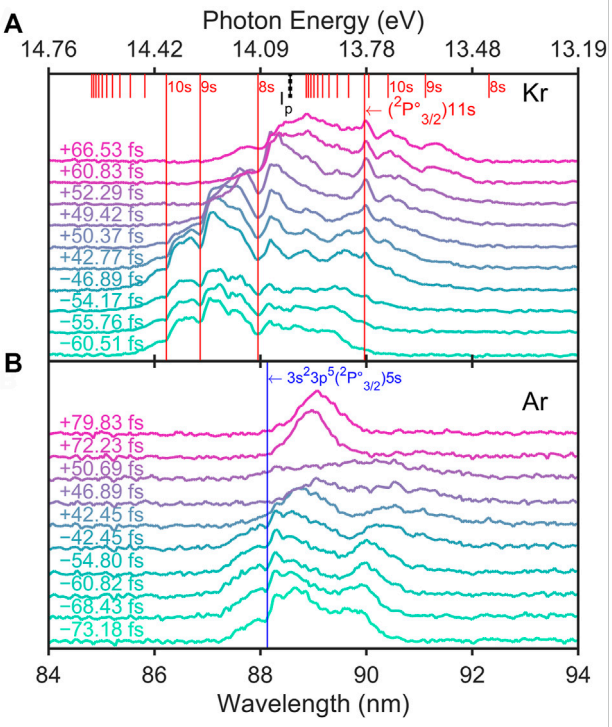

FIGURE 3
Comparison of the 9th-harmonic spectra of Kr **(A)** and Ar **(B)** under different chirps. **(A)** The peak laser intensity of the chirp-free 42-fs pulse was $1.34 \times 10^{14} Wcm^{-2}$. The long red lines are used to highlight absorption and emission under different chirps. **(B)** There is no fixed structure in the argon harmonic expect absorption of the level Ar $[3s^2 3p^5 (^2P^o_{3/2})5s]$ (blue line). The peak laser intensity of the chirp-free 42-fs pulse was $1.88 \times 10^{14} Wcm^{-2}$.

circle, depending on the energy level of Kr and the intensity of emission changes with the value of chirp. However, the harmonic will shift with the change of chirp. When the pulse is positively chirped or negatively chirped, the variation range of the intensity is symmetric about the zero-chirp line (dashed line in Figure 2), and the FTI emission does not exhibit this symmetry; the FTI emission can only be observed when the pulse is positively chirped (pulse duration measured +42.8 to +74.1 fs). Despite the same intensity, no FTI radiation was observed under negatively chirped pulse (pulse duration measured −54.2 to −76.2 fs). As can be seen from Figure 2, chirp plays a key role in the spectral intensity of FTI emission.

To verify whether the enhanced signal is induced by the atomic level, we compare the 9th-harmonic spectra from krypton and argon. In our experimental scheme, the 9th harmonic overlaps the ionization energy and Rydberg-state levels of krypton. But for argon atoms, the photon energy of the 9th harmonic is far below ionization energy. Therefore, when krypton is replaced by argon, the FTI coherent emission will not be observed in the 9th harmonic. Figure 3 displays the comparison of the 9th-harmonic spectra of Kr and Ar under different chirps. In Figure 3A, the levels of Kr near ionization energy are marked above the spectra as red lines, and the FTI coherent emission coincide well with the energy level $4p^5 (^2P^o_{3/2})11s$. Moreover, there are notable absorptions corresponding to the levels $4p^6 \rightarrow 4p^5 (^2P^o_{1/2})8s$ (87.95 nm) and $4p^6 \rightarrow 4p^5 (^2P^o_{1/2})9s$ (86.86 nm), implying the transitions from the ground state. The three levels aforementioned are highlighted in a long red line for comparison purposes. The spectral width of the FTI emission at $4p^5 (^2P^o_{3/2})11s$ is ~0.03 eV, which is comparable to the spectral width of absorption peak at $4p^5 (^2P^o_{1/2})8s$. As seen from the comparison, the 9th harmonic shows a frequency shift, but wavelengths of the absorption and FTI emission are fixed and coincide well with the Kr levels. This suggests that the mechanism of emission at the krypton level is different from that of the 9th-order harmonic generation. For absorption peaks above the threshold, the atom absorbs the 9th harmonic and is excited to the autoionizing state [12, 38], which ionizes almost immediately [39]. The radiation of autoionization propagates at solid angle of 4π, is rarely collected in the spectrometer, and appears as spectral absorption. Figure 3B shows the experimental below-threshold 9th-harmonic spectra generated from Ar, there are only absorptions of the Ar level $[3s^2 3p^5 (^2P^o_{3/2})5s]$ (blue line). In addition, the enhanced structure from the Kr level is chirp-dependent.

In brief, there are several characteristics of the enhanced coherent emission observed in our experiments. First, the frequency of the enhanced coherent emission is determined by the energy level. So, when we change the chirp of driven pulses, the center wavelength of the enhanced coherent emission remains unchanged, while the 9th-harmonic spectrum drifts a little. Also, there is no enhanced coherent emission from Ar since the 9th harmonic does not cover the levels of Ar atoms. Second, the intensity of the enhanced coherent emission depends on the chirp of driven laser. The chirp is reflected in the temporal shape of the driven photoelectric field. We will analyze how the chirp of driven laser affects the enhanced coherent emission next.

3 Simulation and discussion

As seen in experimental results, the enhanced coherent emission exhibits a small divergence (Figure 1) close to harmonics and its intensity could be controlled by adjusting the temporal chirp of a driving laser pulse, which can be explained by the FTI emission through FID progress [18, 22, 26, 30]. By introducing the concept of electron trajectories, the electron dynamics of FTI progress in the strong laser field could be explained with the strong field approximation theory. In the framework of strong field approximation, the Coulomb field is neglected after the ionization compared to the laser field. In the case of well-known HHG, the wave packet tunnels turn out to be the electron wave packet in the continuum, whose trajectory depends on the ionization time. The electron that tunnels out after the peak of the laser electronic field can

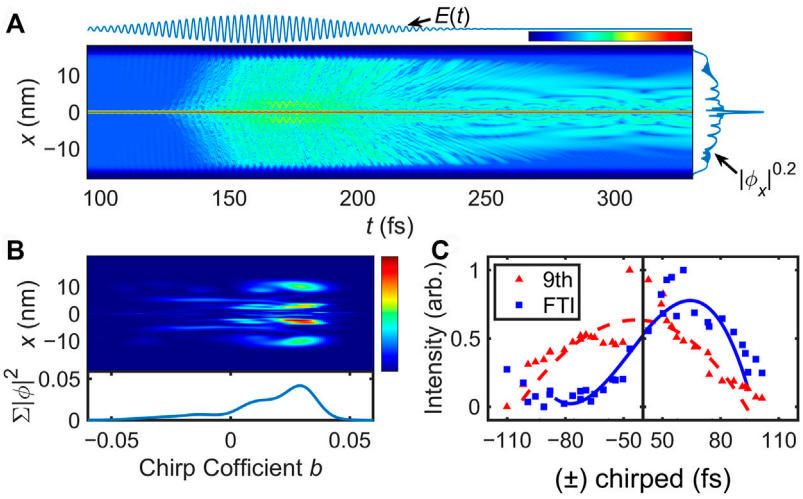

FIGURE 4
(A) Temporal population evolution of a krypton atom exposed to external laser fields in the strong-field tunnelling regime. The top curve is the time domain shape of the laser electric field, and the curve on the right is the populations of krypton when driving laser is off. **(B)** One-dimensional populations of excited states surviving in different chirped intense laser field. The horizontal axis of the coordinate is the chirp coefficient *b* in Eq. 1. The curve below shows the integral of populations under different chirp coefficient *b*. **(C)** Chirp dependence of the harmonic near threshold (9th, red triangle) and the FTI emission (blue square) observed in experiments. The abscissa is the pulse duration of driven laser which represent different chirps.

be captured to the ground state and lead to harmonic generation. As for FTI progress, we focus on the trajectories of the released electron whose wave packet remains near the parent ion with zero kinetic energy after the laser field. Therefore, only electrons ionized at the appropriate ionization time can recombine to the Rydberg states eventually. The electron that tunnels out near the peak of the laser electric field during every half optical cycle has near-zero kinetic energy after the driving pulse, which is also located near the parent ion and has a high-probability of recombination to the Rydberg states. The chirp dependence of the FTI emission in Figure 2 implies that the probability is also chirp-dependent, causes the temporal shape of driven laser to differ with different chirps, which affect the ionization time of electrons that eventually bind to the Rydberg states. Therefore, the transition probability to the Rydberg state can be expressed as the superposition of ionization rate at the ionization time at every half optical cycle. To simplify the analysis, we assume that Kr atoms are in the ground state before the driving laser (Gaussian beam). The field of linearly polarized pulse with a Gaussian amplitude can be expressed as

$$E(t) = e^{-2\ln 2\times\left(\frac{t}{\tau}\right)^2} \times \sqrt{\frac{2I_0}{c\epsilon_0}}\cos\left[\omega_0\left(1+b\frac{t}{\tau}\right)\times t\right] \qquad (1)$$

where b is the chirp coefficient; $I_0 = 6\times10^{13}\mathrm{Wcm}^{-2}$ and ω_0 are the peak intensity and frequency of driving laser, respectively; $\tau = 53fs$ is the FWHM duration; and ϵ_0 is the vacuum dielectric constant. The parameters of simulation are those when FTI signals can be evidently observed experimentally. The parameter b is used to change the laser chirp. The ionized electron oscillates in the intense laser field after ionization whose trajectory is significantly dependent on the ionization time.

We verify this explanation by solving the 1D TDSE. The soft-core Coulomb potential is given as $V(x) = -1/\sqrt{1.873+x^2}$, the constant 1.873 is used for the ionization potential (I_p = 0.5147 *a.u.*) of a Kr atom. The Schrödinger equation in *a.u.* is

$$i\frac{\partial}{\partial t}\psi = \left[-\frac{1}{2}\frac{\partial^2}{\partial x^2} + V(x) - x\cdot E(t)\right]\psi \qquad (2)$$

where ψ is the wavefunction. The half-length of the absorbing boundary R_{abs} = 15.9 nm is sufficiently wide to reveal component of the high-lying Rydberg states. Figure 4A shows the temporal evolution of the ground-state krypton atomic populations. The evolution of the wavefunction is shown by $|\psi|^{0.2}$, where the value of 0.2 is taken for visualization. It can be seen that the ground state evolves into the superposition of the ground state and excited states when the driving laser is turned off. There is a notable electron population in the vicinity of the ion (±10 nm) where it is overlapped with the Rydberg states. Apparently, some of the electrons are released from the parent ion during the laser field and then are captured to the Rydberg states, which is consistent with FTI as discussed in the previous work [18].

The progress of FID [30] suggests that the intensity of FID radiation is related to populations of excited states, which is the high-lying Rydberg states in our study. Previous works have shown

that neutrally excited atoms can survive intense laser fields for a long time [20, 29], suggesting that it is possible to accumulate sufficient excited state populations to generate FID radiation under appropriate laser conditions. For qualitative representation, we calculate the one-dimensional population of the first excited state with differently chirped pulses. The chirp coefficient b (Eq. 1) varies in the range of [−0.06, 0.06], which is similar to experimental conditions. Figure 4B displays one-dimensional populations of the first excited state under action of laser with different chirp coefficient b; the curve below displays the integrations of populations under different laser chirps which shows the asymmetric dependence of populations on chirps of driven laser. Our results show that a higher population survived in the positively chirped driving laser than the negative chirped laser. The excited state population at chirp coefficient b = 0.03 is about 5 times that of the unchirped laser field and 10 times that of b = −0.03 laser field. The final position of tunnel-out electron is ~2.4 nm or ~10.0 nm away from the parent ion where it is overlapped spatially with the Rydberg states. To confirm the assumption of FID radiation, we compared the chirp dependences of population and experimentally measured the FTI emission. As seen in Figure 4C, normalized intensity of the harmonic generation near threshold (9th, red triangle) indicates a higher efficiency using chirp-free laser, while the FTI emission from the level $4s^2 4p^5 ({}^2P^o_{3/2})11s$ (blue square) is significantly enhanced with small positive chirped lasers, showing the same asymmetry changing with chirp to populations in Figure 4B. The consistency of the calculated population and experimentally measured FTI emission suggests that radiation comes from the FID progress of long-lifetime excited states. In other words, the FTI process can be controlled by adjusting the temporal chirp of a driving laser pulse, including the yield of Rydberg atoms and FID radiation. Although the strong field approximation model could reproduce the FTI emission well, there are still many limitations. First, the effect of chirp is associated with the coefficient b; however, the actual laser pulse duration changes with the chirp. The model does not take into account the possible effect of pulse duration. Second, the recombination process of different excited states was not considered. The model can be improved if different excited states and their phase relation were considered.

4 Conclusion

To conclude, in this work we have investigated the enhanced coherent EUV emission from Rydberg atoms. The emission can be generated using a properly and positively chirped driving laser, under which the excited state population is higher than that of the chirp-free or the negative chirped laser. We have achieved the control of the emission intensity by adjusting the temporal chirp of driving laser. By scanning the chirp, we can identify harmonic spectra drifting at wavelength axis and the emission from the Kr level. In addition, the coherent below-threshold FTI emission we observed has a small divergence which is good for EUV light source applications. These findings suggest a possible support to the progress of extreme-ultraviolet emission summarized as four steps: ionization, oscillation in light field, captured to excited states or autoionizing state, and emission of photon. These results enrich the study of atomic spectroscopy and also give some new ideas with the control of extreme-ultraviolet source.

Data availability statement

The raw data supporting the conclusion of this article will be made available by the authors, without undue reservation.

Author contributions

CY contributed to conceptualization, methodology, validation, formal analysis, investigation, data curation, writing—original draft, and visualization. ZL and FY contributed to validation and investigation. XG contributed to resources. YZ and ZZ contributed to conceptualization, methodology, conceptualization, writing—review and editing, supervision, project administration, and funding acquisition. RL contributed to funding acquisition. All authors contributed to the manuscript revision, read, and approved the submitted version.

Funding

This work is supported by the National Natural Science Foundation of China (Grants No. 91950203 and No. 11874374) and the Strategic Priority Research Program of the Chinese Academy of Sciences (Grant No. XDB16).

Conflict of interest

The authors declare that the research was conducted in the absence of any commercial or financial relationships that could be construed as a potential conflict of interest.

Publisher's note

References

1. Mcpherson A, Gibson G, Jara H, Johann U, Luk TS, Mcintyre IA, et al. Studies of multiphoton production of vacuum ultraviolet-radiation in the rare-gases. *J Opt Soc Am B* (1987) 4:595–601. doi:10.1364/Josab.4.000595

2. Krause JL, Schafer KJ, Kulander KC. High-order harmonic generation from atoms and ions in the high intensity regime. *Phys Rev Lett* (1992) 68:3535–8. doi:10.1103/PhysRevLett.68.3535

3. Kulander KC, Schafer KJ, Krause JL. Theoretical model for intense field high-order harmonic generation in rare gases. *Laser Phys* (1993) 3:359–64.

4. Corkum PB. Plasma perspective on strong field multiphoton ionization. *Phys Rev Lett* (1993) 71:1994–7. doi:10.1103/PhysRevLett.71.1994

5. Zeng ZN, Cheng Y, Song XH, Li RX, Xu ZZ. Generation of an extreme ultraviolet supercontinuum in a two-color laser field. *Phys Rev Lett* (2007) 98:203901. doi:10.1103/PhysRevLett.98.203901

6. Zheng YH, Zeng ZN, Zou P, Zhang L, Li XF, Liu P, et al. Dynamic chirp control and pulse compression for attosecond high-order harmonic emission. *Phys Rev Lett* (2009) 103:043904. doi:10.1103/PhysRevLett.103.043904

7. Sansone G, Benedetti E, Calegari F, Vozzi C, Avaldi L, Flammini R, et al. Isolated single-cycle attosecond pulses. *Science* (2006) 314:443–6. doi:10.1126/science.1132838

8. Li J, Ren X, Yin Y, Zhao K, Chew A, Cheng Y, et al. 53-attosecond x-ray pulses reach the carbon k-edge. *Nat Commun* (2017) 8:186. doi:10.1038/s41467-017-00321-0

9. Gaumnitz T, Jain A, Pertot Y, Huppert M, Jordan I, Ardana-Lamas F, et al. Streaking of 43-attosecond soft-x-ray pulses generated by a passively cep-stable mid-infrared driver. *Opt Express* (2017) 25:27506–18. doi:10.1364/OE.25.027506

10. Chini M, Wang XW, Cheng Y, Wang H, Wu Y, Cunningham E, et al. Coherent phase-matched vuv generation by field-controlled bound states. *Nat Photon* (2014) 8:437–41. doi:10.1038/nphoton.2014.83

11. Xiong WH, Geng JW, Tang JY, Peng LY, Gong Q. Mechanisms of below-threshold harmonic generation in atoms. *Phys Rev Lett* (2014) 112:233001. doi:10.1103/PhysRevLett.112.233001

12. Strelkov V. Role of autoionizing state in resonant high-order harmonic generation and attosecond pulse production. *Phys Rev Lett* (2010) 104:123901. doi:10.1103/PhysRevLett.104.123901

13. Xiong WH, Peng LY, Gong QH. Recent progress of below-threshold harmonic generation. *J Phys B: Mol Opt Phys* (2017) 50:032001. doi:10.1088/1361-6455/50/3/032001

14. Yost DC, Schibli TR, Ye J, Tate JL, Hostetter J, Gaarde MB, et al. Vacuum-ultraviolet frequency combs from below-threshold harmonics. *Nat Phys* (2009) 5:815–20. doi:10.1038/Nphys1398

15. Kim S, Jin JH, Kim YJ, Park IY, Kim Y, Kim SW. High-harmonic generation by resonant plasmon field enhancement. *Nature* (2008) 453:757–60. doi:10.1038/nature07012

16. Power EP, March AM, Catoire F, Sistrunk E, Krushelnick K, Agostini P, et al. Xfrog phase measurement of threshold harmonics in a keldysh-scaled system. *Nat Photon* (2010) 4:352–6. doi:10.1038/Nphoton.2010.38

17. Linden S, Giessen H, Kuhl J. Xfrog a new method for amplitude and phase characterization of weak ultrashort pulses. *Phys Stat Sol* (1998) 206:119–24. doi:10.1002/(sici)1521-3951(199803)206:1<119::aid-pssb119>3.0.co;2-x

18. Yun H, Mun JH, Hwang SI, Park SB, Ivanov IA, Nam CH, et al. Coherent extreme-ultraviolet emission generated through frustrated tunnelling ionization. *Nat Photon* (2018) 12:620–4. doi:10.1038/s41566-018-0255-8

19. Mun JH, Ivanov IA, Yun H, Kim KT. Strong-field-approximation model for coherent extreme-ultraviolet emission generated through frustrated tunneling ionization. *Phys Rev A (Coll Park)* (2018) 98:063429. doi:10.1103/PhysRevA.98.063429

20. Nubbemeyer T, Gorling K, Saenz A, Eichmann U, Sandner W. Strong-field tunneling without ionization. *Phys Rev Lett* (2008) 101:233001. doi:10.1103/PhysRevLett.101.233001

21. Liu H, Liu Y, Fu L, Xin G, Ye D, Liu J, et al. Low yield of near-zero-momentum electrons and partial atomic stabilization in strong-field tunneling ionization. *Phys Rev Lett* (2012) 109:093001. doi:10.1103/PhysRevLett.109.093001

22. Popruzhenko SV. Quantum theory of strong-field frustrated tunneling. *J Phys B: Mol Opt Phys* (2018) 51:014002. doi:10.1088/1361-6455/aa948b

23. von Veltheim A, Manschwetus B, Quan W, Borchers B, Steinmeyer G, Rottke H, et al. Frustrated tunnel ionization of noble gas dimers with rydberg-electron shakeoff by electron charge oscillation. *Phys Rev Lett* (2013) 110:023001. doi:10.1103/PhysRevLett.110.023001

24. Popruzhenko SV, Lomonosova TA. Frustrated ionization of atoms in the multiphoton regime. *Laser Phys Lett* (2021) 18:015301. doi:10.1088/1612-202X/abca43

25. Day JO, Brekke E, Walker TG. Dynamics of low-density ultracold rydberg gases. *Phys Rev A (Coll Park)* (2008) 77:052712. doi:10.1103/PhysRevA.77.052712

26. Landsman AS, Pfeiffer AN, Hofmann C, Smolarski M, Cirelli C, Keller U. Rydberg state creation by tunnel ionization. *New J Phys* (2013) 15:013001. doi:10.1088/1367-2630/15/1/013001

27. Piraux B, Mota-Furtado F, O'Mahony PF, Galstyan A, Popov YV. Excitation of rydberg wave packets in the tunneling regime. *Phys Rev A (Coll Park)* (2017) 96:043403. doi:10.1103/PhysRevA.96.043403

28. Li Q, Tong XM, Morishita T, Jin C, Wei H, Lin CD. Rydberg states in the strong field ionization of hydrogen by 800, 1200 and 1600 nm lasers. *J Phys B: Mol Opt Phys* (2014) 47:204019. doi:10.1088/0953-4075/47/20/204019

29. Bing-Bing W, Xiao-Feng L, Pan-Ming F, Jing C, Jie L. Coulomb potential recapture effect in above-barrier ionization in laser pulses. *Chin Phys Lett* (2006) 23:2729–32. doi:10.1088/0256-307X/23/10/029

30. Bengtsson S, Larsen EW, Kroon D, Camp S, Miranda M, Arnold CL, et al. Space-time control of free induction decay in the extreme ultraviolet. *Nat Photon* (2017) 11:252–8. doi:10.1038/Nphoton.2017.30

31. Beaulieu S, Bloch E, Barreau L, Comby A, Descamps D, Geneaux R, et al. Phase-resolved two-dimensional spectroscopy of electronic wave packets by laser-induced xuv free induction decay. *Phys Rev A (Coll Park)* (2017) 95:041401. doi:10.1103/PhysRevA.95.041401

32. Beaulieu S, Camp S, Descamps D, Comby A, Wanie V, Petit S, et al. Role of excited states in high-order harmonic generation. *Phys Rev Lett* (2016) 117:203001. doi:10.1103/PhysRevLett.117.203001

33. Bloch F, Hansen WW, Packard M. Nuclear induction. *Phys Rev* (1946) 69:127. doi:10.1103/PhysRev.69.127

34. Wagner C, Harned N. Lithography gets extreme. *Nat Photon* (2010) 4:24–6. doi:10.1038/nphoton.2009.251

35. Baksh PD, Odstrcil M, Kim HS, Boden SA, Frey JG, Brocklesby WS. Wide-field broadband extreme ultraviolet transmission ptychography using a high-harmonic source. *Opt Lett* (2016) 41:1317–20. doi:10.1364/Ol.41.001317

36. Kramida A, Yu RalchenkoReader JNIST ASD Team. [Dataset]. *NIST atomic spectra Database (ver. 5.8)*. [Online]. Gaithersburg, MD: National Institute of Standards and Technology (2020). Available: https://physics.nist.gov/asd (Accessed on July 1, 2021).

37. Lee DG, Kim JH, Hong KH, Nam CH. Coherent control of high-order harmonics with chirped femtosecond laser pulses. *Phys Rev Lett* (2001) 87:243902. doi:10.1103/PhysRevLett.87.243902

38. Milosevic DB. High-energy stimulated emission from plasma ablation pumped by resonant high-order harmonic generation. *J Phys B: Mol Opt Phys* (2007) 40:3367–76. doi:10.1088/0953-4075/40/17/005

39. Lindle DW, Ferrett TA, Becker U, Kobrin PH, Truesdale CM, Kerkhoff HG, et al. Photoionization of helium above theHe+(n=2) threshold: Autoionization and final-state symmetry. *Phys Rev A (Coll Park)* (1985) 31:714–26. doi:10.1103/physreva.31.714

frontiers | Frontiers in Physics

TYPE Original Research
PUBLISHED 07 November 2022
DOI 10.3389/fphy.2022.974500

OPEN ACCESS

EDITED BY
Weifeng Yang,
Hainan University, China

REVIEWED BY
Hongchuan Du,
Lanzhou University, China
Song-Feng Zhao,
Northwest Normal University, China

*CORRESPONDENCE
Feng-Zheng Zhu,
bluelight01@126.com
Li-Guang Jiao,
lgjiao@jlu.edu.cn
Aihua Liu,
aihualiu@jlu.edu.cn

†These authors have contributed equally to this work

SPECIALTY SECTION
This article was submitted to Optics and Photonics,
a section of the journal
Frontiers in Physics

RECEIVED 21 June 2022
ACCEPTED 10 October 2022
PUBLISHED 07 November 2022

CITATION
Wang J, Li G-L, Liu X, Zhu F-Z, Jiao L-G and Liu A (2022), Photoelectron momentum distribution of hydrogen atoms in a superintense ultrashort high-frequency pulse.
Front. Phys. 10:974500.
doi: 10.3389/fphy.2022.974500

Photoelectron momentum distribution of hydrogen atoms in a superintense ultrashort high-frequency pulse

Jun Wang[1†], Gen-Liang Li[1†], Xiaoyu Liu[1], Feng-Zheng Zhu[2*], Li-Guang Jiao[3*] and Aihua Liu[1*]

[1]Institute of Atomic and Molecular Physics, Jilin University, Changchun, China, [2]School of Mathematics and Physics, Hubei Polytechnic University, Huangshi Hubei, China, [3]College of Physics, Jilin University, Changchun, China

We use a numerically solved time-dependent Schrödinger equation for calculating the photoelectron momentum distribution of ground-state hydrogen atoms in the presence of superintense ultrashort high-frequency pulses. It is demonstrated that the dynamic interference effect within a superintense XUV laser beam has the ability to significantly alter the photoelectron momentum distribution. In our work, a clearly visible dynamic interference pattern is observed when hydrogen atoms are exposed to a superintense circularly polarized laser pulse with a photon energy of $\hbar\omega$ = 53.605 eV, which has previously been found for linearly polarized pulses or the weakly bounded model H^- system for circularly polarized pulses. Angular-distorted interference arises for linear superintense XUV pulses of similar intensity. The significant differences in photoelectron momentum distributions that have been seen by linearly and circularly polarized XUV pulses are caused by the Coulomb rescattering phenomenon.

KEYWORDS

strong field, ultrafast laser, superintense laser, attosecond science, momentum distribution

1 Introduction

On account of the fast improvement of strong-pulsed-laser innovation, people are now focusing on a new research region, which uses laser pulses to explore the light and matter interaction in atoms and molecules (Krausz and Ivanov [1]; Sansone et al. [2]). The first characteristic phenomenon of the intense laser-atom interaction, above-threshold ionization (ATI), has been experimentally observed and extensively studied. Free-electron laser (FEL) light sources, such as the Extreme Light Infrastructure (ELI) Kühn et al. [3], have been designed in recent years to generate superintense laser pulses of the order of 10^{20} W/cm^2 or stronger. Numerous new physical sciences and incredible phenomena are expected with such extreme intensity Kühn et al. [3] and high frequency Young et al. [4]. When the laser intensity surpasses 3.51×10^{16} W/cm^2 (corresponding to 1 atomic unit of laser intensity), the ionization process is stifled until the laser electric field is diminished to

a lower intensity, which is the supposed atomic stabilization effect Eberly and Kulander [5].

In an intense polarized linearly high-frequency laser field, the atoms would be at the same ac Stark shift energy level Sussman [6] at a specific time during the rising edge and falling edge of the laser pulse. Thus, the photoelectrons that are delivered by these atoms have frequencies of the same values. Simultaneously, the phase differences between these wave packets that are produced at various moments (say the time $-t_1$ and t_1 as in the study by Jiang and Burgdörfer [7]) under the effect of atomic stabilization Toyota et al. [8]; Baghery et al. [9]; Jiang and Burgdörfer [7]; Demekhin and Cederbaum [10,11] could remain stable. Then, dynamic interference will appear when the two-electron wave packets superimpose, and the photoelectron spectrum will show an obvious multifringe structure in its ATI peaks Jiang and Burgdörfer [7]; Guo et al. [12].

Theoretically, a simplified model has anticipated the dynamic interference from hydrogen atoms in the *ground state* Demekhin and Cederbaum [10]; Baghery et al. [9]. Unfortunately, there are minor faults or typos in their models Demekhin et al. [13], and Demekhin and Cederbaum [10] and Baghery et al. [9] gave contradicting conclusions. However, the time-dependent Schrödinger equation (TDSE) fully numerical solution corroborated some predictions of dynamic interference in photoemission by powerful extreme ultraviolet (XUV) linearly polarized pulses Guo et al. [12]; Jiang and Burgdörfer [7]; Wang et al. [14]; Wang and Liu [15].

Scientific research and applications utilize the circularly polarized field in contrast to the linearly polarized field Fu et al. [16]; Bauer and Rzazewski [17]; Toyota et al. [18]. In a linearly polarized field, an electron can get back to its core numerous times; yet in a circularly polarized field, there is no returning event. Such discrepancies can fundamentally affect the electronic dynamics of atoms. Aside from some particular elements, for instance, magnesium Ben et al. [19]; Wang et al. [20], there will be no nonsequential double ionization, and it is difficult to see high harmonic generations with atoms in a circularly polarized field Christov et al. [21].

Despite the fact that the energy spectrum and momentum distribution of photoelectrons produced in strong laser fields with arbitrary polarization have already been documented, such as H^- with model potential Toyota et al. [18], the weakly bounded H^- system (the model H^- has an $I_p = 0.76$ eV, whose $I_p \leq 1$ eV.) differs significantly from the tightly bounded H atom system (H atom has an $I_p = 13.6$ eV, whose $I_p > 10$ eV). With the same laser intensity (e.g., $10^{17} W/cm^2$) and potential curve, the dynamic interference is readily visible in the weakly bounded excited states ($n \geq 2$, $|E_n| \leq 3.4$ eV $\ll 10$ eV) of hydrogen atoms Baghery et al. [9], but it is hardly ever seen in the tightly bounded ground state Baghery et al. [9]; Jiang and Burgdörfer [7].

The current study has looked closely at how a circularly polarized pulse affects dynamic interference and how it differs from a linearly polarized pulse. The explicit demonstration of dynamic interference in the basic photoionization phenomena uses the hydrogen atom, which is unaffected by multiple-electron correlation.

The format of this article is as follows. The theoretical foundation for investigating the ionization of ground-state hydrogen atoms is described in the second part. The impact of different circularly polarized laser pulse strengths on the dynamic interference of photoelectron spectra and momentum distributions is covered in Section 3. The conclusion is found in Section 4. Unless stated differently, the atomic units (a.u.) $\hbar = m = e = 1$ are used throughout this article.

2 Theory and models

2.1 2D time-dependent Schrödinger equation and 3D time-dependent Schrödinger equation

To describe the ionization of ground-state hydrogen atoms, we will solve the TDSE precisely. The hydrogen atoms' TDSE when exposed to a laser field is as follows:

$$i\frac{\partial \psi(\boldsymbol{r},t)}{\partial t} = H\psi(\boldsymbol{r},t). \tag{1}$$

The hydrogen atom in the circularly polarized laser field is investigated in the current work using the reduced two-dimensional (2D) TDSE. In the momentum distributions with laser intensity in the perturbation regime ($I_0 = 10^{12}$ W/cm^2) and stabilization regime ($I_0 = 10^{18}$ W/cm^2), respectively, we have compared the corresponding results of 2D TDSE with those of 3D TDSE Patchkovskii and Muller [22], as shown in Figure 1.

All of these findings demonstrate excellent agreement between the perturbation (weak field) and stabilization (strong field) regimes of the 2D (a, c) and 3D (b, d) simulations. Both 2D (Figure 1C) and 3D (Figure 1D) simulations of the stabilization regime show the interference fringes, which have been previously proven Jiang and Burgdörfer [7]; Wang et al. [14].

The 2D TDSE with dipole approximation can be given by:

$$i\frac{\partial \psi(x,y;t)}{\partial t} = H\psi(x,y;t), \tag{2}$$

whose hamiltonian can be written as

$$H = T + V(x,y) + xE_x(t) + yE_y(t), \tag{3}$$

where the kinetic energy operator $T = \frac{p_x^2+p_y^2}{2}$ with $p_i = -i\partial/\partial_i$ (i = x, y) and potential $V(x,y) = -1/\sqrt{x^2+y^2+a}$ is the soft-core potential function of hydrogen atoms, and $a = 0.64$ is the soft-core parameter to avoid the singularity at origin $r = 0$ and to obtain the correct ground-state energy $E_g = -0.5$. In our simulation, the polarized driving laser field is denoted by the variables $E_x(t)$ and $E_y(t)$ for the x-axis and y-axis, respectively. We can write the total time-dependent potential as:

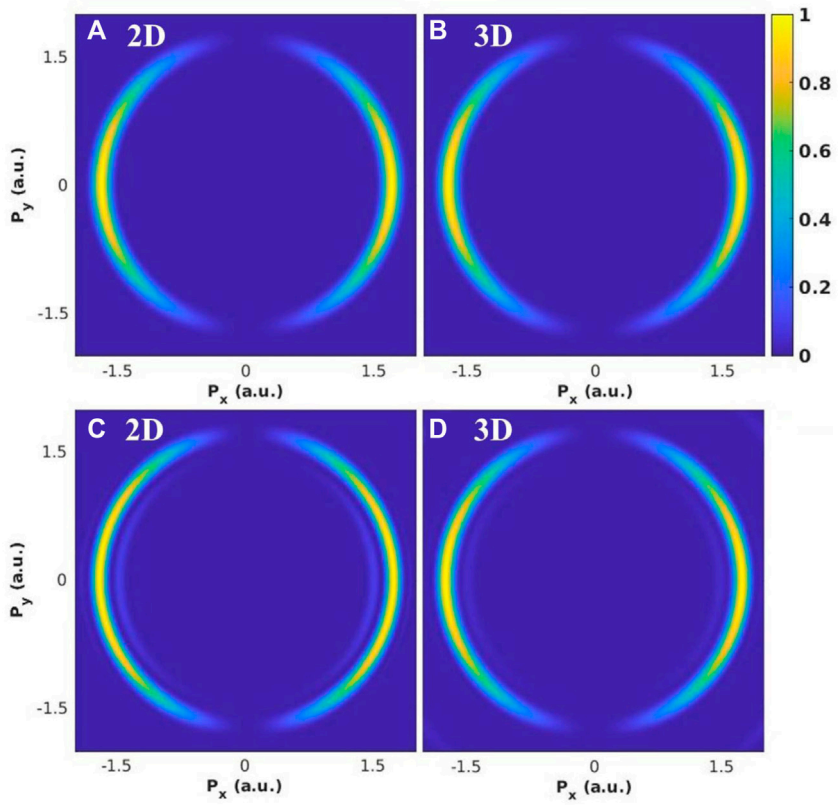

FIGURE 1
(Color online) Numerical results are compared from solving two- and three-dimensional TDSEs. We take the laser parameters as follow: carrier frequency $\hbar\omega_0$ = 53.605 eV and peak intensities are **(A,B)** $I_0 = 10^{12}$ W/cm^2, and **(C,D)** $I_0 = 10^{18}$ W/cm^2, corresponding to the perturbation regime and the stabilization regime. Laser pulse duration τ = 1.5 fs.

$$U(t) = V(x, y) + xE_x(t) + yE_y(t). \tag{4}$$

We use the splitting operator combined with the fast Fourier transform (FFT) method to solve the TDSE and obtain the initial wave packet by the imaginary time propagation method. The wave function time propagation from t to $t + \Delta t$ can be expressed as

$$\psi(t + \Delta t) \approx e^{-iT\Delta t/2} e^{-iU(t+\Delta t/t)\Delta t} e^{-iT\Delta t/2} \psi(t). \tag{5}$$

The box sizes are up to 1200 for each dimension, and the step size of time propagation Δt is 0.01. A mask function of the form $\cos^{1/8}$ was employed to avoid spurious reflections from the boundaries. When the wave function completes the final step of time propagation, we record the ionization part as $[1 - M(r)]\psi(x, y; t_f)$. Here, $\psi(x, y; t_f)$ is the wave function at the last time step. The function expression $M(r)$ for the absorption mask is

$$M(r) = \begin{cases} 1, & r \le r_b; \\ \exp[-\alpha(r - r_b)], & r > r_b, \end{cases} \tag{6}$$

where $\alpha = 1$, $r = \sqrt{(x^2 + y^2)}$, and the $r_b = 30$ (r_b corresponds to the bounded wave function boundary) He et al. [23]. Then, using the fast Fourier transform of the outer wave function, we obtained the photoelectron momentum distribution. Moreover,20 optical cycles make up the pulse duration, while 10 optical cycles can relax due to free field propagation.

2.2 Perturbative superposition model

The laser field is polarized in the xy-plane, as shown in Eq. 4. The associated electric field information of laser pulses is schematically shown in Figure 2. The blue curve represents the electric field of the circularly polarized laser pulse $E(t)$, while the red and golden curves, respectively, depict its projections on the x-axis and y-axis. To put it another way, the $E(t)$ can be split into the two linearly polarized pulses $E_x(t)$ and $E_y(t)$:

$$\begin{aligned} \mathbf{E}(t) &= E_x(t)\hat{e}_x + E_y(t)\hat{e}_y \\ &= f(t)\left[E_x^0 \cos(\omega t)\hat{e}_x + E_y^0 \cos(\omega t + \phi)\hat{e}_y\right], \end{aligned} \tag{7}$$

where $\hat{e}_{x/y}$ is the polarization direction and the ϕ is the relative phase of y-component. When $\phi = \pm\pi/2$ and $E_x^0 = E_y^0$, we obtain

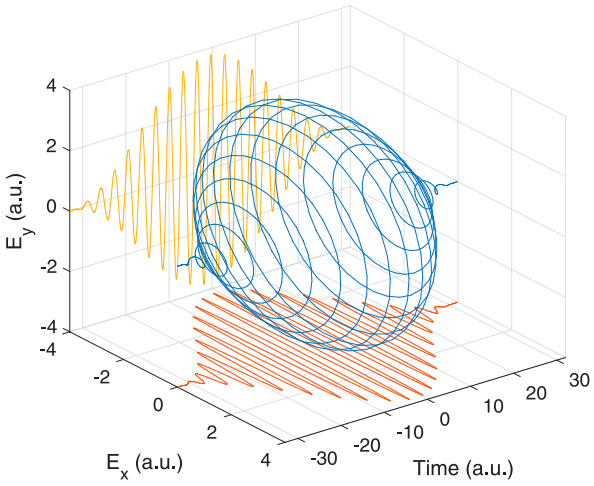

FIGURE 2
(Color online) Schematic electric field of circularly polarized laser pulse $E(t)$ (blue curve) and its projections on the x-axis (red curve) and y-axis (golden curve). In this schematics, we take the laser parameter as follows: carrier frequency $\hbar\omega_0$ = 53.605 eV, peak intensity $I_0 = 10^{18}$ W/cm^2, and pulse duration τ = 1.5 fs.

circular pulses, when either E_x^0 or E_y^0 vanishes, we obtain linear pulses. The pulse profile $f(t)$ is the sine-squared profile, and ω is the central frequency of the laser pulse.

The first-order transition amplitudes (in the electric dipole approximation) from an initial bound state ψ_0 is given by Pronin et al. [24]

$$A_1 = \langle \psi_{\mathbf{p}} | \mathbf{E} \cdot \mathbf{r} | \psi_0 \rangle, \tag{8}$$

Here, $\psi_{\mathbf{p}}$ describes a final continuum state with electron momentum $\mathbf{p}$ and energy $E_k = p^2/2$.

On substituting the electric field $\mathbf{E}$ of Eq. 8 with Eq. 7, Eq. 8 is rewritten as Yuan et al. [25]

$$A_1 = \langle \psi_{\mathbf{p}} | E_x x + E_y y | \psi_0 \rangle = A_1^x(\mathbf{p}) + A_1^y(\mathbf{p}), \tag{9}$$

where

$$A_1^x(\mathbf{p}) = \langle \psi_{\mathbf{p}} | E_x x | \psi_0 \rangle = E_x \langle \psi_{\mathbf{p}} | x | \psi_0 \rangle, \tag{10}$$

$$A_1^y(\mathbf{p}) = \langle \psi_{\mathbf{p}} | E_y y | \psi_0 \rangle = E_y \langle \psi_{\mathbf{p}} | y | \psi_0 \rangle. \tag{11}$$

which means that the total photoelectron momentum distribution $P(\mathbf{p})$ can be decomposed into two components which are related to the independent E_x and E_y, respectively. The interference terms vanish due to the $\pi/2$ phase between them Yuan et al. [25],

$$A_1^{(x,y)} = A_1^{(x)*} A_1^{(y)} + A_1^{(x)} A_1^{(y)*} \propto \cos(\phi). \tag{12}$$

For circularly polarized pulses, $\phi = \pm \pi/2$; thus, the interference term vanishes. Then, we have

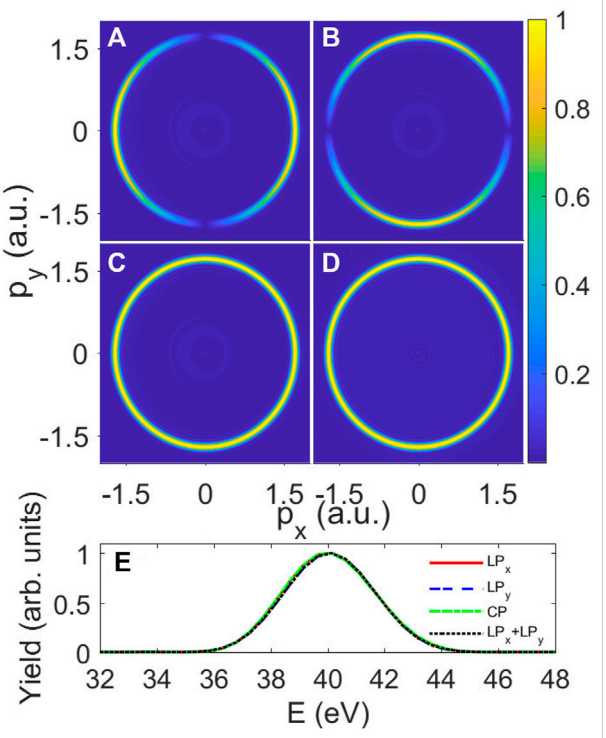

FIGURE 3
(Color online) Photoelectron momentum distribution of hydrogen atoms in the presence of laser pulse with τ_0 = 1.5 fs, carrier frequency $\hbar\omega_0$ = 53.605 eV, and the peak intensities I_0 = 10^{14} W/cm^2. Graphs **(A)** and **(B)** reveal the momentum distributions from the linear polarized x- and y-direction, respectively. Graph **(C)** shows the result from a circularly polarized laser pulse, while **(D)** is the momentum distribution from the superposition of **(A)** and **(B)** two perpendicular linearly polarized pulses. Panel **(E)** is the photoelectron spectra of **(A)** the red solid line, **(B)** the blue dashed line, **(C)** the green dashed–dotted line, and **(D)** the black dotted line.

$$P(\mathbf{p}) = |A_1|^2 = |A_1^x(\mathbf{p})|^2 + |A_1^y(\mathbf{p})|^2 = P_x(\mathbf{p}) + P_y(\mathbf{p}). \tag{13}$$

The following section of this article will examine how the aforementioned decomposition of the photoelectron momentum distribution is destructed when a sufficiently strong laser field is applied, even for this single-photon ionization.

The photoelectron momentum distribution of hydrogen atoms exposed to a laser pulse with a peak intensity of 10^{14} W/cm^2 is shown in Figure 3. Since atomic stabilization does not take place in this situation with such a high laser frequency and low laser intensity, the dynamic interference effect cannot be observed Gavrila [26]. The photoelectron momentum distribution for hydrogen atoms subjected to the laser with polarization parallel to the x-axis is shown in Figure 3A. The electron momentum distribution is primarily in the x-direction since the laser is polarized along that path. This is an example of a single-photon ionization distribution using the dipole approximation Remetter et al. [27]. In Figure 3B, we

display the results for rotating the laser polarization direction to the y-axis (by adding a $\pi/2$ phase difference in the carrier of laser electric field): the photoelectron momentum distribution is again mainly in the laser polarization direction, y-direction. When the circularly polarized laser is utilized, as shown in Figure 3C, the momentum distribution only shows one ring. A similar distribution can be achieved in Figure 3D by superposing $\psi_x(\varepsilon)$ and $\psi_y(\varepsilon)$ coherently (or adding Figures 3A,B incoherently). The photoelectron energy spectra of the aforementioned four panels are shown in Figure 3E, and these four lines act coincidentally. It is well established, both theoretically and experimentally, that the ponderomotive energy is $U_p = E_0^2/4\omega^2 \approx 0.005$ eV for the parameters of the present laser field. The photoelectron spectra show an isolated Gaussian profile in Figure 3E for weak-field single-photon ionization, where the ionization process can be explained by the lowest-order perturbation theory (LOPT), and the profile has its peak at the energy $E = \hbar\omega - I_p - U_p \approx 40$ eV (I_p is the atomic binding energy).

In the LOPT, the single-photon ionization of hydrogen atoms from the ground state ($l = 0$ s-wave) by linearly polarized (say along the x-axis) laser pulses can be described by $H(1s) + h\nu \rightarrow \epsilon p$. The final p-state partial wave ($l = 1$) has the distribution $P_{\parallel}(\theta) \propto \cos^2\theta$, as shown in Figure 3A. If we rotate the laser polarized direction to the perpendicular direction (along the y-axis), the final momentum distribution is now $P_{\perp}(\theta) \propto \cos^2(\frac{\pi}{2} + \theta) = \sin^2\theta$. The photoelectron angular distribution of single-photon ionization by circularly polarized laser pulses is depicted in the superposition model mentioned earlier as $P_{cp}(\theta) \propto \cos^2\theta + \sin^2\theta = 1$, which is constant for all angles and is in excellent agreement with our TDSE simulation of Figure 3C.

3 Results and discussion

We explored the dynamic interference effect in the photoionization of ground-state hydrogen atoms in the presence of superintense linearly and circularly polarized laser pulses based on our *ab initio* numerical solution of the TDSE. We used the central carrier frequency of the laser pulse at 5 eV. The driving laser pulse has a pulse width of 20 optical cycles and a wavelength of 23 nm. These variables ensure the production of dynamic interference and prevent the complete depletion of the ground state population Guo et al. [12]; Jiang and Burgdörfer [7]; Wang et al. [14].

A straightforward temporal two-path interference scenario can explain this dynamic interference. When the instantaneous ac Stark shift of the initial state coincides at two different times, electron wave packets ejected on the rising and falling edges of the linearly polarized laser pulse can interfere with one another and reach the same final energy. They are temporally separated by a time interval of intense-field stabilization against

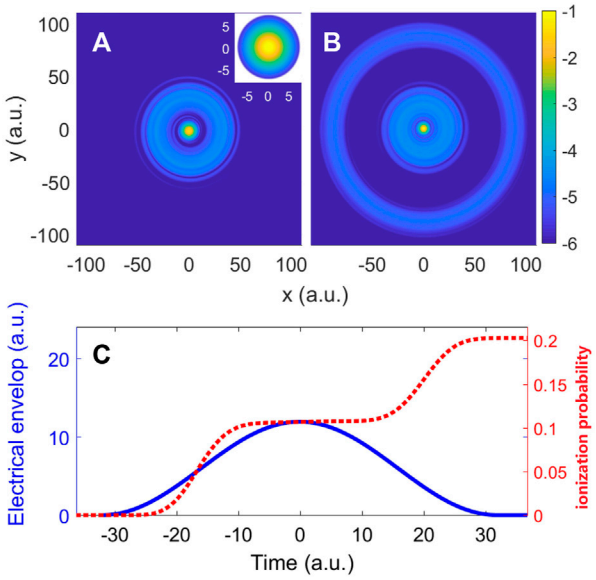

FIGURE 4
(Color online) Probability density of electron in the middle (t = 0) and at the end (t = 32) of a circularly polarized laser pulse in panels **(A,B)**. The initial ground state is plotted as the inset of panel **(A)**. Panel **(C)** is the time-dependent instantaneous ionization probability (red dashed line) of the ground state of hydrogen atoms in the presence of a laser pulse. The electrical envelope of the laser pulse and the blue solid line are plotted. All parameters are the same as those in Figure 3C, except the peak intensity $I_0 = 5 \times 10^{18}$ W/cm^2.

photoemission Eberly and Kulander [5]; Guo et al. [12]; Jiang and Burgdörfer [7].

In a circularly polarized field, the pulled-out laser-dressed electron cannot move back and forth by the driving laser field, and the atomic stabilization effect is anticipated to be more pronounced Protopapas et al. [28]. In Figure 4, we display the density of wave function in the middle (a) and at the end (b) of the laser pulse and the ionization rate of the ground-state hydrogen. We can see the inner and outer rings, which are probabilities of the photoelectron wave packets produced by the laser pulse in the rising and falling ramp of the pulse, from the spatial distribution for the probability of wave function displayed in Figure 4. Between the inner and outer rings, the vanishing gap indicates the atomic stabilization caused by the ultraintense laser field. Such an effect can be also shown in the ionization rate of the ground state, which has been displayed in Figure 4C. In the rising edge, the ionization rate starts to climb swiftly at $t \approx -22$, the ionization speed reaches its maximum at about $t \approx$ -18, and then the speed decreases. When the laser electric field profile is near its peak from $t = -10$ to 10, the ionization process is almost completely stopped. This time zone can be referred to as a stability zone. The gaps between inner and outer wave function rings in Figures 4A,B are produced due to the

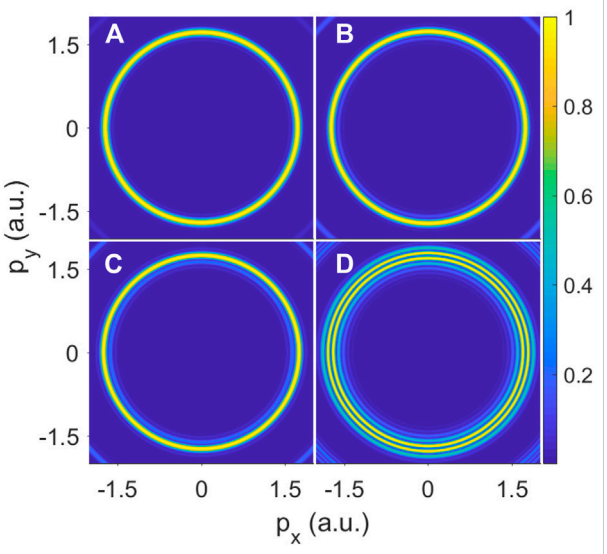

FIGURE 5
(Color online) Normalized photoelectron momentum distribution of hydrogen atoms in the presence of a circularly polarized laser pulse with different intensities: **(A)** 5×10^{16}, **(B)** 5×10^{17}, **(C)** 1×10^{18}, and **(D)** 5×10^{18} W/cm^2. The other parameters are the same as those in Figure 3C.

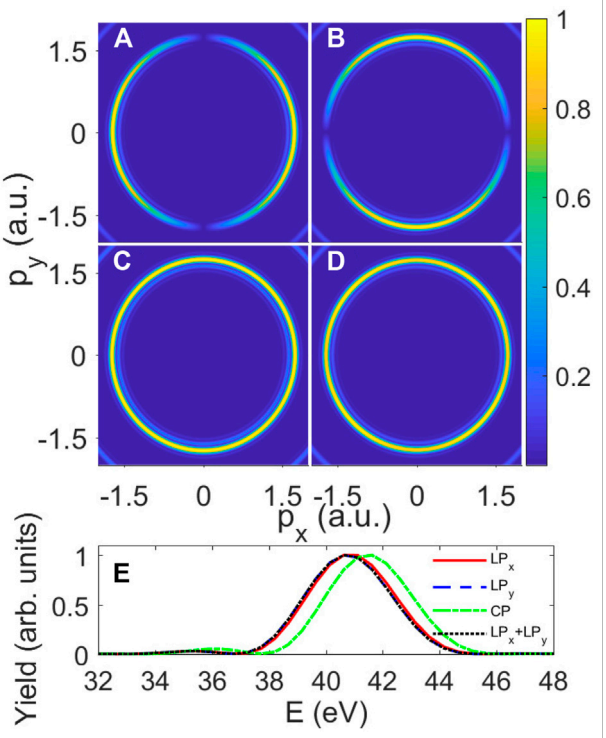

FIGURE 6
Normalized photoelectron momentum distribution of hydrogen atoms in the presence of a circularly polarized laser pulse with different polarization. **(A)** Linearly alone *x*, **(B)** Linearly alone *y*, **(C)** Circularly and **(D)** superposition of **(A,B)**. Curves in the panel **(E)** are the photoelectron spectra of **(A)** the red solid line, **(B)** the blue dashed line, **(C)** the green dashed–dotted line, and **(D)** the black dotted line. Laser intensity is I_0=1×10^{18} W/cm^2. The rest of laser parameters are the same as those in Figures 3A.

stabilization time zone. Then on the falling edge of the field profile, the ionization restarts, and finally ionization rate reaches the maximum at the end of a laser pulse.

The dynamic interference of photoelectrons can also be anticipated in the ionization induced by circularly polarized laser pulses since the ac Stark shift for energy in a circularly polarized field is similar to that in a linearly polarized field. Additionally, because the ac Stark shift is a cycle-average effect, when the peak intensities of linearly and circularly polarized pulses are equal (e.g., $I_0 = E_0^2$), the cycle-averaged intensity of the circularly polarized field ($\langle E \rangle = E_0$) is almost twice that of the linearly polarized field ($\langle E \rangle = 0.707E_0$). We could expect a circularly polarized field to produce a larger ac Stark shift of energy than a linearly polarized pulse. However, the ionization in the weak-intensity laser field does not exhibit the blue shift between the findings of the linearly and circularly polarized fields, as seen in Figure 5. As shown in Figure 5, we increase the laser intensity from 5×10^{16} to 5×10^{18}W/cm^2. In Figure 5A, there is no obvious modulation in the ATI peak of the momentum spectrum when the laser intensity is relatively low (with $I_0 = 5 \times 10^{16}$W/cm^2).

While the laser intensity is increased to 5×10^{17} or 1×10^{18} W/cm^2 as shown in Figures 5B,C, the multiring structure is found in its momentum distribution. On continuing to increase the laser intensity to 5×10^{18} W/cm^2, in Figure 5D, we can observe two bright rings and strongly modulated fringes in the first ATI peak.

Because of the stronger laser field, atomic stabilization occurs sooner and later, resulting in a longer time-delay gap between the wave packet produced on the rising edge of the laser pulse and the one launched on the falling edge of the laser pulse. Furthermore, additional interference fringes are produced as a result of increased phase difference accumulation between rising and falling wave packets due to increased laser intensity. This impact is noticeable in a linearly polarized field Jiang and Burgdörfer [7]. It also implies that the same result can be obtained by decomposing the circularly polarized field into two linearly polarized fields. We will explain how these superposition results coincide with real simulation results in the next two figures (Figures 6, 7).

When the peak intensity of the laser pulse is 1×10^{18} W/cm^2, Figure 6 shows the same consequence as Figure 3 illustrates. Although the spectrum is still almost symmetrical, the maximum is constantly moving to higher energies. It has a solitary Gaussian profile, with the peak located at an energy greater than 40 eV. Demekhin *et al.*

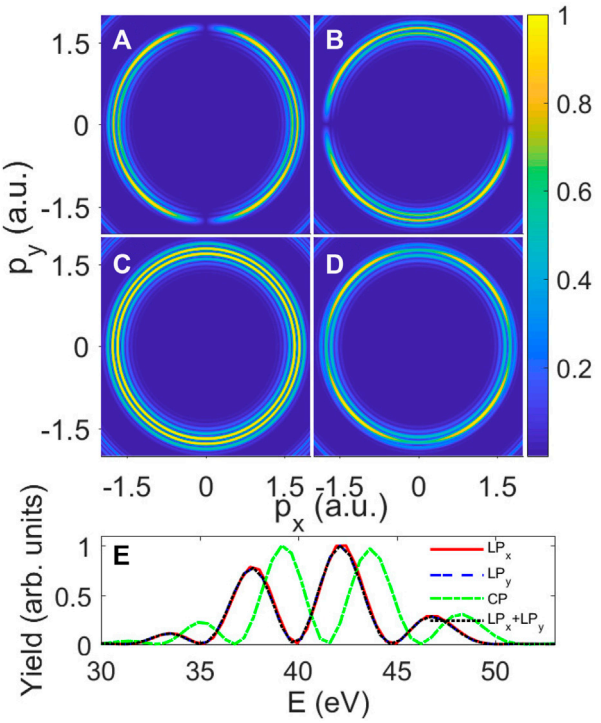

FIGURE 7
Normalized photoelectron momentum distribution of hydrogen atoms in the presence of a circularly polarized laser pulse with different polarization. **(A)** Linearly alone *x*, **(B)** Linearly alone *y*, **(C)** Circularly and **(D)** superposition of **(A,B)**. Curves in the panel **(E)** are the photoelectron spectra of **(A)** the red solid line, **(B)** the blue dashed line, **(C)** the green dashed–dotted line, and **(D)** the black dotted line. Laser intensity is I_0=5×10^{18} W/cm^2. The rest of laser parameters are the same as those in Figure 3A.

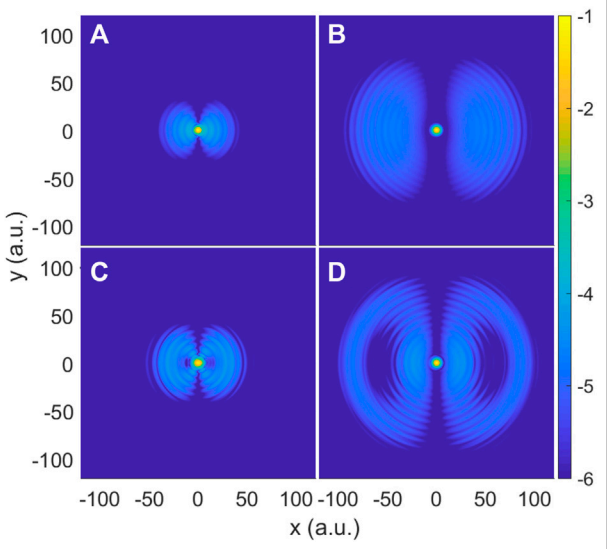

FIGURE 8
(Color online) Probability density of wave function in the middle and at the end of laser pulses. All parameters are the same as those in Figure 3A, except for the peak intensities: **(A,B)** I_0 = 5 × 10^{17} W/cm^2 and **(C,D)** I_0 = 5 × 10^{18} W/cm^2.

have discovered and clarified the underlying physics Demekhin and Cederbaum [10,11]. As usual, this shift follows the intensity envelope of the field Sussman [6]. The circularly polarized field can be decomposed into two perpendicular linearly polarized fields; therefore, each linearly polarized field takes half of the intensity of the circularly polarized field. Compared Figure 6C with Figure 6D, the first-order ATI ring in the circularly polarized laser can be qualitatively in agreement with a model for the superposition of ionization by two linearly polarized pulses, respectively.

As seen in Figure 6E, the peak of the green dashed–dotted curve has larger energy than the peaks of the other curves. This blue shift implies that the atom's ac Stark shift in a circularly polarized field is greater than the atom's ac Stark shift in a linearly polarized pulse. This similar blue shift was also discovered in the research by Liang et al. [29]. As the ac Stark shift for energy in a circularly polarized field is similar to that in the linearly polarized field, the dynamic interference of photoelectrons can also be expected in ionization caused by circularly polarized laser pulses. In addition, according to the fact that the ac Stark shift is a cycle-average effect, the cycle-averaged intensity of circularly polarized field ($\langle E\rangle = E_0$) is about twice that of the linearly polarized field ($\langle E\rangle = 0.707E_0$) when the peak intensities in linearly and circularly polarized pulses take the same value(e.g., $I_0 = E_0^2$). Therefore, we may anticipate that an energy Stark shift induced by a circularly polarized field will be greater than one caused by a linearly polarized pulse. In contrast to the ionization in weak intensity laser field, the blue shift between the data of a linearly polarized field and those of a circularly polarized field, as depicted in Figure 4, is hard to be detected. But as the laser intensity becomes strong (e.g., higher than $I_0 = 1 \times 10^{18}$ W/cm^2), such a blue shift is clearly visible.

When the peak intensity is increased to 5 × 10^{18}W/cm^2 in Figure 7, the multipeak structure of photoelectron momentum distribution and photoelectron spectra of hydrogen atoms exposed to laser pulses are seen clearly and intuitively. Higher laser intensities lead to a reduction in the energy difference between nearby interference fringes and an increase in the phase difference between the two electron wave packets, which results in significantly more dynamic interference fringes being recorded. In actuality, two elements are involved in the growing phase difference. First, the time interval between the emission timings t_1 and t_f increases because the atomic stabilizing effect in a high-intensity laser field has earlier beginning and later ending times than what is required for that in a low-intensity laser field. Second,

the phase difference increases with the increasing vector potential of the field when a stronger laser field is applied. This effect can be observed in the increased fringes both in momentum distribution shown in Figures 7A,B, and the photoelectron spectrum is shown in Figure 7E.

To further understand the origin of differences among the photoelectron spectra induced by a laser pulse with different kinds of polarization, in Figure 8 we plot the probability densities of the wave function at the middle and the end of the interaction with the laser field at low and high intensity, respectively. When the laser intensity is relatively low, as seen in the top panels (a,b), the probability density shows electrons leave the nuclear core in a dipole pattern. However, at high laser intensity, the electron distribution at the end of the pulse displays two hallows, which denotes an electron scattering from the nuclear center. In order to find the reason for the scattering process occurring at such high laser intensity, we compare the ponderomotive energies (U_p) of two cases. For $\hbar\omega = 53.605$ eV laser pulses, $U_p = 25$ eV for $I_0 = 5 \times 10^{17}$ W/cm^2 and $U_p = 250$ eV for $I_0 = 5 \times 10^{18}$ W/cm^2. In the low-intensity case, U_p is only 25 eV, which is less than the photoelectron energy $\hbar\omega = 40$ eV. Therefore, the laser-driven photoelectron is hard to hit the nuclear center. But in the high-intensity case, the U_p, which is up to 250 eV, is much higher than the first-order ATI photoelectron energy. As a result, the photoelectrons will scatter from the hydrogen atom's Coulomb center and follow and oscillate with the electric field. In other words, the nondipole distribution of photoelectron momentum for the hydrogen atoms in a superintense laser field is mostly caused by Coulomb scattering.

4 Conclusion

By solving the TDSE of ground-state hydrogen atoms in the presence of superintense laser pulses numerically, the photoelectron momentum distribution with dynamic interference effect is investigated. It has been demonstrated in this study that we can observe dynamic interference effects even in a tightly bounded system when there are circularly polarized pulses present in addition to the linearly polarized laser field. The coherent superposition of two perpendicular, linearly polarized laser pulses with an intensity no higher than $I_0 = 10^{18}$ W/cm^2 can provide a qualitative explanation for the dynamic interference pattern in momentum distribution caused by circularly polarized pulses. However, when the dynamic interference fringes are well separated, such as at $I_0 = 5 \times 10^{18}$ W/cm^2, the superposition of the LOPT momentum distribution by linearly polarized pulses and that by a circularly polarized field do not match. This discrepancy results from high-order corrections, including the Coulomb effect, during the photoemission process of linearly polarized laser pulses.

Data availability statement

The original contributions presented in the study are included in the article/Supplementary Material; further inquiries can be directed to the corresponding authors.

Author contributions

JW and G-LL contributed equally. AL, L-GJ, and F-ZZ designed the research; G-LL and JW performed time-dependent dynamics simulations; JW, XL, and AL contributed to the analysis of the data; and JW, G-LL, and AL wrote the manuscript.

Funding

This work is supported by the National Natural Science Foundation of China under Grants No.11774131, No.91850114, No.11627807, and No.11604119.

Acknowledgments

Part of the numerical simulation was performed on the high-performance computing cluster Tiger@IAMP at Jilin University.

Conflict of interest

The authors declare that the research was conducted in the absence of any commercial or financial relationships that could be construed as a potential conflict of interest.

Publisher's note

References

1. Krausz F, Ivanov M. Attosecond physics. *Rev Mod Phys* (2009) 81:163–234. doi:10.1103/RevModPhys.81.163

2. Sansone G, Benedetti E, Calegari F, Vozzi C, Avaldi L, Flammini R, et al. Isolated single-cycle attosecond pulses. *Science* (2006) 314:443–6. doi:10.1126/science.1132838

3. Kühn S, Dumergue M, Kahaly S, Mondal S, Füle M, Csizmadia T, et al. The ELI-ALPS facility: The next generation of attosecond sources. *J Phys B: Mol Opt Phys* (2017) 50:132002. doi:10.1088/1361-6455/aa6ee8

4. Young L, Ueda K, Gühr M, Bucksbaum PH, Simon M, Mukamel S, et al. Roadmap of ultrafast x-ray atomic and molecular physics. *J Phys B: Mol Opt Phys* (2018) 51:032003. doi:10.1088/1361-6455/aa9735

5. Eberly JH, Kulander KC. Atomic stabilization by super-intense lasers. *Science* (1993) 262:1229–33. doi:10.1126/science.262.5137.1229

6. Sussman BJ. Five ways to the nonresonant dynamic Stark effect. *Am J Phys* (2011) 79:477–84. doi:10.1119/1.3553018

7. Jiang W-C, Burgdörfer J. Dynamic interference as signature of atomic stabilization. *Opt Express* (2018) 26:19921–31. doi:10.1364/OE.26.019921

8. Toyota K, Tolstikhin OI, Morishita T, Watanabe S. Siegert-state expansion in the kramers-henneberger frame: Interference substructure of above-threshold ionization peaks in the stabilization regime. *Phys Rev A (Coll Park)* (2007) 76: 043418. doi:10.1103/PhysRevA.76.043418

9. Baghery M, Saalmann U, Rost JM. Essential conditions for dynamic interference. *Phys Rev Lett* (2017) 118:143202. doi:10.1103/PhysRevLett.118.143202

10. Demekhin PV, Cederbaum LS. Dynamic interference of photoelectrons produced by high-frequency laser pulses. *Phys Rev Lett* (2012) 108:253001. doi:10.1103/PhysRevLett.108.253001

11. Demekhin PV, Cederbaum LS. Ac Stark effect in the electronic continuum and its impact on the photoionization of atoms by coherent intense short high-frequency laser pulses. *Phys Rev A (Coll Park)* (2013) 88:043414. doi:10.1103/PhysRevA.88.043414

12. Guo J, Guo F, Chen J, Yang Y. Pulse duration effect on photoelectron spectrum of atom irradiated by strong high frequency laser. *Acta Phys Sin* (2018) 67: 073202. doi:10.7498/aps.67.20172440

13. Demekhin PV, Hochstuhl D, Cederbaum LS. Erratum: Photoionization of hydrogen atoms by coherent intense high-frequency short laser pulses: Direct propagation of electron wave packets on large spatial grids. *Phys Rev A (Coll Park)* (2017) 95:049903. doi:10.1103/PhysRevA.95.049903

14. Wang M-X, Liang H, Xiao X-R, Chen S-G, Jiang W-C, Peng L-Y. Nondipole effects in atomic dynamic interference. *Phys Rev A (Coll Park)* (2018) 98:023412. doi:10.1103/PhysRevA.98.023412

15. Wang N, Liu A. Interference effect of photoionization of hydrogen atoms by ultra-short and ultra-fast high-frequency chirped pulses. *Chin Phys B* (2019) 28: 083403. doi:10.1088/1674-1056/28/8/083403

16. Fu LB, Xin GG, Ye DF, Liu J. Recollision dynamics and phase diagram for nonsequential double ionization with circularly polarized laser fields. *Phys Rev Lett* (2012) 108:103601. doi:10.1103/PhysRevLett.108.103601

17. Bauer J, Rzazewski K. SFA applied to the nonsequential double ionization of the helium atom by a circularly polarized plane wave. *J Phys B: Mol Opt Phys* (1996) 29:3351–62. doi:10.1088/0953-4075/29/15/010

18. Toyota K, Tolstikhin OI, Morishita T, Watanabe S. Interference substructure of above-threshold ionization peaks in the stabilization regime. *Phys Rev A (Coll Park)* (2008) 78:033432. doi:10.1103/PhysRevA.78.033432

19. Ben S, Guo P-Y, Song K-L, Xu T-T, Yu W-W, Liu X-S. Nonsequential double ionization of mg from a doubly excited complex driven by circularly polarized laser field. *Opt Express* (2017) 25:1288–95. doi:10.1364/OE.25.001288

20. Wang X, Tian J, Eberly JH. Angular correlation in strong-field double ionization under circular polarization. *Phys Rev Lett* (2013) 110:073001. doi:10.1103/PhysRevLett.110.073001

21. Christov IP, Murnane MM, Kapteyn HC. High-harmonic generation of attosecond pulses in the "single-cycle" regime. *Phys Rev Lett* (1997) 78:1251–4. doi:10.1103/PhysRevLett.78.1251

22. Patchkovskii S, Muller H. Simple, accurate, and efficient implementation of 1-electron atomic time-dependent Schrödinger equation in spherical coordinates. *Comp Phys Commun* (2016) 199:153–69. doi:10.1016/j.cpc.2015.10.014

23. He P-L, Takemoto N, He F. Photoelectron momentum distributions of atomic and molecular systems in strong circularly or elliptically polarized laser fields. *Phys Rev A (Coll Park)* (2015) 91:063413. doi:10.1103/PhysRevA.91.063413

24. Pronin EA, Starace AF, Frolov MV, Manakov NL. Perturbation theory analysis of attosecond photoionization. *Phys Rev A (Coll Park)* (2009) 80: 063403. doi:10.1103/PhysRevA.80.063403

25. Yuan K-J, Chelkowski S, Bandrauk AD. Molecular photoelectron momentum distributions by intense orthogonally polarized attosecond ultraviolet laser pulses. *Chem Phys Lett* (2015) 638:173–8. doi:10.1016/j.cplett.2015.08.046

26. Gavrila M. Atomic stabilization in super-intense laser fields. *J Phys B: Mol Opt Phys* (2002) 35:R147–93. doi:10.1088/0953-4075/35/18/201

27. Remetter T, Johnsson P, Mauritsson J, Varjú K, Ni Y, Lépine F, et al. Attosecond electron wave packet interferometry. *Nat Phys* (2006) 2:323–6. doi:10.1038/nphys290

28. Protopapas M, Lappas DG, Knight PL. Strong field ionization in arbitrary laser polarizations. *Phys Rev Lett* (1997) 79:4550–3. doi:10.1103/PhysRevLett.79.4550

29. Liang J, Jiang W-C, Wang S, Li M, Zhou Y, Lu P. Atomic dynamic interference in intense linearly and circularly polarized xuv pulses. *J Phys B: Mol Opt Phys* (2020) 53:095601. doi:10.1088/1361-6455/ab7527

frontiers | Frontiers in Physics

TYPE Original Research
PUBLISHED 14 December 2022
DOI 10.3389/fphy.2022.1076671

OPEN ACCESS

EDITED BY
Weifeng Yang,
Hainan University, China

REVIEWED BY
Vaibhav Prabhudesai,
Tata Institute of Fundamental Research, India
Ladislau Nagy,
Babeş-Bolyai University, Romania

*CORRESPONDENCE
Xinhua Xie,
xinhua.xie@psi.ch

SPECIALTY SECTION
This article was submitted to Optics and Photonics, a section of the journal Frontiers in Physics

RECEIVED 21 October 2022
ACCEPTED 28 November 2022
PUBLISHED 14 December 2022

CITATION
Hu H, Hung Y, Larimian S, Erattupuzha S, Baltuška A, Zeiler M and Xie X (2022), Laser-induced valence electron excitation in acetylene.
Front. Phys. 10:1076671.
doi: 10.3389/fphy.2022.1076671

Laser-induced valence electron excitation in acetylene

Hongtao Hu[1], Yi Hung[1], Seyedreza Larimian[1], Sonia Erattupuzha[1], Andrius Baltuška[1], Markus Zeiler[1] and Xinhua Xie[2]*

[1]Photonics Institute, Technische Universität Wien, Vienna, Austria, [2]SwissFEL, Paul Scherrer Institute, Villigen, Switzerland

Strong-field induced valence electron excitation is a common process in strong field interaction with atoms and molecules. In the case of polyatomic molecules, the effects of ionization from low-lying molecular orbitals and nuclear dynamics during the interaction can play critical roles for electron excitation. In this work, we investigate the involved molecular orbitals in the electron excitation of singly ionized acetylene in a strong laser field using alignment dependence and laser intensity dependence. Additionally, the involved nuclear dynamics during the electron excitation are identified from the difference in the kinetic energy release and the angular distribution of laser-induced dissociation with different pulse durations and intensities. The laser intensity dependence clearly shows the relative strength change of two excitation pathways in the measured momentum and angle-resolved distributions.

KEYWORDS

electron excitation, strong laser field, molecular dissociation, nuclear dynamics, strong-field ionization, tunneling ionization

Introduction

The ultrafast dynamics of valence electrons play essential roles in the properties and reaction behaviors of atoms and molecules [1]. In general, the valence electron dynamics happens on a time scale of sub-femtosecond or attosecond. Therefore, laser-induced molecular dynamics involving valence electron excitation is of general interest in strong field and attosecond sciences [2]. In a strong laser field, its electric field strength can be equivalent to the Coulomb potential field of valence electrons. When a molecule is exposed to such a laser field, valence electrons can be released through strong-field ionization [3]. After ionization, the electron density of the molecules will be redistributed on a time scale of femtoseconds or sub-femtoseconds and the geometry of the molecule will change to find a new equilibrium accordingly. In many cases, the molecule will become unstable, which leads to the breakage of chemical bonds through molecular dissociation, or the formation of new chemical bonds through molecular isomerization [4–7]. Most of such laser-induced molecular reactions involve electronically excited states. Therefore, valence electron excitation is critical for studies of laser-induced molecular reactions.

Previous experiments demonstrated that there exist several different mechanisms for strong-field electron excitation connected with strong-field ionization. In general, in these experiments, the driving laser field is a non-resonant field with respect to the molecular energy level structure. The four most common processes are 1) electron excitation through laser-induced strong-field ionization from low-lying molecular orbitals [5, 8–13]; 2) electron excitation through laser-induced electron rescattering after strong-field ionization [14–17]; 3) laser-induced electron excitation through single- or multi-photon transitions after strong-field ionization (so-called bond softening process) [18–21]; and 4) laser-induced electron recapture to electron excited states after strong-field ionization [22–25]. All four electron excitation processes start with strong-field ionization.

One important feature of molecular strong-field ionization in a strong laser field is that the ionization rate depends on the angle between the molecular axis and the laser polarization direction [5, 13, 26–29]. The angular ionization probability of a molecule is determined by the shape and symmetry of the involved molecular orbitals [30]. For example, strong-field ionization of electrons from the HOMO of C_2H_2, a π-orbital, reaches a maximum when the laser is polarized perpendicular to the molecular axis, while for the ionization from a σ-orbital, the maximum ionization probability appears when the laser polarization direction is parallel to the molecular axis [5]. Therefore, using the angular dependence of strong-field ionization, we could determine the contributions from certain molecular orbitals in experiments [13].

The laser pulse duration is one of the critical parameters in strong field interaction [21, 31–33]. In the case of molecules, nuclear dynamics can be involved during the interaction. Previous studies showed that the so-called bond-softening process in H_2 can be strongly suppressed when using laser pulses with a pulse duration of shorter than 10 fs [21]. Within a short pulse, the effect of nuclear motion can be minimized because nuclear dynamics is much slower than electron dynamics. Therefore, using the dependence on pulse duration, we can possibly identify the effect from nuclear dynamics.

In this work, using C_2H_2 as an example, we investigate the electron excitation of polyatomic molecules in a strong laser field. We exploit the ionization and dissociation signals of pre-aligned C_2H_2 in a strong laser field with two different pulse durations to reveal the involved molecular orbitals and nuclear dynamics in electron excitation processes.

Experiment

In the experiment, we use a Cold Target Recoil Ion Momentum Spectroscopy (COLTRIMS) apparatus to measure charged particles (electrons and ions) from the laser-molecule interaction [16, 34, 35] with 800 nm and 25 fs laser pulses from a Ti:Sapphire amplifier. From the measurements, we identify non-dissociative and dissociative processes after single and double ionization of C_2H_2. In this work, we focus on electron excitation after single ionization. Figure 1A shows the measured ion signal distribution over the time-of-flight and x position on the detector. In the distribution, non-dissociative ionization signals ($C_2H_2^+$ and its isotopic species) appear as sharp spots, while ion signals (C_2H^+) from dissociation exhibit a broader ring-like or plate-like distribution due to the energy released from the chemical bond breakage. As marked in the figure, we can distinguish the $C_2H_2^+$ signal from non-dissociative and dissociative single ionization. It is to be noted that large ring-like signals belong to the dissociation of doubly ionized $C_2H_2^{2+}$, which is confirmed using two-body coincidence detection of C_2H^+ and H^+.

The molecular axes of molecules in the gas phase are, in general, randomly aligned. When the molecules are exposed to a strong and short laser pulse, they can be aligned through so-called impulsive laser alignment [36]. For the alignment measurements, we split the laser beam into an ionization beam and an alignment beam with a beam splitter. Both beams are linearly polarized along the same direction. The peak intensity of the alignment beam at the focus is below 1×10^{13} W/cm^2 to excite a rotational wave packet in the molecule [36], while the ionization beam with a peak intensity of 4×10^{14} W/cm^2 arrives at the target with a certain time delay controlled by a motorized linear stage. The laser peak intensity is calibrated with the time-of-flight spectrum of H_2 [37]. As shown in Figure 1B, the rotational revival structures are presented in the measured $C_2H_2^{2+}$ signal over the time delay between the alignment and the ionization pulse. In the same figure, we also plot the calculated the alignment quality of C_2H_2, the expectation value to $\cos^2\theta$ with θ the angle between the molecule axis and the laser polarization direction [5]. The measured ion signals overall follow the structures in the simulated data, except for a phase-flip which is introduced by the ionization process from the HOMO of C_2H_2 [5].

To achieve 4.5 fs laser pulses for the short pulse measurement, the ionization beam is focused into a gas-filled hollow capillary in which its spectrum is broadened [38]. After re-collimation, the beam is compressed with chirped mirrors, and a wedge pairs down to 4.5 fs[39]. The pulse duration of the ionization pulses is characterized by a stereo-ATI device [39, 40].

Results and discussions

KER distributions

Since the ground state of $C_2H_2^+$ is metastable and the excited states of $C_2H_2^+$ are mostly dissociative [5], in the experiment, we used the dissociation from single ionization to study the electron excitation of $C_2H_2^+$. In this work, we focus on the dissociation of

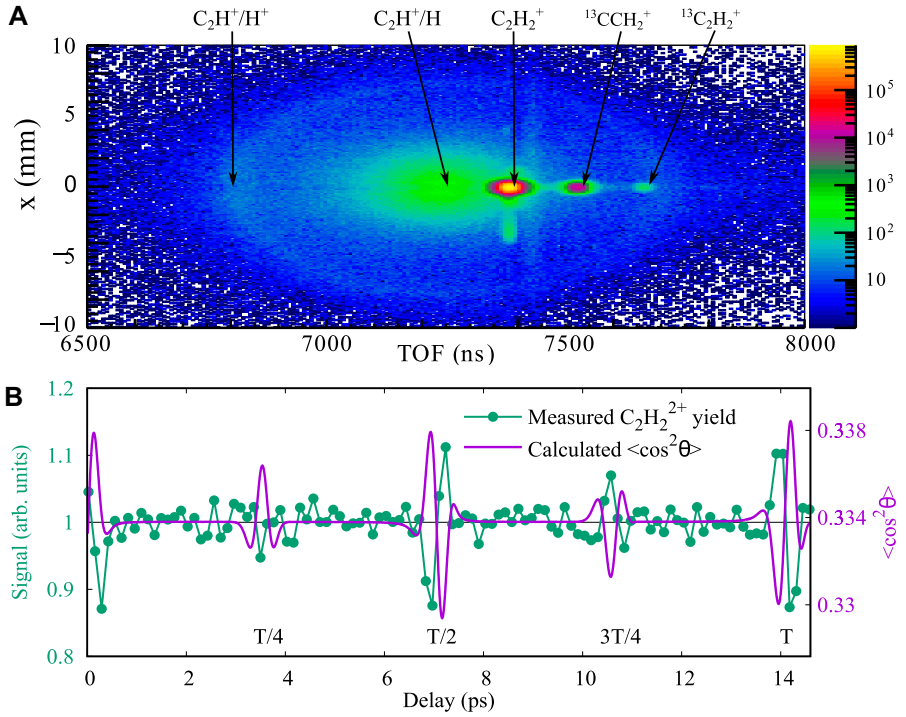

FIGURE 1
(A) Measured ion count distribution over the time-of-flight and x position on the detector. The peak intensity of the laser field is 4×10^{14} W/cm^2, and the pulse duration is 25 fs. **(B)** Measured $C_2H_2^{2+}$ signal and simulated $<\cos^2\theta>$ as a function of the time delay between the alignment and the ionization pulse. For the simulation, the gas temperature of 200 K and the peak intensity of 1×10^{13} W/cm^2 of the alignment pulse are used.

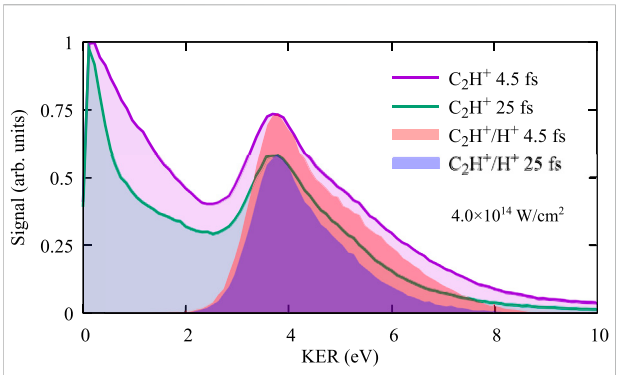

FIGURE 2
Measured KER distributions of laser-induced C-H dissociation for the pulse duration of 4.5 fs and 25 fs, selected with a single C_2H^+ ion and with the two-body coincidence detection of C_2H^+ and H^+.

the C-H bond breakage after single ionization, in which the nuclear dynamics is faster than that of the C-C bond breakage. Using momentum conservation, we calculate the kinetic energy released (KER) with the measured momentum of C_2H^+ through $E_{KER} = p^2_{C_2H}(1/m_{C_2H} + 1/m_H)/2$. In Figure 2, we depict the KER distributions for the two pulse durations with all C_2H^+ signals. The KER distributions show one peak close to zero and another at about 3.8 eV. In the figure, we include also the KER distributions of the two-body fragmentation (C_2H^+/H^+) from double ionization, which exhibit a peak at 3.8 eV. It is clear that the high energy peak of the measured KER with dominant C_2H^+ signals comes from the dissociation of doubly ionized molecules, while the lower energy signals with energy lower than 2 eV are dominantly from the dissociation after single ionization. Thus, we can separate the dissociation signal of single ionization from double ionization. The discrepancies at large energies between the KER distributions from two-body coincidence selection and those from one ion selection are due to the overlap with background water (H_2O^+) signals which are excluded in the coincidence selection. The relative strength of the background signal is sensitive to the gas density and the laser focusing conditions.

Alignment dependence

Comparing the results between 4.5 fs and 25 fs for the dissociation after single ionization in Figure 2, we find that the KER distribution of the measurement with 4.5 fs pulses is

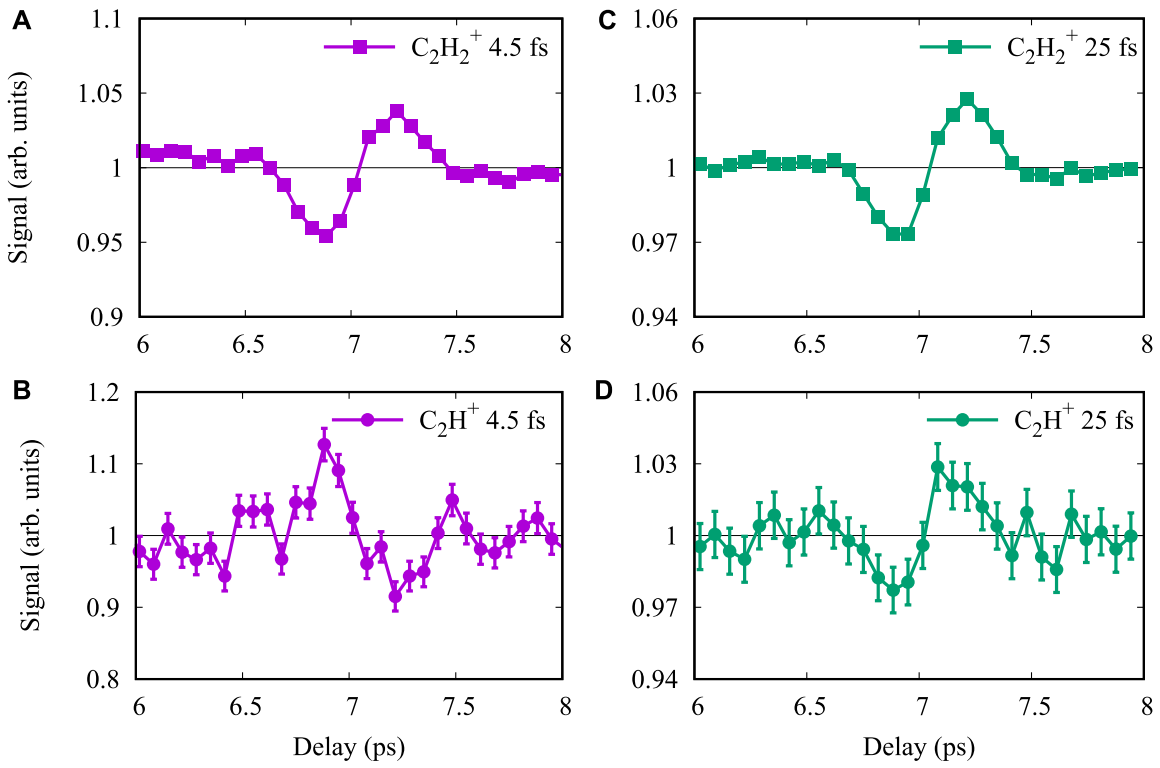

FIGURE 3
Measured ion signals as a function of the time delay between the alignment and the ionization pulse around the half rotational revival. Panels **(A,C)** are for the signals of non-dissociative $C_2H_2^+$, while **(B,D)** are those for the dissociative of $C_2H_2^+$ to C_2H^+/H. The measurements with pulse durations of 4.5 fs and 25 fs are shown in **(A,B)** and **(C,D)**, respectively. The laser peak intensity is 4 × 10^{14} W/cm^2 for both measurements.

broader, which means more high-energy signals than those with 25 fs Since 4.5 fs pulses have a much broader bandwidth than 25 fs laser pulses, an intuitive explanation for the width difference in the KER distributions could be the bandwidths of the driven laser pulses. However, due to the momentum conservation for the ejected electron and the rest of the molecule, the energy gained from the laser field will be mostly carried by the electron due to the significant mass difference between the electron and the ion. Therefore, the kinetic energy release of laser-induced molecular dissociation has minor influence from the laser bandwidth but is rather determined by the initial distribution of the nuclear wave packet and the slope of the involved potential energy surfaces. The difference in KER implies involving of different nuclear dynamics during the dissociation process. To understand the beneath physical mechanism, we further analyze the data of alignment measurements with the selection of KER less than 2 eV for the dissociation of C_2H_2 after single ionization.

For the alignment dependence, we focus on signals around the half-rotational revival, during which the molecules are first aligned parallely at a delay time of 6.8 ps and afterward perpendicular to the laser polarization direction at a delay time of 7.2 ps. Figures 3A,B show the ion signals of non-dissociative and dissociative single ionization of C_2H_2 around the half-rotation revival for the measurement with 4.5 fs ionization pulses. As has been reported previously, for 4.5 fs laser pulses, the $C_2H_2^+$ signal has a maximum at the perpendicular alignment because of ionization from the HOMO, while the C_2H^+ signal shows an opposite dependence on the alignment with the major contribution to ionization from HOMO-2 [5].

Figures 3C,D depict the ion signals for the measurement with 25 fs ionization pulses. The $C_2H_2^+$ signal over the pump-probe delay is similar to that with 4.5 fs laser pulses, which indicates dominant ionization from HOMO as well. However, the C_2H^+ signal with 25 fs exhibits an opposite dependence on the alignment from that with 4.5 fs: the peak signal appears at the perpendicular alignment of the molecular axis to the direction of the laser polarization. Such dependence is the same as the $C_2H_2^+$ and infers that the strong-field ionization is dominantly from HOMO.

Laser-induced electron excitation mechanics

To understand the dependence on laser pulse duration, we draw the potential energy curves of C_2H_2 over the C-H coordination in Figure 4. The removal of a HOMO electron

10.3389/fphy.2022.1076671

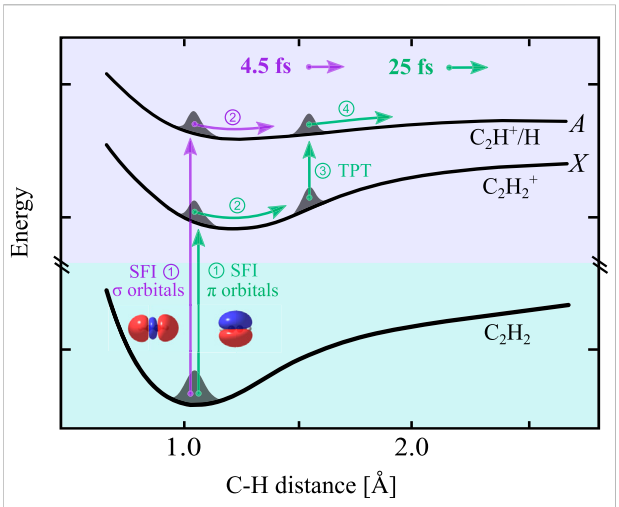

FIGURE 4
Schematic view of electron excitation of C_2H_2 in a strong laser field. Two pathways are represented with arrows of different colors. The HOMO-2 pathway: for the interaction with a short laser pulse with a pulse duration shorter than the C-H vibrational period, strong field ionization (SFI) of a HOMO-2 electron directly leads to the electronically excited and dissociative A state. The HOMO pathway: for the interaction with a long laser pulse with a pulse duration longer than the C-H vibrational period, first, an electron is removed from the HOMO which launches a vibrational wave packet on the potential surface of the $C_2H_2^+$ ground state. The vibrational wave packet moves toward a larger C-H distance and resonant three-photon transition (TPT) occurs once the energy gap fits the energy of three 800-nm photons. The potential energy curves are adapted from Ref. [5].

brings the molecule into the ground state of the cation (X state), and the removal of a HOMO-2 electron directly prompts the molecule into the lowest electronic excited state (A state) of the cation, which is dissociative over the C-H coordination. There are two possible pathways to reach the A state from a neutral C_2H_2. The first one is strong-field ionization directly from HOMO-2. The second one happens sequentially through first reaching the X-state through the removal of a HOMO electron and then a HOMO-2 electron being excited to the hole in the HOMO formed through ionization. The measured signal of $C_2H_2^+$ over alignment pump-probe delays show a clear signature of strong-field ionization of a HOMO electron for both laser pulse durations. On the other hand, the dissociative single ionization shows opposite behavior on the molecular alignment, which refers that the involved ionization and excitation processes are not the same.

In the case of 4.5 fs laser pulses, the C-H coordinate can be treated as frozen during the laser interaction, and therefore, the ionization happens dominantly at the Franck–Condon region. The measured results, shown in Figure 3B, indicate that the population of the dissociative channel is dominated by direct ionization from HOMO-2, which exhibits a peak signal at the parallel alignment. However, the scenario of the dissociation with 25 fs laser pulses is different. The measured results in Figure 3 D show dependence on the alignment from the ionization of a HOMO electron. As we mentioned, with the ionization of a HOMO electron, the molecule ends at the stable X state of the cation. Therefore, to reach the A state, further actions are necessary to excite the cation. After the strong-field ionization at around the peak of the laser field, the tail of the laser pulse can still have actions on the molecule. There are several possible ways to excite an electron from the HOMO-2 to HOMO to reach the A state. The first one is excitation through electron rescattering: the removed HOMO electron is accelerated in the laser field and can be driven back and scattered with its parent. Such electron rescattering can either kick out or excite a second electron, depending on the rescattering energy. In our experimental condition with a peak intensity of 4×10^{14} W/cm^2, the rescattering energy can be as high as 76 eV, which is sufficient to excite $C_2H_2^+$ from the X state to the A state. This energy difference in the distribution also rules out the major contribution from electron rescattering. For an electron rescattering process, the scattering mainly happens within one optical cycle of the laser field which is 2.7 fs. In such a short time scale, the stretching of the C-H bond is minor. Therefore, the nuclear wave packet populated on the A state is still approximately the Franck–Condon region, which shall lead to a similar energy distribution as the direct ionization from HOMO-2.

The second possible pathway is molecular dissociation involving nuclear dynamics, similar to the bond softening in the dissociation of H_2^+ in a strong laser field [18]. In the first step, one electron is released from HOMO at the Franck–Condon region, and the ion ends at the X state with vibrational excitation. The C-H stretching of $C_2H_2^+$ can occur on a fast time scale with a vibrational period of 10.3 fs for asymmetric stretching and 10.6 fs for symmetric stretching [41]. Therefore, when the laser pulse has pulse duration longer than the vibrational period, the nuclear wave packet on the X state can move toward the new equilibrium geometry through the stretching of the C-H bond within the laser pulse. The energy gap between the X and A states is about 5.4 eV which is away from the multi-photon resonance of 800 nm [42, 43]. Along the stretching, the energy gap between the X state and the A state changes as well. The transition from the X state to the A state occurs once the energy gap becomes the three-photon resonance (4.65 eV) of 800-nm photons. After the transition, dissociation from the A state happens with a slightly lower dissociation energy, as shown in Figure 4. Comparing the distribution in the low energy between measurements with the two pulse durations, we notice that the energy edge shifted to the higher value by about 0.5 eV for the 4.5 fs at the half maximum. This observation is direct evidence that the initial nuclear wave packet is at a different position on the potential energy surface, and it supports the bond-softening scenario for the 25 fs case.

On the other side, when the laser pulse duration is 4.5 fs, it is much shorter than the C-H vibrational period. After single ionization, the laser field drops off rapidly before significant stretching of the C-H bond, which prevents the multiphoton transition at a large C-H distance. Therefore, the excitation to the

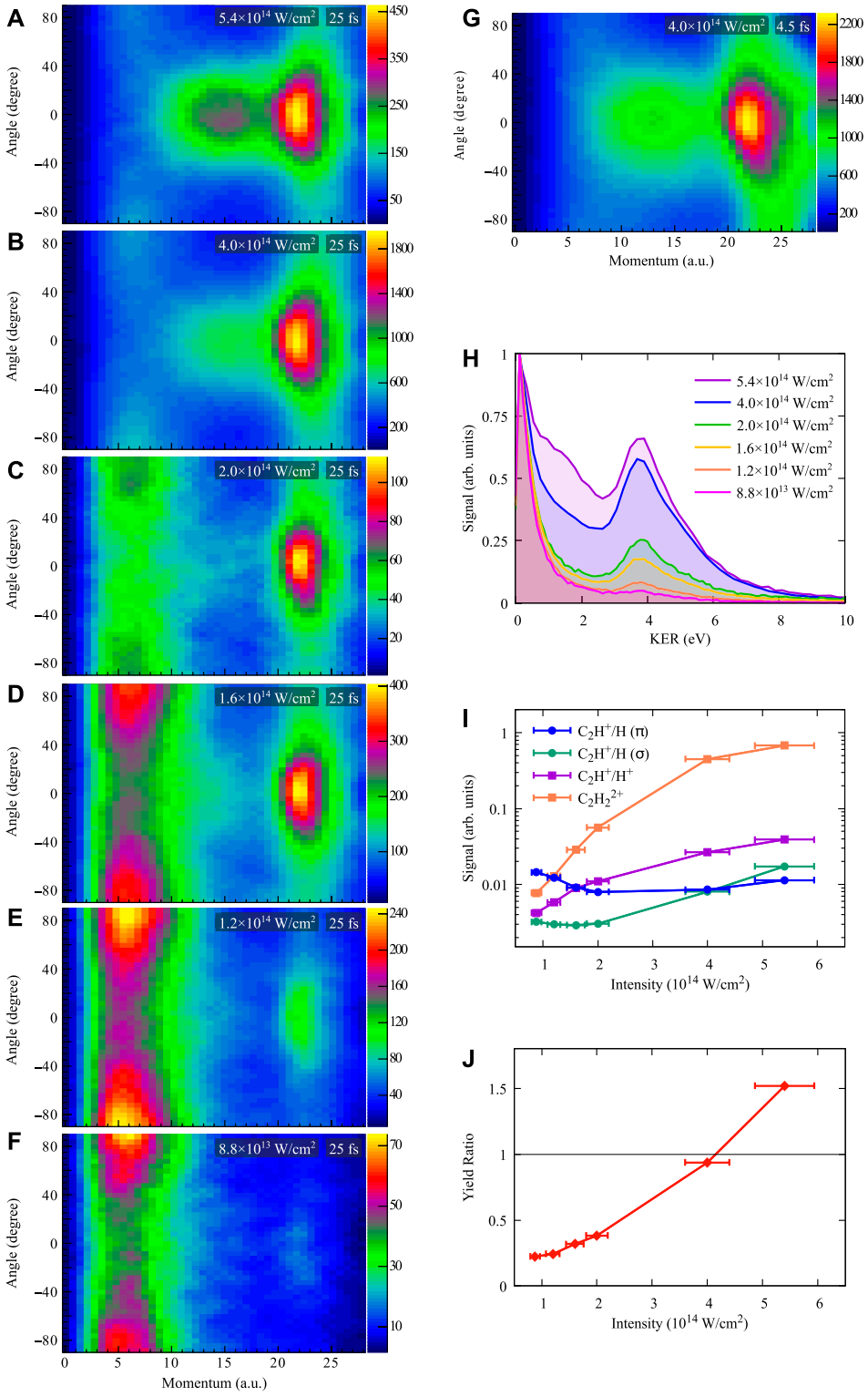

FIGURE 5
Measured ion signal distributions over the momentum and the angle to the laser polarization direction for different laser peak intensities with the pulse duration of 25 fs**(A–F)** and 4.5 fs **(G)**. **(H)** Normalized kinetic energy distributions of the molecular dissociation for different laser peak intensities with the pulse duration of 25 fs. **(I)** Ion yields for different ionization and dissociation channels over laser intensity normalized to the non-dissociative single ionization signal ($C_2H_2^+$). **(J)** The ion yield ratio between the direct (HOMO-2) and indirect (HOMO) dissociative single ionization over laser intensity.

A state is dominant by direct ionization from HOMO-2, and the dissociation ends with a higher KER than that of a bond-softening pathway.

As mentioned, there is one more possible way for valence electron excitation, which is electron recapture after strong-field ionization [22, 24, 25]. Electron recapture after double ionization will lead to singly ionized C_2H_2. It will lead to either stable high-lying Rydberg states of $C_2H_2^+$ or dissociation of $C_2H_2^+$. In case of dissociation, the KER will be similar to that from doubly ionized due to the weak screening effect from the high-lying Rydberg electron to the molecular dissociation of C_2H_2 [23, 44]. Therefore, the signals induced by electron recapture have no contribution to the measured dissociation signals of single ionization with a KER less than 2 eV.

Dependence on laser intensity

Strong laser field-induced molecular ionization and dissociation are highly non-linear processes; therefore, laser intensity is a critical parameter for these processes. For the electron excitation process of singly ionized C_2H_2, both the strong-field ionization and possible transition between two electronic states are sensitive to the laser intensity which shall lead to laser intensity dependence. To demonstrate such dependence, we perform measurements with different laser peak intensities in the range from 8.8×10^{13} to 5.4×10^{14} W/cm^2 with a pulse duration of 25 fs. In the data analysis for the dependence on laser intensity, we integrate signals with all delays between the alignment and the ionizing pulses, with, therefore, no preferential alignment of the molecules. Figure 5H presents the normalized KER distributions for six laser peak intensities. With the increase of the laser peak intensity, the dissociative double ionization signals peaking at 3.8 eV increase monotonically, and the signals around 2 eV increase as well. From the experiment, we obtain three-dimensional momentum vectors of ions. Therefore, in addition to the KER (or momentum) distribution, angular distributions of ions can be derived from the momentum vectors. In Figures 5A–G, we plot the two-dimensional ion (C_2H^+) signal distributions over the momentum ($p_r = \sqrt{p_x^2 + p_y^2 + p_z^2}$) and the angle to the laser polarization direction ($\theta = \tan^{-1}(p_y/p_z)$) for different intensities.

First, let us focus on the distribution at one certain intensity. For instant, in Figure 5B, with the laser peak intensity of 4×10^{14} W/cm^2 and the pulse duration of 25 fs, we can identify three different regions from the distribution: the first region with momentum less than 9 a.u. (KER < 0.6 eV), the second region with momentum larger than 9 a.u. but less than 19 a.u. (0.6 < KER < 2.8 eV), and the third region with momentum larger than 19 a.u. (KER > 2.8 eV). We know that the first and second regions are dissociation signals after single ionization, while the third region originates from double ionization, according to Figure 2. Since the ion ejected along the molecular axis, the measured angle θ represents the molecular axis to the laser polarization direction. For the first region, the angular distribution exhibits a minimum at 0° (parallel to the laser polarization direction) and maxima at ±90° (perpendicular to the laser polarization direction). Such angular distribution indicates strong-field ionization from a π orbital (HOMO) has peak ionization probability when the molecular axis is perpendicular to the laser polarization direction, which is consistent with the findings from the alignment dependence. On the other hand, the angular distribution for the third region (C_2H^+/H^+) shows an opposite behavior, maximum at 0° and minima at ±90°, which indicates at least one electron removed from HOMO-2 σ orbital [5]. We notice that the angular distribution for the second region ($9 < p_r < 19$ a.u.) is different from the first and third regions. The distribution displays maximum at 0° and minima at ±90°, which is opposite to that of the first region and similar to that of the third region but with a narrower distribution. Such distribution implies single ionization from the HOMO-2 which has a maximum ionization probability when the molecular axis is parallel to the laser polarization direction. One previous study on the dissociation from double ionization [5] demonstrated double ionization leading to the C_2H^+/H^+ channel involves one HOMO and one HOMO-2 electron. The convolution of the ionization probability from the HOMO and HOMO-2 broadens the angular distribution and, therefore, yields broader distribution than that of single ionization with one HOMO-2 electron (the second region).

Figure 5G shows the two-dimensional angle-momentum distribution for the same peak intensity but with a pulse duration of 4.5 fs. To compare with the distribution of 25 fs in Figure 5B, the overall structures are similar but the relative signal strength in the three regions are different and with broader angular distributions for the second and third regions. This observation also explains the difference in the KER distributions shown in Figure 2. More signals in the second region for the measurement with 4.5 fs pulses lead to a broader KER distribution for the dissociation of singly ionized C_2H_2. As discussed previously, for the case of 4.5 fs, the dissociation from single ionization happens dominantly from the direct removal of a HOMO-2 electron, which agrees with maximum signals at 0° in the angular distribution for the second region. The narrower angular distributions in the second and third regions for the pulse duration of 25 fs can be explained by the laser-induced alignment after strong-field ionization [45], which has been previously observed in C_2H_4 experiments [6].

In the angle–momentum distributions, we can explicitly identify two pathways with different momentum and angular distributions for the molecular dissociation after single ionization from HOMO and HOMO-2: ionization from HOMO leads to dominant signals at the perpendicular direction with momentum less than 9 a.u. (KER < 0.6 eV) and ionization from HOMO-2 yields dominant signals at the parallel direction with momentum larger than 9 a.u. and less than 19 a.u. ((0.6 < KER < 2.8 eV)).

Such behaviors agree well with the findings in the alignment experiments and support the proposed direct (ionization from HOMO-2) and indirect (bond-softening after ionization from HOMO) electron excitation mechanisms.

Now, let us continue to the dependence of the laser-induced dissociation on the laser intensities with the pulse duration of 25 fs. Figures 5A–F reveal that the dominant dissociation signals from single ionization shift from the first region to the second region with the increasing of the peak intensity from 8.8×10^{13} to 5.4×10^{14} W/cm^2, while the dissociation signals from double ionization increase monotonically. To quantify the dependence on the laser peak intensity, we integrate the signals in the three regions and compare them with the yields of non-dissociative single ($C_2H_2^+$) and double ($C_2H_2^{2+}$) ionization. Figure 5I illustrates the ion yields which are normalized to that of non-dissociative single ionization ($C_2H_2^+$). In the plot, we note that the dissociative (C_2H^+/H^+) and non-dissociative ($C_2H_2^{2+}$) double ionization yields monotonically increase along the increasing of the laser peak intensity and approach saturation at the peak intensity of 5.4×10^{14} W/cm^2. On the other hand, the two pathways of dissociation from single ionization (C_2H^+/H) exhibit different intensity dependence. The signals from the ionization of HOMO (π orbital) first decrease in the low-intensity regime and increase again in the high-intensity regime. This behavior can be explained by the interplay between the depletion of the single ionization to higher charge states with the increasing of laser intensities and the focal volume effect. The signals from the ionization of HOMO-2 (σ orbital) stay on a low level when the peak intensity is below 2×10^{14} W/cm^2, and when the intensity is above this level, the signals start to increase. The ratio between the yield of the two pathways is depicted in Figure 5J, which represents the increase of the HOMO-2 (σ orbital) pathway with respect to the HOMO (π orbital) pathway with a significant increase from 0.2 to 1.5. The HOMO pathway is dominant in the low-intensity regime, but when the intensity increases to above 5×10^{14} W/cm^2, the HOMO-2 pathway becomes stronger.

These results show that not only the absolute yields but also the relative yields of molecular dissociation between different pathways strongly depend on the laser intensity. Therefore, together with the pulse duration and the molecular alignment, the laser intensity can be used as an effective knob to control the laser-induced electron excitation and following molecular dissociation.

Conclusion

In conclusion, we experimentally distinguished the two dominant electron excitation pathways in single ionization of C_2H_2 by strong laser fields. With the alignment dependence of the dissociation signal, we could determine the involved molecular orbitals in the electron excitation. Additionally, the influence of nuclear dynamics after ionization can be identified from the dependence of the dissociation KER on the pulse duration and the intensity of the ionizing laser pulse. The observed electron excitation processes in C_2H_2 can be general in polyatomic molecules since strong-field ionization from low-lying molecular orbital is not a rare process, and nuclear dynamics on the 10 femtosecond timescale, within the duration of laser pulses used in many experiments, takes place in many molecules, in particular those containing C-H bonds. Moreover, the momentum and angle-resolved distributions contain information on both the orbital from which an electron is released and the nuclear dynamics happening during strong-field interaction. In turn, these distributions provide information on the ultrafast electron and nuclear dynamics in polyatomic molecules taking place during and after strong-field ionization.

Data availability statement

The raw data supporting the conclusions of this article will be made available by the authors, without undue reservation.

Author contributions

SL, SE, MZ, and XX conducted the experiment. YH, HH, and XX analyzed the data. All co-authors contributed to the discussion and writing of the manuscript.

Funding

This work was supported by Austrian Science Fund (FWF) under P30465-N27 and ZK 9100-N. Open access funding provided by PSI - Paul Scherrer Institute.

Conflict of interest

The authors declare that the research was conducted in the absence of any commercial or financial relationships that could be construed as a potential conflict of interest.

Publisher's note

References

1. Kauzmann W. *Quantum chemistry: An introduction*. Amsterdam, Netherlands: Elsevier (2013).

2. Corkum PB, Krausz F. Attosecond science. *Nat Phys* (2007) 3:381–7. doi:10.1038/nphys620

3. Augst S, Strickland D, Meyerhofer DD, Chin SL, Eberly JH. Tunneling ionization of noble gases in a high-intensity laser field. *Phys Rev Lett* (1989) 63: 2212–5. doi:10.1103/physrevlett.63.2212

4. Posthumus JH. The dynamics of small molecules in intense laser fields. *Rep Prog Phys* (2004) 67:623–65. doi:10.1088/0034-4885/67/5/r01

5. Xie X, Doblhoff-Dier K, Xu H, Roither S, Schöffler MS, Kartashov D, et al. Selective control over fragmentation reactions in polyatomic molecules using impulsive laser alignment. *Phys Rev Lett* (2014) 112:163003. doi:10.1103/PhysRevLett.112.163003

6. Xie X, Roither S, Schöffler M, Lötstedt E, Kartashov D, Zhang L, et al. Electronic predetermination of ethylene fragmentation dynamics. *Phys Rev X* (2014) 4:021005. doi:10.1103/PhysRevX.4.021005

7. Hartmann N, Bhattacharyya S, Schlaepfer F, Volkov M, Schumacher Z, Lucchini M, et al. Ultrafast nuclear dynamics of the acetylene cation C2H2+ and its impact on the infrared probe pulse induced C-H bond breaking efficiency. *Phys Chem Chem Phys* (2019) 21:18380–5. doi:10.1039/C9CP03138C

8. Yao J, Li G, Jia X, Hao X, Zeng B, Jing C, et al. Alignment-dependent fluorescence emission induced by tunnel ionization of carbon dioxide from lower-lying orbitals. *Phys Rev Lett* (2013) 111:133001. doi:10.1103/PhysRevLett.111.133001

9. Erattupuzha S, Larimian S, Baltuška A, Xie X, Kitzler M. Two-pulse control over double ionization pathways in CO2. *J Chem Phys* (2016) 144:024306. doi:10.1063/1.4939638

10. Farrell JP, Petretti S, Förster J, McFarland BK, Spector LS, Vanne YV, et al. Strong field ionization to multiple electronic states in water. *Phys Rev Lett* (2011) 107:083001. doi:10.1103/PhysRevLett.107.083001

11. Akagi H, Otobe T, Staudte A, Shiner A, Turner F, Dörner R, et al. Laser tunnel ionization from multiple orbitals in hcl. *science* (2009) 325:1364–7. doi:10.1126/science.1175253

12. Wu C, Zhang H, Yang H, Gong Q, Song D, Su H. Tunneling ionization of carbon dioxide from lower-lying orbitals. *Phys Rev A* (2011) 83:033410. doi:10.1103/PhysRevA.83.033410

13. Hu H, Kangaparambi S, Dorner-Kirchner M, Hanus V, Baltuška A, Kitzler-Zeiler M, et al. Quantitative retrieval of the angular dependence of laser-induced electron rescattering in molecules. *Phys Rev A* (2021) 103:013114. doi:10.1103/PhysRevA.103.013114

14. Kopold R, Becker W, Rottke H, Sandner W. Routes to nonsequential double ionization. *Phys Rev Lett* (2000) 85:3781–4. doi:10.1103/PhysRevLett.85.3781

15. Feuerstein B, Moshammer R, Fischer D, Dorn A, Schröter CD, Deipenwisch J, et al. Separation of recollision mechanisms in nonsequential strong field double ionization of ar: The role of excitation tunneling. *Phys Rev Lett* (2001) 87:043003. doi:10.1103/PhysRevLett.87.043003

16. Xie X, Roither S, Kartashov D, Persson E, Arbó DG, Zhang L, et al. Attosecond probe of valence-electron wave packets by subcycle sculpted laser fields. *Phys Rev Lett* (2012) 108:193004. doi:10.1103/PhysRevLett.108.193004

17. Endo T, Matsuda A, Fushitani M, Yasuike T, Tolstikhin OI, Morishita T, et al. Imaging electronic excitation of no by ultrafast laser tunneling ionization. *Phys Rev Lett* (2016) 116:163002. doi:10.1103/PhysRevLett.116.163002

18. Bucksbaum PH, Zavriyev A, Muller HG, Schumacher DW. Softening of the H2+ molecular bond in intense laser fields molecular bond in intense laser fields. *Phys Rev Lett* (1990) 64:1883–6. doi:10.1103/PhysRevLett.64.1883

19. Zavriyev A, Bucksbaum PH, Muller HG, Schumacher DW. Ionization and dissociation ofH2in intense laser fields at 1.064 μm, 532 nm, and 355 nm. *Phys Rev A* (1990) 42:5500–13. doi:10.1103/PhysRevA.42.5500

20. Giusti-Suzor A, He X, Atabek O, Mies FH. Above-threshold dissociation of H2+ in intense laser fieldsnse laser fields. *Phys Rev Lett* (1990) 64:515–8. doi:10.1103/PhysRevLett.64.515

21. McKenna J, Anis F, Sayler AM, Gaire B, Johnson NG, Parke E, et al. Controlling strong-field fragmentation of H2+ by temporal effects with few-cycle laser pulses. *Phys Rev A* (2012) 85:023405. doi:10.1103/physreva.85.023405

22. Nubbemeyer T, Gorling K, Saenz A, Eichmann U, Sandner W. Strong-field tunneling without ionization. *Phys Rev Lett* (2008) 101:233001. doi:10.1103/PhysRevLett.101.233001

23. Manschwetus B, Nubbemeyer T, Gorling K, Steinmeyer G, Eichmann U, Rottke H, et al. Strong laser field fragmentation ofH2: Coulomb explosion without double ionization. *Phys Rev Lett* (2009) 102:113002. doi:10.1103/physrevlett.102.113002

24. Larimian S, Erattupuzha S, Lemell C, Yoshida S, Nagele S, Maurer R, et al. Coincidence spectroscopy of high-lying rydberg states produced in strong laser fields. *Phys Rev A* (2016) 94:033401. doi:10.1103/PhysRevA.94.033401

25. Larimian S, Erattupuzha S, Baltuška A, Kitzler-Zeiler M, Xie X. Frustrated double ionization of argon atoms in strong laser fields. *Phys Rev Res* (2020) 2: 013021. doi:10.1103/PhysRevResearch.2.013021

26. Alnaser AS, Maharjan CM, Tong XM, Ulrich B, Ranitovic P, Shan B, et al. Effects of orbital symmetries in dissociative ionization of molecules by few-cycle laser pulses. *Phys Rev A* (2005) 71:031403. doi:10.1103/PhysRevA.71.031403

27. Śpiewanowski MD, Madsen LB. Alignment- and orientation-dependent strong-field ionization of molecules: Field-induced orbital distortion effects. *Phys Rev A* (2015) 91:043406. doi:10.1103/PhysRevA.91.043406

28. Zeidler D, Staudte A, Bardon AB, Villeneuve DM, Dörner R, Corkum PB. Controlling attosecond double ionization dynamics via molecular alignment. *Phys Rev Lett* (2005) 95:203003. doi:10.1103/PhysRevLett.95.203003

29. Lam HVS, Yarlagadda S, Venkatachalam A, Wangjam TN, Kushawaha RK, Cheng C, et al. Angle-dependent strong-field ionization and fragmentation of carbon dioxide measured using rotational wave packets. *Phys Rev A* (2020) 102: 043119. doi:10.1103/PhysRevA.102.043119

30. Tong XM, Zhao ZX, Lin CD. Theory of molecular tunneling ionization. *Phys Rev A* (2002) 66:033402. doi:10.1103/physreva.66.033402

31. Reischl B, de Vivie-Riedle R, Rutz S, Schreiber E. Ultrafast molecular dynamics controlled by pulse duration: The na3 molecule. *J Chem Phys* (1996) 104:8857–64. doi:10.1063/1.471620

32. Bocharova I, Karimi R, Penka EF, Brichta JP, Lassonde P, Fu X, et al. Charge resonance enhanced ionization of CO2 probed by laser Coulomb explosion imaging. *Phys Rev Lett* (2011) 107:063201. doi:10.1103/PhysRevLett.107.063201

33. Xie X, Lötstedt E, Roither S, Schöffler M, Kartashov D, Midorikawa K, et al. Duration of an intense laser pulse can determine the breakage of multiple chemical bonds. *Sci Rep* (2015) 5:12877–11. doi:10.1038/srep12877

34. Dörner R, Mergel V, Jagutzki O, Spielberger L, Ullrich J, Moshammer R, et al. Cold target recoil ion momentum spectroscopy: A 'momentum microscope' to view atomic collision dynamics. *Phys Rep* (2000) 330:95–192. doi:10.1016/s0370-1573(99)00109-x

35. Roither S, Xie X, Kartashov D, Zhang L, Schöffler M, Xu H, et al. High energy proton ejection from hydrocarbon molecules driven by highly efficient field ionization. *Phys Rev Lett* (2011) 106:163001. doi:10.1103/PhysRevLett.106.163001

36. Stapelfeldt H, Seideman T. Colloquium: Aligning molecules with strong laser pulses. *Rev Mod Phys* (2003) 75:543–57. doi:10.1103/RevModPhys.75.543

37. Alnaser AS, Tong XM, Osipov T, Voss S, Maharjan CM, Shan B, et al. Laser-peak-intensity calibration using recoil-ion momentum imaging. *Phys Rev A* (2004) 70:023413. doi:10.1103/PhysRevA.70.023413

38. Nisoli M, De Silvestri S, Svelto O. Generation of high energy 10 fs pulses by a new pulse compression technique. *Appl Phys Lett* (1996) 68:2793–5. doi:10.1063/1.116609

39. Xie X, Doblhoff-Dier K, Roither S, Schöffler MS, Kartashov D, Xu H, et al. Attosecond-recollision-controlled selective fragmentation of polyatomic molecules. *Phys Rev Lett* (2012) 109:243001. doi:10.1103/PhysRevLett.109.243001

40. Sayler AM, Rathje T, Müller W, Rühle K, Kienberger R, Paulus GG. Precise, real-time, every-single-shot, carrier-envelope phase measurement of ultrashort laser pulses. *Opt Lett* (2011) 36:1–3. doi:10.1364/OL.36.000001

41. Relph RA, Bopp JC, Roscioli JR, Johnson MA. Structural characterization of (C2H2)1-6+ cluster ions by vibrational predissociation spectroscopy. *J Chem Phys* (2009) 131:114305. doi:10.1063/1.3212595

42. Jiang YH, Rudenko A, Herrwerth O, Foucar L, Kurka M, Kühnel KU, et al. Ultrafast extreme ultraviolet induced isomerization of acetylene cations. *Phys Rev Lett* (2010) 105:263002. doi:10.1103/PhysRevLett.105.263002

43. Ibrahim H, Wales B, Beaulieu S, Schmidt BE, Thiré N, Fowe EP, et al. Tabletop imaging of structural evolutions in chemical reactions demonstrated for the acetylene cation. *Nat Commun* (2014) 5:4422–8. doi:10.1038/ncomms5422

44. Hu H, Larimian S, Erattupuzha S, Wen J, Baltuška A, Kitzler-Zeiler M, et al. Laser-induced dissociative recombination of carbon dioxide. *Phys Rev Res* (2019) 1: 033152. doi:10.1103/PhysRevResearch.1.033152

45. Tong XM, Zhao ZX, Alnaser AS, Voss S, Cocke CL, Lin CD. Post ionization alignment of the fragmentation of molecules in an ultrashort intense laser field. *J Phys B: Mol Opt Phys* (2005) 38:333–41. doi:10.1088/0953-4075/38/4/002

frontiers | Frontiers in Physics

TYPE Original Research
PUBLISHED 21 March 2023
DOI 10.3389/fphy.2023.1120654

OPEN ACCESS

EDITED BY
Yiqi Zhang,
Xi'an Jiaotong University, China

REVIEWED BY
Yanpeng Zhang,
Xi'an Jiaotong University, China
Weibin Li,
University of Nottingham,
United Kingdom

*CORRESPONDENCE
Wei Quan,
charlywing@wipm.ac.cn
Xiaolei Hao,
xlhao@sxu.edu.cn
Jing Chen,
chenjing@ustc.edu.cn

SPECIALTY SECTION
This article was submitted to Optics and Photonics, a section of the journal Frontiers in Physics

RECEIVED 10 December 2022
ACCEPTED 03 March 2023
PUBLISHED 21 March 2023

CITATION
Wang Z, Quan W, Hao X, Chen J and Liu X (2023), The ellipticity dependence of Rydberg state excitation of noble gas atoms subject to strong laser fields. *Front. Phys.* 11:1120654. doi: 10.3389/fphy.2023.1120654

The ellipticity dependence of Rydberg state excitation of noble gas atoms subject to strong laser fields

Zhiqiang Wang[1,2], Wei Quan[2,3]*, Xiaolei Hao[1]*, Jing Chen[4,5]* and Xiaojun Liu[2,3]

[1]Institute of Theoretical Physics and Department of Physics, State Key Laboratory of Quantum Optics and Quantum Optics Devices, Collaborative Innovation Center of Extreme Optics, Shanxi University, Taiyuan, China, [2]State Key Laboratory of Magnetic Resonance and Atomic and Molecular Physics, Wuhan Institute of Physics and Mathematics, Innovation Academy for Precision Measurement Science and Technology, Chinese Academy of Sciences, Wuhan, China, [3]School of Physical Sciences, University of Chinese Academy of Sciences, Beijing, China, [4]Hefei National Research Center for Physical Sciences at the Microscale and School of Physical Sciences, Department of Modern Physics, University of Science and Technology of China, Hefei, China, [5]Center for Advanced Material Diagnostic Technology, College of Engineering Physics, Shenzhen Technology University, Shenzhen, China

In this work, we theoretically investigate the ellipticity dependence of the Rydberg state excitation (RSE) and ionization of noble gas atoms subject to strong laser fields at a series of intensities and wavelengthes by a semiclassical model, where the nonadiabtic effect is considered or ignored. Our results demonstrate that, if the nonadiabatic effect has been ignored, the ratio between RSE and ionization yields exhibits an anomalous maximum at a nonzero ellipticity. On the other hand, if the nonadiabatic effect has been considered, this anomalous behavior disappears. The analysis indicates that the absence of this anomalous behavior can be attributed to the nonadiabatic corrections of instantaneous ionization rate and the initial photoelectron momentum distribution at the tunnel exit.

KEYWORDS

rydberg state excitation, elliptically polarized laser field, ultrafast ionization, nonadiabatic effect, electron tunneling

1 Introduction

For an atom or molecule subject to a strong laser field, the valence electron can be released *via* tunneling [1, 2] if the electric field strength of the laser pulse is comparable to that of the Coulomb field of the ionic core. The ionization dynamics may be comprehended with either multiphoton ionization (MPI) or tunneling ionizaiton (TI) [3, 4]. To indicate the transition between these two limits, a pivotal role is given to the Keldysh parameter $\gamma = \sqrt{I_p/2U_p}$ [2, 5–7], where I_p is the ionization potential, $U_p = E_0^2/4\omega^2$ the pondermotive potential, E_0 the field amplitude, and ω the field frequency. For $\gamma \gg 1$, MPI dominates and the ionization rate can be calculated by the perturbation theory. In the case of high laser intensity and long laser wavelength, when the Keldysh parameter γ will be much less than 1 [4, 8], the optical oscillation of laser electric field is so slow that the laser field can be taken as a quasi-static field and the tunneling process is similar to the case of DC field. For $\gamma \sim 1$, which is typical for most current intense field experiments, it is well-accepted that TI still dominates and the nonadiabatic effects are expected to be important [9–11]. As documented [9, 12, 13], the nonadiabatic effect could make the instantaneous tunneling rate less sensitive to the laser

electric field phase, if compared to the adiabatic case. Moreover, the tunneling exit may become closer to the ionic core because of the nonadiabatic effect. In an elliptically polarized laser field, the nonadiabatic effect could induce a transversal momentum shift of the tunneled electron wavepacket at the tunnel exit.

After tunneling of the electron, the electron motion in a strong laser field can be described by a semiclassical model [14]. In this model, driven by the oscillating laser field, part of the tunneled electron wavepacket may return to the ionic core, resulting in a variety of interesting physical phenomena, such as high-order harmonic generation (HHG) [15, 16], nonsequential double ionization (NSDI) [17], and high-order above-threshold ionization (HATI) [18], *etc.* In contrast to the phenomena mentioned above, if the electron does not gain enough drift energy from the laser pulse, it will eventually be captured by the Coulomb field, leading to Rydberg state excitation (RSE) of neutral atoms. This process can be comprehended by the mechanism of frustrated tunneling ionization (FTI) [19]. The application of Rydberg atoms is very attractive in many fields [20].

In addition to the works on RSE process in linearly polarized strong laser fields (see, e.g. [21–27]), studies on the ellipticity dependence of RSE have attracted attention. Experimentally, Nubbemmeyer *et al.* demonstrated a dramatic decrease of RSE yields for He with increasing laser ellipticity, as expected with a rescattering picture [19]. An experimental investigation of high-lying Rydberg state excitation of diatomic atoms and their companion atoms with comparable ionization potentials shows a similar trend [28]. Theoretically, Landsman *et al.* well reproduced the results in [19] by the semiclassical model [29]. Zhao *et al.* found that the decline of the RSE yields with increasing ellipticity can be attributed to a decrease of low-energy electrons that could be captured in the Rydberg states by the Coulomb potential [30]. Recently, an astonishing maximum of the ratio between the RSE and the ionization yields at a nonzero ellipticity was found, based on a 2-dimensional semiclassical calculation [31]. Note that the results in [31] are inconsistent to a more recent time-dependent Schrödinger equation (TDSE) calculations of Pauly *et al.* [32], where the astonishing maximum of the ratio disappears. Thus, the consensus on the ellipticity dependence of RSE has not been reached yet.

Except for RSE and ionization, the high-order harmonic generation (HHG) of atoms and molecules in elliptically polarized laser field has also been studied intensively [33–36]. Although many interesting phenomena, e.g., HHG from N_2 can be strongly elliptically polarized even when driven by linearly polarized laser fields [35], the polarization of HHG depends strongly on the molcular alignment and laser ellipticity [36], have been documented, technically, it is very difficult to measure the HHG and ionization yields with the same spectrometer simultaneously because the sample pressure in the HHG experiments is usually much higher [35]. On the contrary, the ionization yields can be measured easily along with the RSE yields by the identical spectrometer simultaneously [19]. Thus, the investigation of correlation of RSE and ionization yields could be more significant due to the possibility of comparison with experimental results.

In this work, we study the RSE and ionization processes for atoms subject to elliptically polarized laser fields by a semiclassical model, where the nonadiabatic effect can be considered or ignored. Our results demonstrate that, if the nonadiabatic effect has been ignored, the ratio between RSE and ionization yields exhibits an anomalous maximum at a nonzero ellipticity, which is consistent to the results of Ref. [31]. On the other hand, if the nonadiabatic effect has been considered, this anomalous behavior disappears, which matches the results of Ref. [32]. By tracing back the initial photoelectron momenta and the coordinates of the photoelectron trajectories based on the semiclassical calculations, we found that the absence of this anomalous behavior can be attributed to the nonadiabatic corrections of the instantaneous ionization rate and the initial photoelectron momentum distribution at the tunnel exit.

2 Adiabatic model

The excitation and ionization dynamics are numerically simulated by a semiclassical model, which is shown to be invaluable and efficient in providing intuitive understanding and predictive power for the ultrafast dynamics of atoms and molecules subject to strong laser field [37–41]. In this model, it can be chosen to include the nonadiabatic effect or not. According to the documented works (see, e.g., [2, 12]), the nonadiabatic effect can be safely ignored if the Keldysh parameter is much less than unity [2], i.e., the laser intensity is strong enough or the laser wavelength is long enough. In these cases, the semiclassical model ignoring the nonadiabatic effect can be termed the classical-trajectory Monte Carlo (CTMC) model, which has already been widely applied in studying RSE based on the FTI mechanism [19, 29–32]. In contrast, if the above conditions cannot be well satisfied and the Keldysh parameter is close to unity, the nonadiabatic effect [9, 12, 42, 43] of electron tunneling could be too strong to be ignored. In these cases, the semiclassical model including the nonadiabatic effect will be coined the nonadiabatic model in this work.

In the CTMC model, the RSE and ionization processes in elliptically polarized laser field include two steps, i.e., tunneling ionization and classical evolution of the tunneled electron in a combination of the laser field and ionic Coulomb field. In the first step, it is assumed that the electron is adiabatically released from the groundstate to a continuum state through tunneling [44, 45]. The elliptically polarized laser electric field employed in this work can be given by $\mathbf{F}(t) = (E_x(t), 0, E_z(t))$ (atomic units are used unless stated otherwise),

$$E_x(t) = E_n(t)F_0\varepsilon\, sin(\omega t) \tag{1}$$

$$E_z(t) = E_n(t)F_0\, cos(\omega t) \tag{2}$$

where $F_0 = E_0/\sqrt{1+\varepsilon^2}$, E_0 is the peak electric field amplitude, ε the laser ellipticity, ω the laser angular frequency, and $E_n(t)$ the envelope function of the laser pulse,

$$E_n(t) = cos^2\left(\frac{\omega t}{2N}\right),\ -\frac{N\pi}{\omega} < t < \frac{N\pi}{\omega} \tag{3}$$

where N is the number of the laser cycles. In this work, $N = 30$ corresponds to the pulse duration (full width at half maximum) of around 30 fs, which is a typical parameter of the multi-cycle laser pulses generated by the commercial Ti:Sapphire laser system.

In the case of elliptical polarization, in the x-z plane, the laser electric field rotates successively with a period of $T = \frac{2\pi}{\omega}$. Here we introduce a rotating coordinate system (x', y', z'), where the direction of the laser electric field keeps unchanged (in z' axis).

In this coordinate system, the initial spatial coordinates of the tunneled electron are $x_0' = y_0' = 0$ and $z_0' = \eta_0$, where $\boldsymbol{\eta_0 = -I_p/F(t_0)}$ indicates the tunneling exit and t_0 the tunneling instant of the photoelectron. The initial photoelectron momenta are given by $p_{x'0} = p_\perp cos(\theta)$, $p_{y'0} = p_\perp sin(\theta)$, and $p_{z'0} = 0$, where $p_\perp$ is initial photoelectron transverse momentum and given randomly in the range of (0, 1.0 a. u.), θ is a random angle between $p_\perp$ and the x' axis in the plane of x'-y'.

In the laboratory coordinate system, the initial spatial coordinates of the tunneled electron are given by $x_0 = -\eta_0\ cos[arctan[\varepsilon\ tan(\omega t_0)]]$, $y_0 = 0$, $z_0 = -\eta_0\ sin[arctan[\varepsilon\ tan(\omega t_0)]]$ and the initial momenta are given by $p_{x0} = p_\perp cos\,\theta\, cos[arctan[\varepsilon\ tan(\omega t_0)]]$, $p_{y0} = p_\perp sin\,\theta$, $p_{z0} = -p_\perp cos\,\theta\, sin[arctan[\varepsilon\ tan(\omega t_0)]]$, where t_0 is photoelectron tunneling instant. The weight of the trajectory can be determined by [44, 46].

$$\omega\left(t_0, v_{per}\right) = \omega(0)\omega(1) \tag{4}$$

$$\omega(0) = \left|\frac{\left(2|I_p|\right)^2}{F(t_0)}\right|^{2/\sqrt{2|I_p|}-1} exp\left[\frac{-2\left(2|I_p|\right)\frac{3}{2}}{3|F(t_0)|}\right] \tag{5}$$

$$\omega(1) = \frac{v_{per}\sqrt{2|I_p|}}{\pi|F(t_0)|} exp\left[\frac{-v_{per}^2\sqrt{2|I_p|}}{|F(t_0)|}\right] \tag{6}$$

In the second step, the dynamics after tunneling can be described by a classical Newtonian equation [47–52],

$$\frac{d^2\vec{r}}{dt^2} = -\vec{F}(t) - \nabla V(r), \tag{7}$$

where the effective potential, $V(r)$, exerted on the tunneled electron is given by

$$V(r) = -\frac{Z_{eff}}{r}, \tag{8}$$

where $Z_{eff} = \sqrt{2I_p}$ is the effective charge of the ionic core, I_p the ionization potential of the atom in question and r the distance between the tunneled electron and the parent ionic core.

To numerically identify the electron trajectories contributed to RSE yields, along which the electrons will be captured by the Coulomb potential after the laser pulse ends, we search for the electron trajectories with the energies of $E_f = \mathbf{P}^2/2 - Z_{eff}/r < 0$, where $\mathbf{P} = \sqrt{P_x^2 + P_y^2 + P_z^2}$ is the final photoelectron sum momentum, E_f indicates the sum of kinetic energy and potential energy of the electron after the laser pulse ends. While the trajectories with energies of $E_f > 0$ will contribute to ionization yields. The weights of the corresponding photoelectron trajectories are summed up to calculate the yields of the RSE and ionization processes, respectively.

3 Nonadiabatic model

Compared to the CTMC model described above, in our nonadiabatic model, the initial photoelectron momenta, tunnel exit, and instantaneous ionization rate have been further corrected by the nonadiabatic effect [9, 12, 42, 43]. Based on the S-Matrix theory [53, 54], the transition probability from the groundstate to a continuum state can be described by $W = exp\{-2ImS\}$, where $S = \int_{t_s}^{t_0} dt\left\{\frac{1}{2}[\mathbf{P} + \mathbf{A}(t)]^2 + I_p\right\}$, $\mathbf{P} = (P_x, P_y, P_z)$ is the final photoelectron momentum after the laser pulse ends in the laboratory coordinate systems, $\mathbf{A}(t)$ the laser vector potential, and $t_s = t_0 + it_i$ the complex transition point, which can be obtained by the numerical solution of the saddle-point equation $[\mathbf{P} + \mathbf{A}(\mathbf{t_s})]^2 + 2I_p = 0$. The real part ($t_0$) of t_s is the above-mentioned photoelectron tunneling instant and the imaginary part (t_i) of t_s denotes the imaginary time spent by the electron in the sub-barrier process. The saddle-point equation can be rewritten by,

$$\begin{aligned}&\frac{1}{2}\left(P_z - F_0/\omega \sin\omega t_0 \cosh\omega t_i - iF_0/\omega \cos\omega t_0 \sinh\omega t_i\right)^2\\ &+\frac{1}{2}\left(P_x + \varepsilon F_0/\omega \cos\omega t_0 \cosh\omega t_i\right.\\ &\left.-i\varepsilon F_0/\omega \sin\omega t_0 \sinh\omega t_i\right)^2\\ &+\frac{1}{2}P_y^2 + I_p = 0\end{aligned} \tag{9}$$

The initial photoelectron momentum, $\mathbf{p} = (p_x, p_y, p_z)$, satisfies $\mathbf{p} = \mathbf{P} + \mathbf{A}(t_0)$. Thus, one can obtain

$$\begin{aligned}P_z &= p_z + F_0 \sin\omega t_0/\omega\\ P_x &= p_x - \varepsilon F_0 \cos\omega t_0/\omega\\ P_y &= p_y\end{aligned} \tag{10}$$

In the plane of the polarization ellipse, p_z and p_x relate to the initial photoelectron longitudinal ($p_\parallel$) and transverse ($p_\perp$) momentum, where the subscript $\parallel$ ($\perp$) indicates the direction parallel (perpendicular) to the transient laser polarization direction, in the rotating coordinate system by

$$\begin{aligned}p_z &= p_\parallel \cos\beta - p_\perp \sin\beta\\ p_x &= p_\parallel \sin\beta + p_\perp \cos\beta\end{aligned} \tag{11}$$

where $\beta = \tan^{-1}(\varepsilon \tan\omega t_0)$ is the angle between the transient laser polarization direction and the z axis in the x-z plane. Substituting Eqs 10, 11 into Eq. 9, one obtains

$$\cosh\omega t_i = \begin{cases}\frac{1}{a^4-\varepsilon^2}\left[\varepsilon\left(\frac{a\omega}{E_0}p_\perp - \varepsilon\right) \pm a^2 \times \sqrt{\left(\frac{a\omega}{E_0}p_\perp - \varepsilon\right)^2 + (a^4-\varepsilon^2)\left(1 + \frac{\gamma_{eff}^2}{a^2}\right)}\right], & a^2 \neq |\varepsilon|\\ \frac{1}{2}\left(1 - \frac{a\omega}{\varepsilon E_0}p_\perp\right) + \frac{a^2\left(1 + \frac{\gamma_{eff}^2}{a^2}\right)}{2\varepsilon^2\left(1 - \frac{a\omega}{\varepsilon E_0}p_\perp\right)}, & a^2 = |\varepsilon|\end{cases} \tag{12}$$

$$p_\parallel = \frac{(1-\varepsilon^2)F_0 \sin\omega t_0 \cos\omega t_0 (\cosh\omega t_i - 1)}{a\omega} \tag{13}$$

where $a = \sqrt{\cos^2\omega t_0 + \varepsilon^2 \sin^2\omega t_0}$ is the normalized instantaneous laser field and the effective Keldysh parameter $\gamma_{eff} = \omega\sqrt{2(I_p + p_{y0}^2/2)}/E_0$.

In the SFA theory, the electron sub-barrier trajectory can be described by $\mathbf{r}(t) = \int_{t_s}^{t} dt'[\mathbf{P} + \mathbf{A}(t')]$, and the tunnel exit is obtained with the real part of the sub-barrier trajectory at t_0, i.e., $\mathrm{Re}[\mathbf{r}(t_0, t_i)] = \mathrm{Re}[\int_{t_0+it_i}^{t_0} dt'[\mathbf{P} + \mathbf{A}(t')]]$. Thus, the coordinates of the tunnel exit $\mathbf{r}_0 = (x_0, y_0, z_0)$ can be given by,

$$\begin{aligned}x_0 &= \frac{\varepsilon F_0}{\omega^2}\sin\omega t_0 (1 - \cosh\omega t_i)\\ z_0 &= \frac{F_0}{\omega^2}\cos\omega t_0 (1 - \cosh\omega t_i)\\ y_0 &= 0\end{aligned} \tag{14}$$

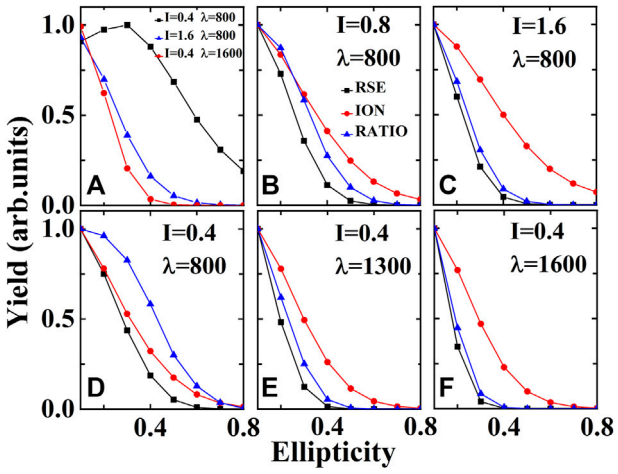

FIGURE 1
(A) The calculated ratio between the yields of RSE and ionization processes as a function of the ellipticity by the adiabatic semiclassical model. The laser intensities are indicated in the unit of $10^{14}W/cm^2$. The laser wavelengthes are 800 nm (black squares and blue triangles) and 1,600 nm (red circles). **(B–F)** The calculations by the nonadiabatic semiclassical model. The calculated normalized yields of RSE (black squares), ionization (red circles) and the ratio between them (blue triangles) as a function of the ellipticity at the intensities of **(D)** 0.4, **(B)** 0.8 and **(C)** 1.6 (in the unit of $10^{14}W/cm^2$) at 800 nm. The ellipticity dependence of the corresponding normalized yields at the wavelengthes of 800 nm **(D)**, 1300 nm **(E)**, 1600 nm **(F)** at $0.4\times10^{14}W/cm^2$ have also been presented.

The ionization probability can be obtained by,

$$\Gamma = \exp\left[-2\left(\frac{P^2}{2} + I_p + U_p\right)t_i + 2P_z\frac{F_0}{\omega^2}\sin\omega t_0 \sinh\omega t_i - 2P_x\frac{\varepsilon F_0}{\omega^2}\cos\omega t_0 \sinh\omega t_i + \frac{F_0^2(1-\varepsilon^2)}{4\omega^3}\cos 2\,\omega t_0 \sinh 2\,\omega t_i\right] \quad (15)$$

where $U_p = (1+\varepsilon^2)F_0^2/4\omega^2$ is the ponderomotive energy.

In our calculations, the tunneling time t_0 and the initial transverse momentum $p_\perp$ are given randomly in their corresponding parameter spaces. While, the initial longitudinal momentum, t_i, tunnel exit and instantaneous ionization probability rate can be obtained with Eqs 12–15, respectively. The following evolution of the photoelectron can be achieved by numerically solving the Newtonian equation Eq 7. The electron trajectories relevant to the RSE and ionization processes are found by the identical procedures described in the last section.

4 Results and discussion

The typical CTMC calculation results for Ar subject to strong elliptically polarized laser fields at a series of laser wavelengthes and intensities are presented in Figure 1A, where a maximum of the ratio between RSE and ionization yields at $\varepsilon = 0.3$ can be identified in the case of the laser pulse with an intensity of $0.4 \times 10^{14}W/cm^2$ and a wavelength of 800 nm. Moreover, the ratio maximum at a nonzero ellipticity disappears at the higher laser intensity or the longer wavelength in Figure 1A. The result is similar to the adiabatic semiclassical calculations in [31], except that the anomalous ratio maximum at a nonzero ellipticity persists at a higher intensity of $0.8 \times 10^{14}W/cm^2$ at 800 nm in [31]. The difference can be attributed to the fact that, compared to the 2-dimensional adiabatic semiclassical model employed in [31], where the influence of Coulomb potential has been overestimated, a 3-dimensional adiabatic semiclassical model, which could be closer to the real physical scenario, is employed in this work. The numerical results in [31] can be well reproduced if the photoelectron dynamics in our model are confined in the 2-dimensional polarization ellipse plane at $y = 0$.

In order to comprehend the ellipticity dependence of the ratio between the RSE and the ionization yields, based on the calculations of adiabatic model, we present the laser phase dependence of the initial photoelectron transverse momentum distributions at $\varepsilon = 0$, $\varepsilon = 0.1$, $\varepsilon = 0.3$ for tunneling (including the contributions of both ionization and RSE processes) (Figures 2A–C), ionization (Figures 2F–H) and RSE (Figures 2K–M), respectively. In addition, the distributions of the RSE process with $V(r) = 0$ applied in Eq. 7 except in the calculation of the final energy of the electron are depicted in Figures 2P–T. In this case, since the final kinetic energy of the tunneled electron is solely determined by the initial transverse momentum and tunneling phase which gives the acceleration $p = -A(t_i)$, the distribution shows a symmetric filled circle in Figure 2P) for $\varepsilon = 0$. When the ellipticity increases, the initial transverse momentum shifts toward positive direction to compensate the additional acceleration due to the increasing minor axis of the laser field. The distribution becomes asymmetric with respect to $p_\perp$ considering the Guassian distribution Eq. 6 (see Figures 2P, Q)). If the Coulomb potential is included in the calculation, comparing Figure 2P) with Figure 2K, the distribution is modified significantly. Firstly, the distribution region is enlarged prominently due to attraction of the Coulomb potential which reduces the final kinetic energy of the electron. Secondly, different regions inside the circle are modified in different manner due to influence of the Coulomb potential. The regions denoted by A and C, which possess large initial transverse momentum and tunneling moment near the crest of the field, are affected by the Coulomb potential most slightly because of relatively large initial transverse momentum which makes the electron move far away from the core during evolution after tunneling. When the tunneling phase moves away from the crest of the laser field, i. e., entering region B, the electron will move closer to the core due to relatively small initial transverse momentum and hence interact strongly with the Coulomb potential, resulting in decreased capture probability. Especially, according to the simple-man picture, electron tunneled out with positive phase ($\omega t_0 > 0$) will return to the core or return to re-cross the x-y plane if the initial transverse momentum of the electron is considered in the 3-dimensional case [55]. Rescattering of the electron upon the core, or in other words, strong interaction between the electron and the core, will significantly increase the kinetic energy that the electron gains in the field. This effect leads to missing upper part of the circle, especially for the small initial transverse

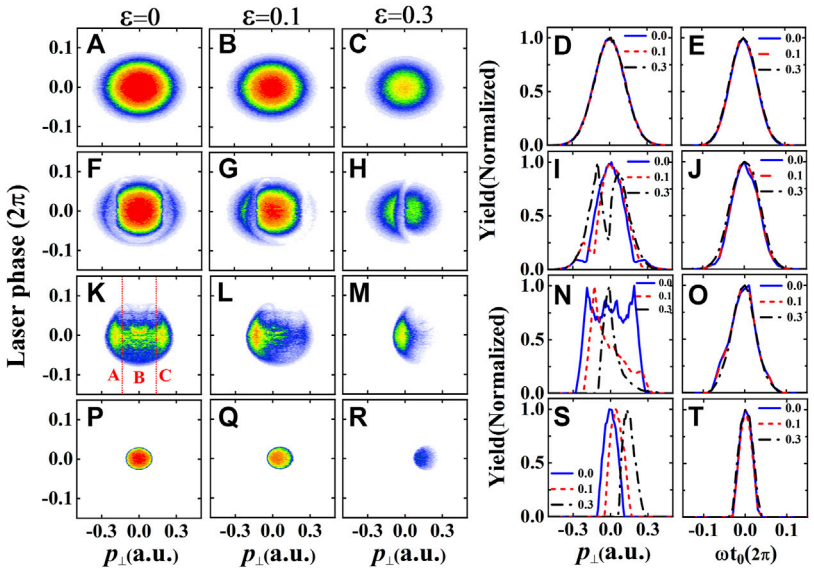

FIGURE 2
The laser phase dependence of the initial photoelectron transverse momentum distributions for tunneling **(A–C)**, ionization **(F–H)** and RSE **(K–M)**, **(P–R)** processes at the ellipticities of ε =0 **(A, F, K, P)**, ε =0.1 **(B, G, L, Q)**, ε =0.3 **(C, H, M, R)**. The initial photoelectron transverse momentum distributions in **(D, I, N,S)** and laser phase distributions in **(E, J, O, T)** are extracted from the data of **(A–C)**, **(F–H)**, **(K–M)** and **(P–R)**, respectively. These data are calculated by the CTMC model with the laser intensity of 4×10^{13}W/cm^2 and the wavelength of 800 nm. For the data in **(P–R)**, the Coulomb potential corrections of the photoelectron trajectories are ignored. Please find more details in the text.

momentum region, resulting in two symmetric hook-like structures shown in Figure 2K. For the region of negative tunneling phase (ωt_0 < 0) considered here, the electron will also return to re-cross the x-y plane due to attraction of the Coulomb potential though it should directly move out without return according to the simple-man picture which does not take into account the Coulomb potential. Depending on the initial condition, some of the tunneled electrons will interact with the core strongly, gains large kinetic energy and escapes. It is noteworthy that the overall shape of the RSE region is very similar to that obtain by the 2-dimensional simulation in Ref. [31], the distribution inside the RSE region possesses more structures for the 3-dimensional calculation while it is almost empty for the 2-dimensional simulation. This difference can be attributed to that, in 2-dimensional case, the electron will interact with the core much strongly and then gains enough energy to escape, resulting in two symmetric crescent-like structures, while, in the 3-dimensional case, the situation is much more complicated. Note that there are even more structures near the center of the RSE region which can be ascribed to chaotic behavior of the electron moving in the combined Coulomb potential and external laser field. Many electrons will experience multiple returns and some may even circle around the core many time before they move away from the core [56], giving rise to complex structures in the region. When the ellipticity increases, the RSE region shifts to the positive direction of the initial transverse momentum for the same reason as that in the calculation without considering Coulomb potential (Figures 2P–R). To show the ellipticity dependent probabilities more clearly, we plot the distributions of initial transverse momentum (integral over tunneling phase) and tunneling phase (integral over initial transverse momentum) in the right two columns in Figure 2. One can find that all the distributions of tunneling phase are symmetric with respect to the crest of the laser field and hardly change with increasing ellipticity while the distributions of initial transverse momentum change noticeably with ellipticity. For the calculation without taking into account the Coulomb potential in evolution, the distribution of RSE shifts toward positive momentum but the shape keeps unchanged (see Figure 2S). When the Coulomb potential is fully considered, the distribution of RSE becomes much broader and possesses multi-peak structure for ε = 0. It shifts toward positive momentum and changes to a single-peak distribution with increasing ellipticity. This can be understood that since the distribution of the tunneling hardly changes with ellipticity, the regions B and C drop fast when the distribution of RSE shifts, so only the peak in region A remains. In addition, when the ellipticity increases, the peak in the region A shift toward the peak of the distribution of tunneling and coincides with the peak of tunneling at ε = 0.3, thus the ratio between RSE and ionization yields increases and reaches maximum at ε = 0.3. If the ellipticity increases further, the peak in the region A shifts away from the peak of tunneling distribution and thus drops quickly (see black squares in Figure 1A).

To understand the laser intensity and wavelength dependence of the ratio between the RSE yields and the ionization yields in Figure 1A, the laser phase dependence of the initial photoelectron transverse momentum distributions for tunneling, ionization and RSE processes at the ellipticities of 0.1 and 0.3 at a

10.3389/fphy.2023.1120654

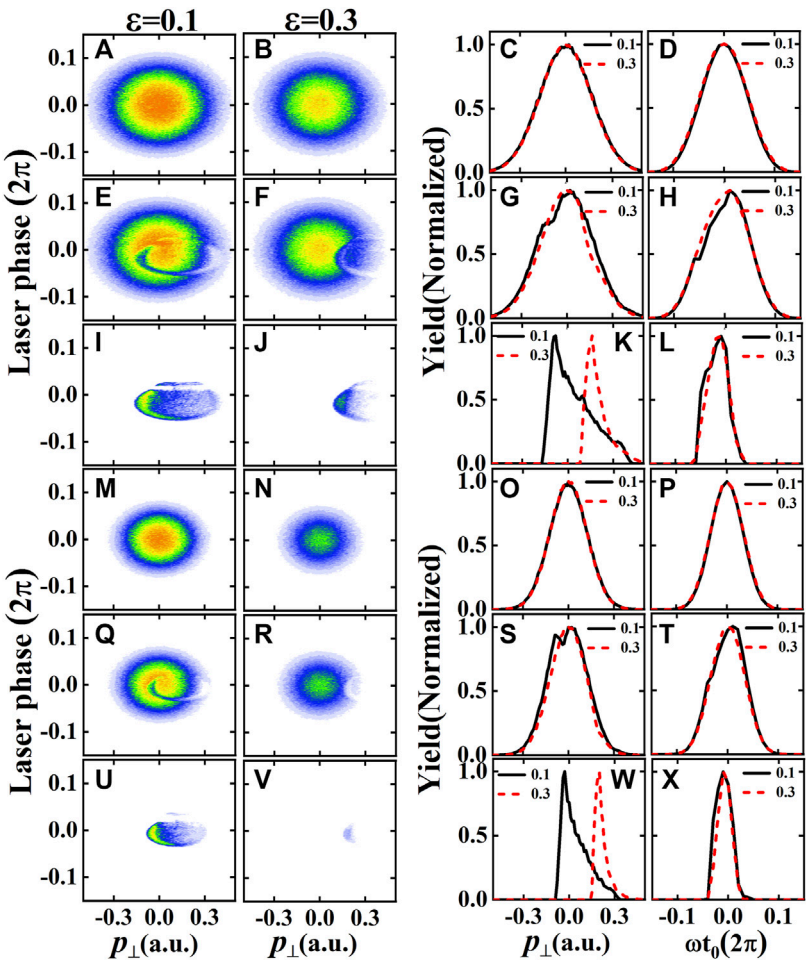

FIGURE 3
The laser phase dependence of the initial photoelectron transverse momentum distributions for tunneling **(A, B, M, N)**, ionization **(E, F, Q, R)** and RSE **(I, J, U, V)** processes at the ellipticities of ε =0.1 **(A, E, I, M, Q, U)**, ε =0.3 **(B, F, J, N, R, V)**. The initial photoelectron transverse momentum distributions in **(C, G, K, O, S, W)** and laser phase distributions in **(D, H, L, P, T, X)** are extracted from the data of **(A, B, E, F, I, J, M, N, Q, R, U, V)**, respectively. The laser intensities are 1.6×10^{14}W/cm^2 **(A–L)** and 0.4×10^{14}W/cm^2 **(M–X)**. The laser wavelengthes are 800 nm **(A–L)** and 1,600 nm **(M–X)**. These data are calculated by the CTMC model.

higher intensity of 1.6×10^{13}W/cm^2 (at 800 nm) and a longer wavelength of 1,600 nm (at 0.4×10^{14}W/cm^2) are given in Figure 3. Firstly, we concentrate on the laser intensity dependence of the ratio between RSE and ionization yields. When the intensity increases, the tunneling exit shifts toward the core and hence leads to stronger rescattering effect of the tunneled electron. Moreover, considering that the kinetic energy of the electron gained from the laser field is proportional to the intensity, the tunneling phase will be reduced significantly in the positive direction for the initial phase distribution of RSE. In the negative direction of the tunneling phase, since these electrons interact with the core softly, the distribution also shrinks but not so prominently as that in the positive direction. Therefore, the maximum of the RSE distribution shifts to negative tunneling phase as can be seen in Figures 3I–L) which show clear asymmetry with respect to the crest of the laser field. In this case, when the ellipticity increases, the RSE distribution shifts toward positive momentum but the maximum will miss the peak of the tunneling phase distribution (see Figures 3I, J), resulting in decreasing ratio of RSE/Ion as shown in Figure 1A (blue triangles) for high intensity. The same analysis given above can also be applied to the case of longer wavelength (1,600 nm) depicted in Figure 3. It should be noted that, since the intensity of the laser field is the same as that used in Figure 2, the tunneling exit does not shift but the kinetic energy gained by the electron, which is proportional to $U_p \propto I\lambda^2$, is the same as that of the high intensity case for 800 nm, so the asymmetry in the tunneling phase direction is less pronounced than that of the former case (comparing Figure 3X) with Figure 3L)). However, the maximum is still in the negative tunneling phase and it will also miss the peak of the tunneling phase distribution with increasing ellipticity, giving rise to decreasing ratio of RSE/Ion shown in Figure 1A (red circles).

Based on the above analysis of the CTMC calculation results, we further investigate the nonadiabatic effect on the ratio of RSE yields over ionization yields. The calculations with the nonadiabatic model are presented in Figures 1B–F). As shown

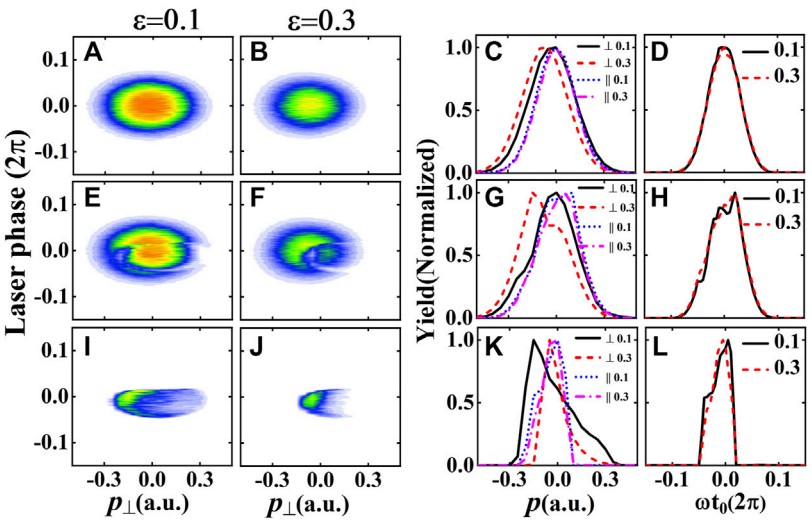

FIGURE 4
The laser phase dependence of the initial photoelectron transverse momentum distributions for tunneling **(A, B)**, ionization **(E, F)** and RSE **(I, J)** processes at the ellipticities of ε =0.1 **(A, E, I)**, ε =0.3 **(B, F, J)**. The initial photoelectron transverse momentum distributions in **(C, G, K)** and laser phase distributions in **(D, H, L)** are extracted from the data of **(A, B)**, **(E, F)**, and **(I, J)**, respectively. The initial photoelectron longitudinal momentum distributions for tunneling **(C)**, ionization **(G)** and RSE **(K)** are also presented. These data are calculated by the nonadiabatic model with the laser intensity of 4×10^{13}W/cm^2 and the wavelength of 800 nm.

in these panels, with rising ellipticity, both the ionization and RSE yields decrease rapidly. With closer inspection, the RSE yields decrease even faster than the ionization yields for all the laser intensities and wavelengthes investigated in this work. It can be found that the slope of the ellipticity dependence of RSE (ionization) yields becomes more and more steep (flat) for higher laser intensities or longer wavelengthes. As a result, the ratios between the RSE yields and the ionization yields become steeper with rising ellipticity for stronger laser intensities or longer wavelengthes. Therefore, the ratio maximum at a nonzero ellipticity disappear if the nonadiabatic effect has been considered in the semiclassical model.

The calculation results of the nonadiabatic model are in stark contrast to those in [31] (and also the data in Figure 1A), where a radical maximum of the ratio can be identified at $\varepsilon \approx 0.2$ (or ε = 0.3) at 800 nm. On the contrary, the calculation results of nonadiabatic model are qualitatively consistent to those in [32], where the RSE yields also decrease faster at higher laser intensity. Considering that our CTMC calculations qualitatively match the results in [31] where the nonadiabatic effect has been ignored, we can conclude that the nonadiabatic effect must be the physical origin behind the difference between the results of [31, 32].

To comprehend the influence of the nonadiabatic effect on the ellipticity dependence of the ratio, we present the laser phase dependence of the initial photoelectron transverse momentum distributions for tunneling, ionization and RSE processes at the ellipticities of ε = 0.1 and ε = 0.3 in Figure 4. Although the laser parameters of Figure 4 is identical to those of Figure 2, **as** well documented (see, e.g., [9]), the nonadiabatic effect will lead to a shift of the tunneling exit to the core, compared to its adiabatic counterpart. Therefore, the contribution of the rescattering process could be significantly enhanced, giving rise to the shift of the RSE area to the negative direction of the laser phase. Furthermore, in contrast to the zero photoelectron longitudinal momentum employed in the CTMC model, a significant nonzero photoelectron longitudinal momentum is introduced by the nonadiabatic effect. As shown in Ref. [54], the initial longitudinal momentum is always along the direction of $-A(t)$, i. e., the final kinetic energy of the tunneled electron will be increased if the initial longitudinal momentum is taken into account. So the RSE distribution shrinks in the direction of tunneling phase. In addition, in the falling edge of the laser field where the electron is expected to return to the x-y plane in the simple-man picture, the initial longitudinal momentum always points to the core, so the rescattering effect is also enhanced, which will reduce the distribution in the positive initial longitudinal momentum region. As shown in Figures 4K, L), strong asymmetry can be found in the distributions of initial longitudinal momentum and tunneling phase for RSE process. Therefore, the nonadiabatic modification of the tunneling exit and the initial photoelectron longitudinal momentum lead to that laser phase range of RSE area in Figures 4I–LJ) becomes narrower and shifts to the negative direction of laser phase, if compared to the results in Figures 2L, M, O. Meanwhile, the laser phase range of the tunneling areas in Figures 4A, B, D is still symmetric (close to that of Figures 2A, B, D). Thus, with rising ellipticity, the dominant yields of RSE distribution will miss the peak of the tunneling distribution (Figure 4A), which, in turn, leads to the absence of the ratio maximum at a nonzero ellipticity.

In Figure 5, calculation results by the nonadiabatic model at a higher laser intensity and a longer wavelength are presented. At a higher intensity, as shown in Figures 5A, B, D, the laser phase

10.3389/fphy.2023.1120654

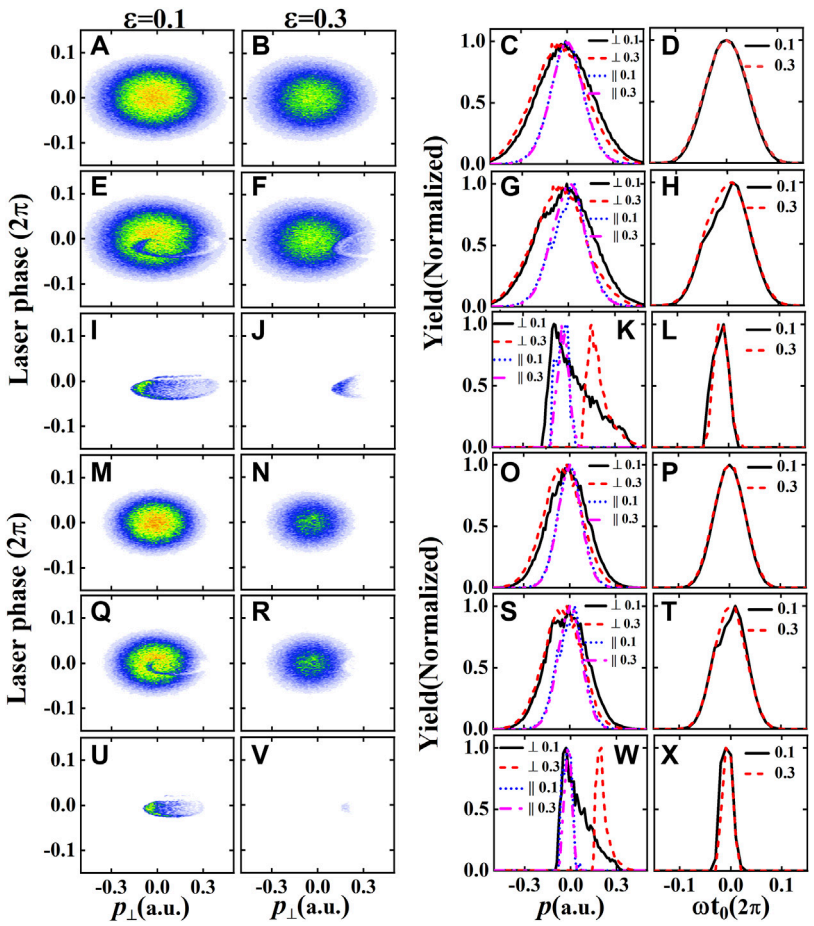

FIGURE 5
The laser phase dependence of the initial photoelectron transverse momentum distributions for tunneling **(A, B, M, N)**, ionization **(E, F, Q, R)** and RSE **(I, J, U, V)** processes at the ellipticities of ε =0.1 **(A, E, I, M, Q, U)** and ε =0.3 **(B, F, J, N, R, V)**. The initial photoelectron transverse momentum distributions in **(C, G, K, O, S, W)** and laser phase distributions in **(D, H, L, P, T, X)** are extracted from the data of **(A, B, (E, F, I, J, M, N, Q, R, U, V)**, respectively. The initial photoelectron longitudinal momentum distributions for tunneling **(C,O)**, ionization **(G, S)** and RSE **(K, W)** are also presented. The laser intensities are 1.6×10^{14}W/cm^2 **(A–L)** and 0.4×10^{14}W/cm^2 **(M–X)**. The laser wavelengthes are 800 nm **(A–L)** and 1,600 nm **(M–X)**. These data are calculated by the nonadiabatic model.

ranges of the tunneling areas become wider, compared to its lower intensity counterpart (see Figures 4A, B, D). In the meantime, at the higher intensity, the width of lase phase range of the RSE distribution hardly changes and but its peak shifts to the negative direction of laser phase due to the larger contribution of rescattering process, resulting from shift of tunneling exit towards the core at higher laser intensity. Thus, the peak of the RSE distribution shifts by passing the region farther away from the tunneling distribution with rising ellipticity than that in the lower intensity case, which, in turn, leads to a monotonous faster decrease of the ratio (comparing Figures 1C, D). In the case of a longer wavelength, in Figures 5M, N, P, the laser phase ranges of the tunneling areas are close to the case of 800 nm (see Figures 4A, B, D). However, the laser phase ranges of the RSE areas become obviously narrower and shifts to negative laser phase compared to the case of 800 nm due to the larger photoelectron acceleration by the laser field at the longer wavelength. In addition, since the acceleration of the field is proportional to E_0/ω, the RSE distribution shifts much faster in the initial transverse momentum axis for long wavelength case comparing with the shorter wavelength with the same intensity (comparing Figures 5U–W with Figures 4I–K). Thus, the ratio of RSE/Ion decreases faster with rising ellipticity for longer wavelength than that in the 800 nm case which can be clearly seen by comparing Figures 1D, F).

5 Conclusion

Using a semiclassical model where the nonadiabatic effect can be chosen to be included or ignored, we found that the documented anomalous behavior of the ratio between RSE and the ionization yields, which maximizes at a nonzero ellipticity, is absent when the nonadiabatic effects are taken into account. Our analysis indicates that this result can be attributed to the nonadiabatic modification of the tunneling exit and the initial momentum distribution of the tunneled electron at the tunneling exit.

Data availability statement

The original contributions presented in the study are included in the article/supplementary material further inquiries can be directed to the corresponding authors.

Author contributions

ZW and WQ performed the calculations; ZW, WQ, JC, XH, and XL performed the data analysis; WQ, JC, and XH. planned the calculations and supervised the work; all authors contributed to the discussion of the results; the manuscript was prepared by ZW, WQ, JC, XH, and XL.

Funding

This work is supported by the National Key Research and Development Program (No. 2019YFA0307700), the National Natural Science Foundation of China (Nos. 11834015, 11974383, 12121004 and 12274273), the Science and Technology Department of Hubei Province (No. 2020CFA029).

Acknowledgments

We thank Prof. Y. M. Zhou for his help and stimulating discussions.

Conflict of interest

The authors declare that the research was conducted in the absence of any commercial or financial relationships that could be construed as a potential conflict of interest.

Publisher's note

References

1. Protopapas M, Keitel C, Knight P. Atomic physics with super-high intensity lasers. *Rep.Prog.Phys.* (1997) 60:389–486. doi:10.1088/0034-4885/60/4/001

2. Keldysh L. Ionization in the field of a strong electromagnetic wave. *Sov.Phys.JETP.* (1965) 20(5):1307–14.

3. Milosevic DB, Fritz E. Scattering and reaction processes in powerful laser fields. *Adv.At.Mol.Opt.Phys.* (2003) 49:373–532. doi:10.1016/S1049-250X(03)80007-1

4. Agostini P, DiMauro L. Atoms in high intensity mid-infrared pulses. *Contemp.Phys.* (2008) 49:179–97. doi:10.1080/00107510802221630

5. Walker B, Mevel E, Yang B, Breger P, Chambaret J, Antonetti A, et al. Double ionization in the perturbative and tunneling regimes. *Phys.Rev.A* (1993) 48:R894–R897. doi:10.1103/PhysRevA.48.R894

6. Mevel E, Breger P, Trainham R, Petite G, Agostini P, Migus A, et al. Atoms in strong optical fields: Evolution from multiphoton to tunnel ionization. *Phys.Rev.Lett.* (1993) 70:406–9. doi:10.1103/PhysRevLett.70.406

7. Chaloupka J, Rudati J, Lafon R, Agostini P, Kulander K, DiMauro L. Observation of a transition in the dynamics of strong-field double ionization. *Phys.Rev.Lett.* (2003) 90: 033002. doi:10.1103/PhysRevLett.90.033002

8. Colosimo P, Doumy G, Blaga C, Wheeler J, Hauri C, Catoire F, et al. Scaling strong-field interactions towards the classical limit. *NaturePhysics* (2008) 4:386–9. doi:10.1038/nphys914

9. Yudin G, Ivanov M. Nonadiabatic tunnel ionization: Looking inside a laser cycle. *Phys.Rev.A* (2001) 64:013409. doi:10.1103/PhysRevA.64.013409

10. Boge R, Cirelli C, Landsman A, Heuser S, Ludwig A, Maurer J, et al. Probing nonadiabatic effects in strong-field tunnel ionization. *Phys.Rev.Lett.* (2013) 111:103003. doi:10.1103/PhysRevLett.111.103003

11. Ni H-C, Eicke N, Ruiz C, Cai J, Oppermann F, Nikolay I, et al. Tunneling criteria and a nonadiabatic term for strong-field ionization. *Phys.Rev.A* (2018) 98:013411. doi:10.1103/PhysRevA.98.013411

12. Landsman A, Keller U. Attosecond science and the tunnelling time problem. *Phys.Rep.* (2015) 547:1–24. doi:10.1016/j.physrep.2014.09.002

13. Klaiber M, Hatsagortsyan K, Keitel C. Tunneling dynamics in multiphoton ionization and attoclock calibration. *Phys.Rev.Lett.* (2015) 114:083001. doi:10.1103/PhysRevLett.114.083001

14. Corkum P. Plasma perspective on strong field multiphoton ionization. *Phys.Rev.Lett.* (1993) 71:1994–7. doi:10.1103/physrevlett.71.1994

15. Shiner A, Schmidt B, Trallero H, Wörner H, Patchkovskii S, Corkum PB, et al. Probing collective multi-electron dynamics in xenon with high-harmonic spectroscopy. *Nat.Phys.* (2011) 7:464–7. doi:10.1038/NPHYS1940

16. Gao X-Z, Landsman AS, Cao H-B, Zhang Y-P, Wang Y-S, Fu Y-X, et al. Influence of initial tunneling step on the return energy of high-order harmonic generation. *Phys.Rev.A* (2022) 106:053105. doi:10.1103/PhysRevA.106.053105

17. Becker W, Liu X-J, Ho P, Eberly J. Theories of photoelectron correlation in laser-driven multiple atomic ionization. *Rev.Mod.Phys.* (2012) 84:1011–43. doi:10.1103/RevModPhys.84.1011

18. Paulus GG, Nicklich W, Xu H, Lambropoulos P, Walther H. Plateau in above threshold ionization spectra. *Phys.Rev.Lett.* (1994) 72:2851–4. doi:10.1103/PhysRevLett.72.2851

19. Nubbemeyer T, Gorling K, Saenz A, Eichmann U, Sandner W. Strong-field tunneling without ionization. *Phys.Rev.Lett.* (2008) 101:233001. doi:10.1103/PhysRevLett.101.233001

20. Zhang Z-Y, Guo J, Gu B-L, Hao L, Yang G-G, Wang K, et al. Parametric amplification of Rydberg six- and eight-wave mixing processes. *PhotonicsResearch* (2018) 6:000713. doi:10.1364/PRJ.6.000713

21. Eichmann U, Nubbemeyer T, Rottke H, Sandner W. Acceleration of neutral atoms in strong short-pulse laser fields. *Nature* (2009) 461(7268):1261–4. doi:10.1038/nature08481

22. Shomsky K, Smith Z, Haan S. Frustrated nonsequential double ionization: A classical model. *Phys.Rev.A* (2009) 79:061402(R). doi:10.1103/PhysRevA.79.061402

23. Manschwetus B, Nubbemeyer T, Gorling K, Steinmeyer G, Eichmann U, Rottke H, et al. Strong laser field fragmentation ofH2: Coulomb explosion without double ionization. *Phys.Rev.Lett.* (2009) 102:113002. doi:10.1103/PhysRevLett.102.113002

24. McKenna J, Gaire CK, Esry B, Ben I, Zohrabi M, Johnson NG, et al. Frustrated tunneling ionization during laser-induced D^2 fragmentation: Detection of excited metastable D^* atoms. *Phys.Rev.A* (2011) 84:043425. doi:10.1103/PhysRevA.84.043425

25. Hu S-L, Hao X-L, Lv H, Liu M-Q, Yang T-X, Xu H-F, et al. Quantum dynamics of atomic Rydberg excitation in strong laser fields. *Opt.Express.* (2019) 27:031629. doi:10.1364/OE.27.031629

26. Liu M, Xu S, Hu S, Becker W, Quan W, Liu X, et al. Electron dynamics in laser-driven atoms near the continuum threshold. *Optica* (2021) 8:765. doi:10.1364/optica.418636

27. Xu S, Liu M, Hu S, Shu Z, Quan W, Xiao Z, et al. Observation of a transition in the dynamics of strong-field atomic excitation. *Phys.Rev.A* (2020) 102:043104. doi:10.1103/PhysRevA.102.043104

28. Sun F-H, Lu C-X, Ma Y-Z, Pan S-Z, Wang J-W, Zhang W, et al. Orbital effects in strong-field Rydberg state excitation of N_2, Ar, O_2 and Xe. *Opt.Express.* (2021) 29:31240. doi:10.1364/OE.437437

29. Landsman A, Pfeiffer A, Hofmann C, Smolarski M, Cirelli C, Keller U. Rydberg state creation by tunnel ionization. *NewJ.Phys.* (2013) 15:013001. doi:10.1088/1367-2630/15/1/013001

30. Zhao L, Dong J-W, Lv H, Yang T-X, Lian Y, Jing M-X, et al. Ellipticity dependence of neutral Rydberg excitation of atoms in strong laser fields. *Phy.Rev.A* (2016) 94: 053403. doi:10.1103/PhysRevA.94.053403

31. Zhao Y, Zhou Y, Liang J, Zeng Z, Ke Q, Liu Y, et al. Frustrated tunneling ionization in the elliptically polarized strong laser fields. *Opt.Express.* (2019) 27:21689. doi:10.1364/OE.27.021689

32. Pauly T, Bondy A, Hamilton K, Douguet N, Tong X-M, Chetty D, et al. Ellipticity dependence of excitation and ionization of argon atoms by short-pulse infrared radiation. *Phy.Rev.A* (2020) 102:013116. doi:10.1103/PhysRevA.102.013116

33. Nagai M, Mukai N, Minowa Y, Ashida M, Takayanagi J, Ohtake H. Achromatic THz wave plate composed of stacked parallel metal plates. *Opt.Letters.* (2014) 39:146. doi:10.1364/OL.39.000146

34. Strelkov VV. Theory of high-order harmonic generation and attosecond pulse emission by a low-frequency elliptically polarized laser field. *Phys.Rev.A* (2006) 74:013405. doi:10.1103/PhysRevA.74.013405

35. Zhou X-B, Lock R, Wagner N, Li W, Kapteyn H, Murnane MM. Elliptically polarized high-order harmonic emission from molecules in linearly polarized laser fields. *Phys.Rev.Lett.* (2009) 102:073902. doi:10.1103/PhysRevLett.102.073902

36. Sun F-J, Chen C, Li W-Y, Liu X, Li W, Chen Y-J. High ellipticity of harmonics from molecules in strong laser fields of small ellipticity. *Phy.Rev.A* (2021) 103:053108. doi:10.1103/PhysRevA.103.053108

37. Chen J, Liu J, Chen S-G. Rescattering effect on phase-dependent ionization of atoms in two-color intense fields. *Phy.Rev.A* (2000) 61:033402. doi:10.1103/PhysRevA.61.033402

38. Hao X-L, Wang G-Q, Jia X-Y, Li W-D, Liu J, Chen J. Nonsequential double ionization of Ne in an elliptically polarized intense laser field. *Phys.Rev.A* (2009) 80:023408. doi:10.1103/PhysRevA.80.023408

39. Quan W, Lin Z, Wu M, Kang H, Liu H, Liu X, et al. Classical aspects in above-threshold ionization with a midinfrared strong laser field. *Phys.Rev.Lett.* (2009) 103:093001. doi:10.1103/PhysRevLett.103.093001

40. Wang Y-L, Xu S-P, Chen Y-J, Kang H-P, Lai X-Y, Quan W, et al. Wavelength scaling of atomic nonsequential double ionization in intense laser fields. *Phys.Rev.A* (2017) 95:063415. doi:10.1103/PhysRevA.95.063415

41. Quan W, Hao X, Chen Y, Yu S, Xu S, Wang Y, et al. Long-range Coulomb effect in intense laser-driven photoelectron dynamics. *Sci.Rep.* (2016) 6:27108. doi:10.1038/srep27108

42. Trabert D, Anders N, Brennecke S, chöffler M, Jahnke T, Schmidt L, et al. Nonadiabatic strong field ionization of atomic hydrogen. *Phys.Rev.Lett.* (2021) 127:273201. doi:10.1103/PhysRevLett.127.273201

43. Xiao Z, Quan W, Yu S, Lai X, Liu X, Wei Z, et al. Nonadiabatic strong field ionization of noble gas atoms in elliptically polarized laser pulses. *Opt.Express.* (2022) 30:14873. doi:10.1364/OE.454846

44. Ammosov M, Delone N, Krainov V. Tunnel ionization of complex atoms and of atomic ions in an alternating electromagnetic field. *Sov.Phys.JETP.* (1986) 64(6):2008–13.

45. Delone N, Krainov V. Energy and angular electron spectra for the tunnel ionization of atoms by strong low-frequency radiation. *J.Opt.Soc.Am.B.* (1991) 8:1207. doi:10.1364/JOSAB.8.001207

46. Perelomov A, Popov V, Terent'ev M. Ionization of atoms in an alternating electric field. *Sov.Phys.JETP.* (1967) 24:207.

47. Brabec T, Ivanov MY, Corkum P. Coulomb focusing in intense field atomic processes. *Phys.Rev.A* (1996) 54:R2551–4. doi:10.1103/PhysRevA.54.R2551

48. Chen J, Liu J, Fu L-B, Zheng WM. Interpretation of momentum distribution of recoil ions from laser-induced nonsequential double ionization by semiclassical rescattering model. *Phys.Rev.A* (2000) 63:011404(R). doi:10.1103/PhysRevA.63.011404

49. Fu L-B, Liu J, Chen J, Chen S-G. Classical collisional trajectories as the source of strong-field double ionization of helium in the knee regime. *Phys.Rev.A* (2001) 63:043416. doi:10.1103/PhysRevA.63.043416

50. Chen J, Liu J, Zheng W-M. Characteristic photoelectron spectra and angular distributions of single and double ionization. *Phys.Rev.A* (2002) 66:043410. doi:10.1103/PhysRevA.66.043410

51. Ye D-F, Liu X, Liu J. Classical trajectory diagnosis of a fingerlike pattern in the correlated electron momentum distribution in strong field double ionization of helium. *Phys.Rev.Lett.* (2008) 101:233003. doi:10.1103/PhysRevLett.101.233003

52. Xia Q-Z, Ye D-F, Fu L-B, Han X-Y, Liu J. Momentum distribution of near-zero-energy photoelectrons in the strong-field tunneling ionization in the long wavelength limit. *Sci.Rep.* (2015) 5:11473. doi:10.1038/srep11473

53. Becker W, Grasbon F, Kopold R, Milošević D, Paulus G, Walther H. Above-threshold ionization: From classical features to quantum effects. *Adv.At.Mol.Opt.Phys.* (2002) 48:35–98. doi:10.1016/S1049-250X(02)80006-4

54. Li M, Liu M, Geng J, Han M, Sun X, Shao Y, et al. Experimental verification of the nonadiabatic effect in strong-field ionization with elliptical polarization. *Phys.Rev.A* (2017) 95:053425. doi:10.1103/PhysRevA.95.053425

55. Paulus G, Becker W, Nicklich W, Walther H. Rescattering effects in above-threshold ionization: A classical model. *J.Phys.B* (1994) 27:L703–8. doi:10.1088/0953-4075/27/21/003

56. Chen J, Nam CH. Ion momentum distributions for He single and double ionization in strong laser fields. *Phys.Rev.A* (2002) 66:053415. doi:10.1103/PhysRevA.66.053415

Frontiers in Physics

Investigates complex questions in physics to understand the nature of the physical world

Addresses the biggest questions in physics, from macro to micro, and from theoretical to experimental and applied physics.

Discover the latest Research Topics

See more →

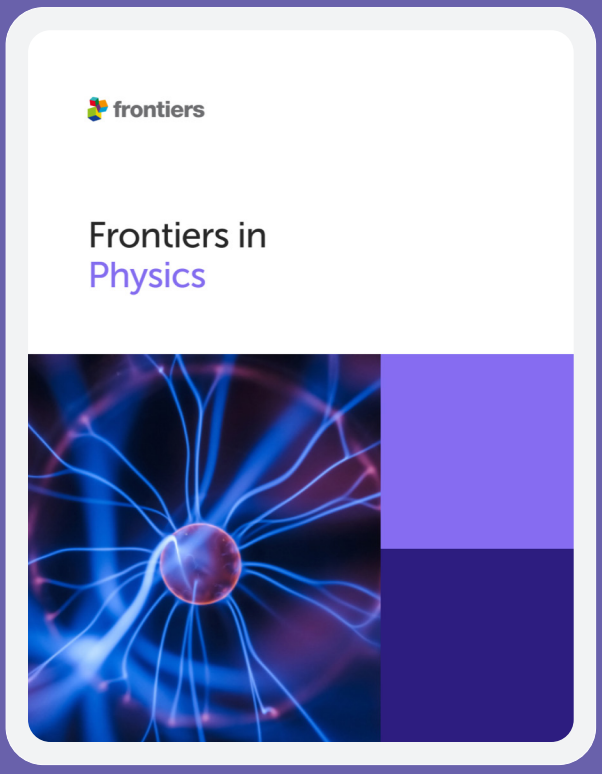

Frontiers

Avenue du Tribunal-Fédéral 34
1005 Lausanne, Switzerland
frontiersin.org

Contact us

+41 (0)21 510 17 00
frontiersin.org/about/contact